Implementation of Multiple Image Radiography on Tilted Laue Analyser-Based Phase-Contrast Imaging

Author:
Jayan J. Gunasekera

Supervisors:
Dr. Konstantin M. Pavlov and A/Prof. Marcus J. Kitchen

A thesis submitted in fulfilment of the requirements for the degree of Master of Science.

Date: June 14, 2021

Abstract

Phase contrast X-ray imaging is a promising imaging modality, which is capable of differentiating minute structural differences inside the object with similar attenuating properties. Tilted Laue analyser-based phase-contrast imaging is a variation of the traditional Analyser-Based Imaging setup, which uses a tilted position of the analyser crystal with respect to the rotation axis of the sample. This essentially eradicates the limitation of one-dimensional phase sensitivity of Analyser-Based Imaging and allows one to extract both the orthogonal components of the two-dimensional phase gradients. The work presented in this thesis introduces a new variation of multiple image radiography where the rocking curve without (intrinsic rocking curve) and with (sample rocking curve) the sample present in the beam is estimated using two different mathematical models. In this body of work, the intrinsic rocking curves were estimated using the Pseudo-Voigt (PsV) model, while the sample rocking curves were estimated using the Lorentzian model. The application of multiple image radiography on tilted Laue analyser-based phase-contrast imaging allowed the reconstruction of attenuation, phase, and the ultra small-angle scattering information simultaneously. This study successfully reconstructed this information for two samples, namely the three-material phantom and the clay loam sample. The experimental estimations of the imaginary part, β, of the index of refraction for Perspex ($C_5H_8O_2$), PTFE (C_2F_4), and Aluminium in the three-material phantom deviated from the theoretical β values by approximately 7%, 5%, and 11%, respectively. The experimental estimations for the real part, δ, of the index of refraction for PTFE and Aluminium in the three-material phantom overestimated their theoretical δ values by approximately 35%, while for Perspex the experimental estimation overestimated its theoretical δ value by approximately 36%. Three-dimensional images of ultra small angle scattering information of both the three-material phantom and the clay loam sample provided evidences that tilted Laue analyser-based phase-contrast imaging could potentially be used for directional dark-field imaging. Furthermore, by comparing the β map, δ map, and the ultra small angle scattering information reconstructions of clay loam particulates this study has shown that the application of multiple image radiography on tilted Laue analyser-based phase-contrast imaging will provide complementary information regarding structures in micrometre length scale.

Acknowledgements

I owe a debt of gratitude to both of my supervisors, Dr Konstantin M. Pavlov and A/Proff Marcus J. Kitchen, for their advice, guidance, and immeasurable patience throughout this project.

To Dr Konstantin M. Pavlov, thank you for always subtly pushing me to read more, patiently explaining to me the theoretical basis for x-ray phase-contrast imaging, driving me to present at conferences, and always reminding me to be on schedule. To A/Proff Marcus J. Kitchen, thank you for patiently explaining to me the workings of the multiple image radiography algorithm, helping me with my code, and all the insights you have given me on improving my writing skills. Both of you have equally encouraged me to try new ideas and constructively question the findings of this thesis. I appreciate everything you have done for me.

Furthermore, I would like to thank the team, namely, M.J. Kitchen, K. Uesugi, D.M. Paganin, T.E. Gureyev, I.M. Young, G. Falzon, P. R. Quin, and K.M. Pavlov, who was involved in acquiring the data reconstructed in this thesis. Special thanks to Dr P.R. Quin for providing me with information regarding the clay loam sample, and Dr K. Uesugi for taking time to discuss the anomalous behaviour seen on the analyser crystal angular position. The experimentations for data acquisition were performed at beamline BL20B2 of SPring-8 with the approval of the Japan Synchrotron Radiation Research Institute (JASRI) (Proposal 2012B1315). Also, a special thanks to the International Synchrotron Access Program (ISAP) managed by the Australian Synchrotron, part of ANSTO (AS/IA124/6149), for providing necessary travel funding.

Finally, I would like to thank my parents for their unconditional support and faith in me throughout my studies. Without the love and support of my family, this thesis would not have been possible.

Contents

List of Figures

List of Tables

Chapter 1

Introduction

Since the conception of x-ray imaging by Wilhem Conrad Röntgen in 1895, there have been numerous developments (Bradley, 2008). These developments have led x-ray based imaging systems to become one of the most commonly used diagnostic imaging tools in diagnostic medicine. Though current systems give us the ability to image human body in intricate detail, conventional radiographic images still have some loss of information, especially in soft tissue contrast (Pfeiffer et al., 2013). It is because conventional radiography is based only on the effects of attenuation of x-rays as they traverse the imaging object, and it does not explicitly use both the effects of refraction and scattering of x-rays.

The principle interactions between matter and x-ray photons at diagnostic energies (between 20 keV and 150 keV (Bushberg et al., 2011)) are photoelectric absorption, coherent (Rayleigh or elastic scattering) and incoherent scattering (Compton or inelastic scattering) (IAEA, 2014). In photoelectric absorption, when a photon interacts with a bound electron of a material its total energy is absorbed and transferred to the bound electron. Since x-ray interaction to orbital electrons are highly dependent upon the atomic number of the sample (Spiers, 1946; White, 1977) for a lower energy photon traversing a sample with a high Z (atomic number) material the dominant interaction becomes the photoelectric absorption. Mass attenuation coefficient for photoelectric absorption is proportional to the Z^3/E^3 and its change is most noticeable at absorption edges (e.g.,*K-edge*) of a material (Podgoršak, 2010). The *K-edge* energy represents the minimum energy required to eject K-shell electrons. Soft tissue is mostly comprised of materials such as carbon, hydrogen, oxygen and water (Zhou and Brahme, 2008). All these elements have very low energy *K-edges*. As depicted in figure 1.1, mass attenuation coefficient for soft tissue decreases rapidly with increasing x-ray energies for photoelectric cross section. Typically, conventional attenuation-based imaging modalities provide lower contrast-to-noise ratio while imaging soft tissue because of weak photoelectric absorption in materials with low atomic numbers (Bushberg et al., 2011). Therefore, to increase absorption contrast in such materials, low energy x-rays are used. A downside of using low energy x-rays is the substantial increase in radiation dose to the patient (Bushberg et al., 2011).

In conventional attenuation-based x-ray imaging, both Rayleigh and Compton scattering are considered as interactions causing background noise (IAEA, 2014). In Rayleigh scattering, the atom is neither ionised nor excited due to the incident photon. After the interaction, the bound electrons will return to its original state. The atom will absorb the momentum transferred by

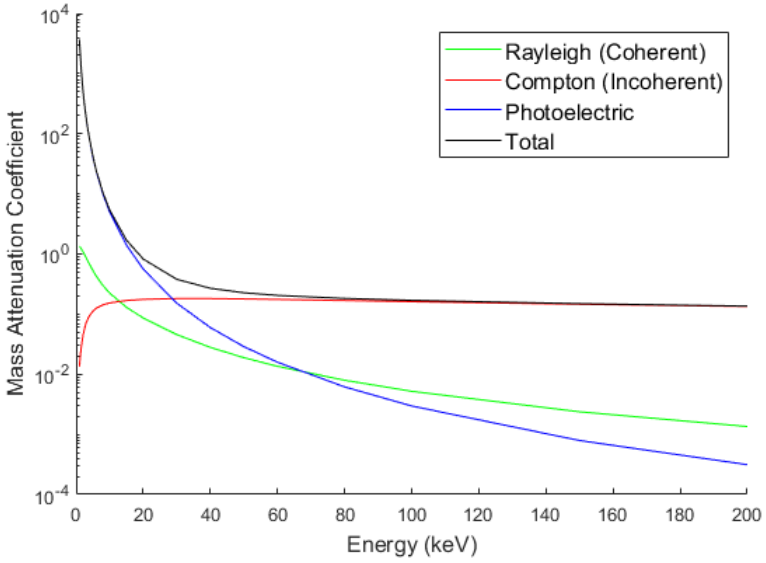

Figure 1.1: *Mass attenuation coefficient as a function of varying x-ray energies for soft tissue, and principle interaction cross sections. Generated using XCOM: Photon Cross Section Database (Berger et al., 2010). Soft tissue composition was taken from ICRU Report 44 (ICRU, 1989).*

the incident photon and scatter it with a small angular deviation with respect to the propagation direction of the incident photon. The energy of incident and scattered photon are essentially the same. The average angular deviation of the scattering photon is dependent on the Z of the absorber and the incident photon energy (Podgoršak, 2010). Compton scattering is the interaction of photons with a free or loosely bound electron, which becomes a recoil electron. After the interaction, a scattered photon with energy less than the energy of the incident photon will deflect with an angle θ with respect to the incident direction of the photon, and the loosely bound electron will be ejected from the atom with an angle of ϕ with respect to the incident photon direction. The two angles θ and ϕ are related to each other. This relationship can be derived using conservation of momentum to be (Podgoršak, 2010):

$$\cot\phi = (1+\varepsilon)\tan\frac{\theta}{2}. \tag{1.1}$$

here, $\varepsilon = h\nu/m_e c^2$ where, $h\nu$ is the incident photon energy and $m_e c^2$ is the electron rest mass energy (0.511keV)[1]. At higher energies the Compton scattering dominates the photoelectric effect for lower Z materials such as soft tissue (Bushberg et al., 2011). This is shown in figure 1.1. Though photon scattering may play a significant role in characterising properties of soft tissue, its effect is eliminated or ignored in conventional attenuation-based imaging (Zhou and Brahme, 2008).

Contrarily, phase-contrast imaging (PCI) utilizes measurements of disturbances in phase of the x-ray wavefield traversing the sample giving rise to phase contrast. The main advantage of PCI over conventional attenuation-based imaging is that it enables differentiation of structures with similar attenuation properties. PCI also gives higher signal-to-noise (SNR) and contrast-to-noise (CNR) ratios with respect to attenuation-based imaging for the same radiation dose

[1] A detailed derivation can be found in Podgoršak (2010)

(Gureyev et al., 2014). When a wavefield traverses through structures with different densities, the direction of the wave fronts changes. These changes in the wavefront can be understood using electromagnetic interactions in the matter, where the index of refraction can be used to characterize optical properties of material[2] (Paganin, 2006). Some variants of PCI are also capable of capturing sub-pixel structures, which are typically responsible for ultra small angle scattering (USAXS)[3] (Wernick et al., 2003).

For x-rays, the directional changes in the wavefront is very small. The intensity variations due to these directional changes can be measured using specialised optical setups. Zernike, in the 1940s, first introduced phase-contrast methods using visible light (Zernike, 1942, 1955). Then in mid 1990s, x-ray phase-contrast was first reported, leading to numerous studies for the development of different techniques for x-ray PCI (Zhou and Brahme, 2008). Because of PCI's unique abilities, in recent years it has been studied extensively for the purpose of biomedical applications (Bravin et al., 2013).

There are a multitude of techniques currently in use that employ PCI. Four commonly used techniques are reviewed in section 2.3. However, the focus of this thesis is the x-ray PCI method known as tilted Laue analyser-based imaging (TLABI)[4], which is capable of extracting 2D information about the phase gradient (Chalmers et al., 2021) and USAXS.

1.1 Aim and Motivation

The aim of this thesis is the reconstruction and analysis of the three-dimensional (3D) images of attenuation, phase, and USAXS information of two samples using Multiple Image Radiography (MIR)[5] (Wernick et al., 2003). As part of this thesis work, MIR has been successfully implemented on TLABI for the first time to extract attenuation, phase, and USAXS properties.

TLABI is a novel variant of the traditional analyser-based imaging (ABI)[6], which was first introduced by Chalmers et al. (2021). ABI is a phase contrast imaging technique, which employ a highly sensitive, near perfect analyser crystal to render phase contrast. This high sensitivity helps to capture fine variations in the x-ray wavefield due to changes in density within the imaging object. In typical ABI setups, the analyser crystal is only sensitive to the gradient of phase along the axis perpendicular to the crystallographic planes of the analyser crystal (vertical axis). This means if the imaged sample were to produce phase contrast in lateral directions, the traditional ABI setup will neglect these contributions. This limitation of one-dimensional (1D) phase sensitivity is true for most other commonly used PCI techniques, with the exception of Propagation-based PCI. Rutishauser et al. (2011) proposed a method to overcome this limitation using grating based PCI setup[7]. In their seminal work, they showed that the extraction of two-dimensional (2D) phase contrast is possible by simply tilting the gratings. For ABI, Chalmers et al. (2021) successfully demonstrated that using the new TLABI variant, the extraction of quantitative 2D phase contrast is possible.

[2] See section 2.1 for a detailed review.
[3] See section 2.2 for a detailed description of USAXS
[4] Section 3.1 give detailed description on TLABI experimental setup.
[5] See subsection 2.4.2 for a detailed description on MIR.
[6] See subsection 2.3.6 for a detailed review on ABI
[7] Grating based phase contrast imaging method is reviewed in section 2.3.4

The way Chalmers et al. (2021) achieved 2D phase contrast was by tilting the sample and the detector by 8° around the optical axis during imaging, while using ABI in Laue geometry. An advantage of the Laue geometry is that it allows the acquisition of the diffracted image and the transmitted image simultaneously. Essentially, images were taken around the Bragg position at multiple analyser crystal angular positions (working points) producing the rocking curves with (sample) and without (intrinsic) the sample present in the beam. Chapter 3 of this thesis provides a detailed description of this experimental setup and the process of data acquisition.

Chalmers et al. (2021) only utilised the images at the two working points at half the peak intensity of the rocking curve, which restricted them from extracting the USAXS information. This body of work extends the work carried out by Chalmers et al. (2021) to the USAXS regime by implementing MIR on TLABI for the first time. An advantage of MIR is that it can produce the attenuation, phase, and the USAXS information simultaneously. To use MIR, images were taken around the Bragg position at eight working points with the sample and 261 working points without the sample. By comparing these curves on a pixel-by-pixel basis, one can extract the attenuation, phase, and the USAXS images. Subsection 2.4.2 provides a detailed description of MIR.

The raw images used in the reconstructions were acquired using a fibre optic taper camera. A disadvantage of this detector is that the fibre optic taper causes the photons to deviate from its rectilinear trajectory. This results in an asymmetrical distortion in images (Islam et al., 2010). This work presents a robust and efficient Python-based distortion correction method in chapter 3 as a solution to the asymmetrical distortion generated by the camera. For a successful extraction of attenuation, phase, and USAXS information, one should first find the mathematical models that would best estimate the said rocking curves. Therefore, chapter 4 is dedicated to the analysis of potential mathematical models. The literature in ABI always utilises the same mathematical model to estimate both the intrinsic rocking curve and the sample rocking curve. In this body of work, for the first time, the two curves will be fitted with two different mathematical models. This work also introduces an analytical solution to estimate the angular position of the analyser crystal for each image taken around the rocking curve using the Lorentzian function in chapter 4.

The extraction of 2D phase information was done by using the two opposing centroid shift images, one at tomographic angular position ψ and the other at $\psi + 180°$. Essentially, these projections enabled the separation of the horizontal and the vertical components of the phase gradients. Then using 2D Fourier integration the horizontal and the vertical components of the phase gradients were combined to give the 2D phase maps of the sample. Thereafter, 180° tomographic reconstruction was performed to reconstruct the δ map. Subsection 2.4.3 of this thesis provides a detailed description of 2D phase retrieval using TLABI and chapter 5 presents its implementation. Furthermore, chapter 5 also presents the tomographic reconstructions of attenuation and phase for two samples.

To accurately reconstruct the USAXS information, the scattering function must be deconvolved from the sample rocking curve. Therefore, chapter 6 will be dedicated to the study of two deconvolution techniques, namely the Wiener and Richardson-Lucy deconvolution methods. Furthermore, chapter 6 presents the tomographic reconstruction of USAXS information for two

samples. Finally, chapter 7 is dedicated to discuss possible avenues of future research and a detailed thesis conclusion.

Chapter 2

Theory

A thorough understanding of the theory which constitutes the nature of x-ray interactions with matter is essential for understanding phase-contrast imaging. This chapter introduces the theory of electromagnetic waves and provides a theoretical foundation for phase-contrast x-ray imaging. This chapter will provide a description on USAXS, and it will briefly review four phase-contrast x-ray imaging techniques, which are in competition with ABI. This is followed by a detailed description of ABI and MIR, which is the focus of the thesis. Finally, a description is given of the two-dimensional phase retrieval process and computed tomography.

2.1 Coherent X-ray Optics

This section introduces the fundamental concepts one would require to describe different forms of phase-contrast x-ray imaging techniques.

2.1.1 Wave Equations and Spectral Decomposition

The most fundamental concept one requires from electromagnetism to describe x-ray PCI is the propagation of scalar fields. Therefore, let us begin by defining the complex scalar field function, $\Psi(x, y, z, t)$ where x, y, and z corresponds to the three spatial coordinates for each spatial dimension, respectively, and t corresponds to time. In free space, this complex scalar function obeys the d'Alembert equation, so that (Paganin, 2006):

$$\left(\frac{1}{c^2}\frac{\partial^2}{\partial t^2} - \nabla^2\right)\Psi(x, y, z, t) = 0. \tag{2.1}$$

In equation (2.1), $\nabla^2 = (\frac{\partial^2}{\partial x^2}) + (\frac{\partial^2}{\partial y^2}) + (\frac{\partial^2}{\partial z^2})$ is the Laplacian operator in three dimensions, and c is the speed of light, which is defined using the dielectric constant (permittivity) of free space ε_0 and the magnetic permeability of free space μ_0 to be,

$$c = \frac{1}{\sqrt{\varepsilon_0 \mu_0}}. \tag{2.2}$$

Following the approach taken by Paganin (2006), lets consider a set of monochromatic waves travelling in vacuum where these waves are represented by the complex scalar function

$\Psi(x, y, z, t)$. Given some general conditions[1] are satisfied by this scalar function we may use the Fourier integral to describe it (Paganin, 2006):

$$\Psi(x, y, z, t) = \frac{1}{\sqrt{2\pi}} \int_0^\infty \psi_\omega(x, y, z) \exp(-i\omega t) d\omega. \tag{2.3}$$

The Fourier integral above, in equation (2.3) allows us to regard any wave as a superposition of monochromatic fields. This is also known as spectral decomposition of a complex analytic signal (Paganin, 2006; Mandel and Wolf, 1995). Each monochromatic wave is described by the $\psi_\omega(x, y, z) \exp(-i\omega t)$ and the subscript ω denotes the functional dependence of the spatial wave-function, $\psi_\omega(x, y, z)$ on angular frequency. The $\exp(-i\omega t)$ represents the harmonic time factor.

2.1.2 The Helmholtz Equation

If we assume that the wave field is strictly monochromatic, making it perfectly temporally coherent, we can reduce the wave function[2] to $\psi_\omega(x, y, z) \exp(-i\omega t)$, describing a wave oscillating with a fixed angular frequency. Substituting this wave function into the d'Alembert equation (2.1) would give us the time-independent Helmholtz equation in a vacuum:

$$\left(\nabla^2 + k^2\right) \psi_\omega(x, y, z) = 0. \tag{2.4}$$

where k is the wave number related to the vacuum wavelength λ:

$$k = \frac{2\pi}{\lambda}. \tag{2.5}$$

The Helmholtz equation is usually used to describe the imaging process when the beam of x-rays is monochromatic or quasi-monochromatic. This is common in situations where x-ray imaging is performed at a synchrotron, where a monochromator is used. However, in clinical practice we will be dealing with polychromatic wave fields. The ability to describe monochromatic wave fields using spectral decomposition is advantageous as it permits us to describe the imaging process using the time-independent Helmholtz equation and combine it within a polychromatic wave field (Pelliccia et al., 2018).

So far the focus was on developing the theory for monochromatic waves travelling in an empty space. However, any form of x-ray imaging requires us to develop an understanding of the effects of introducing a sample into the wave field, meaning the space is no longer empty. Therefore, let us generalise the time-independent Helmholtz equation in a vacuum (equation (2.4)) to account for the existence of scattering media. First, let's assume the sample media is static, non-magnetic and spatially slowly varying. Then we are able to describe the sample media by introducing a quantity called the index of refraction $n(x, y, z)$[3]. This quantity is both position and frequency dependent, yet time-independent (Pelliccia et al., 2018). The index of refraction defines a change in wavelength and wave speed in medium. Thus,

[1] Detailed descriptions can be found on Mandel and Wolf (1995) chapter 3.
[2] The complex scalar function $\Psi(x, y, z, t)$ is also known as the wave function as it describes a wave-field.
[3] Also known as the refractive index.

$$\lambda \longrightarrow \frac{\lambda_\omega}{n_\omega(x,y,z)}, \tag{2.6}$$

therefore,

$$k \longrightarrow k n_\omega(x,y,z). \tag{2.7}$$

Hence, equation (2.4), the Helmholtz equation in a vacuum, can be rewritten as,

$$\left(\nabla^2 + k^2 n_\omega^2(x,y,z)\right)\psi_\omega(x,y,z) = 0. \tag{2.8}$$

This is the time-independent Helmholtz equation describing a monochromatic wave field in the presence of sample media.

2.1.3 Index of Refraction

As described in section 2.1.2, the index of refraction plays a vital role when describing electromagnetic waves in the presence of sample media. Hence, it is important for us to understand the characteristics of it in the x-ray energies. Therefore, this section will be devoted to discussing the index of refraction.

At a given wavelength λ, the index of refraction describes the effect on electrons in matter due the electromagnetic wave field, and it can be expressed as a complex quantity (Paganin, 2006):

$$n = 1 - \delta + i\beta. \tag{2.9}$$

Here δ is the real function which describes refraction and β is the imaginary part which describes the effect of attenuation. Figure 2.1 illustrates how β is considerably smaller than δ for typical medical radiography energies (IAEA, 2014).

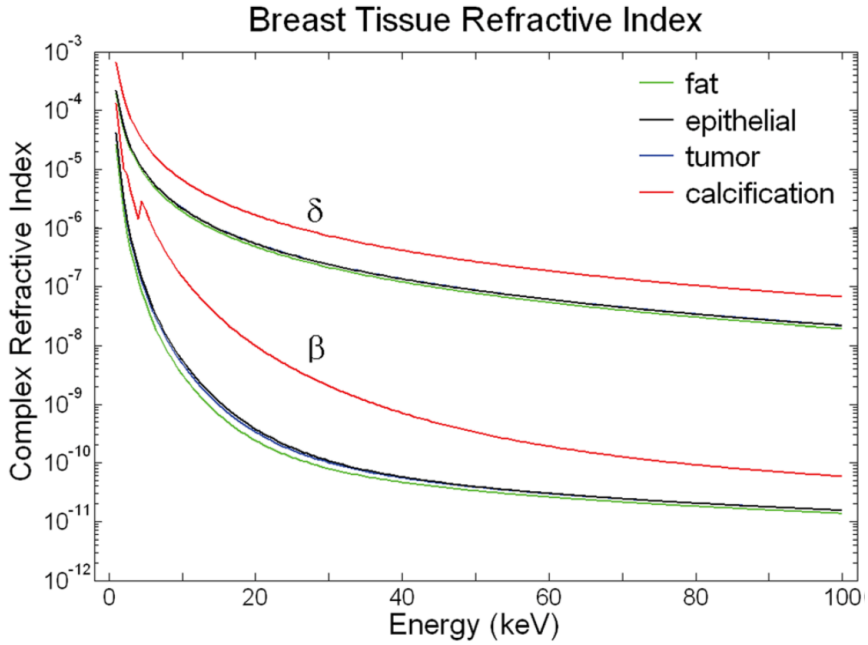

Figure 2.1: *β and δ over a range of x-ray energies for fat, epithelial, tumour and calcification in breast tissue (Zysk et al., 2012). Reproduced with permission.*

The index of refraction is related to the total atomic form factor $f(\mathbf{Q},\omega) = f^{(0)}(\mathbf{Q}) + f'(\omega) + if''(\omega)$, where $f'(\omega)$, and $f''(\omega)$, respectively, correspond to the real and the imaginary components of the dispersion corrections for the classical atomic form factor $f^{(0)}(\mathbf{Q})$. $f^{(0)}(\mathbf{Q})$ is the Fourier Transform of the charge density normalised to Z (atomic number) at the scattering vector $\mathbf{Q} = 0$ (Als-Nielsen and McMorrow, 2011). It is worth noting that $\mathbf{Q} = 0$ describes elastic scattering in the forward direction. The atomic form factor provides a measure of the scattering contribution due to an isolated single atom. It is defined by the type of scattering and, therefore, the nature of the incident radiation (e.g., electron, photon, neutron etc.). In this thesis we shall focus only on x-ray radiation, and x-rays are typically scattered by the electron cloud of a given sample. Therefore, the scattering contribution depends on the atomic number Z.

Dispersion corrections are frequency-dependent. Therefore, we may use the dispersion corrections to describe the frequency dependence of the index of refraction as (Als-Nielsen and McMorrow, 2011),

$$n^2 = 1 + \left(\frac{e^2\rho_e}{\varepsilon_0 m_e}\right)\frac{1}{(\omega_s^2 - \omega^2 - i\omega\Gamma)} \tag{2.10}$$

where, e is the charge of an electron, ρ_e is the density of electrons, ε_0 is the electrical permittivity of free space and m_e is the mass of an electron. ω, ω_s and Γ represent the wave field frequency, the resonant frequency and the damping constant, respectively. The imaginary part, representing the absorption, peaks when $\omega = \omega_s$. For frequencies where $\omega < \omega_s$ then the index of refraction is greater than 1. This is typical for the optical regime of the electromagnetic spectrum. For frequencies where $\omega > \omega_s$ the index of refraction is less than 1. This is typical in the x-ray regime of the spectrum[4]. Also, it is worth noting that scattering and refraction are different viewpoints of the same physical phenomenon.

In the x-ray regime, the relationship between the atomic form factor and the index of refraction is as follows (Als-Nielsen and McMorrow, 2011; Willmott, 2011).

$$n = 1 - \frac{2\pi\rho_{at}r_0}{k^2}[f^0(0) + f'(\omega) + if''(\omega)] \tag{2.11}$$

where, k is the wave vector equalling $2\pi/\lambda$, ρ_{at} is the atomic number density, r_0 (2.818×10^{-15} m) is the classical radius of an electron and $f^0(0)$ represents the scattering in the forward direction.

At energies above the absorption peak, where $\omega > \omega_s$, the index of refraction drops below unity. This means that the phase velocity will have a value greater than the speed of light. Though the phase velocity is greater than the speed of light, the group velocity which describes the energy transfer will stay bellow speed of light, preserving the laws of special relativity (Als-Nielsen and McMorrow, 2011).

In equation (2.10) if $\omega \gg \omega_s \gg \Gamma$ the index of refraction reduces to

$$n \approx 1 - \frac{1}{2}\frac{e^2\rho_e}{\varepsilon_0 m_e\omega^2} = 1 - \frac{2\pi\rho_e r_0}{k^2}. \tag{2.12}$$

Therefore the real function describing the refraction from equation 2.9 is equal to,

[4]Refer to Als-Nielson and McMorrow (2011) for a detailed description

$$\delta = \frac{2\pi\rho_e r_0}{k^2} = \frac{2\pi\rho_e r_0 \hbar^2 c^2}{E^2}. \tag{2.13}$$

where, $\hbar$ is the modified version of plank constant, E^2 is the photon energy. Therefore, δ is inversely proportional to the square of the photon energy, emphasising the fact that the real part of the index of refraction differs only very slightly from unity (Als-Nielsen and McMorrow, 2011). Hence, it can be challenging to extract the real part of the index of refraction (Ruiz-Yaniz et al., 2015).

Snell's Law

As explained in the section above, when an x-ray beam traverse through the sample, variations in refractive indices in the sample will refract the traversing x-rays changing their amplitude and phase leading to a slight angular change in the incident x-ray beam (wave-field). Snells law describes these angular change as (Als-Nielsen and McMorrow, 2011),

$$\frac{\cos\theta}{\cos\theta'} = n_r \tag{2.14}$$

where, n_r is the real part of the refractive index, θ is the incident angle and θ' is the refracted or reflected angle (see figure 2.2).

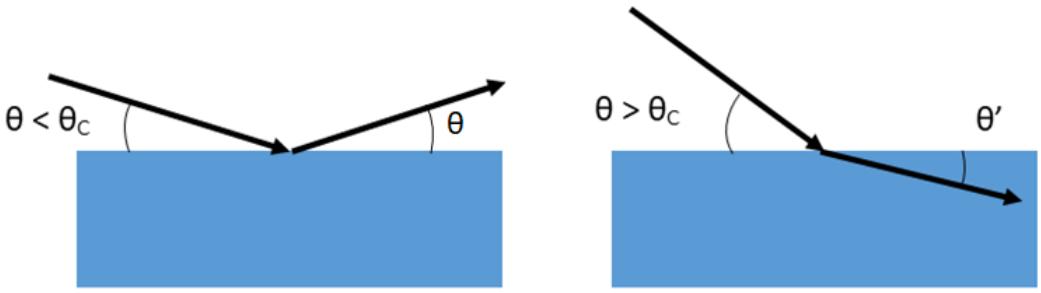

Figure 2.2: *The reflection and refraction of x-rays where the index of refraction is less than unity. Reflection occurs when the incident angle θ is less than the critical angle θ_c. Refraction occurs when the incident angle θ is greater than the critical angle θ_c. Here, θ' refers to the refracted or reflected angle and when $\theta' = 0$, the θ_c will equal the incident angle θ.*

Attenuation

As well as scattering, attenuation also takes place in a given sample as an electromagnetic wave traversing through it. The imaginary part of the refractive index refers to the attenuation, as described by equation (2.9). Let us consider the general case where an electromagnetic wave traversing through a homogeneous sample with a thickness, z. The drop of intensity of the wave by an amount of e over a distance of μ^{-1} is defined as attenuation. Here, μ is known as the linear attenuation coefficient. The intensity of the wave is reduced exponentially while traversing a distance of z inside the sample, and it is expressed by the Beer-Lambert law of attenuation,

$$\frac{I}{I_0} = \exp\left(-\int_0^{z'} \mu(z)dz\right). \tag{2.15}$$

Here, I is the intensity after traversing z' distance and I_0 is the initial incident intensity. Now if we consider the index of refraction to be a complex function, the wave traversing through the sample can be expressed as $E_0 \exp(ikz - \delta ikz) \exp(-\beta kz)$. Since the intensity is proportional to the square modulus of the amplitude, from equation (2.15), β can be deduced to be $\mu/2k$.

From equations 2.11 and 2.9, f'' the imaginary part of the dispersion correction is related to β by,

$$\beta = \frac{2\pi\rho_{at} r_0}{k^2} f''. \tag{2.16}$$

As f'' is inversely proportional to the square of photon energy after the absorption edge (Willmott, 2011), it is evident from equation 2.16 that the β reduces as the forth power of photon energy.

2.1.4 Coherent Paraxial Fields

It is possible to generate highly directional fields with smaller angular spread known as beams (Pelliccia et al., 2018; Mandel and Wolf, 1995). One can use the the angular spectrum of plane waves to acquire a representation of a beam (Mandel and Wolf, 1995). However, here we will be looking at an alternative method considering a wave travelling in the positive z-direction as a solution to the homogeneous Helmholtz equation (2.4):

$$\psi(x, y, z) = \Phi(x, y, z) e^{ikz}. \tag{2.17}$$

here, the ω term is dropped as we consider a strictly monochromatic wave field. For a homogeneous plane wave propagating in the z-direction, Φ can be considered to be constant. However, in reality, for any wave that is propagating close to z-axis, $\Phi(x, y, z)$ will certainly fluctuate with x, y, and z. But considering the angular spread of this wave to be sufficiently small, we may expect $\Phi(x, y, z)$ to fluctuate extremely slowly with respect to its propagation direction z. This allows $\psi(x, y, z)$ to propagate with beam-like proprieties in z-direction. With this in mind we shall rewrite the Helmholtz equation (2.4) as,

$$\left(\frac{\partial^2}{\partial x^2} + \frac{\partial^2}{\partial y^2} + \frac{\partial^2}{\partial z^2}\right)\left(\Phi(x, y, z) e^{ikz}\right) + k^2 \Phi(x, y, z) e^{ikz} = 0 \tag{2.18}$$

Now,

$$\frac{\partial^2}{\partial z^2}\left(\Phi(x, y, z) e^{ikz}\right) \cong \left(-2ik\frac{\partial}{\partial z} - k^2\right) \Phi(x, y, z) e^{ikz}. \tag{2.19}$$

As we are considering the angular variations to be sufficiently small with respect to the propagation distance z, we can see that the change in $\Phi(x, y, z)$ within an interval of z of the order of wavelength must be small compared to $\Phi(x, y, z)$ itself. Therefore, it can be shown that $\left|\frac{\partial \Phi(x,y,z)}{\partial z}\right| \ll k \left|\Phi(x, y, z)\right|$ and $\left|\frac{\partial^2 \Phi(x,y,z)}{\partial z^2}\right| \ll k^2 \left|\frac{\partial \Phi(x,y,z)}{\partial z}\right|$ (Mandel and Wolf, 1995; Pelliccia et al., 2018). Hence, on neglecting the term $\frac{\partial^2 \Phi}{\partial z^2}$ with respect to $\frac{\partial \Phi}{\partial z}$ and $k^2\Phi$ we find that,

$$\nabla_T^2 \Phi(x, y, z) + 2ik\frac{\partial \Phi(x, y, z)}{\partial z} = 0. \tag{2.20}$$

This is known as the *paraxial* homogeneous Helmholtz equation, where ∇_T^2 denotes the transverse Laplacian $\nabla_T^2 = \left(\frac{\partial^2}{\partial x^2}\right) + \left(\frac{\partial^2}{\partial y^2}\right)$. Furthermore, since we can assume that the paraxial conditions

to be true in a medium, following a similar argument and using equation (2.8), we can write the paraxial inhomogeneous Helmholtz equation in a medium as,

$$\nabla_T^2\Phi(x,y,z) + 2ik\frac{\partial\Phi(x,y,z)}{\partial z} + k^2(n^2(x,y,z)-1)\Phi(x,y,z) = 0. \tag{2.21}$$

The mathematical formalism of paraxial fields helps to simplify the equations used in phase contrast imaging and helps to simplify phase retrieval algorithms (Pelliccia et al., 2018).

2.1.5 Projection Approximation and Visualising X-ray Phase Contrast

Let's consider a monochromatic plane wave travelling in the z-direction traversing through a static non-magnetic sample, as shown in figure 2.3. For hard x-rays, the index of refraction being smaller than unity (see section 2.1.3) means that the strength at which x-rays will interact with the sample matter will be very small. It is, nonetheless, incredibly useful when developing the underpinning mathematics.

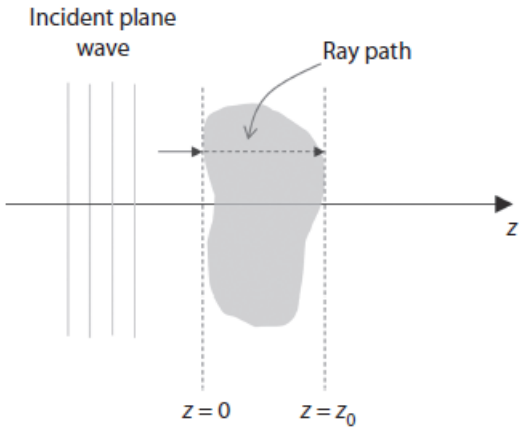

Figure 2.3: *A plane wave propagating in the positive z direction is incident upon the sample at $z = 0$ and exit the sample at $z = z_0$ under the projection approximation (Pelliccia et al., 2018). Reproduced with permission.*

Here we aim to find the wave function that will describe the wave exiting the sample at $z = z_0$ in terms of both the entrance wave function at $z = 0$ and the index of refraction distribution of the object. Assuming all x-rays follow a straight line with negligible scattering/refraction within the sample when traversing through it, (depicted in figure 2.3 as *a ray path*) we can approximate the exiting wave as,

$$\frac{\partial\Phi(x,y,z)}{\partial z} \approx \frac{k}{2i}(1-n^2(x,y,z))\Phi(x,y,z). \tag{2.22}$$

this is known as the *projection approximation*. Equation 2.22 is derived from the paraxial inhomogeneous Helmholtz 2.21 by dropping the transverse Laplacian term, which is responsible for coupling the neighbouring ray trajectories. This is because we make the assumption that there is negligible scattering and the accumulated transverse changes in the phase and amplitude by the unscattered wavefront are imprinted in the exiting wave (Paganin, 2006; Pelliccia et al., 2018).

Paganin (2006) showed that one can solve the boundary value problem for the partial differential equation (2.22) and obtain the wave field when $z = z_0$ to be,

$$\Phi(x, y, z_0) \approx \exp\left[\frac{k}{2i}\int_{z=0}^{z=z_0}(1 - n^2(x, y, z)dz\right]\Phi(x, y, z = 0). \tag{2.23}$$

Since, $\delta, \beta \ll 1$ for hard x-rays, we can make the approximation $n^2 \approx 1-2\delta+2i\beta$. Therefore, we get,

$$\Phi(x, y, z_0) \approx \exp\left[-ik\int_{z=0}^{z=z_0}(\delta(x, y, z) - i\beta(x, y, z))dz\right]\Phi(x, y, z = 0). \tag{2.24}$$

According to equation 2.24, the phase shift imparted on an x-ray wave field as it traverses through a weakly scattering sample, under the projection approximation is:

$$\Delta\phi(x, y) = -k\int \delta(x, y, z)dz, \tag{2.25}$$

and, the attenuation is given by the $-k\int\beta(x, y, z)dz$. Also in the case of the sample being entirely homogeneous (monomorphous), equation (2.25) reduces to, $\Delta\phi(x, y) = -k\delta T(x, y,)$ where, $T(x, y)$ is the projected thickness in the z direction.

Now consider the square modulus of equation (2.24) where $|\Phi(x, y, z)|^2$ is equal to the intensity $I(x, y, z)$ of the wave field. Therefore, we get,

$$I(x, y, z = z_0) = I(x, y, z = 0)\exp\left[-2k\int\beta(x, y, z)dz\right]. \tag{2.26}$$

For the case of sample being monomorphous, equation (2.26) reduces to the well known Beer's Law of absorption,

$$I(x, y, z = z_0) = I(x, y, z = 0)\exp\left[-\mu T(x, y)\right], \tag{2.27}$$

where, $T(x, y)$ is the projected thickness in the z direction and $\mu = 2k\beta$.

2.1.6 Geometrical Optical Approximation and its Validity

Another important formalism for phase contrast imaging is the eikonal approximation for geometrical optics (GO) (Paganin, 2006). This approximation is a limiting case of wave theory of x-ray radiation, which approximates x-ray radiation as rays that evolve continuously as they travel through a refractive medium. Understanding this formalism and its validity is important because most of the phase retrieval methods for ABI are based on this approximation (Nesterets et al., 2006).

Let us begin this formalism by deriving the so called hydrodynamic formulation of coherent scalar x-ray wave-fields. Consider the inhomogeneous Helmholtz equation (2.8). Identifying the square modulus of the coherent wave field $|\psi_\omega(x, y, z)||^2$ equal to intensity $I_\omega(x, y, z)$ and writing phase as $arg\left[\psi_\omega(x, y, z)\right] \equiv \phi_\omega(x, y, z)$ we can rewrite equation (2.8) as (Paganin, 2006),

$$\left(\nabla^2 + k^2n_\omega^2(x, y, z)\right)\left(\sqrt{I_\omega(x, y, z)}\exp\left[i\phi_\omega(x, y, z)\right]\right) = 0. \tag{2.28}$$

Paganin (2006) showed that by expanding the Laplacian term, then separating the real part

from the imaginary part and simplifying the real part, one can arrive at the hydrodynamic formulation of the inhomogeneous Helmholtz equation[5].

$$|\nabla\phi_\omega(x,y,z)|^2 = k^2 n_\omega^2(x,y,z) + \frac{\nabla^2\sqrt{I_\omega(x,y,z)}}{\sqrt{I_\omega(x,y,z)}}, \tag{2.29}$$

Equation (2.29) is known as the eikonal equation. Now, let us consider the limiting case of equation (2.29) as the wave vector $k \to \infty$, which corresponds to the GO limit. At this instance the wavelength will be much smaller than the length scale over which the intensity change appreciably, leading to second term on the right hand side of equation (2.29) to be very small compared to the first term. Here, also note that the gradient of phase is inversely proportional to wavelength. Therefore, the gradient of phase changes with respect to k. Hence, in equation 2.29, both the left hand side and the first term of the right hand side changes with respect to k^2. However, the second term on the right hand side of equation 2.29 is independent of k, making it negligible in the GO limit as $k \to \infty$.

$$|\nabla\phi_\omega(x,y,z)| = k n_\omega(x,y,z), \quad k \to \infty. \tag{2.30}$$

This limited form is known as the eikonal approximation for geometrical optics or the geometrical optical approximation (GOA). Under the GOA, one can treat the wavefront engaging with the sample as multiple photons traversing the sample along different trajectories or rays (Gasilov and Coan, 2012). The trajectory of these rays within a homogeneous media or in the absence of media, where the GO limit of wavelength equalling zero can be approximated as a straight line. (Kohn, 1998; Paganin, 2006). However, if one were to relax the GO limit, the second term on right hand side of equation 2.29 will appear, thereby accounting for the diffraction of these rays (Paganin, 2006). It allows the refraction effects within the sample to be taken into account. Therefore, the GOA can be used to explain wave propagation through a sample with random inhomogeneities.

For propagation based phase contrast imaging (PB-PCI) discussed in section 2.3.3, the Fresnel Number N_F is used to define the GOA, where the GOA is valid for Fresnel numbers much greater than unity ($N_F \gg 1$). N_F is a dimensionless parameter defined by whichever is the largest out of the smallest feature in the sample, or the limit of resolution of the imaging system h, the wavelength of x-ray radiation λ and the propagation distance Δ (Paganin, 2006).

$$N_F \equiv \frac{h^2}{\lambda\Delta} \tag{2.31}$$

2.2 Ultra Small Angle Scattering

Ultra Small Angle Scattering (USAXS) information can provide micrometre or sub-micrometre length scale information of a sample structure. Refraction through an object will result in multiple rays emanating from the object at multiple different angles from which they entered the object. If the object is gently varying and the pixels are small enough, it may be possible to determine the angle of these rays. However, in the opposite extreme, as figure 2.4 shows,

[5]Refer to Paganin (2006) for the full derivation.

sharp edges or multiple small structures can result in a broad distribution of rays trajectories being simultaneously incident on a given pixel. Therefore, these are not typically resolved by the imaging system.

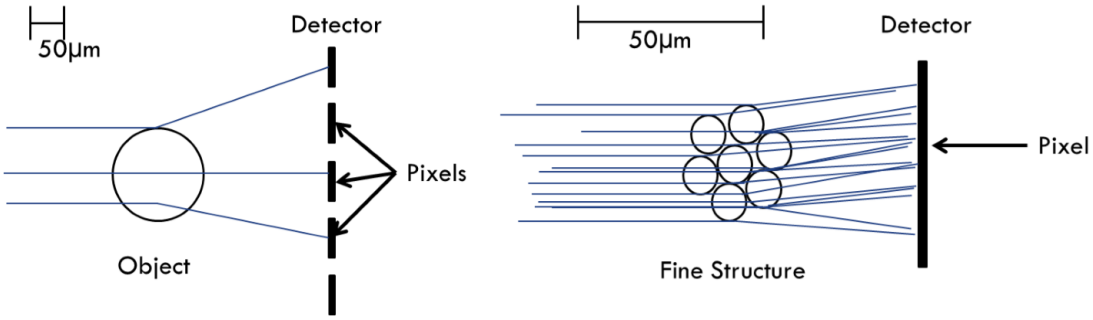

Figure 2.4: *The object can be resolved by the detector if the structure of the object is larger than pixels (left). If the fine structures of the object imaged are smaller than the pixel size, then these structures cannot be resolved (right).*

Typically in medical imaging, a sample would introduce both the variation in phase of the x-ray wavefield and scattering. This is illustrated in figure 2.5. One can use specialised optical set-ups and mathematical modelling of the behaviour to extract the information given by these coherent scatterings.

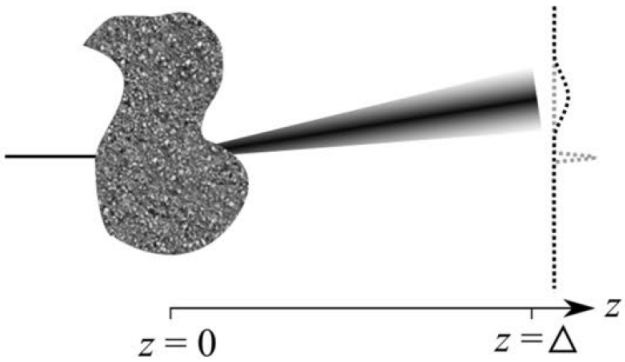

Figure 2.5: *The effect of variation in phase and coherent scattering of a single beamlet of x-ray due to sub-pixel structures of a sample. It results in broadening of beam profile at the detector causing reduced visibility (Morgan and Paganin, 2019). Reproduced with permission.*

As depicted in figure 2.5, coherent scattering increases the width of the beamlet due to sub-pixel structures. This broadens the probability distribution function that describe the beam profile at the detector and causes reduced visibility. Khelashvili et al. (2006) described the scattering signal as the symmetrical increase in width of the scattering cross section with the propagation distance. Their description consider the imaged object to be a stratified medium with discrete scattering centres. They showed that the scattering distribution can be approximated using a Gaussian distribution.

2.3 X-ray Phase Contrast Imaging

x-ray phase contrast imaging utilizes the small angular changes to the x-ray wave field propagation direction when traversing a sample. For materials such as soft biological tissues which are composed of low atomic numbers, x-ray PCI imaging produces better quality images (at the same radiation dose) compared to traditional attenuation-based imaging (Bravin et al., 2013). δ and β components of the index of refraction have different functional dependency on the incident photon energy and $\delta \gg \beta$ in materials with lower atomic numbers. It is shown that within the energy ranges between 10 kev and 150 kev δ for breast tissue is two to three orders of magnitude higher than β for breast tissue (White et al., 2016).

There are several techniques which are currently being investigated for the purpose of x-ray PCI. We shall briefly review interferometry, propagation based phase contrast, grating-based phase contrast, edge illumination and finally the subject of this thesis, namely analyser based phase contrast. How these techniques produce phase contrast can be understood using the Transport-of-Intensity Equation (TIE) (Teague, 1983).

2.3.1 Transport-of-Intensity Equation

Let us consider a plane wave traversing a sample. The outgoing wave at z_0 (see figure 2.3) can be described by the projection approximation, equation (2.24). If we assume that the outgoing wave field is propagating in a vacuum, the paraxial homogeneous Helmholtz (2.20) equation can be used to describe this wave field at any position $z > z_0$.

Now, considering $I(x, y, z) \equiv |\psi(x, y, z)|^2$ we may write the wave field at z_0 as,

$$\psi(x, y, z_0) = \sqrt{I(x, y, z_0)} \exp(i\phi(x, y, z_0)). \tag{2.32}$$

substituting this into (2.20), the paraxial homogeneous Helmholtz equation and expanding the result and cancelling the common factor and equating it to zero, the imaginary component yields a continuity equation known as the Transport-of-Intensity Equation (TIE) (Paganin, 2006).

$$-\nabla_T \cdot [I(x, y, z_0)\nabla_T \phi(x, y, z_0)] = k\frac{\partial I(x, y, z_0)}{\partial z}. \tag{2.33}$$

The TIE describes the evolution of intensity of a slowly varying scalar electromagnetic wave and its relationship to the corresponding phase (Pelliccia et al., 2018). We can make use of the finite difference approximation since, in comparison the longitudinal changes of the complex wave field is smaller than the transverse changes at any position greater than z_0.

$$\frac{\partial I(x, y, z_0)}{\partial z} \approx \frac{I(x, y, z) - I(x, y, z_0)}{\delta z}. \tag{2.34}$$

The intensity for a uniform sample right after the sample is denoted as $I(x, y, z_0)$ and $\delta z = z - z_0$ denotes a sufficiently small distance of propagation where the evolution of intensity is linear in z. Then by substituting equation (2.33) into equation (2.34), an equation for the propagated intensity can be found,

$$I(x,y,z) = I(x,y,z_0) - \frac{\delta z}{k}\left[\nabla_T I(x,y,z_0)\cdot\nabla_T\phi(x,y,z_0) + I(x,y,z_0)\nabla_T^2\phi(x,y,z_0)\right]. \quad (2.35)$$

According to the equation above, the intensity measured at any point where $z > z_0$ downstream is the sum of contributions. The first term is $I(x,y,z_0)$ representing the attenuation by the sample. This part produces poor attenuation-based contrast for cases where the sample is weakly attenuating. The second term contains $\nabla_T I(x,y,z_0)\cdot\nabla_T\phi(x,y,z_0)$, which can be referred to as the 'prism term' (Paganin et al., 2018) containing the dot product between the intensity gradient and the phase gradient. This term gives rise to differential phase-contrast imaging, where typically, one would require optical elements before or after the sample to visualise phase contrast. Several differential phase-contrast imaging methods are discussed in the following sections.

The third component contains $I(x,y,z_0)\nabla_T^2\phi(x,y,z_0)$ which represents the other phase derivative which can be referred to as the 'lensing term' (Paganin et al., 2018). This term contains the transverse Laplacian which modulates the attenuation image and this increases as the propagation distance from the sample increases. Propagation phase-contrast is further explored in section 2.3.3.

2.3.2 Interferometry

Interferometry was the first x-ray PCI method developed. It uses a Laue-Laue-Laue configuration of a monolithic crystal which was pioneered by Bonse and Hart (1965a,b). Interferometric imaging was later advanced by Ando and Hosoya (1972), and in the 1990s it was used for biomedical imaging (Momose, 1995; Takeda et al., 1998). Figure 2.6 represents a schematic diagram of an x-ray interferometer. The incoming x-rays beam is diffracted and split into two beams by Crystal 1 and again these beams will split at Crystal 2. Finally, both inner beams meet at Crystal 3 and generate an interference pattern on the detector located behind Crystal 3.

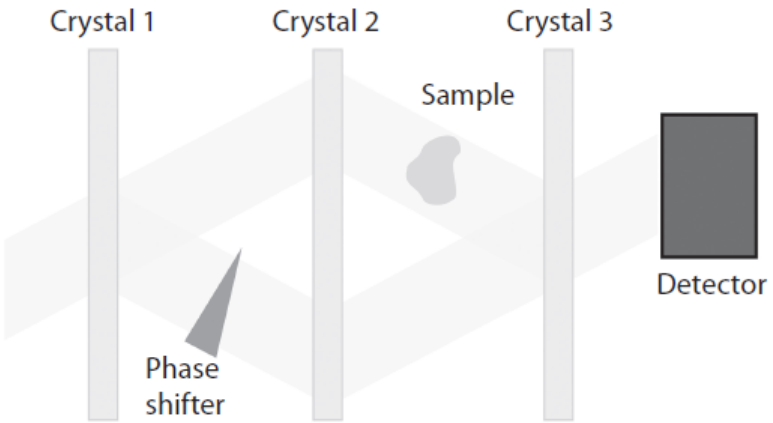

Figure 2.6: *A schematic diagram of phase imaging using x-ray interferometry (Pelliccia et al., 2018). Reproduced with permission.*

There are several interferometric methods in which phase shift can be extracted of a given

sample. In an ideal case where the crystals are free of any defects and the wave is perfectly planar, until a sample is placed in the wave field the wave would be perfectly uniform. The phase changes due to the introduction of the sample would then be recorded in the image (Endrizzi, 2018). Another method would be to introduce a known phase modulator (phase shifter as shown in figure 2.6) into one of the beams and introduce the sample into another beam as shown in figure 2.6. The phase shifter will create a ramp in phase, generating a series of linear periodic fringes at the detector. When a a sample is introduced as shown in figure 2.6, the phase shift of the sample will distort the fringes (Pelliccia et al., 2018). This distortion is recorded by the detector and if they posses high spatial frequency, phase shifts may be extracted using a Fourier method (Takeda et al., 1982).

2.3.3 Propagation Based Phase Contrast Imaging

This can be referred to as the experimentally simplest method of acquiring phase contrast (Bravin et al., 2013; Endrizzi, 2018). Propagation based phase contrast imaging (PB-PCI) utilizes the interference pattern in the wave field due to the phase changes caused by the small variations in the imaged sample to produce a phase contrast image. The sample is typically placed in a coherent x-ray beam with the detector placed at a sufficient distance where the intensity variations from the interference pattern can be recorded. Figure 2.7 show a schematic diagram of the PB-PCI.

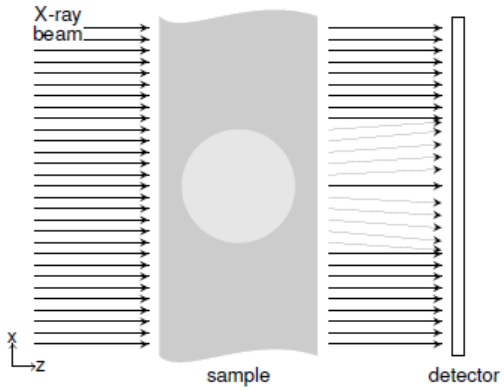

Figure 2.7: *A schematic diagram of propagation based imaging (Endrizzi, 2018). Reproduced with permission.*

PB-PCI exploits Fresnel diffraction and was developed on the principles put forth by Gabor in 1948 (Snigirev et al., 1995; Paganin, 2006). Snigirev et al. (1995) first showed the possibility of PB-PCI using high energy coherent synchrotron x-ray radiation. Wilkins et al. (1996) showed the possibility of this method using polychromatic micro-focus x-ray sources. Therefore, this method has the potential to be used clinically (Bravin et al., 2013). However, the radiation must provide a certain degree of spatial or lateral coherence (Nesterets et al., 2015). Given R_1 is the distance between the source and the object, λ is the x-ray wavelength and s is the focal spot size of the x-ray, transverse (lateral) coherence length can be defined as $L_{coh} = \lambda R_1/s$ (Zhou and Brahme, 2008; Bravin et al., 2013). A feasibility study on using this method for phase-contrast mammographic tomography was carried out by Nesterets et al. (2015). They

showed that high-quality soft tissue phase contrast CT imaging can be done with PB-PCI at radiologically acceptable doses by optimizing parameters such as x-ray dose, x-ray energy, distance between the sample and the detector, and image processing steps. Imaging systems must have high enough spatial resolution so the interference patterns are not washed out and a detailed description of factors effecting image quality can be found in Nesterets et al. (2005); Gureyev et al. (2008). Furthermore, the ability to extract USAXS information using PB-PCI is yet to be known.

2.3.4 Grating Based Phase Contrast imaging

The foundation of grating based phase contrast imaging is based on the Talbot effects which describes a near field diffraction pattern due to a plane wave illuminating a periodic diffraction grating (Talbot, 1836; Rayleigh, 1881). As shown in figure 2.8, there are three gratings: G_0 the source grating, G_1 the phase grating and G_2 the analyser absorption gratings, p_0, p_1 and p_2 represent their respective periods, and each grating is separated by regular distances. The distance between gratings is given by $2p_n^2/\lambda$ where p_n refers to the corresponding period. This distance is known as the Talbot distance.

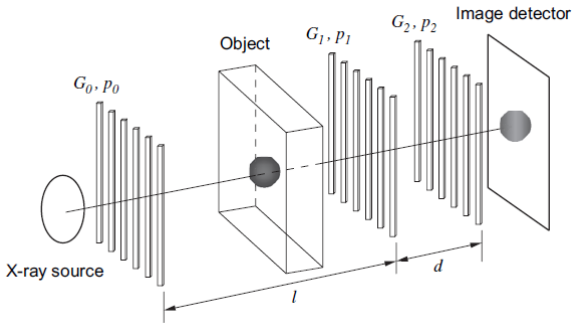

Figure 2.8: *A schematic diagram of grating based phase imaging (Zhou and Brahme, 2008). Reproduced with permission.*

Use of this technique for imaging dates back to early 1990s (Endrizzi, 2018). Initially, only two transmission gratings were used with a synchrotron x-ray source (David et al., 2002; Momose et al., 2003). The first grating, the phase grating G_1 acts as the beam splitter, splitting the x-ray wave field into multiple smaller beams. These smaller beams then traverse though the sample where these beams will be scattered, absorbed and refracted due to the presence of the sample[6]. When the wave field exits the sample it will create a distortion pattern. This distortion pattern is most visible at Talbot distance from the first grating G_1. Therefore, the second grating G_2, the analyser grating, is positioned at a Talbot distance. The detected intensity in each pixel when one grating is scanned along the other grating laterally, while no sample is present in the x-ray wave field, can be fitted with a sinusoid. This curve is known as the phase-stepping curve. By comparing the phase-stepping curve on a pixel-by-pixel basis with and without the sample one could extract the attenuation, refraction, and dark-field images of the sample. Here the dark-field image is described by the reduction in visibility due to scattering by sub-pixel length scale structures. It is described by the reduction in the amplitude. The reduction of the baseline

[6]One can alternatively place the sample before the first grating as well

of the curve gives the attenuation information and the lateral shift of the curve corresponds to refraction information.

The use of polychromatic sources was enabled by introducing a third grating (Pfeiffer et al., 2006). This third grating, G_0 as depicted in figure 2.8 increases the effective spatial (transverse) coherence of the primary x-ray field by splitting it into smaller beams. The distance between G_0 and G_1 is equal to the Talbot distance where a Talbot image with the same period and position as G_1 is observed (Pelliccia et al., 2018). This method has the potential to be used in clinical environments in the near future (Andrejewski et al., 2021).

2.3.5 Edge Illumination

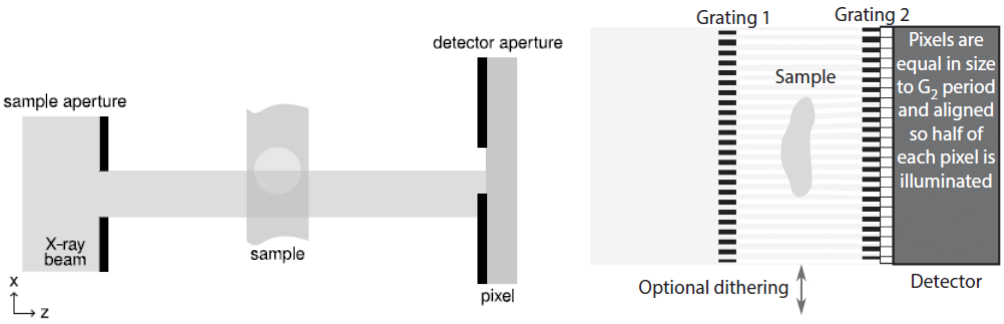

Figure 2.9: *A diagram depicting the working principle of edge illumination (left) (Endrizzi, 2018) and the experimental setup of edge illumination used in phase contrast imaging (right) (Pelliccia et al., 2018). Reproduced with permission.*

The initial development of this method can be attributed to Olivo et al. (2001) and it is said that it was inspired by the analyser based methods (Endrizzi, 2018). The left image of figure 2.9 depicts the working principles of edge illumination. The sample aperture first shapes an x-ray beam, which also improves beam coherence. Then this beam traverses the sample and strikes at the edge of the detector aperture. Then the intensity recorded is modulated by moving one of the apertures in x direction (laterally) while the other aperture is stationary. The intensity recorded will reach its maximum (if no sample is placed in the beam) when the two apertures are fully in line with each other. As they move away the intensity will slowly decrease, generating a bell-like curve. The intensity distribution is modulated by refraction due to the presence of the sample.

With the use of line gratings, as shown in the right image of figure 2.9, this method allows the observation of one-dimensional differential phase images directly at the detector (Pelliccia et al., 2018). Using two-dimensional grating arrangement, one can also acquire the differential phase contrast in two directions (Pelliccia et al., 2018). To extract refraction and absorption information of an absorbing sample, at least two images must be taken (Olivo et al., 2001). Endrizzi et al. (2014) also showed that with three projection images and using a Gaussian distribution to represent the intensity, quantitative retrieval of USAXS information is possible with edge illumination. An advantage of this method is that it can be used with conventional x-ray sources (Diemoz et al., 2013).

2.3.6 Analyser Based Phase Contrast X-ray Imaging

Analyser Based Imaging (ABI) or Diffraction Enhanced Imaging (DEI) employs a near-perfect analyser crystal, which is positioned between the sample and the pixelated detector (see figure 2.10). This analyser crystal, typically a silicon crystal, acts as a fine angular filter. Two analyser crystal orientations have been investigated for acquisition of images. Bragg geometry (Chapman et al., 1997; Davis et al., 1995; Kitchen et al., 2007), as depicted in figure 2.10, and Laue geometry (Kitchen et al., 2011; Ingal and Beliaevskaya, 1995; Bushuev et al., 1996; Kitchen et al., 2010), as shown in figure 2.11. Förster et al. (1980) can be credited for pioneering ABI.

ABI uses a monochromatic x-ray beam, which is typically generated using a double crystal monochromator. The analyser crystal can be setup in a mutually non-dispersive orientation to the crystal monochromators so that the effects caused by energy band-width and beam divergence are mitigated (Suortti and Thomlinson, 2003). In the absence of a sample in the x-ray beam, the maximum intensity is recorded when the crystal is aligned at the Bragg angular position:

$$2d_{hkl} \sin \theta_B = \lambda. \tag{2.36}$$

where θ_B is the Bragg angle, and λ is the x-ray wavelength that satisfies the Bragg condition. For the analyser crystal, hkl represents the chosen Miller indices. As the crystal rotates (or rocks) around the Bragg angular position, the angular intensity profile takes the shape of a bell curve by dropping the intensity rapidly as the crystal rotates away from Bragg angle. This curve is commonly known as the rocking curve (see figure 2.10). The width of the rocking curve is determined by the incident wave divergence, energy spectrum of the wave, the material of the crystal, the chosen reflection plane, and the thickness variations in the crystal (Zhong et al., 2000).

The analyser crystal behaves like a fine angular filter. It will only diffract the rays that satisfy the Bragg condition and, those that do not satisfy the Bragg condition are transmitted into the crystal. The rocking curve governs this process by giving the reflected intensity for the incident angle of photons after traversing through the sample. Essentially, the analyser crystal reflects different intensities for different incident angles leading to a variable spatial intensity distribution at the detector. The width of the rocking curve is responsible for the strength of phase contrast. When the rocking curve is narrower, the gradient of the rocking curve slopes increases, hence if the beam is aligned to the slope of the crystal then strong intensity changes will result from angular deviations of the beam. This leads to providing better phase contrast for smaller angles of refraction produced by the sample. In the diagnostic energy regime, the refraction angles for biological samples are typically in the range of μradian (Pelliccia et al., 2018). Therefore, reducing the width of the rocking curve can increase the strength of phase contrast in biological samples. That can be achieved by limiting the energy band-width. Hence, high temporal coherence and low beam divergence are a necessity for ABI. Despite the fact that these elements are required, the literature on ABI demonstrates that quantitative phase-contrast imaging using a laboratory x-ray source is conceivable (Vine et al., 2007).

In the Bragg crystal geometry, typically only the reflected beam is recorded (see figure 2.10). However, if the crystal is thin enough one can transmit through a Bragg crystal, but at small

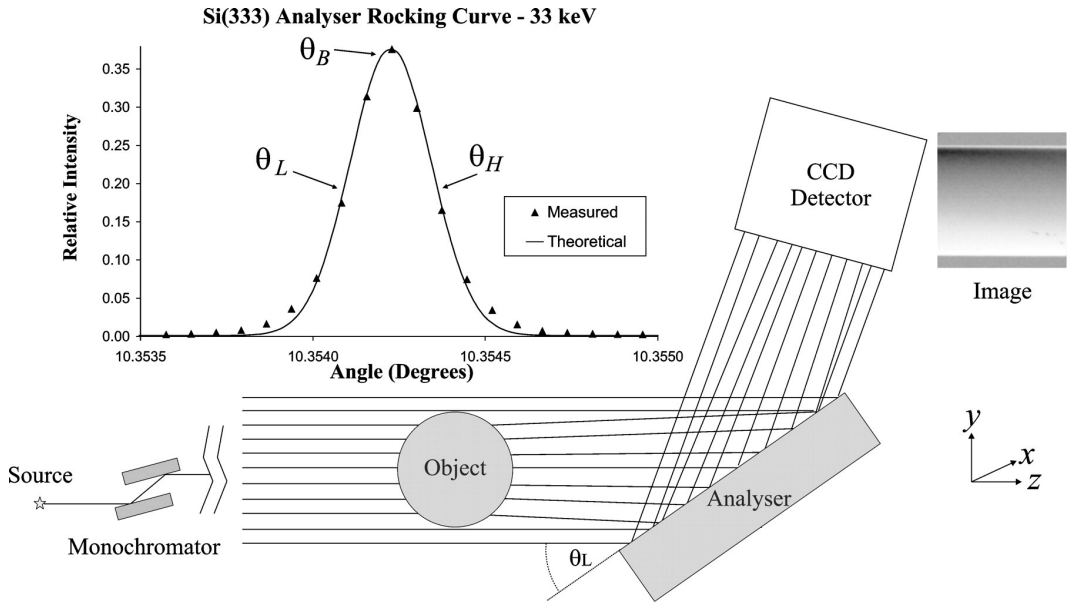

Figure 2.10: *A schematic diagram of ABI using Bragg crystal geometry using a Si(3,3,3) analyser crystal and the analyser rocking curve for a Si(3,3,3) crystal measured at 33 keV. θ_B is the Bragg angle at which the peek intensity is recorded. θ_L and θ_B indicate the low and high angle points, respectively. The intensity at these points corresponds to half the peek intensity (Kitchen et al., 2005). Reproduced with permission.*

Bragg angles, the projected thickness of the crystal becomes large so the transmitted beam is highly attenuated.

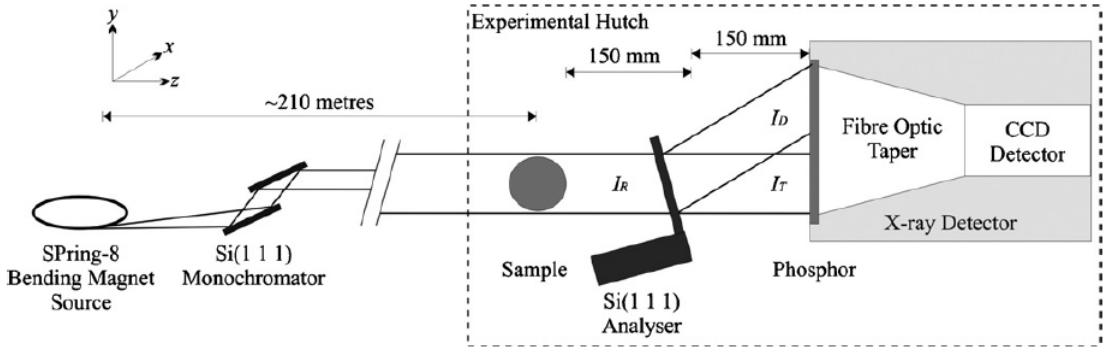

Figure 2.11: *The experimental set up for ABI using Laue crystal geometry. Simultaneous acquisition of refracted and transmitted images using Laue crystal geometry (Kitchen et al., 2011). Reproduced with permission.*

An alternative method for Bragg geometry is the use of Laue geometry. Figure 2.11 shows the experimental setup for Laue geometry. A major advantage of the Laue crystal geometry is that it allows the capture of both the diffracted and the transmitted beams simultaneously. Another benefit of the Laue geometry is that the beam footprint on the analyser crystal surface is smaller. This means one can fit a larger beam onto a smaller surface in the Laue geometry. Therefore, the analyser crystal used for the Laue geometry can be smaller compared to the analyser crystal used for the Bragg geometry. This is because in the Laue geometry the analyser crystal is typically almost parallel (see figure 2.11) to the object height while in Bragg geometry, the analyser

crystal is typically almost perpendicular to the object height. They are also proportionately more expensive.

In the Laue geometry, the intensity of the transmitted rocking curve displays an opposing trend to the diffracted curve, reaching a minimum at the Bragg angle since the intensity is deflected into the Bragg reflection. Rocking the analyser crystal around the Bragg position yields a roughly equal and opposite intensity gradients for the diffracted and transmitted beams. The rocking curve can be extremely oscillatory under plane wave illumination and the thickness of the crystal regulates the period of oscillation (Authier and Malgrange, 1998; Mocella, 2005). This could be a challenge for the Laue geometry because the crystal thickness could change due to thermal expansion during imaging. However, these oscillations are not always observed due to imperfections in the imaging system such as beam divergence and finite band-width.

The plane of diffraction is determined by the orientation of the crystallographic planes of the analyser crystal. The $y-z$ plane is the plane of diffraction (see figure 2.11). This plane therefore will dictate in which plane the phase contrast will be produced, meaning that this method only produces phase contrast in one dimension. Chalmers et al. (2021) introduced a variant of ABI[7], which enabled the extraction of phase-contrast in both the x and y directions. However, their use of two working points on either side of the rocking curve at half the Bragg peak intensity (see figure 2.10) restricted them from extracting the USAXS information. In this body of work, the goal is to extent their work into the USAXS regime by estimating the rocking curve using eight working points. Use of three or more working points allows the quantitative extraction of attenuation, gradient of phase, and the USAXS information[8].

The width of the rocking curve of the analyser crystal is typically in the range of microradians (Suortti et al., 2013). Any scattering larger than this width, for instance Compton scattering (Diemoz et al., 2012), will be mostly rejected the analyser crystal. The accepted scatter by the analyser crystal are therefore mostly Small Angle Scattering (SAXS) or USAXS (Suortti et al., 2013), making the ABI experimental setup well suited for quantitative reconstruction of the USAXS information.

2.4 Analyser-Based X-ray Phase Retrieval

2.4.1 Diffraction Enhanced Imaging

Diffraction Enhanced Imaging (DEI), developed by Chapman et al. (1997), is one of the first phase retrieval algorithms for ABI. This method uses two images, recorded using the Bragg geometry, one at either side of the rocking curve at half of the peak reflectivity. The rocking curve at these positions has the largest gradient and it is approximately linear over a limited range of angles. Consequently, the phase gradient in the direction parallel to the diffraction plane (y-direction; see figure 2.10) is approximately proportional to the relative intensity variation. DEI method by Chapman et al. (1997) uses the Taylor series approximation to estimate the rocking curve at each working point θ_L and θ_H (see figure 2.10). Using these two images, they successfully separated and reconstructed the refraction image. The refraction image display a

[7]Subsection 2.4.3 and section 3.1 give a detailed description of this ABI variant.

[8]The use of more than three working points to estimate the rocking curve is referred to as Multiple Image Radiography (MIR) and it is discussed in detail in subsection 2.4.2

map of the angular deviation of the x-ray beam due to different refractive indices within the imaged object.

The analyser crystal can be extremely sensitive to USAXS (Pelliccia et al., 2018). The angular spread of the USAXS fan increases when a sample producing a significant number of USAXS is introduced into the x-ray beam. As a result of this, the width of the rocking curve increases. Therefore, if the sample were to produce USAXS, it can be beneficial not to neglect it during the reconstruction process. A disadvantage of DEI is that it considers USAXS to be negligible, leading to considerable artifacts. This is especially true for biological material where USAXS can be a common occurrence (Wernick et al., 2003; Khelashvili et al., 2006).

2.4.2 Multiple Image Radiography

Wernick et al. (2002) proposed an alternative method known as Multiple Image Radiography (MIR). They described the relationship between the recorded intensity $I(\theta)$ as the convolution of the intensity before the sample $I_0(\theta)$ and the scattering function $S(\theta)$ where θ represents the angular position of the analyser crystal.

$$I(\theta) \approx I_0(\theta) \otimes S(\theta) \tag{2.37}$$

MIR is capable of extracting absorption, refraction, and USAXS information. This method uses three or more images recorded at multiple angular positions on the rocking curve. MIR separates the absorption, refraction, and USAXS information by comparing the rocking curve with the sample (sample rocking curve) to the rocking curve without the sample (intrinsic rocking curve) on a pixel by pixel basis. The absorption image is equal to the change in area under the two curves (sample rocking curve and the intrinsic rocking curve). The centroid shift (between sample rocking curve and the intrinsic rocking curve) gives the refraction image, while the full width at half maximum of the deconvolved scattering distribution gives the USAXS information. Figure 2.12 shows a graphical interpretation of this process.

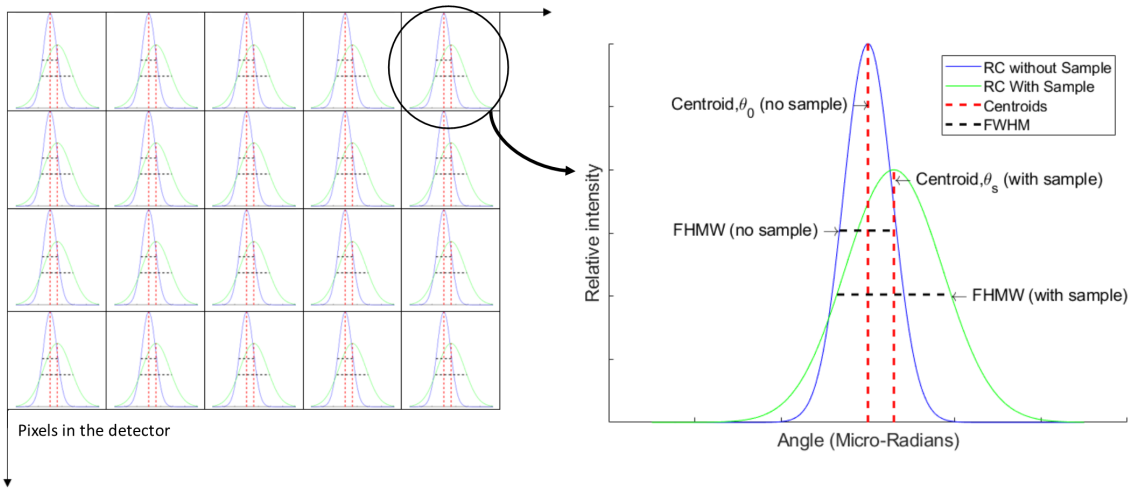

Figure 2.12: *Change in the rocking curve in each pixel (left). An enlarged view of the centroid shift and the change in width of the rocking curve due to the presence of the sample (right) in a single pixel.*

Finding an appropriate function which best estimates the rocking curve is important (see chapter 4). Taylor series expansions (Pavlov et al., 2001; Rigon et al., 2007; Chou et al., 2007), Gaussian (Nesterets et al., 2006; Oltulu et al., 2003; Pagot et al., 2003), Voigtian (Suhonen et al., 2007) and Pearson VII functions (Kitchen et al., 2007, 2010) have been shown to approximate the rocking curve. Most of these methods are based on the GOA discussed in section 2.1.6. The GOA allows a simple linear relationship relating the wave intensity of the beams transmitted (I_T) and diffracted (I_D) by the analyser crystal to the transmitted intensity through the sample (I_R) and the transmitted ($T(\theta)$) and diffracted ($R(\theta)$) rocking curves as a function of angular change θ (Nesterets et al., 2006; Bushuev et al., 1996; Kitchen et al., 2010):

$$\begin{bmatrix} I_D \\ I_T \end{bmatrix} = I_R \begin{bmatrix} R(\theta_0 + \Delta\theta) \\ T(\theta_0 + \Delta\theta) \end{bmatrix}. \tag{2.38}$$

Here θ_0 is the angle of incidence of the x-ray wave field with the analyser crystal relative to its crystallographic planes without the sample while $\Delta\theta$ corresponds to the change in the incident angle due to refraction when a sample is introduced to the x-ray wave field. This approximation holds when the Takagi Number, $N_T \gg 1$ or the phase change of the wave is slowly varying over the length scale of the crystal's extinction length (Pavlov et al., 2004; Nesterets et al., 2006).

By analogy with the GOA validity condition for PB-PCI, which was discussed in section 2.1.6), the Takagi number was derived by Pavlov et al. (2004) to define GOA for Analyser-Based Imaging (ABI). They have shown that for ABI, the GOA is valid under the condition that the Takagi number is much larger than unity ($N_T \gg 1$). According to Pavlov et al. (2004) the Takagi number for a monochromatic wave incident upon an object has the following form,

$$N_T = h^2 \left| R(q_0)/R''(q_0) \right|. \tag{2.39}$$

Here, h is the size of the smallest feature in the sample, or the limit of resolution of the imaging system, whichever is the largest. q_0 is the angular position of the analyser crystal, $R(q_0)$ is the amplitude reflection coefficient of the analyser crystal as a function of the angular position of the crystal. At the edges of objects poor phase reconstruction can be observed as a result of violating the condition $N_T \gg 1$, where the induced phase curvature is large (Nesterets et al., 2006).

Kitchen et al. (2010) utilised GOA for phase retrieval with the Laue geometry. They estimated the rocking curves of the diffracted and transmitted beams using the following form of the Pearson VII approximation:

$$y = c[1 + (x - \tilde{x})^2/(ma^2)]^{-m} \tag{2.40}$$

Here c is the amplitude, $\tilde{x}$ represents the centroid, and both a and m determine the width of the profile. Also note that a, c and m are all greater than zero and $\{-\infty < x < \infty\}$. They showed that one can find the angular orientation of the beam by fitting equation (2.40) to the ratio of the diffracted and transmitted rocking curves:

$$\frac{I_D}{I_T} = \frac{I_R R(\theta)}{I_R T(\theta)} = c\left[1 + \frac{\theta^2}{(ma^2)}\right]^{-m}. \tag{2.41}$$

Here the centroid is defined as zero. Therefore, by rearranging the above equation, one can find a solution for the deviation of the crystal from the Bragg position to be,

$$\theta = \pm a\sqrt{m[(cI_T(\theta)/I_D(\theta)]^{1/m} - 1]}. \tag{2.42}$$

As a consequence of the square root in equation (2.42), the solution for theta is a non-unique solution. Therefore, one cannot differentiate to which side of the Bragg peak the working point was shifted. Hence, for both cases with and without the sample, one must assume that the same side of the Bragg peak is illuminated by the beam. Then the refraction angle map (i.e., the angular deviation of the x-ray beam due to refraction) can be reconstructed by subtracting the solutions for equation (2.42) for images taken with (θ_s) and without (θ_0) the sample:

$$\Delta\theta = \theta_s - \theta_0. \tag{2.43}$$

By fitting the transmitted rocking curve with an inverted Pearson VII distribution, of the form ($f - d[1 + \theta^2/(nb^2)^{-n}]$), one can solve for the apparent absorption image. The coefficients here are changed to avoid confusion with the coefficients in equation (2.41):

$$I_R = I_T(\theta)\left(f - d[1 + \theta^2/(nb^2)]^{-n}\right)^{-1}. \tag{2.44}$$

Recall equation (2.25), it gives the phase shift of an x-ray wave when it traverse through a sample as $-k\int\delta(x, y, z)dz$. This phase shift over the axis of phase sensitivity, y, or the phase gradient (one-dimensional) relates to the angular change due to the introduction of the sample. It can be determined using the following relationship, which can be solved using numerical methods to obtain the phase shift (Davis et al., 1995).

$$\frac{\partial\Phi}{\partial y} = k\Delta\theta_y = -k\left[\frac{\partial}{\partial y}\int\delta(x, y, z)dz\right]. \tag{2.45}$$

The extraction of USAXS information is accomplished by deconvolving the intrinsic rocking curve from the sample rocking curve. Deconvolution is an ill-posed problem, and it can be unstable. It is especially true when using data containing noise. Kitchen et al. (2010) overcame this by approximating the rocking curve using noise-free Pearson VII fitting and Wiener deconvolution. The Wiener deconvolution method uses a small regularization value to avoid division by zero in Fourier space, which helps to prevent instability. This method is discussed in detail in section 6.1. Furthermore, Kitchen et al. (2010) fitted the deconvolved scattering curve $P(\theta_{Scat})$ with another Pearson VII function. Then the half-width at half-maximum (HWHM) of the scattering curve was calculated for each pixel using,

$$P(\theta_{Scat})_{HWHM} = a\sqrt{m(2^{1/m} - 1)}. \tag{2.46}$$

2.4.3 Two-Dimensional Phase Retrieval Using the Laue Geometry

Although the phase gradient is a two-dimensional vector, up to this point we have only considered phase retrieval of a single dimension for ABI. This is because the diffraction direction depends on the analyser crystal's Bragg plane orientation. The orientation of the Bragg planes,

therefore, determines the direction of contrast. As a consequence to this, structures producing a gradient of phase in the direction perpendicular to the diffraction plane are visible only due to the attenuation-based contrast. This restricts the recovery of the phase shift Φ using both components of its gradient, preventing the accurate tomographic reconstruction of the 3D distribution of δ (Rutishauser et al., 2011). The two-dimensional method investigated in this section aims to retrieve the components of the phase gradient in both the x and y directions. Acquisition of the two-dimensional gradient vector helps reduce phase clipping and low-frequency reconstruction artefacts (Rutishauser et al., 2011).

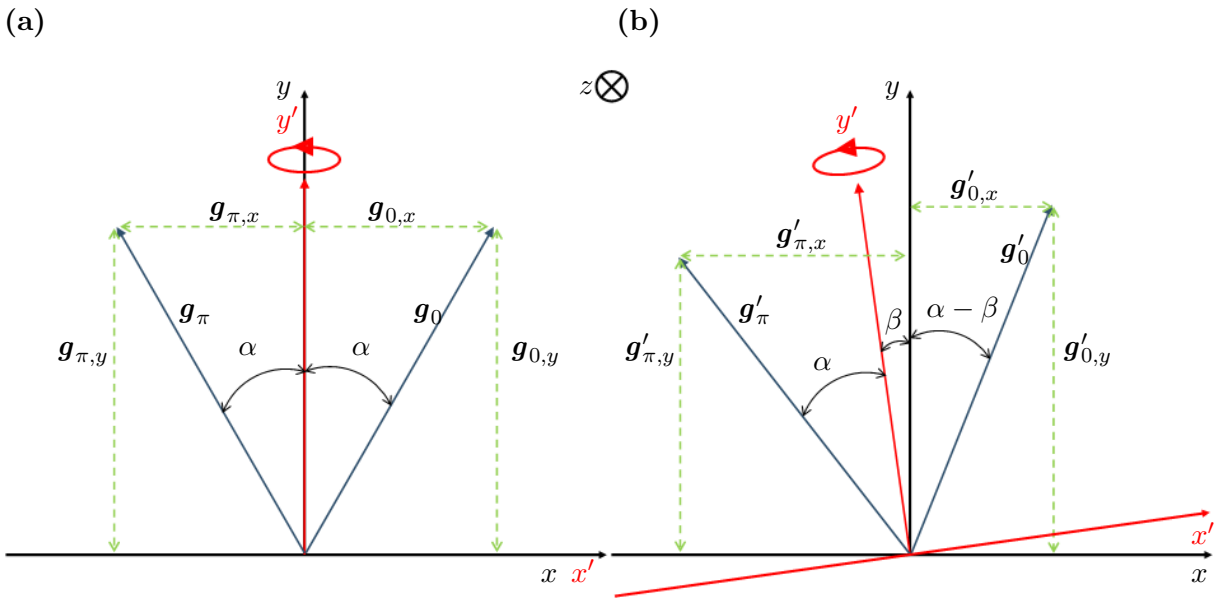

Figure 2.13: *A vector diagram depicting the imaging setup before (a) and after (b) tilting the object and detector by some angle β (right). x' and y' represents the object and detector coordinate system while x and y represents the analyser crystal coordinate system. In diagram (a), $\boldsymbol{g}_0$ and $\boldsymbol{g}_\pi$ corresponds to the projection vectors at tomographic projection angle ψ and the other at $\psi + \pi$, respectively. In diagram (b), $\boldsymbol{g}'_0$ and $\boldsymbol{g}'_\pi$ corresponds to the projection vectors at tomographic projection angle ψ and the other at $\psi + \pi$, respectively.*

With the aim of recovering the phase gradient in both the x and y directions, let us consider an experimental setup where we tilt the sample and the detector by some angle β with respect to the axis of sensitivity y. Figure 2.13 (a) and (b) depict the vector diagrams of the setup before and after tilting the sample and the detector, respectively. This gives the ability to measure the out-of-plane gradient component perpendicular to the diffraction planes. In figure 2.13 (b), the $x - axis$ is still perpendicular to the diffraction plan when the system is tilted. If we record two projection images, one at the tomographic projection angle ψ and the other at $\psi + \pi$, we will have enough information to reconstruct both $\frac{\partial \Phi}{\partial y}$ and $\frac{\partial \Phi}{\partial x}$ (Rutishauser et al., 2011; Chalmers et al., 2021). In figure 2.13 (b), the projections taken at tomographic projection angle ψ and the other at $\psi + \pi$ are denoted by $\boldsymbol{g}'_{0,y}$ and $\boldsymbol{g}'_{\pi,y}$, respectively.

Now consider the left diagram of figure 2.13 where the object is rotated around the axis of sensitivity (not tilted). We can write the following expressions to describe the x and y components of the projection vector $\boldsymbol{g}_0$:

$$\boldsymbol{g}_{0,y} = |\boldsymbol{g}| \cos\alpha = \boldsymbol{g}_{0,y'}, \tag{2.47}$$

$$\boldsymbol{g}_{0,x} = |\boldsymbol{g}| \sin\alpha = \boldsymbol{g}_{0,x'}, \tag{2.48}$$

where, $|\boldsymbol{g}|$ is the magnitude of vector $\boldsymbol{g}_0$. When the object is not tilted it is clear that the components $\boldsymbol{g}_{0,y'}$ and $\boldsymbol{g}_{0,x'}$ of the object-detector coordinate system are equal to the $\boldsymbol{g}_{0,y}$ and $\boldsymbol{g}_{0,x}$ of the analyser coordinate system, respectively. Here, α represents the angle between the projection vector and the y' axis. Similarly, when we tilt the object-detector coordinate system by some angle β with respect to the analyser's coordinate system, we can write the following expressions to describe the components $\boldsymbol{g}'_{0,y}$ and $\boldsymbol{g}'_{\pi,y}$ (see figure 2.13 (b)):

$$\boldsymbol{g}'_{0,y} = |\boldsymbol{g}| \cos(\alpha - \beta) = |\boldsymbol{g}|(\cos\alpha\cos\beta + \sin\alpha\sin\beta), \tag{2.49}$$

$$\boldsymbol{g}'_{\pi,y} = |\boldsymbol{g}| \cos(\alpha + \beta) = |\boldsymbol{g}|(\cos\alpha\cos\beta - \sin\alpha\sin\beta). \tag{2.50}$$

Equations (2.49) and (2.50) make use of the sum and difference identity of cosine, $\cos(X \pm Y) = \cos X cos Y \mp \sin X \sin Y$. Now taking the sum of equations (2.47) and (2.48) and substituting equation (2.47) we can derive the following for $\frac{\partial\Phi}{\partial y}$:

$$\frac{1}{-k}\frac{\partial\Phi}{\partial y} = \boldsymbol{g}_{0,y'} = \frac{\boldsymbol{g}'_{0,y} + \boldsymbol{g}'_{\pi,y}}{2\cos\beta}, \tag{2.51}$$

Furthermore, taking the difference between these two equations (2.47) and (2.48) and substituting equation (2.48), we can derive the following for $\frac{\partial\Phi}{\partial x}$:

$$\frac{1}{-k}\frac{\partial\Phi}{\partial x} = \boldsymbol{g}_{0,x'} = \frac{\boldsymbol{g}'_{0,y} - \boldsymbol{g}'_{\pi,y}}{2\sin\beta}. \tag{2.52}$$

Remember that $\boldsymbol{g}'_{0,y}$ and $\boldsymbol{g}'_{\pi,y}$ are the extracted refraction angle maps from the two projections acquired at ψ and $\psi + \pi$. Therefore, we can see that by tilting the object by some angle β we are able to measure the phase in both the x and y directions. This means that we are able to extract the 2D phase map, which will provide a more detailed image of the minute structural changes in a given object.

Once the $\frac{\partial\Phi}{\partial y}$ and $\frac{\partial\Phi}{\partial x}$ are extracted, we can combine these using 2D Fourier integration described by Kottler et al. (2007):

$$\Phi(x,y) = \mathcal{F}^{-1}\left[\frac{\mathcal{F}\left[\frac{\partial\Phi}{\partial x} + i\frac{\partial\Phi}{\partial y}\right](k,l)}{2\pi i(k+il)}\right](x,y). \tag{2.53}$$

where $\Phi(x,y)$ is the reconstructed phase shift and (k,l) are the reciprocal coordinates corresponding to (x,y).

Chalmers et al. (2021) first introduced the two-dimensional phase retrieval using the tilted Laue geometry in ABI phase contrast imaging. This thesis will apply this 2D phase retrieval method to a heterogeneous sample (see section 3.3) for the first time (see section 5.4).

2.5 Computed Tomography

The goal of this thesis is to reconstruct the 3D images of the attenuation, phase, and USAXS information. However, in radiography, the imaging setups are only capable of acquiring 2D projections of a 3D object causing it to loose naturally accompanying spatial information. However, this can be mitigated by utilising Computed Tomography (CT), which enables the 3D reconstruction of a volume using 2D projections taken at different angular positions (Kak and Slaney, 2001). The mathematical foundations for Computed Tomography (CT) were started by the German mathematician Johann Radon in 1917 (Ramlau and Scherzer, 2018). In 1963, Allan Macleod Cormak laid the foundation to describe a method for calculating the distribution of x-ray absorption in the human body (Cierniak and Cierniak, 2011). In conventional x-ray CT , these projections are line integrals at each angular position containing the total attenuation information of the sample. The projection data $\rho(r, \phi)$ are typically referred to as a sinogram. Here, x and y coordinates from the object space are transformed to observation space by $r = x\cos\phi + y\sin\phi$ and $s = y\cos\phi - x\sin\phi$.

Reconstructing the image is an inverse problem, which can be solved using backprojection. For instance the filtered back projection algorithm. In backprojection, large numbers of projections taken at different angular positions around 360 degrees are summed together to generate the final image. However, this process results in a characteristic $1/r$ blurring. Here, r is the radial distance. The reconstructed image $f'(x, y)$ is the convolution of the original image $f(x, y)$ with $1/r$:

$$f'(x, y) = f(x, y) \otimes (1/r). \tag{2.54}$$

In practice, Fourier-based mathematics is used to implement the convolution process and it can be shown that by multiplying with an appropriate kernel in Fourier domain one can correct the $1/r$ blurring (Bushberg et al., 2011). Figure 2.14 show a graphical representation of such kernels.

The Ram-Lak filter (ramp filter) is a high pass filter that restricts the low frequencies and amplifies the high frequencies to compensate for the blurring, which occurs during backprojection. A disadvantage to this is that it can amplify the quantum noise in the image (Bushberg et al., 2011). The Shepp-Logan filter belongs to the low pass category and it is a multiplication of the Ram-Lak filter by a sinc function. The third filter depicted in the above figure is another low pass filter named the Hann filter. This filter is extremely effective in reducing noise but its disadvantage is that it tends not to preserve edges (Lyra and Ploussi, 2011). This filter is described only by the cut-off or the critical frequency and it uses a window function called the Hann window (Lyra and Ploussi, 2011).

To use CT reconstruction on refraction angle and USAXS information, these quantities must satisfy the line integral condition. Therefore, these quantities must behave linearly with the thickness of the object imaged. For MIR, theoretically and experimentally, Khelashvili et al. (2006) showed that both the refraction angle and the USAXS parameters satisfy the line integral conditions and behave linearly with object thickness. In this thesis, filtered backprojection will be used to reconstruct the volumetric attenuation, phase, and USAXS information. How-

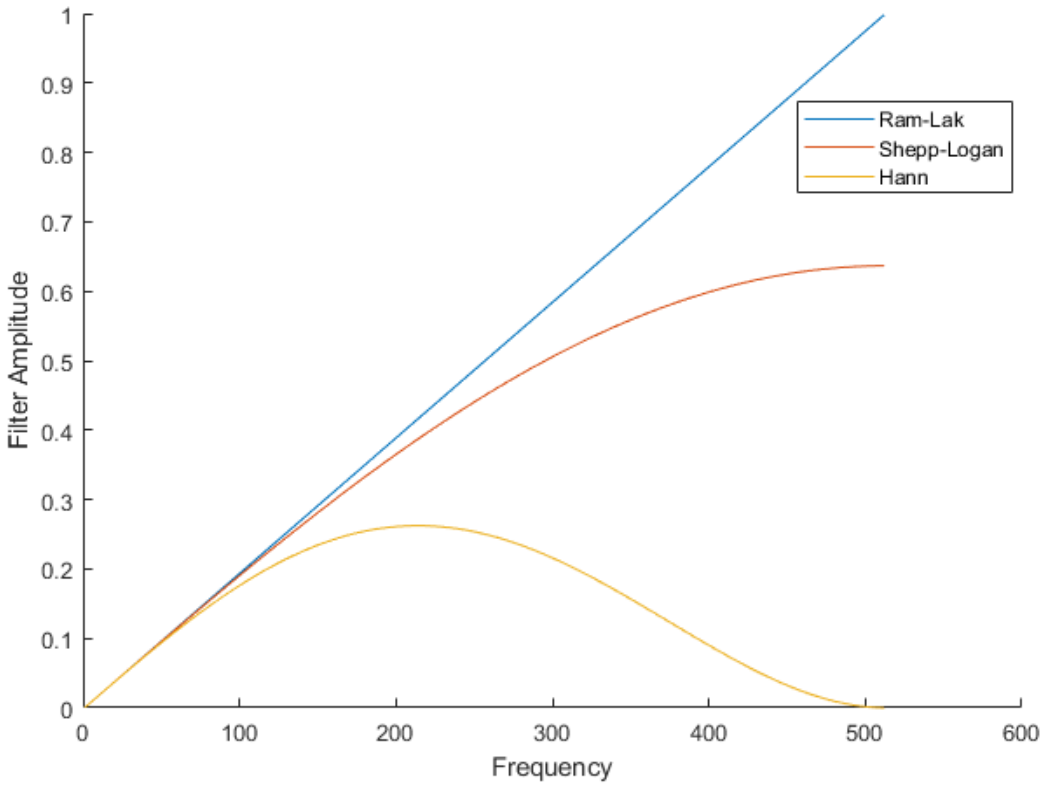

Figure 2.14: *A Comparison Between Ram-Lak, Shepp-Logan and Hann kernals.*

ever, it must be noted that Khelashvili et al. (2006) approximate the scattering distribution to be radially symmetric. Although this approximation holds for scattering from spherical partials, this approximation might not be accurate enough for a quantitative reconstruction of a heterogeneous sample.

Chapter 3

Experimental Setup and Image Preprocessing

This chapter provides a detailed description of the tilted-Laue analyser-based imaging experimental setup and the data acquisition process used to obtain the raw images used in this thesis in the first two sections. This is followed by a description of the composition of the samples, which were imaged using the tilted-Laue analyser-based imaging experimental setup and reconstructed in this thesis. Sections 3.4 and 3.5 introduce two Python-based distortion correction methods to correct two different geometrical distortions in the raw images. One is to correct the inherent asymmetrical distortion generated by the camera used to obtain the images, and the other is an unavoidable consequence of this imaging setup described below. Section 3.6 describes separating of transmitted and diffracted images, isolating the sample region from the diffracted images, and evaluates image alignment. The final three sections will provide a briefly describe the use of Python multiprocessing, chapter discussion, and conclusion, respectively.

3.1 Experimental Setup

This section is dedicated to describe the tilted-Laue analyser-based imaging (TLABI) experimental setup used for the acquisition of raw images used in this thesis. The experiment was conducted at beamline 20B2, hutch 3 (see figure 3.1) of the SPring-8 third-generation synchrotron facility in Japan. The experiment used a 26 keV monochromatic beam, which was generated using a Si(1,1,1) double crystal parallel monochromator with (+,-) non-dispersive arrangement[1]. As illustrated in figure 3.2 (a) and on the right image of figure 3.1, the sample and the detector was tilted 8° clockwise around the optical z-axis with the aim of extracting the phase in 2D. When considering equations (2.51) and (2.52), it is clear that a 45° tilt would yield equal gradient of phase in both the x and y directions. However, the restrictions in the experimental setup only allowed a maximum tilt of 8°. For clarity, the orientation of the sample with respect to Bragg planes as seen from the incoming x-ray beam is depicted in Figure 3.2 (b).

Then the 26 keV monochromatic beam traverse through the sample and strikes the near-

[1]For an extensive review on monochromators used in x-ray synchrotron radiation see Caciuffo et al. (1987).

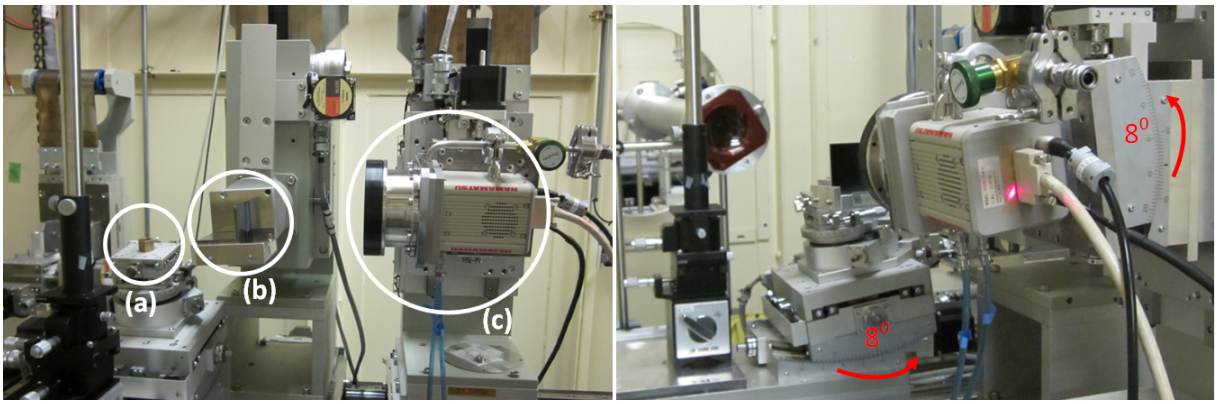

Figure 3.1: *These pictures display the experimental setup inside hutch 3 of beamline 20B2. (a), (b) and (c) on the picture to left show the sample stage, the analyser crystal mount, and the detector, respectively. The picture to the right display the setup from a different vantage point, displaying the* 8^0 *tilt of the sample stage and the detector.*

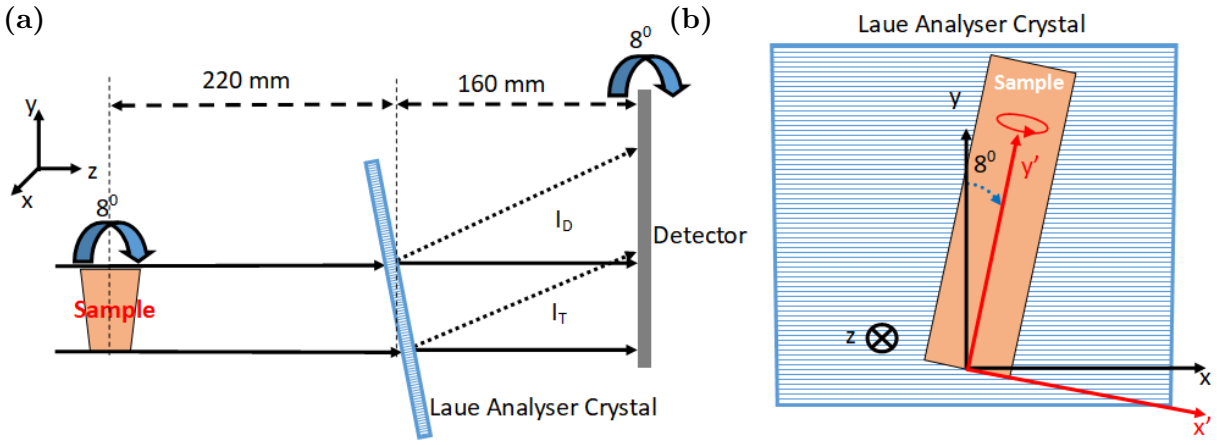

Figure 3.2: *(a) Side view of the Tilted Laue Analyser-Based experimental setup where the sample and the detector are tilted by* 8^0 *around the optical axis, z, and b) the sample orientation with respect to Bragg planes of the analyser crystal as seen by the incoming x-ray beam.*

perfect analyser crystal setup in the Laue geometry, which is mounted 220 mm from the centre of the object. The analyser crystal, behaving similar to an angular filter, separates the diffracted beam I_D from the transmitted beam I_T. As depicted in figure 3.2 (a), these two beams is then detected simultaneously by the detector which is located 160 mm from the analyser crystal.

The images were captured using a fibre optic camera and its large field of view enabled the capture of both the diffracted and the transmitted beams simultaneously. The detector used for the experiment was C9300-124F detector made by Hamamatsu Photonics KK. It was a 4000 × 2672 pixel fibre optic camera, which had an effective pixel size of 16.2 μm. This detector has a demagnification ratio of 1.8:1 and was made by directly bonding one end of the tapered fibre bundle onto the CCD chip and by directly depositing a 20 μm thick, GADOX ($P43, Gd_2O_2S : Tb^+$) phosphor to the other end as the scintillation material (Uesugi et al., 2011). A disadvantage of using a fibre optic camera is that the deviation of photons from its rectilinear trajectory due to the fibre optic taper results in an asymmetrical distortion (FOT distortion) in images (Islam et al., 2010; Uesugi et al., 2011). This distortion was mapped by

Islam et al. (2010) using a precision made grid pattern for the above mentioned camera. Any form of geometrical distortions could lead to distortion artefacts in the CT reconstructions (Vo et al., 2015). Therefore, using the distortion map created by Islam et al. (2010), a solution to this asymmetrical distortion is discussed in section 3.4.

The analyser crystal was a 100 μm thick monolithic Si(1,1,1) wafer. It was used in non-dispersive scheme with respect to the monochromator crystal to eliminate the effects of dispersion caused by band-width and beam divergence (Suortti and Thomlinson, 2003). The diffracted and the transmitted beams are misaligned by $2\theta_B$, in this experiment, their misalignment is 8.722^0 (Chalmers et al., 2021). This makes the diffracted image stretch vertically by a factor of $1/cos(2\theta_B)$ (crystal distortion). A correction to this is discussed in detail in section 3.5.

3.2 Data Acquisition

This thesis reconstructs and analyses the attenuation, 2D phase gradient and dark-field information of two samples. Specific details about the two samples used in this experiment are described in the following section. The data acquisition process for both samples was the same. This section details the process of data acquisition using the setup described in section 3.1.

First, dark-current images were taken by stopping the beam with a shutter. These were used to correct the dark-current signal, which is inherent to the detector, by subtracting the average of dark-current images from the projection images. Then flat-field images were taken without the sample present, but with the analyser crystal in place. These were used to correct the background inhomogeneities in the projection images. A fiducial marker image (see figure 3.7 (a) and (b)) was taken by placing circular markers in the beam. This was then used to correct the vertical stretch on diffracted images and align them with the transmitted image. Let us call this the crystal distortion[2].

As detailed in section 2.4.2, representing the intrinsic rocking curve, 261 projections were taken at 261 analyser angular positions without the sample present in the beam. Then the sample was positioned in the beam with a tilt of 8° clockwise (see figure 3.2). The sample was rotated around y' (see figure 3.2 (b)) in increments of 0.1° over 360° to acquire 3600 tomographic projections. Tomographic projections were collected for eight analyser crystal positions around the rocking curve. The eight locations represent the 5%, 25%, 50%, and 80% of the Bragg peak reflectivity on either side of the rocking curve (see figure 3.3). The region of interest in the detector was diminished from 4000×2672 pixels to 735×1448 pixels to speed up the image reconstruction. Therefore, each projection consists of 735×1448 pixels with a pixel size of 16.2 µm.

3.3 Samples

Two samples were reconstructed and analysed in this thesis (see figure 3.4). This section aims to introduce these samples and describe their composition.

[2]See section 3.5 for more details on the correction method.

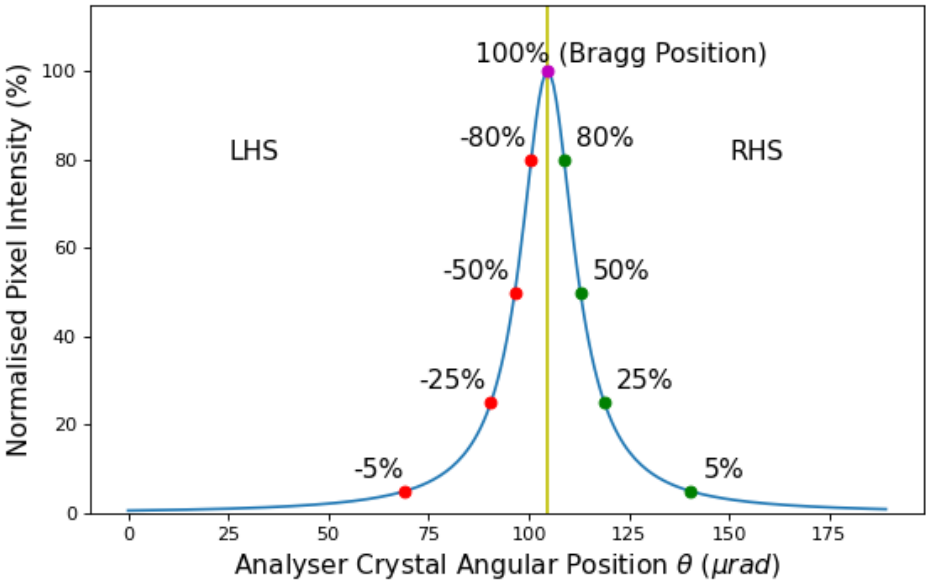

Figure 3.3: *The eight imaging locations on the rocking curve. Point 100% illustrates the maximum intensity, which is the Bragg angle. During data acquisition, 3600 tomographic projections covering* 360^0 *were taken at each location denoted as -5%, -25%, -50%, -80%, +80%, +50%, +25%, and +5% on the rocking curve. Here, the negative and positive signs on 5%, 25%, 50%, and 80% values corresponds to left and right hand sides of the rocking curve, respectively.*

Three-Material Phantom

This phantom was made using a 12.75 ± 0.05 mm diameter Perspex (PMMA) cylinder with a height of 10 mm. It has four cylindrical cavities cut into it with cavity having a diameter of 1.02 ± 0.05 mm. This is illustrated in figure 3.4 (a). Two of these cavities were left empty and the other two are filled with a small aluminium and Teflon (PTFE) pins. Since this phantom had materials with known δ and β values (see table 3.1), it can also serve as a test case to verify that the reconstruction algorithm gives the desired output compared to the algorithm used by Chalmers et al. (2021). With this phantom we can expect to see a USAXS signal originating at the boundaries between media. Since Teflon has been known to produce strong visible light scattering (Qinghe Li et al., 2008), the Teflon pin was also expected to produce some USAXS signal.

Table 3.1: *The components of the index of refraction for the material used to construct the sample at* 26 *keV. Values taken from https://henke.lbl.gov/optical_constants/. Accessed date: 10/02/2021.*

Material	$\delta(\times 10^{-7})$	$\beta(\times 10^{-10})$
Perspex ($C_5H_8O_2$)	3.943	1.392
PTFE (C_2F_4)	6.488	3.730
Aluminium	8.003	15.20

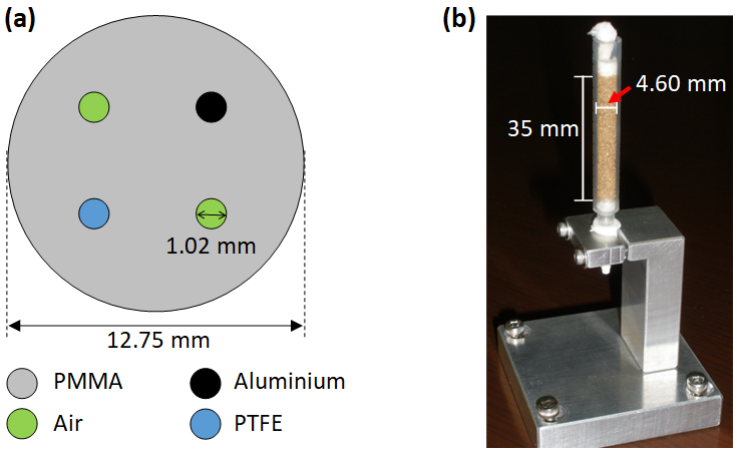

Figure 3.4: *(a) A cross sectional view of the 3-material phantom. It is a* 12.75 *mm diameter Perspex (PMMA) cylinder with four cavities, each with a diameter of* 1.02 *mm. Two of these are left empty and the other two contain Aluminium and Teflon (PTFE) pins. (b) A picture of the* 4.6 *mm diameter cylinder packed with sieved clay loam into a column section of* 35 *mm attached onto a mounting bracket.*

Clay Loam Sample

This sample contained dried and sieved clay loam. For its preparation, clay loam was dried and sieved to sizes between 125 µm and 1400 µm. Then it was tightly packed into a 35 mm column section of a 4.6 mm diameter syringe. The top and the bottom of the column section was plugged with tissue paper to hold the sand in place. This is important because during data acquisition, the sample was rotated around its central axis for tomographic data acquisition. The vibrations from this rotation and the vibrations from the stepping motor used to rotate the analyser crystal could move clay loam particulates hindering the results from this experiment. With this sample we can expect a very high USAXS signal because small clay loam particulates have many interfaces with air and having large number of them in projection are likely to cause considerable USAXS. Figure 3.4 (b) display a picture of the sample attached onto a mounting bracket.

3.4 FOT Distortion Correction

To correct the FOT distortion, Kitchen et al. (2010) and Chalmers et al. (2021) employed the the `Warp_tri` function in the commercially available application Interactive Data Language (IDL) by Harris Geospatial Solutions[3]. This software uses tie points (set of selected coordinates) to map the distorted image to an undistorted image grid using Delaunay trianulation. Islam et al. (2010) did a quantitative analysis on the `Warp_tri`[4] function output and compared it to two other approaches, global polynomial fitting and local polynomial fitting. They found that for distortion correction `Warp_tri` gave the most satisfactory results with sub-pixel accuracy.

Triangulated interpolation or Piecewise Affine Transformation (PAT) (Cootes and Taylor, 2004) works by taking the source image (distorted image) and dividing it into triangular tessel-

[3]Kitchen et al. (2010) and Chalmers et al. (2021) also used this software for their reconstructions.
[4]Islam et al. (2010) called the process which `Warp_tri` uses triangulated interpolation.

lations using a pre-determined map of warped tie points (source points) as the vertices. First, it uses Delaunay triangulation to partition the source image. Then using the corresponding vertices for each triangle in the undistorted tie points (destination points), the affine transform between the triangles are calculated. This is done to each triangle, and the pixels in each triangle are then transformed using the transformation matrix corresponding to that triangle.

Islam et al. (2010) mapped the distortion in the detector used for the acquisition of projection images used in this thesis. They used a precision made grid pattern, which had 67,731 small holes equal length apart. Imaging this object provided 67,731 tie points covering a 4000×2672 pixel image, which can be used as a map to correct the distortion. Since one of the goals of this research is to use Python as the main programming language, Scikit image's piecewise affine transform (van der Walt et al., 2014)[5] was considered as a potential candidate to replace IDL's `Warp_tri` function.. This program was tested using a synthetic 4000×2672 pixel image, which was generated using the 67,731 tie points (see figure 3.5 (a) and (b)). The test was run on an Intel core i7 8^{th} generation 3.2Ghz computer with 32GB of RAM[6] and this program took approximately one and half hours to process a single 4000×2672 pixel image. Considering the large number of images ($\sim 30,000$ per sample) needed to be processed for this research, it was evident that the direct implementation of this program was not viable.

Scikit Image Implementation

Using a version of the Scikit image's PAT, a Python program was written to accomplish the FOT distortion correction with an efficiency of approximately 3.5 seconds per image (see appendix A.1.5). First, all the unnecessary lines of code was removed because Scikit image's PAT is written as a general purpose tool to distort low resolution RGB images. Then functions were defined to determine which parts of the streamlined program took the longest time. Once it was broken down to its core functions, it was evident that the heaviest (in terms of run time[7]) function was only needed to run one time as the distortion in all images are the same. Therefore, the output of this function was saved as a TIFF file to be imported in the future. The purpose of this function was the estimation of the output pixel map containing the information on which pixel corresponds to which triangle. Elimination of this function by replacing it with the importation of pre-calculated arrays (the aforementioned TIFF file) reduced the run time down to approximately 7 seconds for a 4000×2672 pixel image.

As mentioned in section 3.2, to speed up the tomographic image acquisition, the region of interest of the detector was reduced to 735×1448 pixels. This meant that the number of tie points used in could be reduced significantly, which reduced the number of triangular tessellations leading to lower number of matrix calculations per image. Therefore, the coordinates of the tie points covering the ROI were separated. This reduced the number of tie points from 67,731 to 39,457. The program was then run again using this reduced number of tie points, and found that the run time per image reduced to approximately 3.5 seconds.

Once the efficiency issues were fixed, this program was compared to the IDL's `Warp_tri` function using the synthetic grid image. It was soon realised that unfortunately, this code did

[5] An open source image processing library: https://scikit-image.org/.

[6] This computer was used for all of the computations discussed in this thesis.

[7] This function took 193.62 seconds for 67,731 tie points. Appendix A.1.5 shows the source code of this function.

not provide the same distortion correction accuracy as IDL's `Warp_tri` function. Figure 3.5 (c) and (d) show a visual comparison between the output of this implementation and the output of IDL's `Warp_tri` function, respectively.

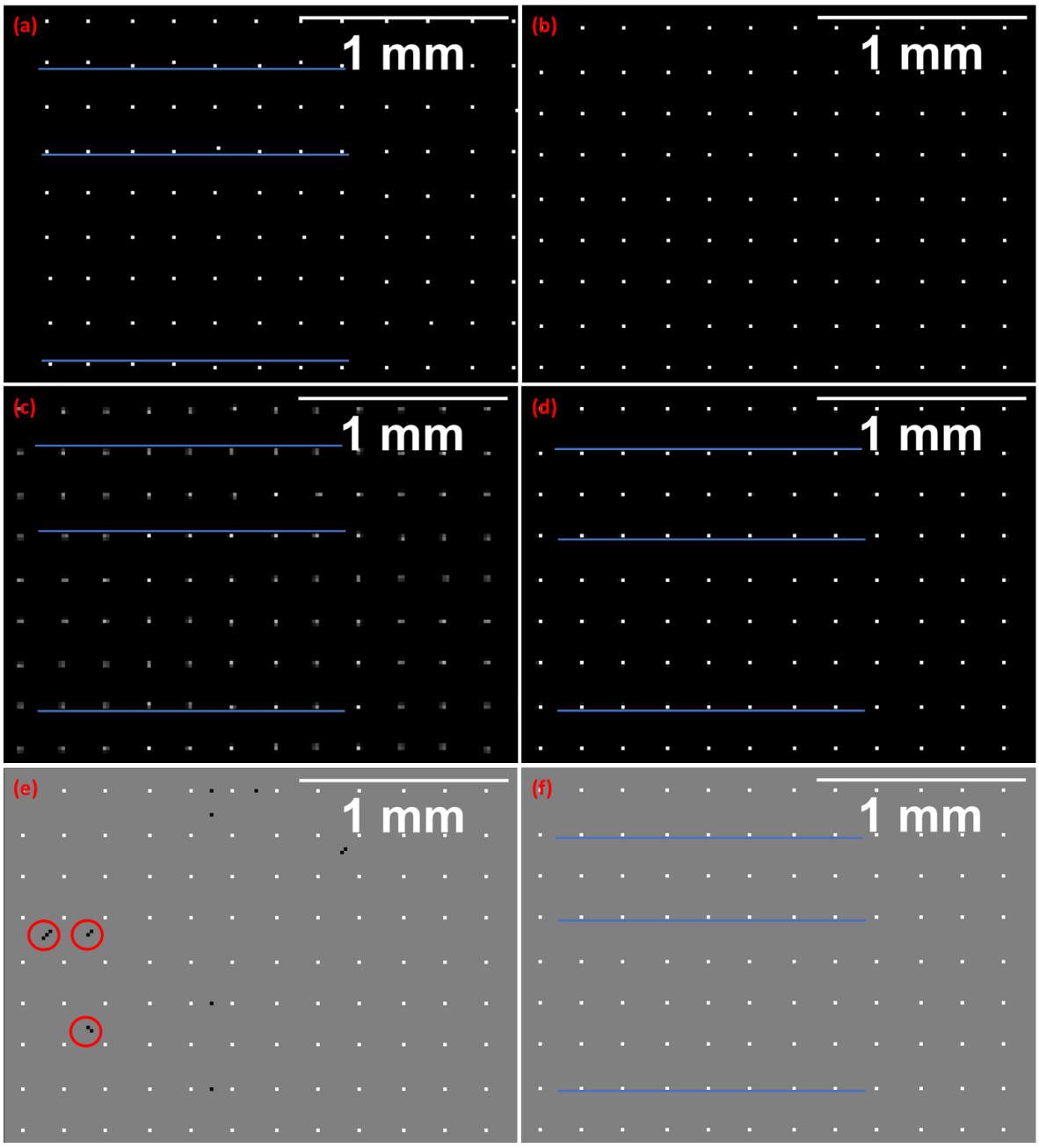

Figure 3.5: *A comparison between asymmetrical distortion corrections. Blue straight lines are to check straightness. (a) Distorted grid image generated using distorted tie points, (b) Undistorted grid image generated using undistorted tie points, (c) Scikit image implementation results, (d) IDL's* ***`Warp_tri`*** *result, (e) OpenCV implementation result without interpolation showing empty pixels, and (f) the final result of OpenCV implementation after applying the nearest neighbour interpolation with a Gaussian kernel to the empty pixels.*

OpenCV Implementation

The development of Scikit image implementation gave a deeper understanding into how to use Delaunay triangulation to correct an asymmetrical distortion. It was evident that to achieve better image quality, better algorithms implementing each step was necessary. This led to the search for better libraries, which can implement each individual step reliably. OpenCV (Bradski, 2000)[8], which is a library used for computer vision, was identified as a potential candidate. Therefore, using the following functions from OpenCV, PAT was implemented as a potential replacement for the Scikit image implementation. Appendix A.1.1 shows the source code of the OpenCV Implementation.

Step 1 Delaunay triangulation using tie points : **cv2.Subdiv2D() and getTriangleList()**.

Step 2 Isolating the rectangle bounding the triangle : **cv2.boundingRect()**

Step 3 Isolating pixels within the triangle : **cv2.fillConvexPoly() and cv2.bitwise_and()**.

Step 4 Finding the transformation matrix between the source triangle and the destination triangle : **cv2.getAffineTransform()**.

Step 5 Apply affine transformation to the pixels within the triangle : **cv2.warpAffine()**.

Similar to Scikit image implementation, for OpenCV Implementation, step 1 was executed once and the output was saved to be imported later. Using a reduced number of tie points, covering the ROI, this implementation corrected the distortion in approximately 7 seconds. Though the execution time is doubled that of Scikit image implementation, the OpenCV Implementation gave an almost perfect distortion correction. (see figure 3.5 (e) and (f)).

Figure 3.5 (e) illustrate the initial output of the dewarp process which gave zero value pixels. These pixels coincide with the the lines connecting the vertices. Nearest neighbour interpolation was used with a Gaussian kernel to correct these pixels. Figure 3.5 (f) show the final result of this interpolation.

Quantification of Distortion Correction Accuracy

To get a better understanding of these three methods, normalized Root Mean Square Error intensity differences between dewarped and the ideal image for 1,448 pixel rows was plotted for Scikit image implementation, IDL `Warp_tri`, and OpenCV Implementation (see figure 3.6 (d), (e), and (f)). To calculate the RMSE, first a synthetic image of the ideal output was generated using the destination tie points (see figure 3.5 (b)). This image was used as the expected parameter when calculating the RMSE. Plots in figure 3.6 clearly indicate that OpenCV Implementation was significantly better at preserving pixel intensities when correcting the distortion. Figure 3.6 (a), (b), and (c) show a single pixel from Scikit image implementation, IDL `Warp_tri`, and OpenCV Implementation outputs, respectively. While Scikit image implementation and IDL `Warp_tri` show pixel blurring, the OpenCV Implementation shows no blurring.

[8] https://docs.opencv.org/

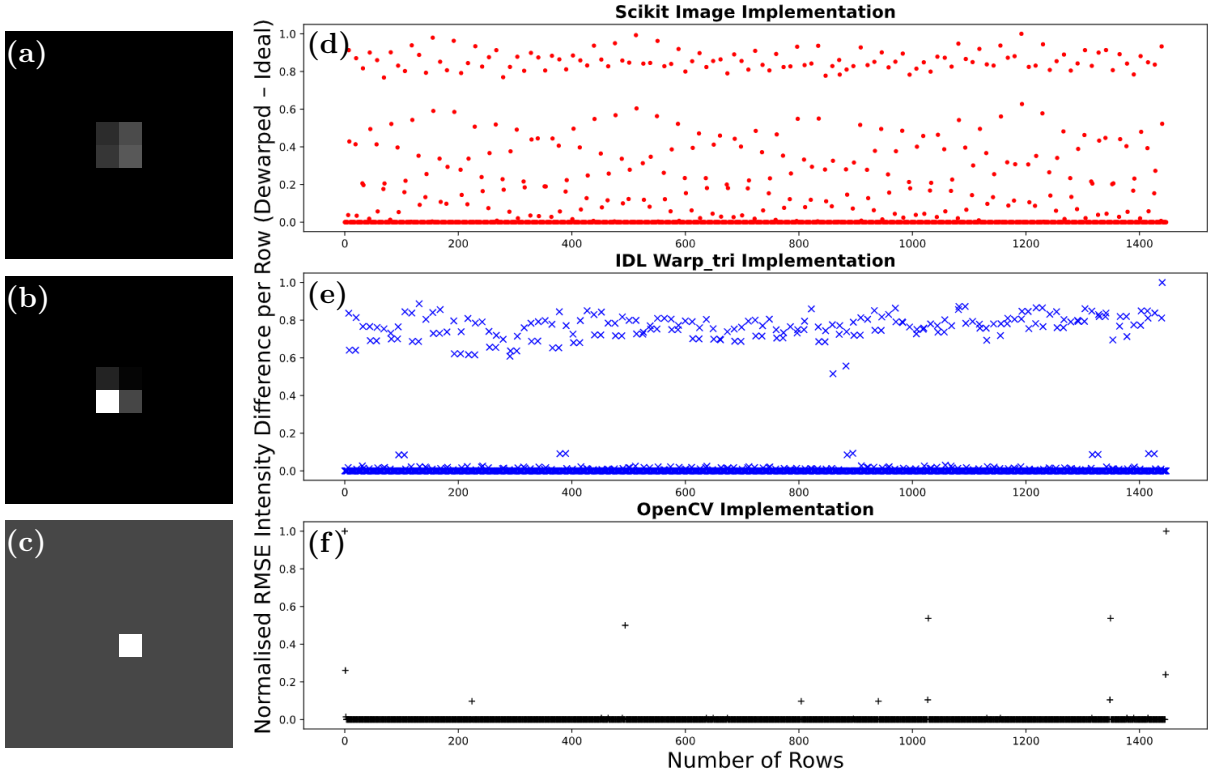

Figure 3.6: *(a), (b) and (c) show examples of magnified tie point pixels from corrected images using the Scikit image implementation, IDL* `Warp_tri`*, and the OpenCV Implementation, respectively. As shown in image (c), OpenCV Implementation show no pixel blurring near tie points. (d), (e), and (f) show the plots of normalized Root Mean Square Error (RMSE) intensity difference between dewarped and ideal image for 1448 pixel rows for Scikit image implementation, IDL* `Warp_tri`*, and OpenCV Implementation, respectively. In comparison, plot (f) clearly gives the lowest overall RMSE, showing OpenCV Implementation (OpenCV implementation) is significantly more accurate than the IDL* `Warp_tri` *implementation.*

3.5 Crystal Distortion Correction

As discussed in section 3.1, the misalignment between the diffracted beam I_D and the transmitted beam I_T (see figure 3.2) by $2 \times \theta_B$ stretches the diffracted image vertically by a factor of $1/cos(2\theta_B)$. For accurate phase retrieval utilising diffracted images, this vertical stretch must be corrected and the diffracted images must be aligned accurately with the transmitted images. Aligning the diffracted images properly require a shift, a stretch, and a rotation. Essentially, this can be achieved using an affine transformation.

To do this affine transformation a fiducial marker image was taken and its FOT distortion was corrected using the OpenCV Implementation introduced above. Then the diffracted and the transmitted fiducial images were separated (appendix A.1.2 provides the Python image separation function). The separated diffracted and transmitted fiducial images are displayed in figure 3.7 (a) and (b), respectively. Following that, the centre points of these markers were calculated using imageJ. This provided indices for two triangles representing a source triangle and a destination triangle corresponding to the diffracted image and the transmitted image, respectively. Using these triangle indices, the transformation matrix between the transmitted and the diffracted image planes was estimated. Instead of applying this matrix for the pixels

with in the triangle enclosed by the three points, it was applied to all the pixels in the diffracted image. This was accomplished using cv2.getAffineTransform() and cv2.warpAffine() modules from OpenCV (see appendix A.1.3). In this thesis this method shall be referred to as the OpenCV affine transform.

The resulting diffracted image from the OpenCV affine transform was then subtracted by the transmitted image to check if the markers line up. Figure 3.7 (d) displays this subtracted image. This output was then compared to the output from the method developed by (Kitchen et al., 2010) (see figure 3.7). For conveniences, this method will be referred to as Kitchen's method. In Kitchen's method output, figure 3.7 (c), a circular set of white pixels can be seen around the upper fiducial marker. A similar effect is also seen in the inner circle of the lower fiducial marker. This is an indication of slight misalignment between the transmitted image and the diffracted image. However, the OpenCV affine transform output in figure 3.7 (d) show a much smaller number of white pixels around the fiducial markers. Compared to Kitchen's method output, it is less pronounced and they seem to be evenly distributed.

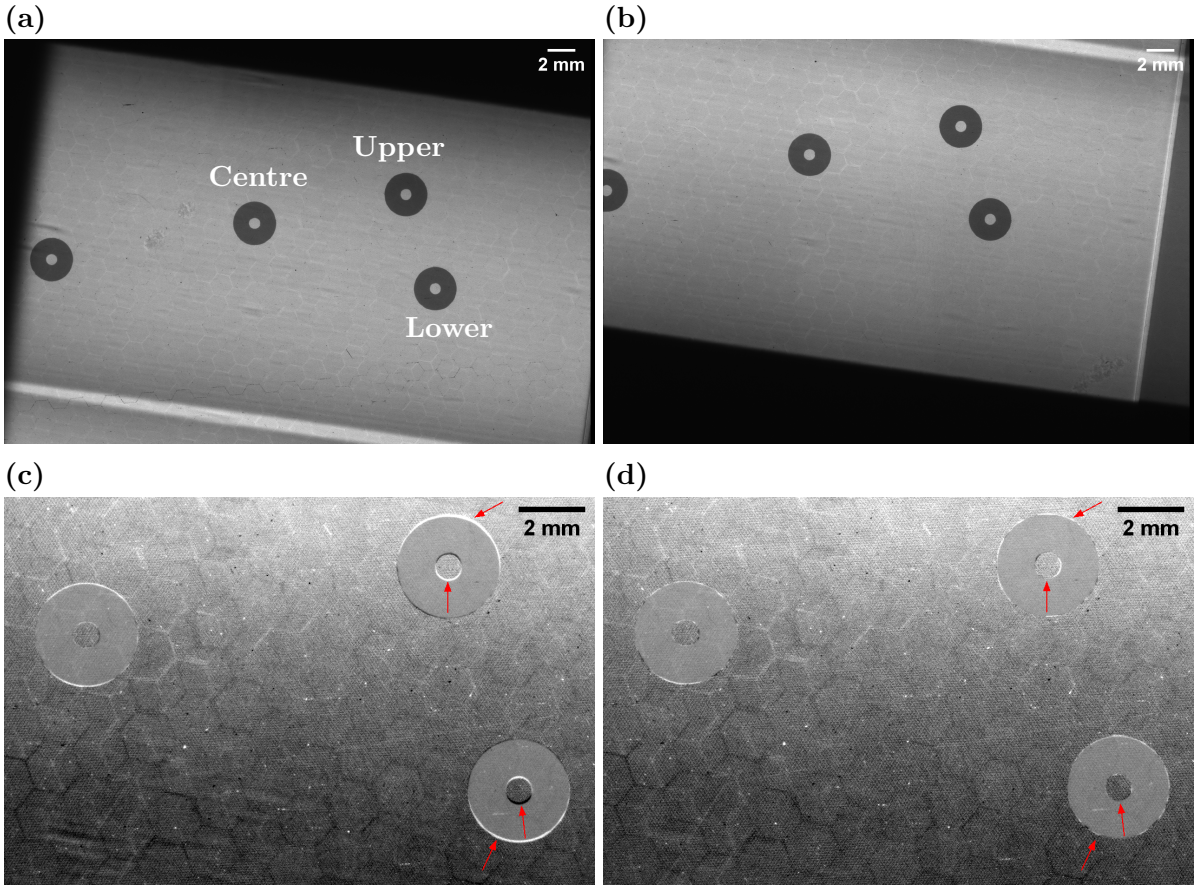

Figure 3.7: *(a) and (b) are fiducial marker images of diffracted and transmitted beams, respectively. (c) and (d) compare the outputs of Kitchen's method and the OpenCV affine transform program, respectively. Here, the arrows point to subtle differences between the outputs of Kitchen's method and the OpenCV affine transform program. Here, to ensure a fair comparison, it was made certain that the pre-processing steps on the fiducial marker images were identical for both crystal distortion correction methods.*

3.6 Image Cropping and Alignment Testing

As a result of poor alignment of the centre of rotation of the CT stage and the detector pixels, during tomographic projection acquisition, in the recorded images the samples display a side to side swaying. This swaying is illustrated in figure 3.8. When cropping the projection images, this side to side sway must be taken into account so that sections of the sample are not cropped out. For both samples, namely the 3-material phantom and the clay loam sample, the ROIs were carefully estimated. Then these ROIs were applied to both the measured projections (with sample images) and the intrinsic projections (without the sample images). The three-material phantom images were cropped to a size of 1090×770 pixels and the clay loam sample images were cropped to a size of 935×780 pixels.

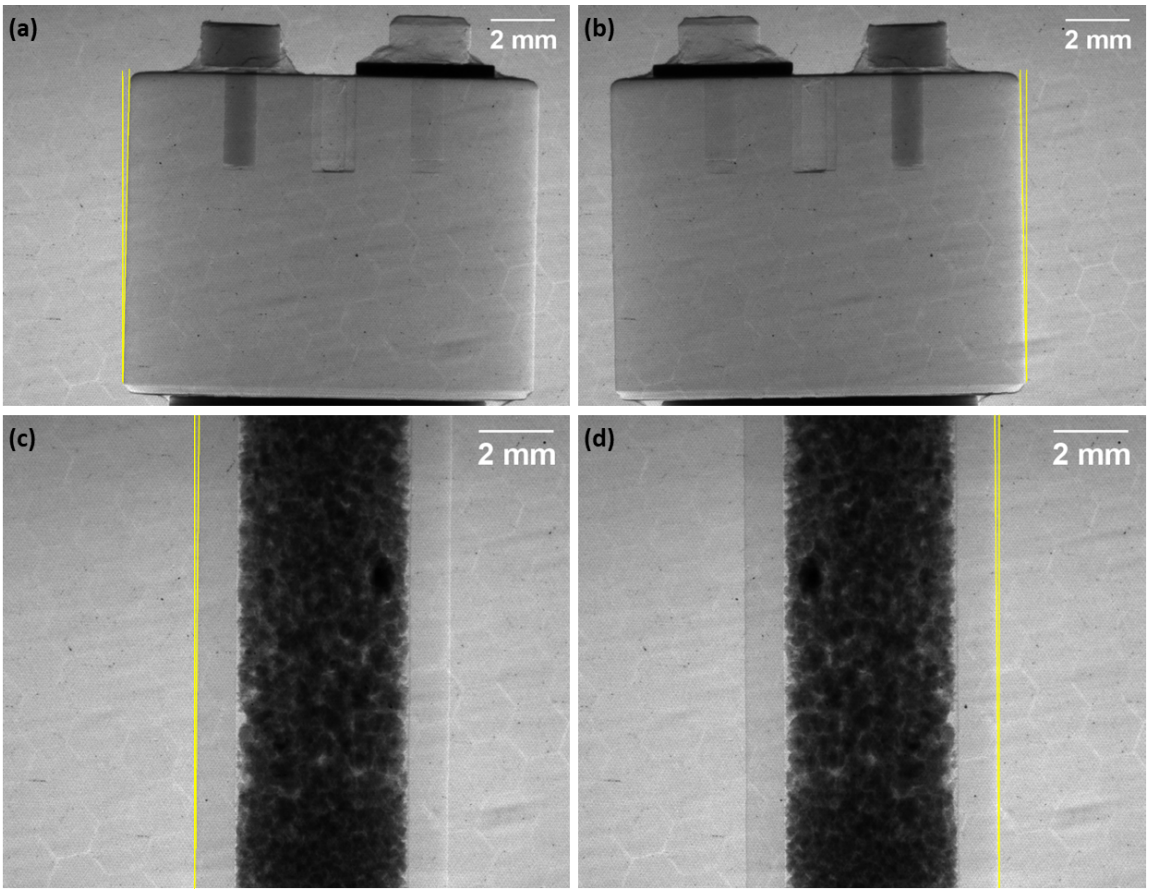

Figure 3.8: *Display the side to side swaying of the sample during tomographic data collection. (a) and (c) illustrates the first tomographic projection at rotation angle* $0°$ *of the three-material phantom and the clay loam sample, respectively. (b) and (d) illustrate the* 1800^{th} *tomographic projection at rotation angle* $180°$ *of the three-material phantom and the clay loam sample, respectively. The angular deviation at each projection (a), (b), (c), and (d) from its normal was measured to be* $1.27°$*,* $1.27°$*,* $0.52°$*, and* $0.52°$*, respectively. Yellow lines illustrates this angular deviation.*

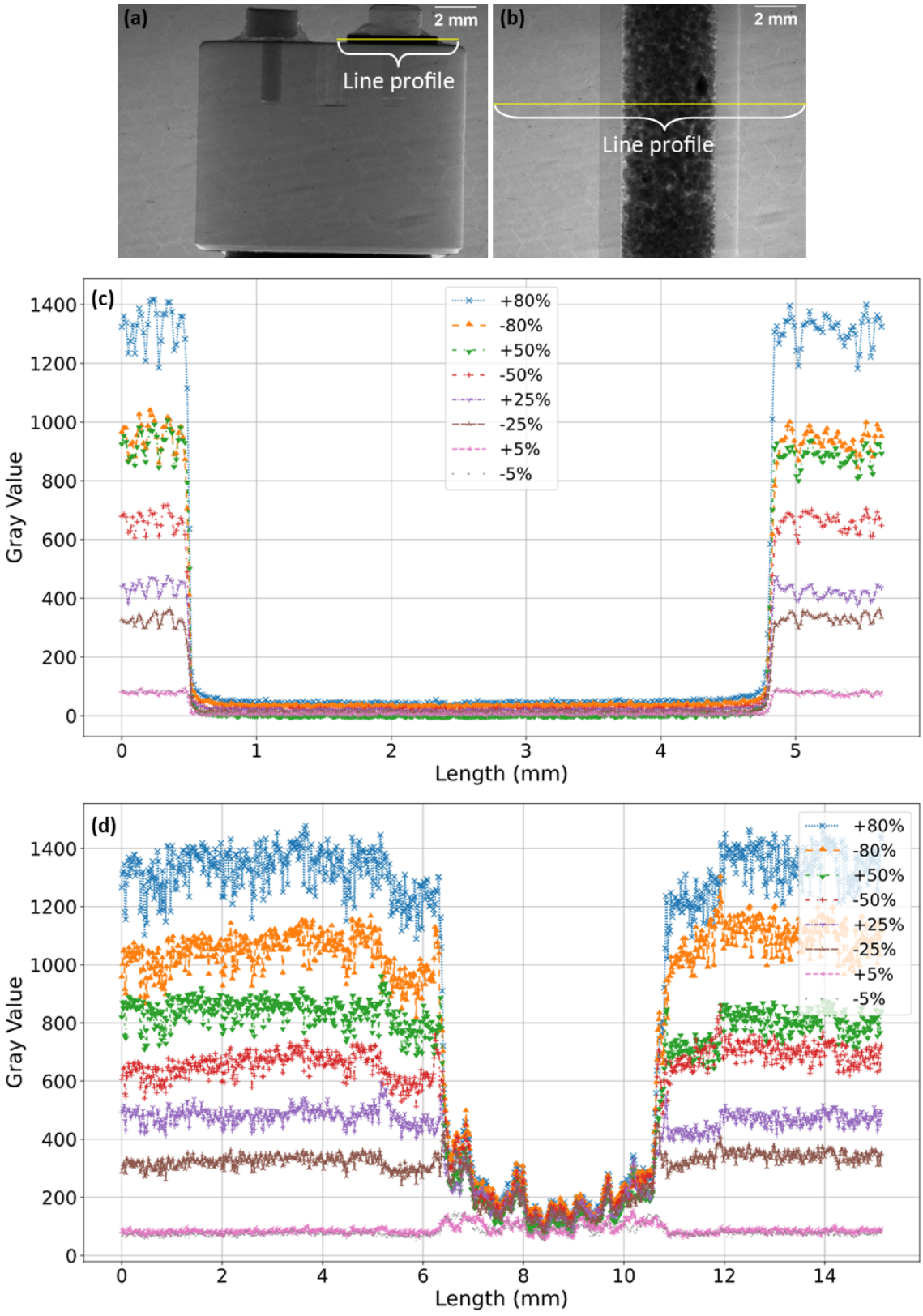

Figure 3.9: *Superimposed line profiles of the projection images at each working point around the rocking curve for the purpose of alignment testing. Line profiles were drawn on each image taken at each working point -5%, -25%, -50%, -80%, +80%, +50%, +25%, and +5% and was plotted on top of each other for both the three-material phantom (c) and the clay loam sample (d). The location of the line profiles are displayed in (a) and (b). The tomographic angular position used here is* 1.5° *(*15^{th} *projection).*

Once cropped, the sample features in the projection images at each working point around the rocking curve at each tomographic position must be aligned properly. During the experiment the samples were moved in and out of the beam between the scans to run flat-field corrections. Therefore, imperfect repositioning of the samples between scans could lead to translation offsets. This was tested by drawing line profiles at the same position on projection images taken at each working point for a randomly selected tomographic position. Figure 3.9 display the superimposed line profiles of all working point images taken at tomographic angular position 1.5^0 for both the three-material phantom and the clay loam sample. In the superimposed line profiles for the three-material phantom in figure 3.9 (c), the lines corresponding to the air-phantom boundary clearly indicate that the features are well aligned. The superimposed line profiles for the clay loam sample in figure 3.9 (d) also indicate this to be true.

3.7 Implementing Python Multiprocessing

Python multiprocessing[9] gives the ability to leverage multiple processors to process a given work load. The CPU used in this project had eight cores, therefore, the Python multiprocessing package was used to increase hardware utilisation during this project. First, the dark-field correction, FOT distortion correction (OpenCV implementation), diffraction and transmitted image separation, crystal distortion correction, and the process of image cropping were combined into a single program (see appendix A.1.4). This allowed for the parallelization of a function's execution over numerous input values, as well as the distribution of input data across processes (data parallelism). Effectively, this enabled the possibility of processing approximately 56,000 (combined number of projection images for both samples) high resolution x-ray images in approximately eight hours.

3.8 Discussion

The primary objectives of this chapter were to introduce the experimental setup of TLABI, the process of data acquisition, the samples analysed in this thesis, and the introduction of two Python-based distortion corrections to correct the FOT distortion and the crystal distortion correction. This chapter also discussed the process of diffracted and transmitted image separation, image cropping and the use of multiprocessing to increase runtime efficiency.

As pointed out in the section 3.1, fibre optic cameras produce an asymmetrical distortion. To correct this distortion, this chapter introduced a Python based asymmetrical distortion correction method, which is both efficient and robust. Quantitative analysis done by Islam et al. (2010) on several distortion correction methods[10] using the same detector used for this project concluded that triangulated interpolation gave the most satisfactory outcome for correcting asymmetrical distortions. They used IDL's `Warp_tri` to implement triangulated interpolation. Therefore, the IDL's `Warp_tri` was used as a baseline to test the Python based asymmetrical distortion correction methods proposed in this chapter.

[9] https://docs.python.org/3/library/multiprocessing.html#module-multiprocessing

[10] Islam et al. (2010) compared triangulated interpolation to both a global polynomial fitting method and a local polynomial fitting

Though triangulated interpolation or piecewise affine transformation (PAT) is not commonly used to correct asymmetrical distortions in high resolution x-ray images, it is heavily used in computer vision for image morphing (Davison et al., 2018; Chen et al., 2019). The Scikit image implementation, which is an accelerated version of Scikit-image's PAT modules source code, corrected the distortion of an image of size image size to 735 × 1448 pixels to 3.5 seconds. Run time efficiency was paramount considering the number of total images required corrected (approximately 56,000) and the total time allocated for this project (12 months). The Scikit image implementation was tested using a synthetic grid image (see figure 3.5 (c)) and it was compared to the output by the IDL's `Warp_tri` (see figure 3.5 (d)). Visual examination of the Scikit image implementation output of the synthetic grid image showed excessive pixel blurring near tie points. This was further confirmed by plotting the normalised RMSE intensity difference between the Scikit image implementation output and the ideal image for 1,448 rows (see figure 3.6 (a) and (d)). This pixel blurring could be attributed to bilinear interpolation used to map the pixels from the source image to the destination image. In the `Warp_tri` output, the pixel blurring was visually less pronounced compared to the Scikit image implementation output. However, the RMSE plot showed that `Warp_tri` does apply some pixel blurring to achieve its results (see figure 3.6 (b) and (e)). Similar to the Scikit image implementation, the origins of `Warp_tri` outputs pixel blurring could be likely due to the way in which they utilise interpolation to map pixels. When comparing the Scikit image implementation output to `Warp_tri` output, the Scikit image implementation output was found to lack the accuracy required for an accurate phase retrieval.

The OpenCV implementation corrected the distortion in an image of size 735 × 1448 pixels in approximately 7 seconds. Although the OpenCV implementation provided nearly a perfect result, its initial output included some empty pixels (see figure 3.5(e)). Close visual investigation showed that they seem to lie on top of lines connecting the vertices of the triangular tessellations from Delaunay triangulation. There are two possible explanations for these empty pixels. First is that the number of pixels in the destination triangle is higher than the source triangle. The second explanation is that the OpenCV module cv2.warpAffine() fails to efficiently identify and map all pixels on the edges of the triangle boarders. These empty pixels were corrected using nearest neighbour interpolation with a Gaussian blur. It was found that visually the output was indistinguishable from the ideal output (see figure 3.5 (f)). However, RMSE plot in figure 3.6 (f) show some anomalies. These are largely due to the empty pixels corrected using the nearest neighbour interpolation with a Gaussian blur. This analysis provides great confidence to use the OpenCV implementation to correct the FOT distortion in all projection images used in this thesis. However, further analysis in the future using actual x-ray images, similar to the quantitative analysis done by Islam et al. (2010), would be helpful to fully understand the accuracy of the OpenCV implementation. This type of camera is used by many researchers around the world, and asymmetrical distortion is an inherent problem with these cameras. Therefore, these findings were presented as a poster at the Australian Synchrotron Users Meeting 2020 hosted by Australia's Nuclear Science and Technology Organisation (ANSTO) (Gunasekera, 2020).

For crystal distortion, two correction methods were tested, Kitchen's method and the OpenCV

affine transform method (see figure 3.7 (c) and (d)). A close visual comparison of outputs found that the OpenCV affine transform method aligned the transmitted image and the diffracted image with high precision, as indicated by the fiducial markers blending into the background (3.7 (d)). However, Kitchen's method output displayed slight gradients at the top edge of the upper fiducial marker and also on the lower half of the inner circle of the lower fiducial marker (see figure 3.7 (c)). Therefore, for this thesis, the OpenCV affine transform will be used to correct the crystal distortion in projection images.

Another preprocessing step presented in this chapter was image cropping. An advantage of this was that it reduced the number of pixels by removing the extra air regions. This effectively lowered the overall reconstruction time by reducing the total number of pixel-by-pixel basis curve fittings. Furthermore, the alignment testing showed that the projection images for both samples, namely the three-material phantom and the clay loam sample, taken around the rocking curve are well aligned (see figure 3.9). Any misalignment between sample features in the projection images taken around the rocking curve can result in significant errors in the estimated phase later. Chapter 4 discusses the pixel-by-pixel basis curve fitting and further discusses the importance of image alignment.

The use of Python multiprocessing helped reduce overall processing times significantly, making it a highly useful tool. Considering the limited time available for this project, multiprocessing will be heavily implemented in other areas of this project.

3.9 Conclusion

This chapter provided a detailed description of the experimental setup of TLABI, data acquisition process, and the composition of the samples imaged and analysed in this thesis. This chapter also presented two Python-based distortion corrections, which were both highly accurate and provided high speed solutions to correct FOT distortion and crystal distortion, respectively. It was found that the Python-based OpenCV implementation introduced in this chapter to correct the asymmetrical FOT distortion was both superior and robust compared to the existing triangulated interpolation method, IDL's `Warp_tri`. Furthermore, the OpenCV affine transform method for crystal distortion was found to provide a superior result and was easier to implement compared to Kitchen's method. Therefore, the OpenCV implementation of the FOT distortion correction and the OpenCV affine transform method were combined into a single program and Python multiprocessing was implemented to further accelerate these processes. This final program was then used to correct the FOT distortion and the crystal distortion in images analysed in this thesis. Furthermore, this chapter has provided evidence that the images taken around the rocking curve at a given tomographic projection position align perfectly well after running the process of image cropping to reduce the region of air.

Chapter 4

Rocking Curve Parameterisation

Once the distortions of the projection images were corrected, the next step in the reconstruction process was finding the best models for fitting (or parameterising) the rocking curves with (sample rocking curve) and without (intrinsic rocking curve) the sample present in the x-ray wavefield. Therefore, this chapter is dedicated to discussing the process of rocking curve parameterisation. The first section compares potential mathematical models, which can be used to estimate the intrinsic rocking curve. The second section introduces a method for the estimation of the angular positions of the analyser crystal for the eight locations around the rocking curve corresponding to the 5%, 25%, 50% and 80% of the Bragg peak reflectivity on either side of the rocking curve. The subject of the third section is finding the correct mathematical model to parameterise the sample rocking curve and the final two sections will provide a chapter discussion and a conclusion, respectively.

4.1 Intrinsic Rocking Curve Parameterisation

Intrinsic rocking curve fitting was done on pixel-by-pixel basis by stacking the 261 diffracted beam projections[1] with no sample present in the x-ray wavefield. Stacking of these images is illustrated in figure 4.1 (a). A plot of the single pixel array in z direction against the crystal angular position θ is shown in figure 4.1 (b). Here, the rocking curve corresponds to the pixel location x,y = 500, 350.

Using the Python curve fitting library known as LMFIT[2] (Newville et al., 2014), Pearson VII (P7), Voigt, and Pseudo-Voigt (PsV) models were tested as potential candidates to estimate the intrinsic rocking curve. This library utilises the well known Levenberg-Marquardt iterative algorithm (Levenberg, 1944; Marquardt, 1963) to solve non-linear least squares problems. A detailed description of Levenberg-Marquardt iterative algorithm can be found on Press et al. (2007) (pp. 801-805).

Figure 4.2 displays a visual comparison of these three models. For each model, its residuals were plotted to better visualise the behaviour of each model. Figure 4.2 (a), (c), and (e) display the rocking curve corresponding to pixel location $x, y = 500, 350$ fitted with the P7, Voigt, and PsV models, respectively. Here (b), (d), and (f) correspond to the residuals of the P7, Voigt,

[1] See section 3.2 for more details.
[2] https://lmfit.github.io/lmfit-py/index.html

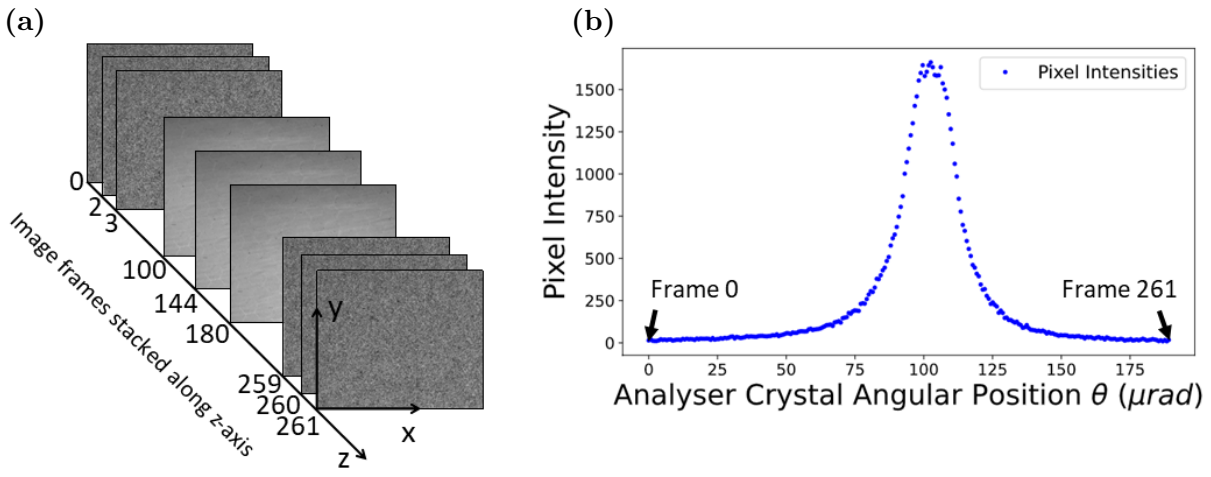

Figure 4.1: *(a) An illustration of projection image stacking in preparation of fitting curves on a pixel-by-pixel basis. The images are stacked along the $z-axis$. (b) Plotted pixel intensities depicting the intrinsic rocking curve corresponding to pixel location $x, y = 500, 350$ against crystal angular position θ. Here, 0^{th} and 261^{st} projections corresponds to $\theta = 0$ μrad and $\theta = 1.89 \times 10^2$ μrad, respectively.*

and PsV models, respectively. Here, when fitting these curves, no weights were used. Weighted curve fitting is discussed in detail in the next section (see section 4.1.1). Looking at the best fits by the three models, and their respective residuals, it is apparent that all three models tend to underestimate the left tail of the rocking curve. When comparing residuals for these three models closely, one could conclude that PsV give a slightly better estimation of the left tail. The residuals of the P7 model show that it slightly underestimates the right tail, while the residuals of PsV model indicate that it overestimates the right tail. Residuals of the Voigt model indicate that its estimation of the right tail is well balanced compared to both P7 model and PsV model. The upper half of the rocking curve seem to be well estimated by all three models. For all three models the residuals corresponding to the upper half of the rocking curve tend to be symmetrically distributed.

Table 4.1: *Calculated χ^2 averages and their standard deviations for Pearson VII, Voigt, and Pseudo-Voigt models. Here, the χ^2 was estimated and averaged by fitting a 935 × 780 pixel region on a pixel-by-pixel basis for all three models. The lowest χ^2 values represent the best fits*

Model	Average χ^2	Standard Deviation
Pearson VII	793.41	216.71
Voigt	790.63	170.36
Pseudo-Voigt	449.33	49.33

The number of intrinsic rocking curve fittings needed for a single sample is of the order of 10^6. Therefore, the analysis of individual fits was not feasible. The overall fitting quality was therefore estimated by fitting a 935 × 780 pixels on a pixel-by-pixel basis and calculating the average χ^2 and its standard deviation. This process was carried out for all three models, namely the P7, Voigt, and the PsV. The results are tabulated and displayed in table 4.1. Considering the low average χ^2 values and the low standard deviation across the image, it can be concluded

that the PsV model is the best of the three models to parameterise all the intrinsic rocking curves of the diffracted beam.

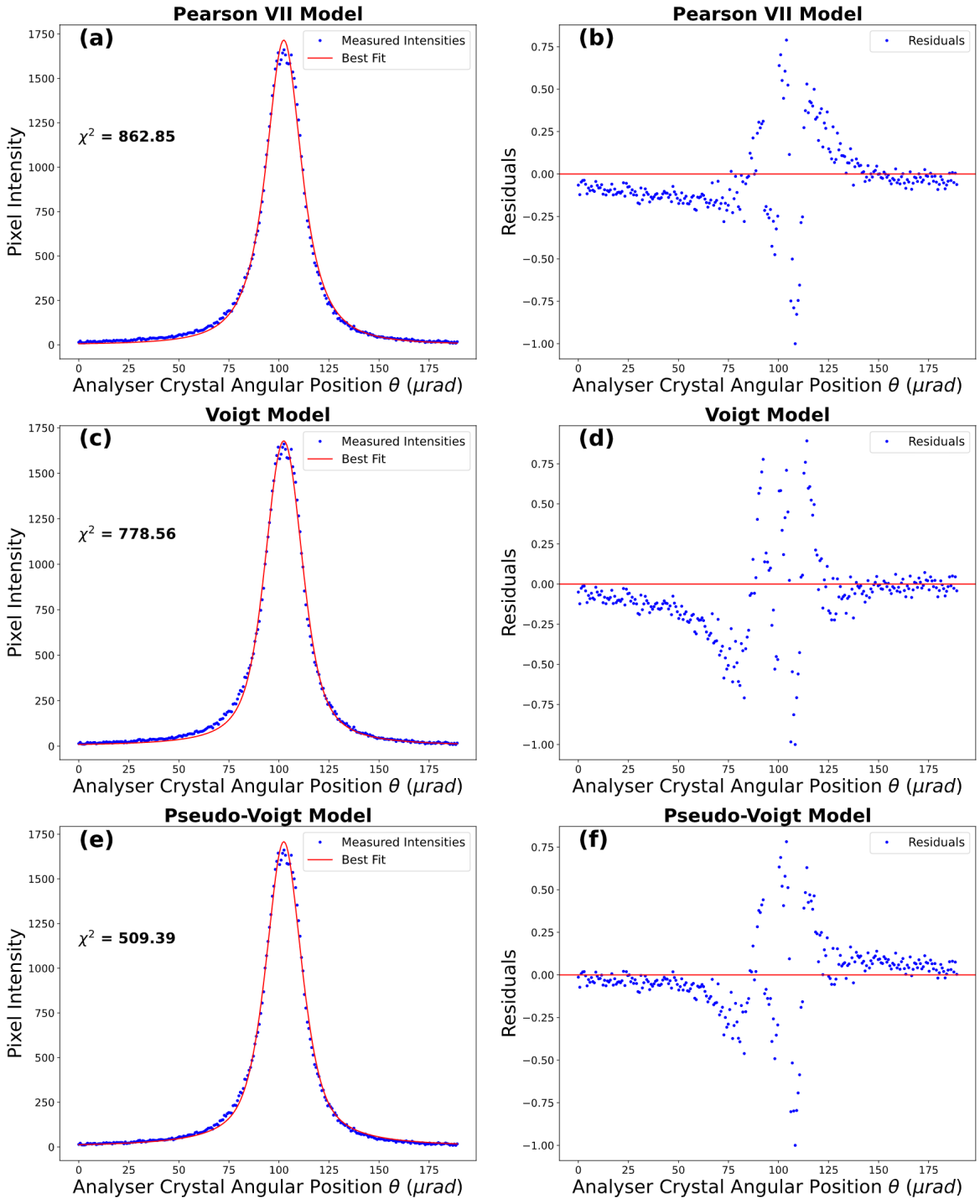

Figure 4.2: *(a), (c), and (e) show the 261 pixel intensities corresponding to the pixel location x,y = 500,350 fitted with Pearson VII, Voigt, and Pseudo-Voigt models, respectively. Here, the corresponding χ^2 for each estimation is shown for direct quantitative comparison and these model were fitted without using any weights. (b), (d), and (f) show the residuals for Pearson VII, Voigt, and Pseudo-Voigt models, respectively.*

4.1.1 Weighted Fitting of the Pseudo-Voigt Model

Two different sample weights were tested to see if the intrinsic rocking curve fitting can be improved. The sample weights tested were $1/y$ and $log(y)$. Here, y corresponds to pixel intensities. Since it was firmly established in the section above that the PsV model best fits the intrinsic rocking curve, the intrinsic curve fitting analysis from this point will be focused on the PsV model.

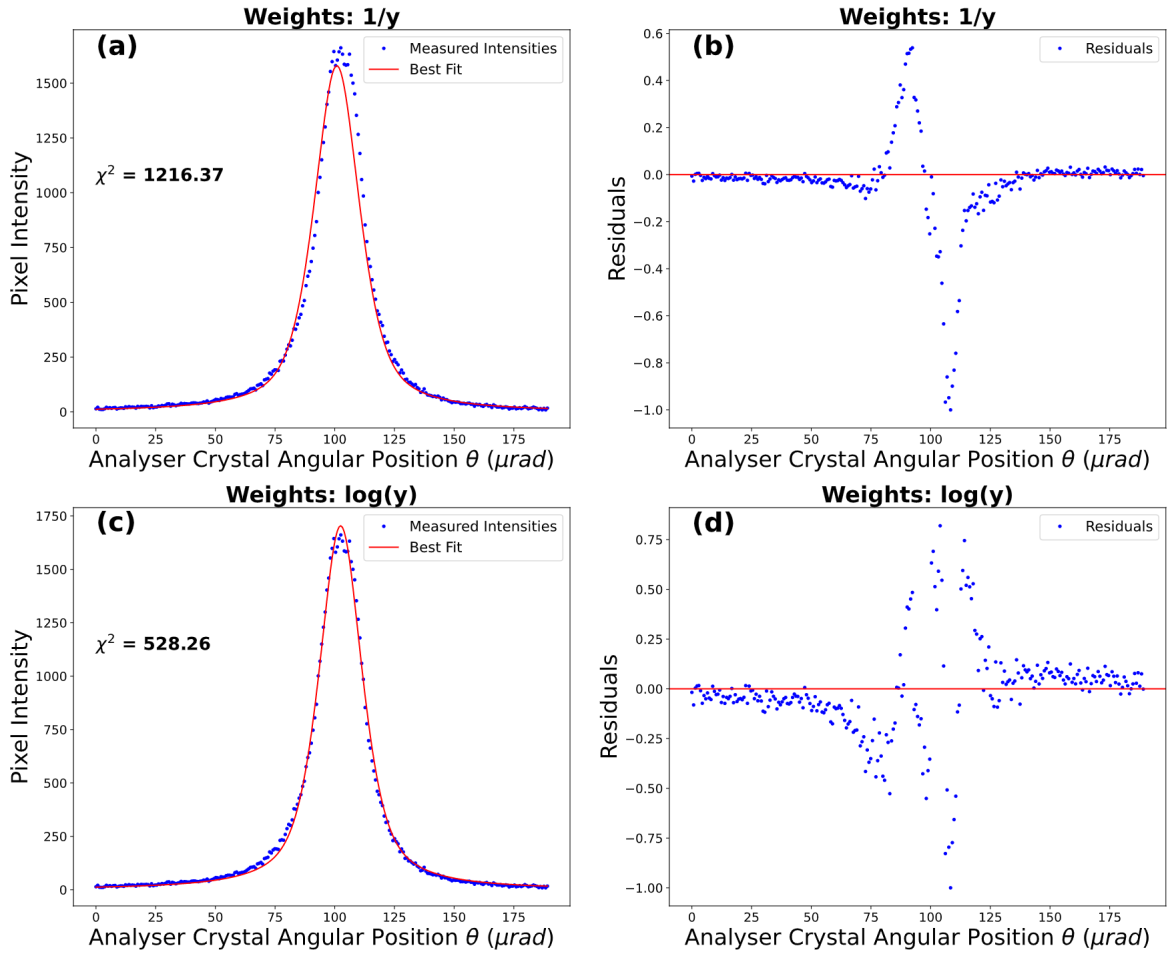

Figure 4.3: *(a) and (c) display the 261 pixel intensities corresponding to pixel location x,y = 500,350 fitted with the weighted Pseudo-Voigt model using the weights $1/y$ and $log(y)$, respectively. The χ^2 values are displayed to compare the weighting effects quantitatively. (b) and (d) display the residuals of (a) and (c), respectively.*

To better understand the behavioural changes of the rocking curve estimation due to different weights, the rocking curve corresponding to the pixel at $x, y = 500, 350$ was fitted with the PsV model using the weightings $1/y$ and $log(y)$, respectively. Figure 4.3 (a) and (c) displays the two weighted fits corresponding to $1/y$ and $log(y)$, respectively. Figure 4.3 (b) and (d) displays the residuals corresponding to the fits (a) and (c), respectively. When comparing the residuals in figure 4.3, it is evident that the weighting $1/y$ tend to better estimate the tails of the intrinsic rocking curve. However, it provides a less accurate estimation of the peak of the rocking curve (see figure 4.3 (a)). Although the $log(y)$ weighting seems to provide a more balanced estimation of the rocking curve peak, figure 4.3 (c) and (d) show clearly that it still underestimates the left

tail while overestimating the right tail. Furthermore, the intrinsic rocking curve fitting without weights gives a lower χ^2 value compared to the $log(y)$ weighted fitting (see figures 4.2 (e) and 4.3 (c)) suggesting that intrinsic rocking curve fitting without weights gives a better fit.

Comparison of individual weighted intrinsic rocking curve estimations using each weighting criterion is not feasible due to the large number of rocking curves. Therefore, the overall accuracy of each weighting criteria was estimated by fitting a 935×780 pixels on a pixel-by-pixel basis and calculating the average χ^2 and its standard deviation. This was done for each weighting criteria, namely $1/y$ and $log(y)$. The results are tabulated and displayed in table 4.2. The averaged χ^2 estimations indicate that it is best to use no weighting when estimating the intrinsic rocking curves.

Table 4.2: *Calculated χ^2 averages and their respective standard deviations for intrinsic rocking curve estimations by applying $1/y$ and $log(y)$, and no weights. Here, the χ^2 was estimated and averaged by fitting a Pseudo-Voigt model to 935×780 pixels on a pixel-by-pixel basis using each type of weighting.*

Weighting	Averaged χ^2	Standard Deviation
$1/y$	1053.22	533.80
$log(y)$	477.51	66.30
No Weights	449.33	49.33

4.1.2 Pseudo-Voigt Curve Fitting

The Pseudo-Voigt (PsV) function is an approximation to the Voigt function proposed by Kielkopf (1973) as the weighted sum of a Gaussian and a Lorentzian distribution.

$$PsV(\theta) \approx (1 - \alpha)G(\theta) + \alpha L(\theta) \tag{4.1}$$

here $G(\theta)$ and $L(\theta)$ represents the Gaussian and the Lorentzian distributions, respectively. Both $G(\theta)$ and $L(\theta)$ share the same full width at half maximum (FWHM) and height. α describes the weighting factor such that when $\alpha = 0$, equation (4.1) reduces to a pure Gaussian distribution. When $\alpha = 1$, equation (4.1) reduces to a pure Lorentzian distribution. A complete account on the PsV function can be found on Kielkopf (1973).

Using LMFIT's inbuilt model of PsV, curve-fitting of intrinsic rocking curves was carried out using all 261 projection images stacked together (see figure 4.1) on pixel-by-pixel basis. For each curve, its area under the curve, centroid, and FWHM was recorded as a 2D array of size equivalent to a projection image individually. Since the number of intrinsic curve fittings per sample being of the order of 10^6, Python multiprocessing was used to increase the speed of calculations. Although Python multiprocessing was utilised, the estimation of area under the curve, centroid, and FWHM for all the intrinsic rocking curves still took 18 minutes to compute (see figure 4.4). Therefore, the arrays of area under the curve, centroid, and FWHM were saved in TIFF format to be imported later to decrease processing time. Appendix A.2.1 displays the Python program written to accomplish this task. Figure 4.4 (a), (b), and (c) display the area under the curve, centroid, and FWHM information of pixel-by-pixel intrinsic rocking

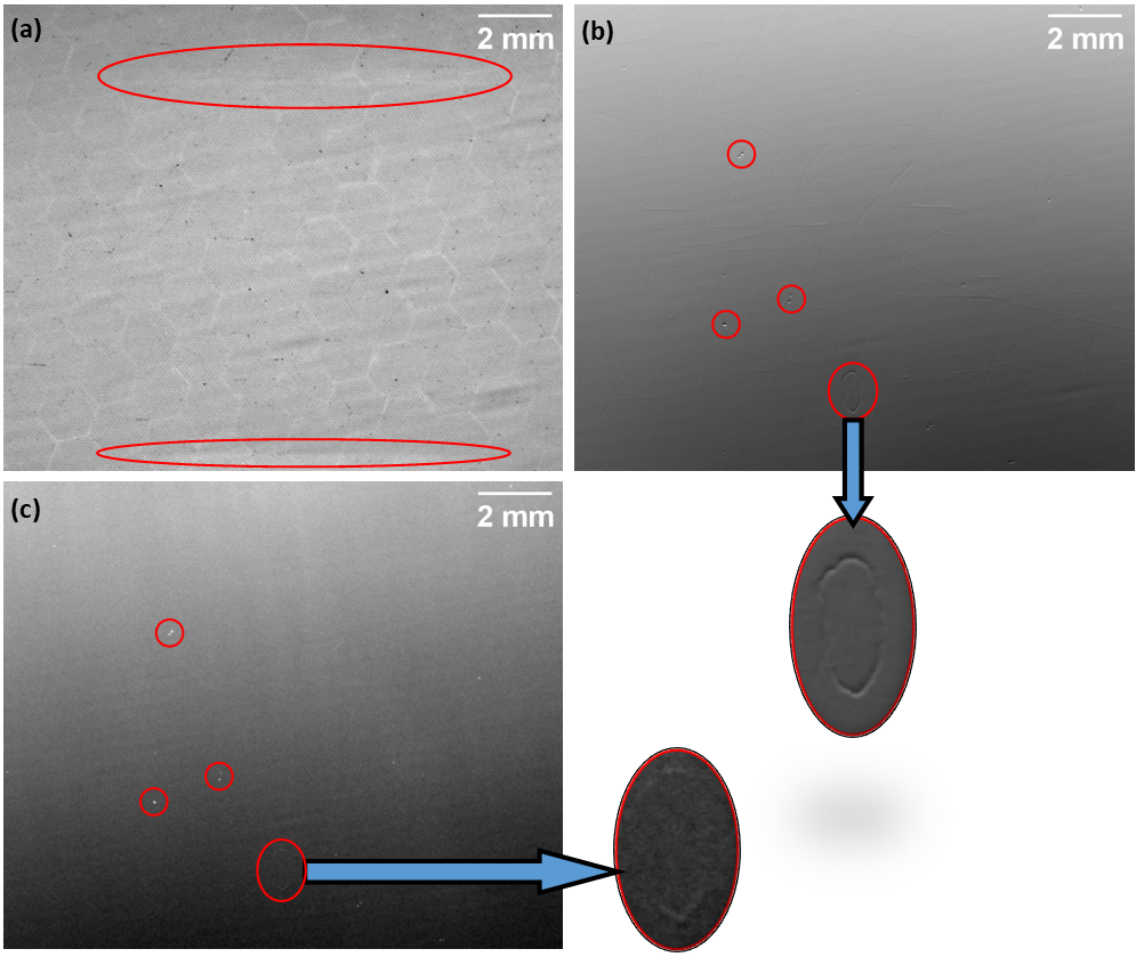

Figure 4.4: *(a), (b), and (c) display the extracted area under the curve, centroid, and FWHM by fitting* 935 × 780 *pixels on pixel-by-pixel basis with a PsV model, respectively. These were extracted using the 261 intrinsic rocking curve projections taken before the clay loam sample measurements. The horizontal markings indicated by the two ellipses in (a) seem to correspond to the upper and lower edges of the three-material phantom. Identical artefacts can be seen in both (b) and (c), which are highlighted by the circles. The origins of these artefacts and the "chicken wire" pattern seen in (a) are discussed in detail in section 4.4*

curve fitting, respectively, for the intrinsic rocking curves collected before the clay loam sample measurements. From here onwards, the area under the curve, centroid, and the FWHM outputs of intrinsic rocking curves will be referred to as the intrinsic integral image, intrinsic centroid image, and the intrinsic FWHM image for convenience.

The two horizontal markings indicated by the ellipses in figure 4.4 (a) are most likely caused by the browning of the detector scintillator. These horizontal markings resemble the outline of the three-material phantom, which was imaged earlier using this detector. The browning effect on the detector used for this experiment is further explored by Uesugi et al. (2011). These same effects can also be seen in the intrinsic integral, centroid, and FWHM images related to the three-material phantom (see appendix B.1.2).

Figures 4.5 and 4.6 illustrates vertical line profiles on the centroid and the FWHM images, respectively. On both images the line profile was drawn across the same pixel column for direct comparison. The best fit of the centroid line profile (right image of figure 4.5) gave a gradient

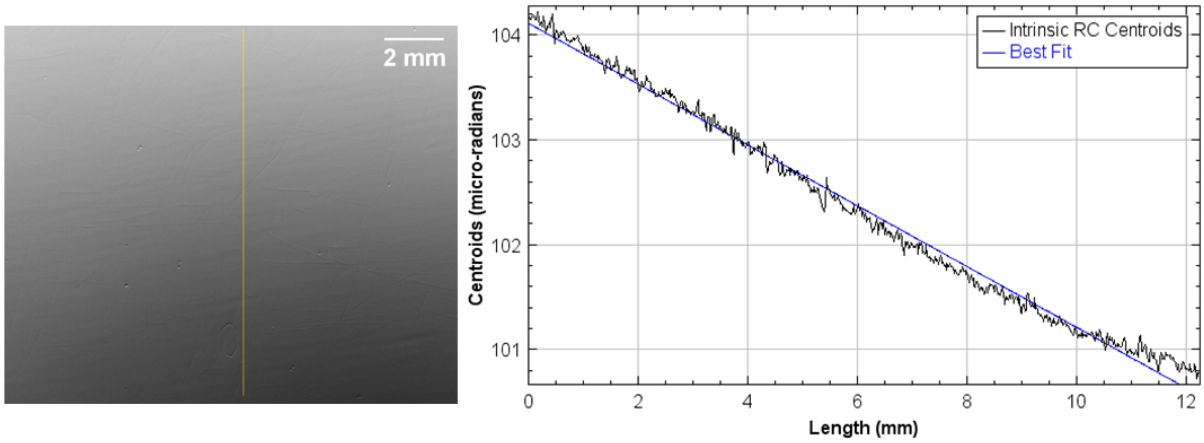

Figure 4.5: *A line profile vertically across the centroid image and its best fit (right). Here the gradient of the best fit is 0.270 µrad/mm. The line vertically drawn across intrinsic centroid image (left) illustrate column of pixels used for the line profile.*

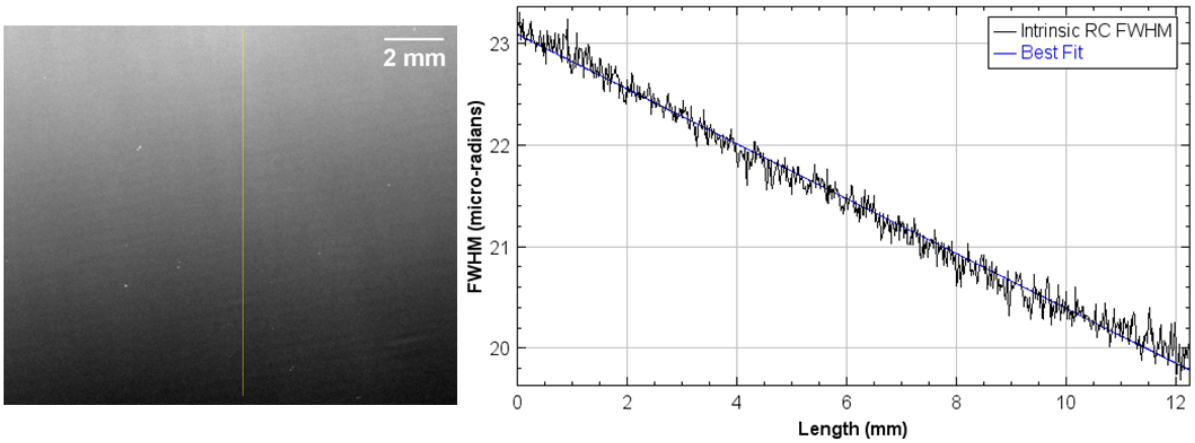

Figure 4.6: *A line profile vertically across the FWHM image and its best fit (right). Here the gradient of the best fit is 0.290 µrad/mm. The line vertically drawn across intrinsic FWHM image (left) illustrate column of pixels used for the line profile.*

of 0.270 µrad/mm and the best fit of the FWHM line profile (right image of figure 4.6) gave a gradient of 0.290 µrad/mm. These gradients suggests that there could be some beam divergence. Furthermore, the α (see equation 4.1) for all intrinsic curve estimations were recorded. The average α value was recorded to be 0.764 with a standard deviation of 0.057. The maximum and minimum α values recorded were 0.973 and 0.649.

4.2 Analyser Crystal Angular Position Estimation

As explained in section 3.2, sample rocking curves were recorded at eight positions representing 5%, 25%, 50%, and 80% of the Bragg peak reflectivity on either side of the rocking curve (see figure 3.3). Since the analyser crystal is extremely sensitive to the incoming beam, smallest vibrations, typically due to tomographic rotation of the sample could vary the real angular positions of the analyser crystal during data acquisition. Therefore, this section introduces an

analytical solution to accurately estimate the analyser crystal angular position at each working point using the ratio between the diffracted intensity I_D and transmitted intensity I_T. This takes a similar approach to the method introduced by Kitchen et al. (2010) (see section 2.4.2) where they utilised the P7 function to analytically solve for the analyser crystal angular position at each working point. However, instead of using a P7 function, this thesis utilises a Lorentzian function to calculate the analyser crystal angular position at each working point around the rocking curve.

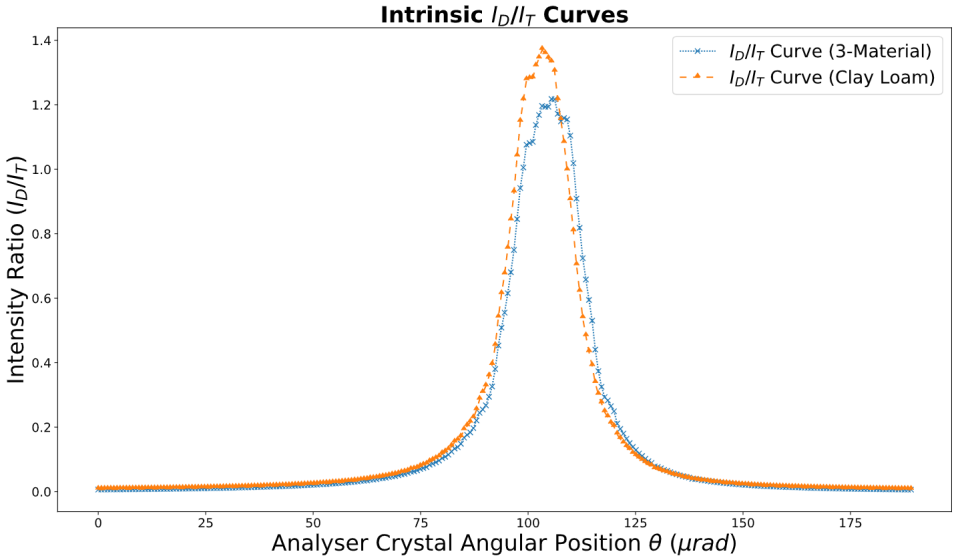

Figure 4.7: *The two curves represents the ratio rocking curves generated using the ratio of the diffracted (I_D) and transmitted (I_T) intrinsic projections taken before the three-material phantom and the clay loam sample, respectively.*

First, for each intrinsic rocking curve projection, I_D/I_T was estimated by taking the average of a ROI in air (outside the sample area) of the diffracted image and dividing it by the average ROI in air of the transmitted image. It was made certain that the location of the ROI on the diffracted image match the location of the ROI on the transmitted image. Figure 4.7 show the ratio curves generated using the 261 intrinsic projections taken before the three-material phantom and the clay loam sample were introduced into the beam. Then following the same process, I_D/I_T for the sample rocking curve projections at each working point was also estimated. For these estimations, it was made certain that the ROI positioning matched the position used for the intrinsic projections. Figure 4.8 illustrates the positioning of the ROI in a diffracted image and a transmitted image. The general premise of this method is that the ratio of the sample rocking curve projections at each working point should lie on the estimated intrinsic ratio rocking curve. This is plausible because the intensity recorded outside the sample area (in air) in sample rocking curve projections at a given analyser angle must be equal to the intensity recorded at the same location in the intrinsic rocking curve projections.

In section 4.1, it was identified that the PsV function is the ideal function to fit the intrinsic rocking curve. However, the PsV function cannot be analytically solved to give the analyser crystal angular position, due to its complex form. In contrast, the Lorentzian function is a much simpler function that can be solved analytically, as demonstrated below. The Lorentzian

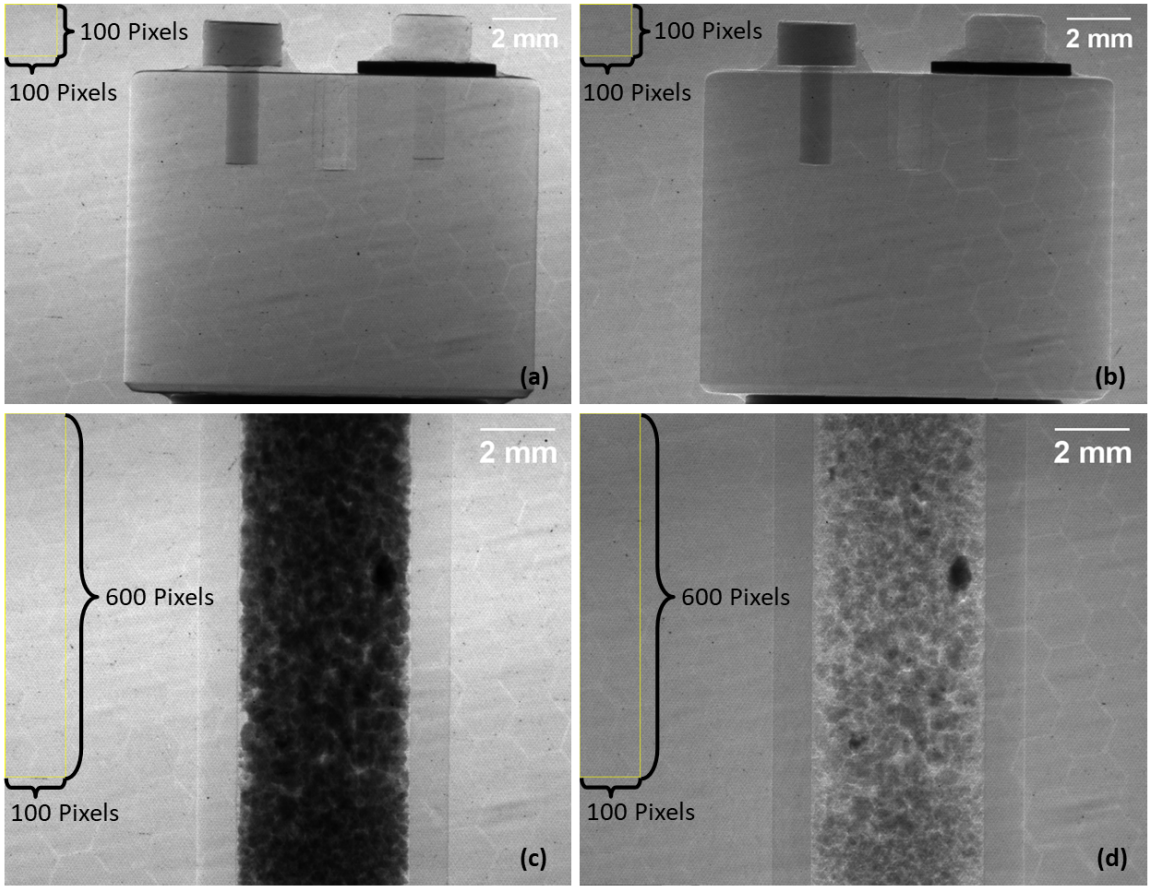

Figure 4.8: *(a) and (b) display the diffracted and transmitted projection, respectively, of the three-material phantom. The* 100×100 *pixels square encapsulated in yellow lines display the ROI selected to calculate the sample ratio curve. (c) and (d) illustrate the diffracted and transmitted projections of the clay loam sample, respectively. Here, the an ROI of* 100×600 *pixels were used to calculate the sample ratio curve. During tomographic projection acquisition, samples displayed horizontal swaying (see figure 3.8). Therefore, to avoid the samples being captured in the ROIs this swaying had to be taken into consideration.*

function was found to accurately fit the left and the right sides of the intrinsic ratio rocking curve separately. Therefore, effectively parameterizing the intrinsic ratio rocking curve as two separate curves, each representing the left and right sides of the curve (see figures 4.9 and 4.10). Tables 4.3 (left) and 4.3 (right) show the Lorentzian fitting parameters the centre (p), the width (w) and the peak height (h) for the three-material phantom intrinsic ratio curve and the clay loam sample intrinsic curve, respectively. In the case of intrinsic ratio curve for three-material phantom, the left and the right-hand side estimations gave χ^2 values of 1.40×10^{-2} and 1.80×10^{-2}, respectively. For the intrinsic ratio curve of the clay loam sample, the left and the right-hand side estimations gave χ^2 values of 1.20×10^{-2} and 7.80×10^{-2}, respectively.

Now, consider the Lorentzian function, which can be written as,

$$I_R(\theta) = \frac{h}{1 + (\frac{\theta - p}{0.5w})^2} \tag{4.2}$$

where θ defines the angular position of the analyser crystal and $I_R(\theta) = I_D(\theta)/I_T(\theta)$. Rearranging equation 4.2, one can find a solution to the position of the analyser crystal for a given

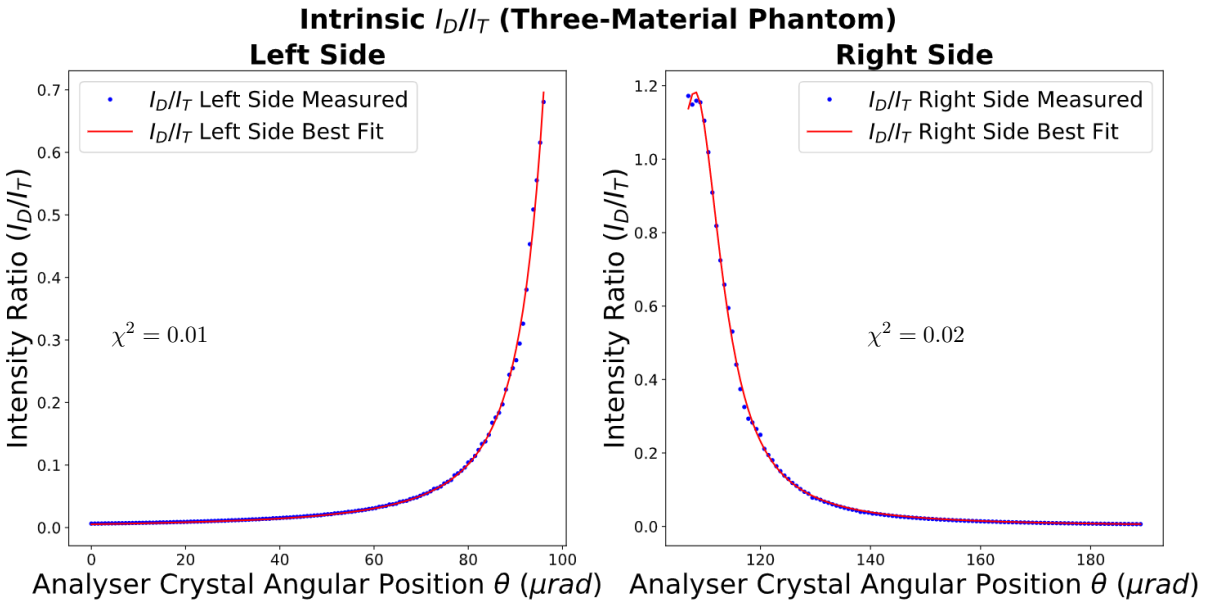

Figure 4.9: *Left and right side of the intrinsic I_D/I_T curve pertaining to three-material phantom (see figure 4.7) fitted using a Lorentzian function. Here, the left side is estimation only uses the first 133 points and the right side uses points from 147 to 261. The low χ^2 values indicates that the Lorentzian model provides a near-perfect fit.*

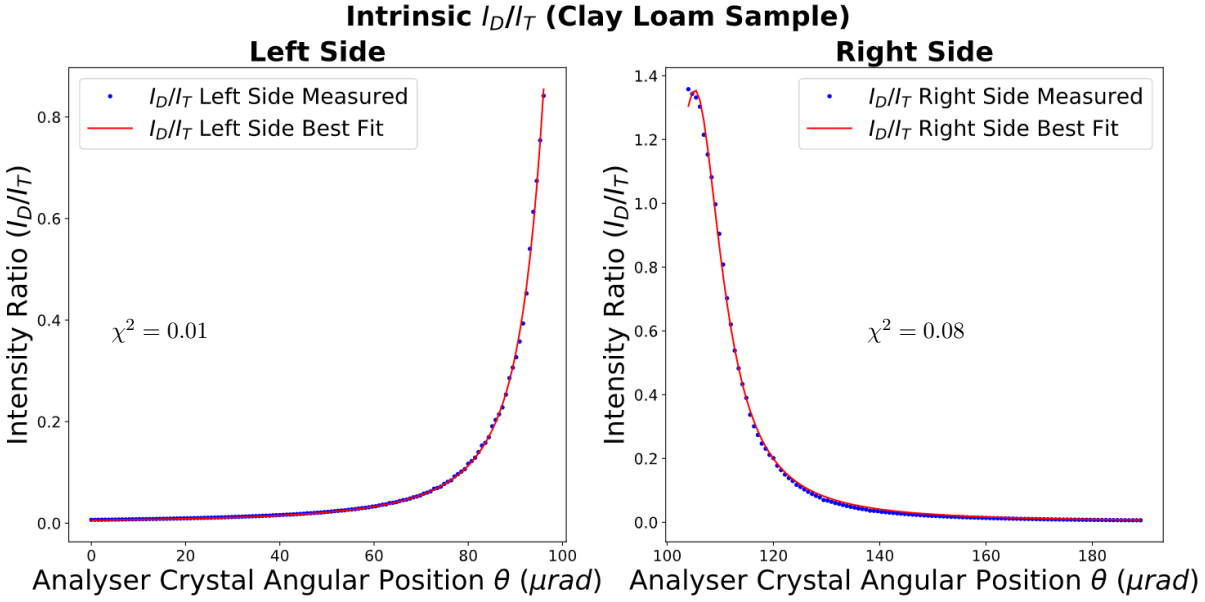

Figure 4.10: *Left and right side of the intrinsic I_D/I_T curve pertaining to clay loam sample (see figure 4.7) fitted using a Lorentzian function. Here, the left side is estimation only uses the first 133 points and the right side uses points from 143 to 261. The low χ^2 values indicates that the Lorentzians model provide a near-perfect fit.*

intensity ratio I_R as,

$$\theta = \left(\pm \sqrt{\frac{h}{I_R} - 1} \right) 0.5w + p \tag{4.3}$$

here, as evident by the square root sign it will produce a non-unique solution for θ. However, remember that the left and the right-hand sides of the intrinsic I_R curve is estimated as two

Table 4.3: *Left and right tables display the Lorentzian best fit parameters for the left and right-side of the intrinsic I_R curves displayed in figures 4.9 and 4.10 , respectively. These parameters will be used to estimate the analyser crystal angular position for a given working point projection. Here, the centroids and widths are given in μ radians.*

Lorentzian Parameter	Left Side	Right Side
Height	2.007	1.184
Centre	103.396	108.09
Width	10.787	11.751

Lorentzian Parameter	Left Side	Right Side
Height	1.875	1.356
Centre	102.129	105.205
Width	11.234	12.275

separate curves. Therefore, the θ values corresponding to the left four working points -5%, -25%, -50%, and -80% will be given by,

$$\theta_l = \left(-\sqrt{\frac{h_l}{I_R} - 1}\right) 0.5w_l + p_l \tag{4.4}$$

where h_l, w_l, and p_l define the estimated peak height, width, and the centre, respectively, for the left-hand side estimation of the intrinsic I_R curve (see table 4.3). The θ values corresponding to the right four working points +5%, +25%, +50%, and +80% is given by,

$$\theta_r = \left(+\sqrt{\frac{h_r}{I_R} - 1}\right) 0.5w_r + p_r \tag{4.5}$$

where h_r, w_r, and p_r define the estimated peak height, width, and the centre, respectively, for the right-hand side estimation of the intrinsic I_R curve (see table 4.3).

Notice how for both samples, the left-hand side of the intrinsic I_R curve estimation does not reach the peak (see figures 4.9 and 4.10). This is because, it was found that if the ratio values at the peak can be avoided, a better estimation of the tail can be achieved. Therefore, by overlaying the sample I_R values for the -80% and +80% working points on top of the left and right-hand side of the intrinsic I_R curves, their intersecting points were calculated. This information was then used to approximate the range of values needed for a good Lorentzian estimation of the left and right-hand sides of the intrinsic I_R curve. Figure 4.11 illustrates the points at which the -80% and +80% working point sample I_R values positioned on the left and right-hand sides of the intrinsic I_R curves.

To understand the possible instabilities of the analyser crystal during tomographic image acquisition, using equations (4.4) and (4.5) and the information on table 4.3, the analyser crystal position θ at each working point was estimated for all tomographic projections. Figure 4.12 displays the change in θ over the tomographic image acquisition process for all eight working points for both the three-material phantom and the clay loam sample. The overall behaviour of the analyser crystal appears to be different during tomographic data acquisition of each sample. During the three-material phantom image acquisition (figure 4.12 ((a) and (b))), at working points -50%, -80%, +50%, and +5%, the analyser crystal tended to drift away from the Bragg position, whilst at the working point -5%, the analyser crystal tended to drift towards the Bragg position. At the working point +80%, θ displays a sharp shift towards the Bragg position at

around 822^{nd} tomographic projection. At the working point +25%, the analyser crystal position θ reaches a peak at around 965^{th} tomographic projection and start to decrease slowly, while at the working point -25%, θ shows no apparent trend. For the clay loam sample (figure 4.12 ((c) and (d))), the overall trend of θ at working points -50%, -80%, +50%, and +25% shows that at these working points the analyser crystal is moving away from the Bragg position. However, the overall trend of θ at working points -5%, -25%, +80%, and +5% indicate that at these locations the analyser crystal moves towards the Bragg position.

Figure 4.11 gives a visual interpretation of the variation of analyser crystal angular position θ during tomographic image acquisition and the relative variation in intensity at each working point for both three-material phantom and the clay loam sample. Tables 4.4 and 4.5 display the average values of θ and sample I_R at each working point with their variation as a percentage for the three-material phantom and the clay loam sample, respectively. From figure 4.11 and tables 4.4 and 4.5 it is evident that the working points -50%, -80%, +80%, and +50% display the largest intensity variations for both samples. Considering these working points cover the steepest sections of the rocking curve, such variations were not surprising. Furthermore, it must be noted that the right hand side angular deviations for the clay loam sample is fairly large, with the +50% position recording 28% (+-14%) deviation from the average intensity ratio (see figure 4.11 (b) and table 4.5). These will effect the sample rocking curve estimations, which is the subject of the following section.

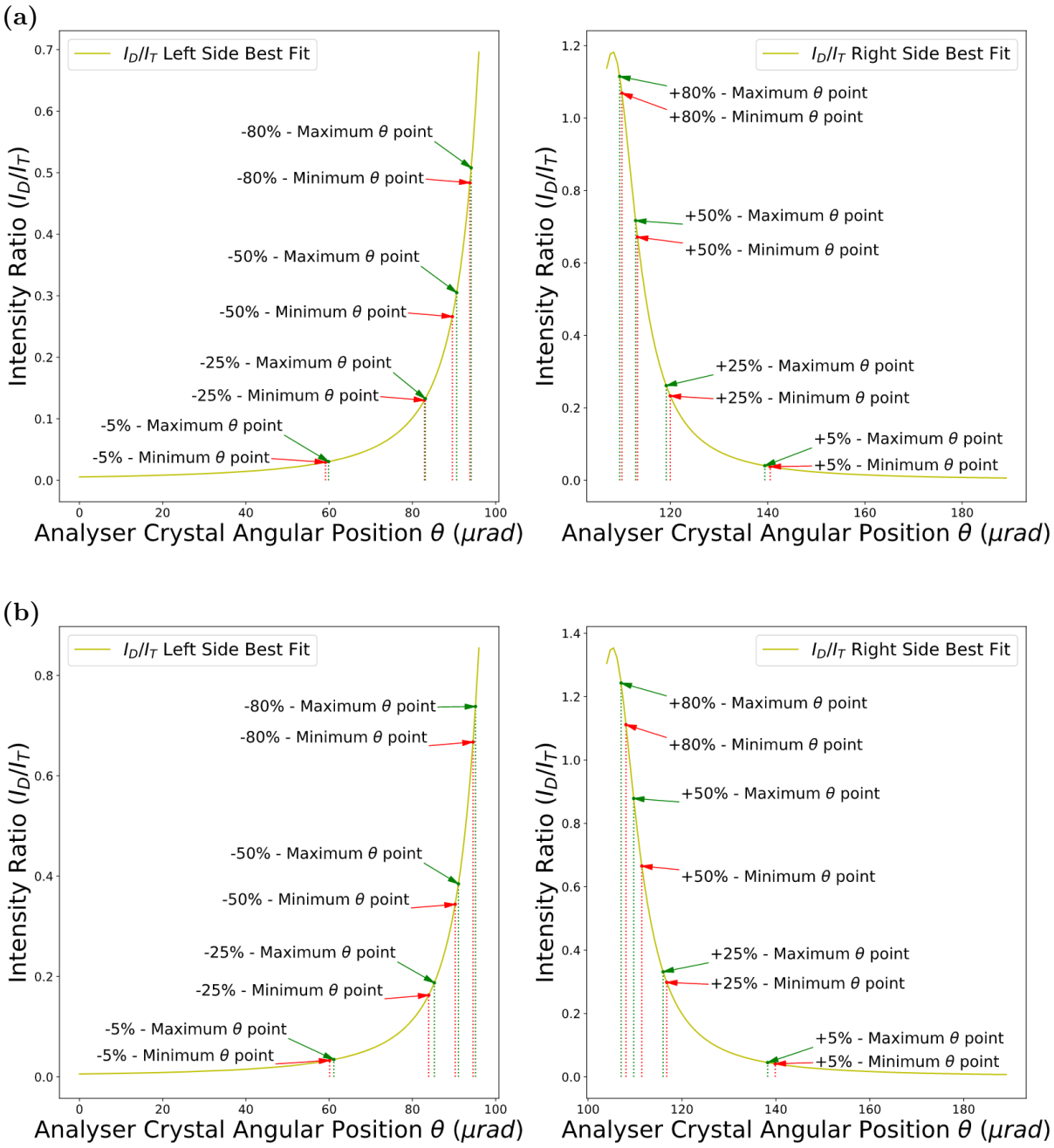

Figure 4.11: *(a) and (b) illustrates the maximum and minimum sample intensity ratio variation at each working point due to the angular drift of the analyser crystal during tomographic image collection of the three-material phantom and the clay loam sample, respectively. Here, the vertical lines correspond to the lower and upper limits of θ at each working point. The arrows on the left hand side figures in (a) and (b) points to the maximum and minimum sample intensity ratios corresponding to the lower and upper θ values, respectively, of the left-hand side working points overlaid on top of the left-hand side intrinsic ratio curve. The arrows on the right hand side figures in (a) and (b) points to the maximum and minimum sample intensity ratios corresponding to the lower and upper θ values, respectively, of the right-hand side working points overlaid on top of the right-hand side intrinsic ratio curve.*

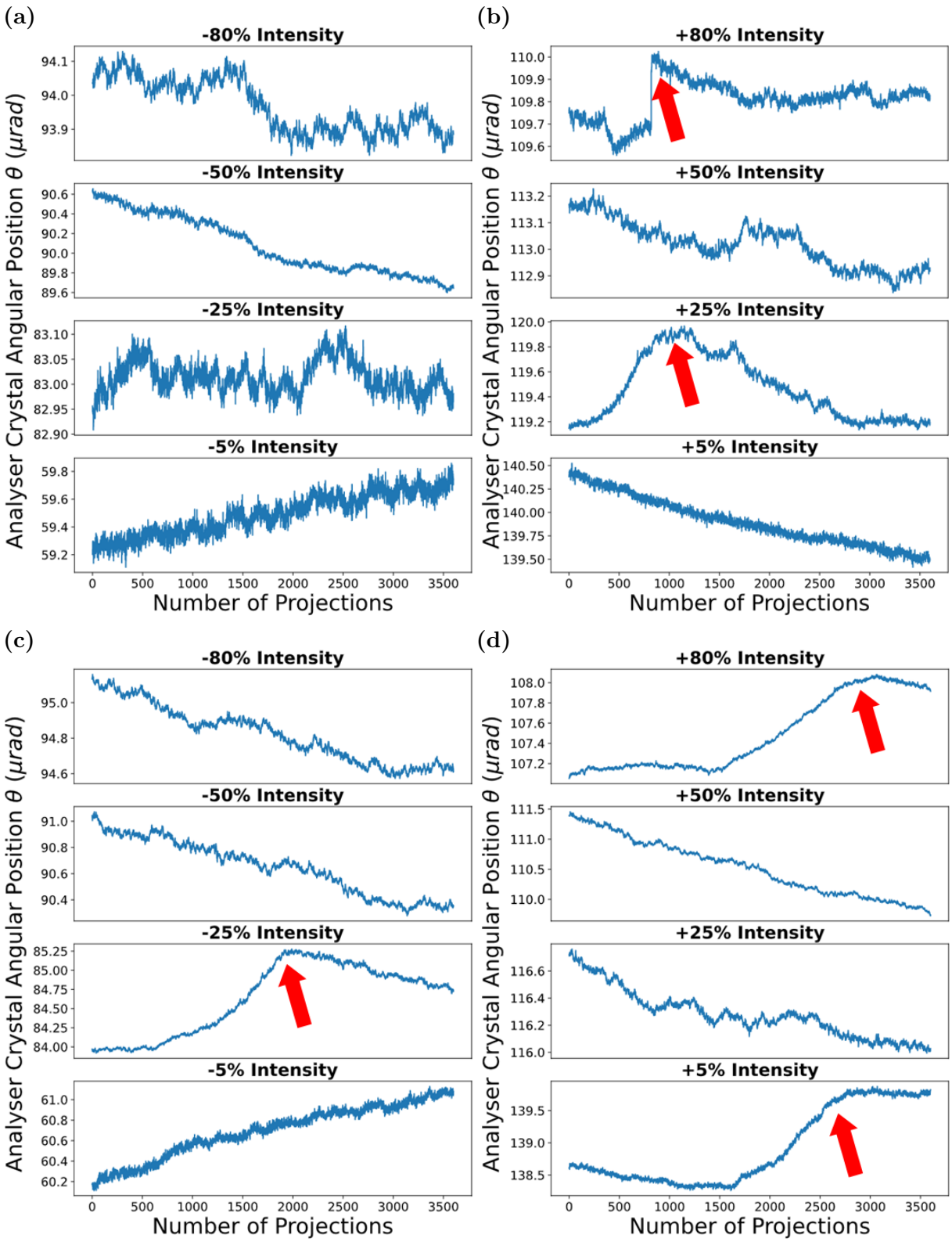

Figure 4.12: *Angular drift of the analyser crystal during tomographic image collection of the three-material phantom ((a) and (b)) and the clay loam sample ((c) and (d)) at each working point around the rocking curve. (a), (c) corresponds to the left-hand side working points of the three-material phantom and the clay loam sample, respectively. (b) and (d) corresponds to the right-hand side working points of the three-material phantom and the clay loam sample, respectively. Furthermore, the arrows illustrate anomalous behaviour of the analyser crystal during tomographic image acquisition when compared to the other working points for the respective sample.*

Table 4.4: *The average θ values and the average sample intensity ratios at each working point for the three-material phantom. Here the maximum and minimum variation of θ and the sample intensity ratio at each working point is given as a percentage from their average values.*

	Three-Material Phantom			
Working Point	Average θ (μrad)	θ Shift (%)	Average I_D/I_T	I_D/I_T Shift (%)
-5%	59.5	$\pm 6.3 \times 10^{-1}$	3.0×10^{-2}	± 1.7
-25%	83.0	$\pm 1.3 \times 10^{-1}$	1.3×10^{-1}	$\pm 9.6 \times 10^{-1}$
-50%	90.1	$\pm 5.9 \times 10^{-1}$	2.8×10^{-1}	± 7.2
-80%	94.0	$\pm 1.6 \times 10^{-1}$	5.0×10^{-1}	± 2.5
+80%	1.10×10^{2}	$\pm 2.1 \times 10^{-1}$	1.1	± 2.0
+50%	1.13×10^{2}	$\pm 1.7 \times 10^{-1}$	6.9×10^{-1}	± 3.3
+25%	1.20×10^{2}	$\pm 3.5 \times 10^{-1}$	2.5×10^{-1}	± 6.0
+5%	1.40×10^{2}	$\pm 4.0 \times 10^{-1}$	3.9×10^{-2}	± 3.5

Table 4.5: *The average θ values and the average sample intensity ratios at each working point for the clay loam sample. Here the maximum and minimum variation of θ and the sample intensity ratio at each working point is given as a percentage from their average values.*

	Clay Loam Sample			
Working Point	Average θ (μrad)	θ Shift (%)	Average I_D/I_T	I_D/I_T Shift (%)
-5%	60.6	$\pm 8.4 \times 10^{-1}$	3.4×10^{-2}	± 2.4
-25%	84.6	$\pm 8.0 \times 10^{-1}$	1.7×10^{-1}	± 7.4
-50%	90.7	$\pm 4.4 \times 10^{-1}$	3.6×10^{-1}	± 5.8
-80%	94.9	$\pm 3.1 \times 10^{-1}$	7.0×10^{-1}	± 5.2
+80%	1.08×10^{2}	$\pm 4.9 \times 10^{-1}$	1.2	± 5.3
+50%	1.11×10^{2}	$\pm 7.8 \times 10^{-1}$	7.7×10^{-1}	$\pm 1.4 \times 10^{1}$
+25%	1.16×10^{2}	$\pm 3.3 \times 10^{-1}$	3.1×10^{-1}	± 5.5
+5%	1.39×10^{2}	$\pm 5.8 \times 10^{-1}$	4.3×10^{-2}	± 4.8

4.3 Sample Rocking Curve

This section is dedicated to the investigation of the parameterisation of the rocking curve with (sample rocking curve) the sample in the x-ray wavefield. First, following the same procedure illustrated in figure 4.1, the eight projections taken at each working point from -5% to +5% for a given tomographic position was stacked in ascending order along the z-axis. This essentially resulted in 3600 image stacks (sample stacks) where each stack corresponds to a tomographic position around 360^0. Each sample stack contains 8 projection images where each projection image corresponds to a working point around the rocking curve at the same tomographic angular position.

The Gaussian, Pearson VII, Pseudo-Voigt, and the Lorentzian models were tested using LMFIT curve fitting library to find which model best parameterises the sample rocking curve. This was accomplished by fitting each model on a pixel-by-pixel basis and calculating the average χ^2 value and the corresponding standard deviation for each model. Each model was tested for both the three-material phantom and the clay-loam sample. Tables 4.6 and 4.7 show their respective results. Here, for both samples, the 15^{th} sample stack, corresponding to the tomographic angular position 1.5°, was used for testing. The analyser crystal angular positions corresponding to each working point in the stacks (the three-material phantom stack and the clay-loam sample stack) were estimated using the equations (4.4) and (4.5) and their respective parameters (see table 4.3)

Table 4.6: *Average χ^2 values and their standard deviations for Gaussian, Pearson VII, Pseudo-Voigt, and Lorentzian model estimations of the sample rocking curve of the three-material phantom. The horizontal lines on the image to the left show the pixel-rows used to calculate the average χ^2 values.*

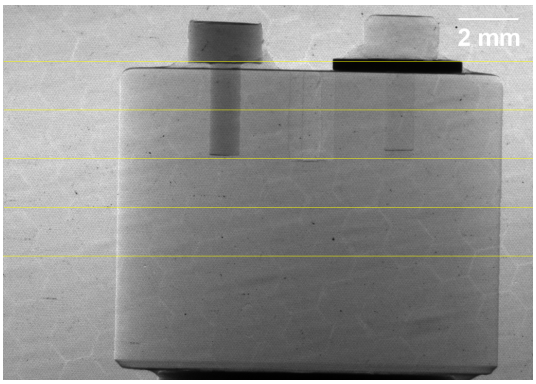

Model	Averaged χ^2	Standard Deviation
Gaussian	155	45.4
Pearson VII	15.4	8.30
Pseudo-Voigt	14.9	7.45
Lorentzian	15.9	7.97

When considering the results in tables 4.6 and 4.7, it is evident that the PsV model is the best candidate to parameterise the sample rocking curve followed by the P7 and the Lorentzian model. Furthermore, considering the χ^2 values, it is certain that the Gaussian model is the worst candidate to parameterise the sample rocking curve. The number of curve fittings required for a single stack of images is of the order of 10^6. Therefore, the run-time efficiency of using LMFIT library was tested by estimating pixel-by-pixel rocking curves for a single three-material phantom image stack. With the implementation of Python multiprocessing (using all eight cores)[3] each model took on average 20 minutes to parameterise the rocking curves in a single

[3]Chapter 4 gives a description of the specifications of the computer used for this project.

Table 4.7: *Average χ^2 values and their standard deviations for Gaussian, Pearson VII, Pseudo-Voigt, and Lorentzian model estimations of the sample rocking curve of the clay-loam sample. The horizontal lines on the image to the left show the pixel-rows used to calculate the average χ^2 values.*

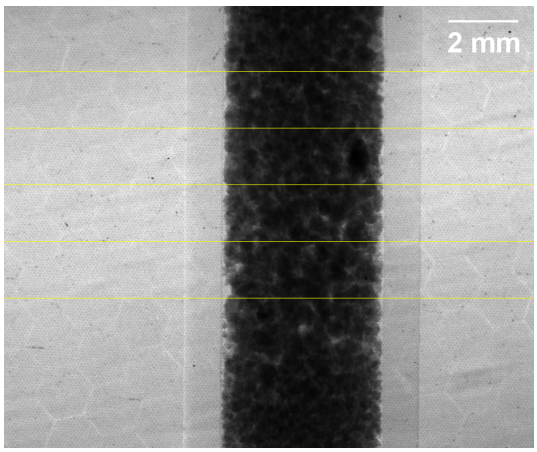

Model	Averaged χ^2	Standard Deviation
Gaussian	141.0	84.4
Pearson VII	5.97	4.14
Pseudo-Voigt	5.10	3.33
Lorentzian	7.18	4.33

stack of images. Since there were 3600 image stacks per sample and each image stack taking 20 minutes, processing all image stacks for a single sample will take approximately 50 days. With the time allocated to this project (12 months), the use of LMFIT library was therefore not feasible.

However, the Lorentzian model is an inverse of a second-order polynomial (see equation (4.2)). Therefore, it is possible to parameterise the Lorentzian parameters by fitting a quadratic to the reciprocal of the experimental intensities at each working point around the rocking curve using χ^2 regression[4] (O'Haver, 2021). This method was programmed in Python and it was further accelerated using the just-in-time (JIT) compiler for Python known as Numba[5] (Lam et al., 2015). Python code for this method is displayed in appendix A.2.2. For convenience, let us call this method the quadratic fitting method (QF). The QF method improved the run-time efficiency significantly, allowing the processing of a single three-material phantom image stack in 4.3 seconds without Python multiprocessing. The accuracy of this method was tested by comparing it to the iterative method used by the LMFIT library (LMFIT method).

Figures 4.13 and 4.14 illustrate three different sample rocking curves for both the three-material phantom and the clay loam sample, respectively. Each rocking curve in figures 4.13 and 4.14 are fitted with a Lorentzian curve using both the QF method and the LMFIT method for comparison. Here, the pixel locations were carefully selected to cover positions of the samples which are of interest. For the three-material phantom, the selected rocking curves correspond to positions inside the aluminium rod, the top edge of the phantom where high USAXS can be expected, and an area with very low photon count (metal strip) as shown in figure 4.13 (a). Figure 4.13 (b), (c), and (d) display the respective rocking curves and their estimations. Similarly, for the clay loam sample, the rocking curves correspond to a location outside the sample (air), a position on the syringe, and one inside the clay loam sample as shown in figure 4.14

[4]Since the primary goal of this body of work is not regression analysis, this thesis will not be providing the mathematical background for χ^2 regression. However, a detailed description of χ^2 regression can be found Press et al. (2007) chapter 15.

[5]For further information refer to https://numba.pydata.org/.

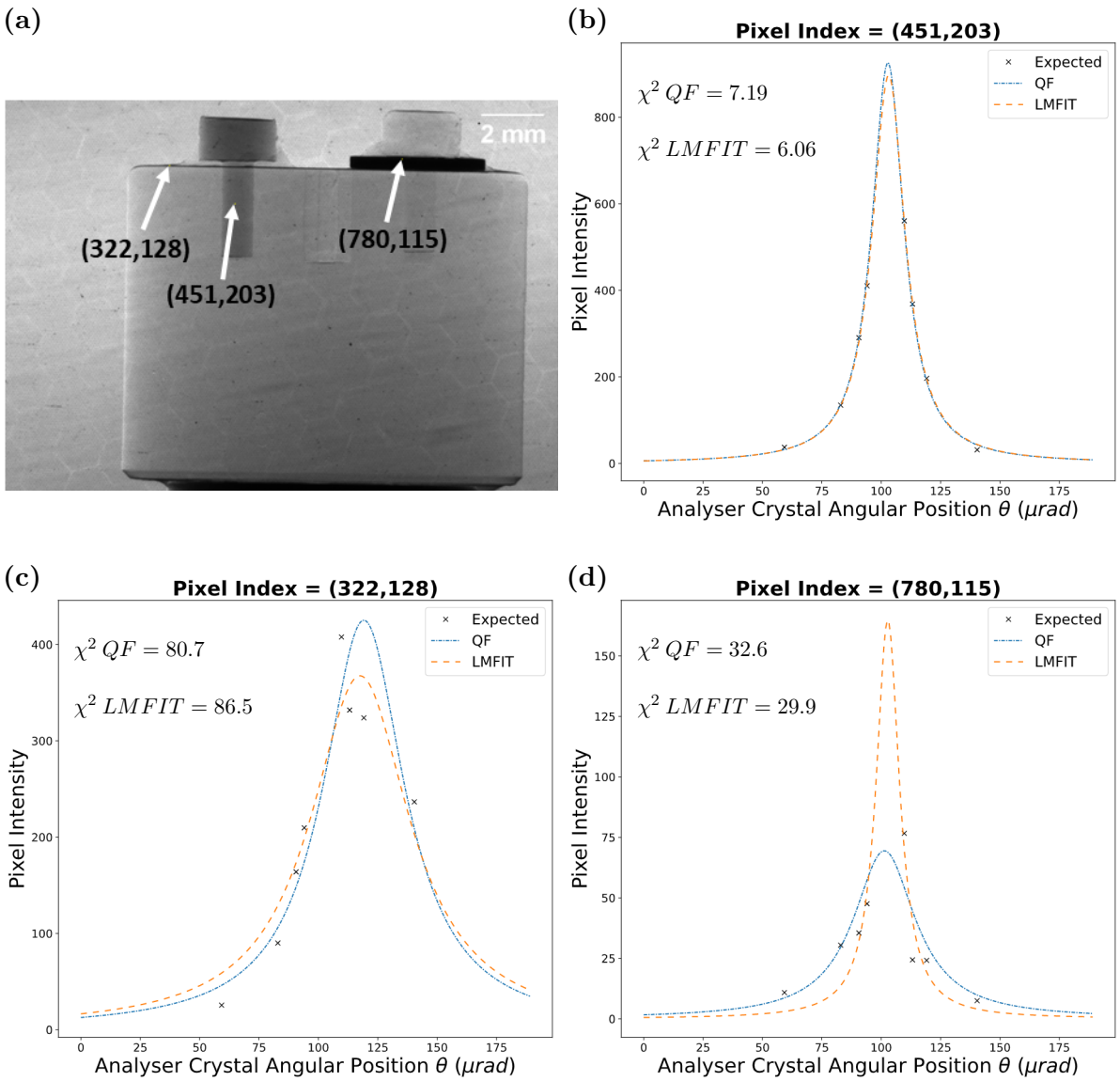

Figure 4.13: *Three rocking curves of from the* 15^{th} *three-material phantom sample stack fitted with both the QF method and the LMFIT method. (a) depicts the x and y coordinates of the selected rocking curves on the +80% working point projection image. Here, (b), (c), and (d) show the rocking curves at pixel indexes shown in (a) fitted with both the QF method and the LMFIT method.*

Table 4.8: *Lorentzian fit parameters for left and right side of the* I_D/I_T *curve pertaining to clay loam sample. Figure 4.10 display these fitted curved. Here, the centroids and widths are given in μrad.*

	LMFIT Method			QF Method		
Figure 4.14	Height	Centre	Width	Height	Centre	Width
(b)	897.4	103.1	16.9	926.7	102.8	16.5
(c)	367.5	117.5	50.9	425.3	119.1	41.8
(d)	164.9	102.8	11.9	69.5	101.3	31.8

(a). Figure 4.14 (b), (c), and (d) display these respective rocking curves and their estimations.

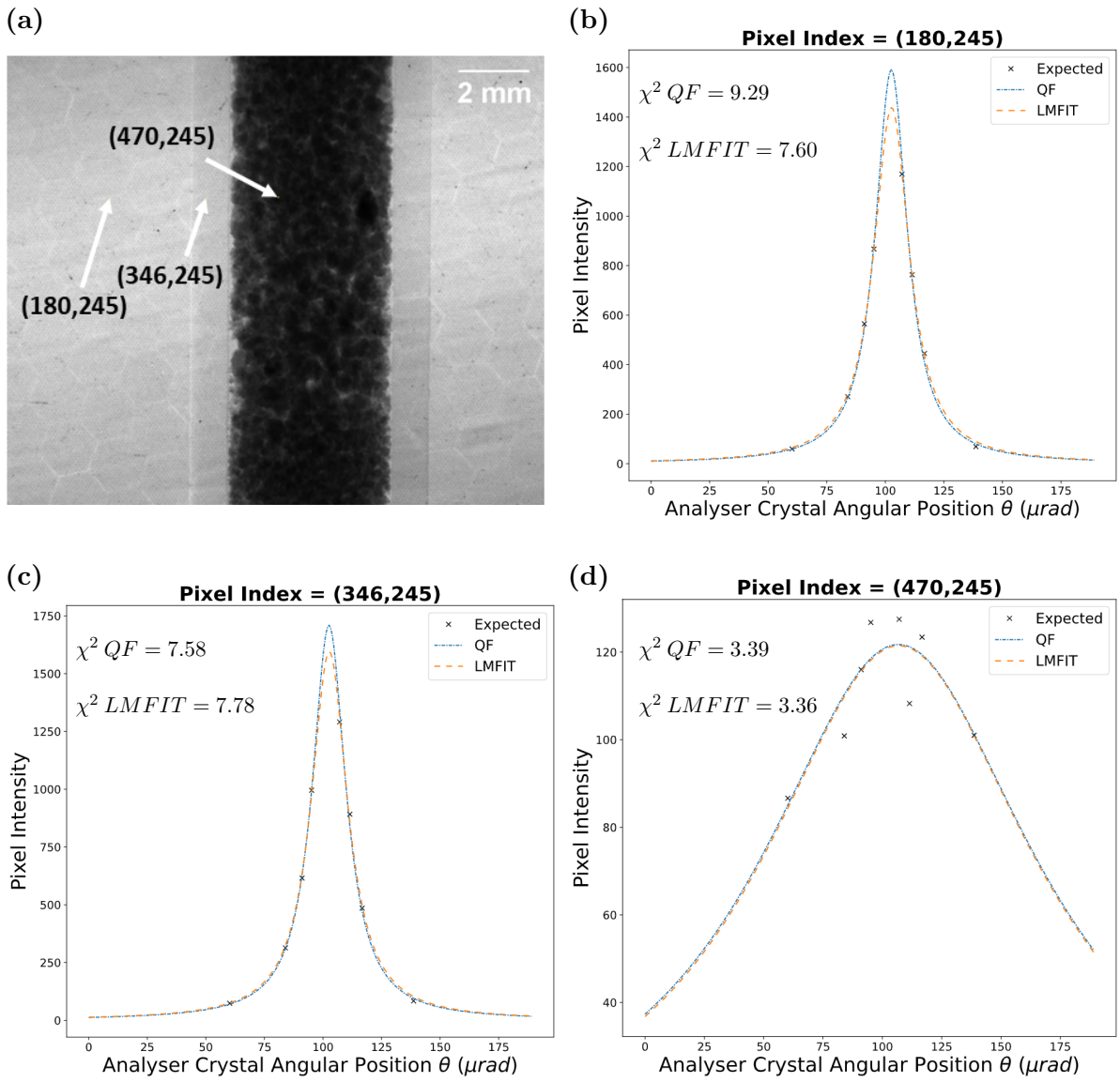

Figure 4.14: *Three rocking curves of from the* 15^{th} *clay loam sample stack fitted with both the QF method and the LMFIT method. (a) depicts the x and y coordinates of the selected rocking curves on the +80% working point projection image. Here, (b), (c), and (d) show the rocking curves at pixel indexes shown in (a) fitted with both the QF method and the LMFIT method, respectively.*

Table 4.9: *Lorentzian fit parameters for left and right side of the* I_D/I_T *curve pertaining to clay loam sample. Figure 4.10 display these fitted curved. Here, the centroids and widths are given in μrad.*

	LMFIT Method			QF Method		
Figure 4.14	Height	Centre	Width	Height	Centre	Width
(b)	1438	102.7	18.6	1591	102.4	16.7
(c)	1595	102.7	18.9	1709	102.5	17.5
(d)	121.4	106.9	140.9	121.7	106.8	142

Consider the rocking curve inside the aluminium rod (figure 4.13 (b)), in air (figure 4.14 (b)), and in the syringe (figure 4.14 (c)). It is clear that the intensity values at each working point around the rocking curve for these three curves are well behaved. Therefore, the estimations by the two methods are also seems to be well behaved and are in good agreement. Furthermore, the rocking curve displays an increase in width as it encounters USAXS, as expected. This can be clearly seen in the rocking curve corresponding to the top edge of the three-material phantom (see figure 4.13 (c) and table 4.8). The first four expected points (experimental values) corresponding to the working points -5%, -25%, -50%, and -80% seems to be reasonably well behaved. However, the behaviour of the last four expected points corresponding to the working points +80%, +50%, +25%, and +5% seems to be inconsistent. This erratic behaviour seems to contribute to the error in estimation of the position of the peak. From figures 4.13 (c) and 4.13 (d) it is apparent that, as the overall photon count gets lower, the intensity at +50% working point reduces rapidly. In figure 4.13 (d) the pixel intensities at working points +50% and +25% was measured to be 24.4 and 24.2, respectively. Furthermore, although the χ^2 statistic for QF method and LMFIT Lorentzian method are reasonably close for the rocking curve in figure 4.13 (d), both visually and when considering the respective fit parameters in table 4.8, it is clear that the two estimations are significantly different from each other. The rocking curve inside the clay loam, which is depicted in figure 4.14 (d) further illustrates that the intensity at +50% working point even go below the intensity recoded at the +25% working point intensity as the peak intensity decreases. In fact, the average intensity of a ROI covering the clay loam of the +50% working point projection[6] was measured to be 162.1 with a standard deviation of 69.2 while for the same ROI in the +25% projection gave an average intensity of 167.7 with a standard deviation of 57.1. However, for a ROI on air (outside the sample area) in the +50% working point projection the average intensity was measured to be 818.1 with a standard deviation of 76.5 and for the same ROI in the +25% working point projection gave an average intensity of 471.4 with a standard deviation of 34.0. Also, for the rocking curve depicted in figure 4.14 (d), the χ^2 statistic for the estimations by the QF method and the LMFIT Lorentzian method are in almost perfect agreement.

Essentially, the rocking curves in figures 4.13 (b), 4.14 (b), and 4.14 (c) show that if the intensity values are sufficiently large and hence well behaved, both the QF method and the LMFIT method tend to provide reasonably identical estimations of the rocking curve. However, as photon count starts to reduce or the effects of USAXS emerge (see figure 4.13 (c) and (d)), the parameterisation of the rocking curves by the QF method start to differ from the parameterisation of the rocking curves by the LMFIT method. Furthermore, figure 4.15 (a) and (b) display the χ^2 images estimated using the LMFIT method and the QF method, respectively. From figures 4.15 (a) and 4.15 (b), it is evident that for both curve fitting methods, the χ^2 values increase for locations where one expects a low photon count (e.g., metal strip) or an increase in USAXS (e.g., phantom edges). Furthermore, when comparing average χ^2 values for the LMFIT method and the QF method, it was found that the average χ^2 value for LMFIT method is 39% lower than the QF method. However, when comparing the speed differences, it was found that the QF method is 278 times faster than the LMFIT method.

[6]Here, for consistency, +50% and +25% working point projections were taken from the 15^{th} image stack.

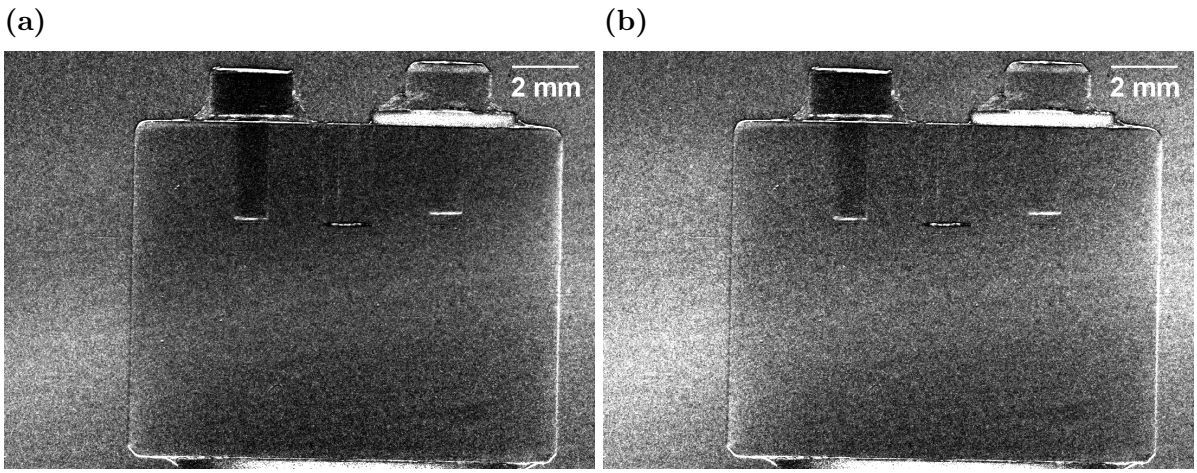

Figure 4.15: *Estimated χ^2 vales using both the LMFIT Lorentzian curve fitting method (a) and the QF method (b) for the 15^{th} stack of the three-material phantom. Here, the χ^2 values were estimated by fitting curves on a pixel-by-pixel basis for each curve in the stack using each method and the outputs were recorded as a 2D array of size equivalent to a projection image (1090 × 770 pixels). Here, (a) is slightly darker than (b), meaning that the fitting done using the QF method is slightly worse.*

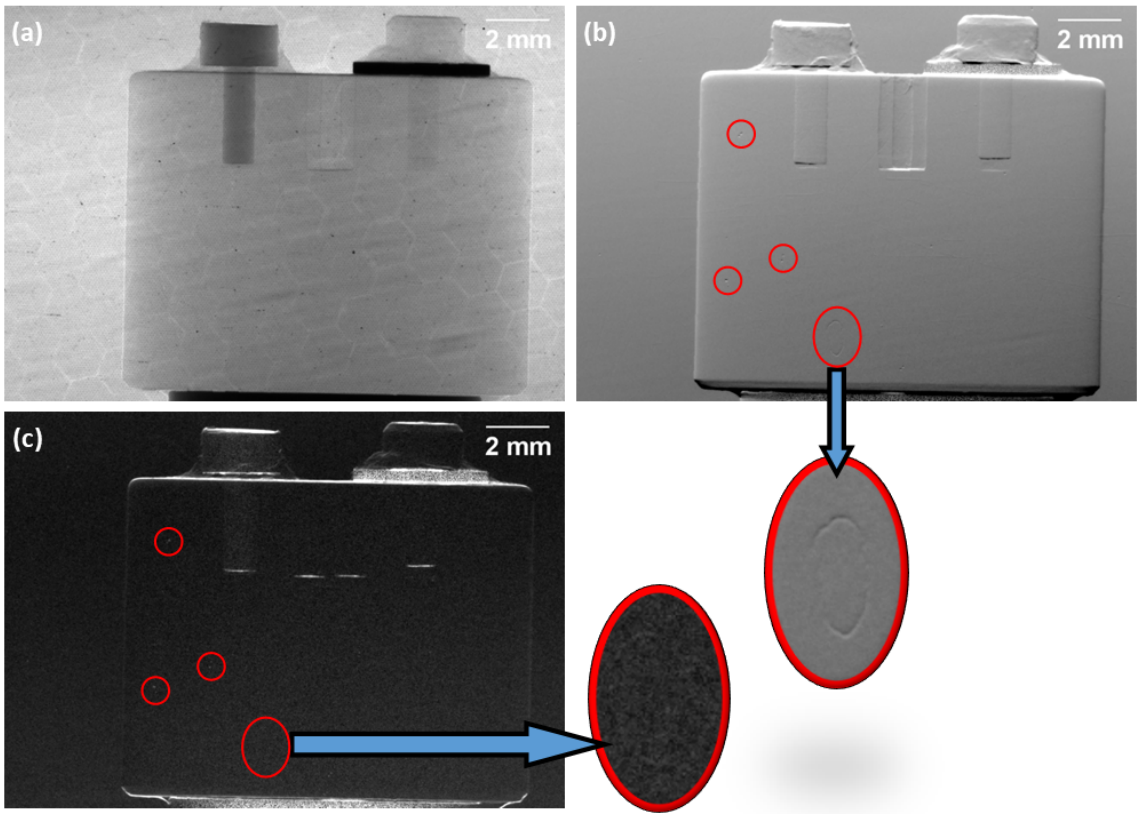

Figure 4.16: *The area under the curve (a), centroid (b), and, the FWHM (c) images estimated by fitting a Lorentzian model to each rocking curve in the 15^{th} three-material phantom stack on a pixel-by-pixel basis. Here, each image is consists of 1090 × 770 pixels. Some artefacts can be seen in both (a) and (b), which are highlighted by the circles. The same artefacts can be seen in both the centroid image and the FWHM image at the same locations.*

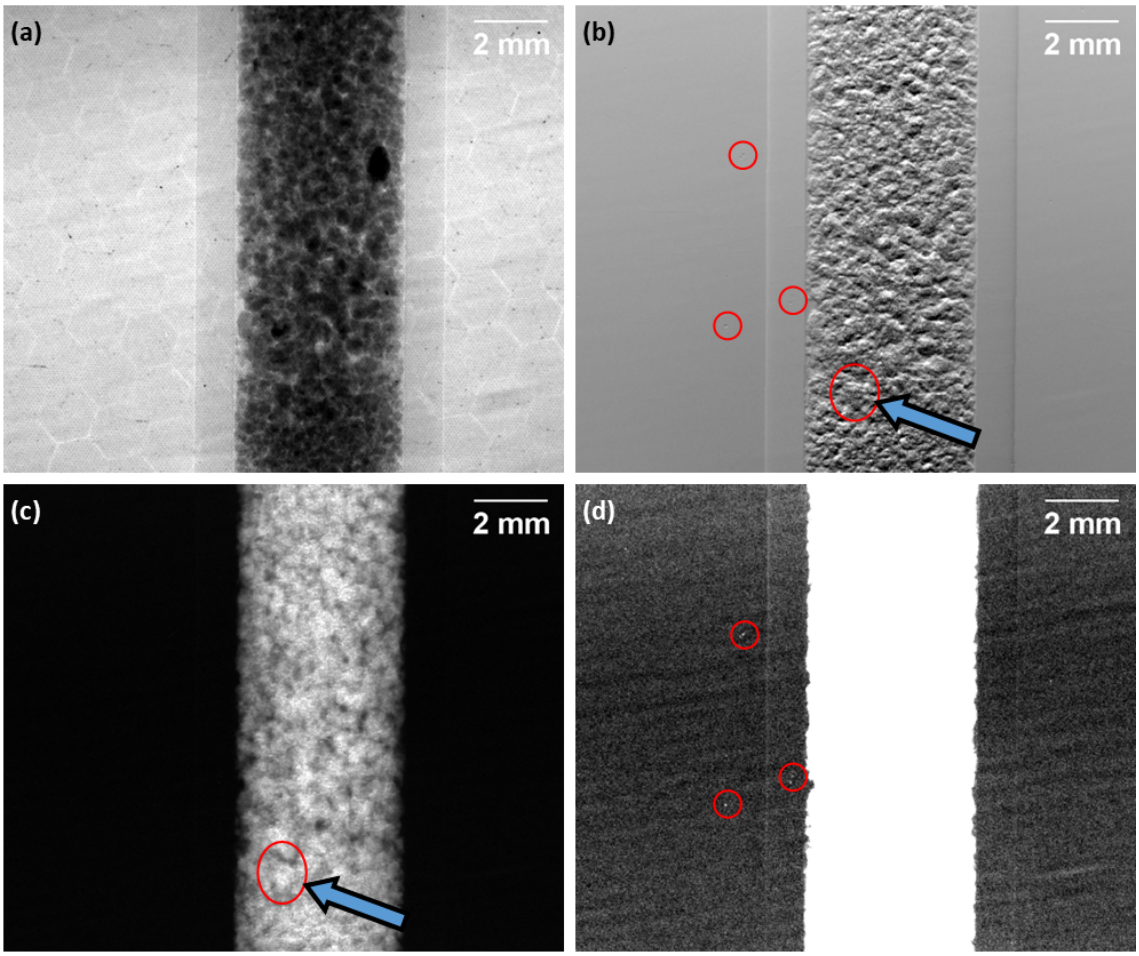

Figure 4.17: *The area under the curve (a), centroid (b), and, the FWHM (c) images estimated by fitting a Lorentzian model to each rocking curve in the* 15^{th} *soil sample stack on a pixel-by-pixel basis. Here, each image is consists of 935 × 780 pixels. (d) shows the FWHM image in (c) with brightness and contrast adjusted for better visualisation of the artefacts. The smaller circles in images (b) and (d) points to the same artefacts which were seen in 4.16 (b) and (c). However, due to high attenuation and scattering produced by the clay loam, the larger artefacts cannot be seen, which are visible in both 4.16 (b) and (c). The arrows in (b) and (c) points to the location of the larger artefact.*

Considering the time allocated for this project, the implementation of the Lorentzian model using QF method was found to be the best option to estimate the sample rocking curves. Therefore, for both samples reconstructed in this thesis, namely the three-material phantom and the clay loam sample, the Lorentzian model was implemented using the QF method to estimate all the sample rocking curves. For both samples, the sample rocking curves on each image stack were estimated on a pixel-by-pixel basis. Then the area under the curve, centroid, and the FWHM of every rocking curve on each image stack was computed. These extractions will be referred to as the sample integral image, sample centroid image, and sample FWHM image for convenience. Figures 4.16 and 4.17 display the area under the curve, centroid and the FWHM outputs of the 15^{th} image stacks of the three-material phantom and the clay loam sample, respectively. Images 4.16 (a) and 4.17 (a) display the sample integral images for the three-material phantom and the clay loam sample, respectively. In both of these images, the

"chicken wire" pattern in clearly visible. In both the sample centroid images and the sample FWHM images pertaining to both samples, same artefacts can be seen (see 4.16 (b), (c) and 4.17 (b), (d)).

4.4 Discussion

To utilise MIR radiography, one must first find a mathematical model which can best approximate the intrinsic rocking curve (without the sample present in the wavefield) and the sample rocking curve (sample present in the wavefield). When considering the literature for ABI, there seem to be a lack of consensus on which mathematical model would best estimate the rocking curves. Therefore, this body of work compared five commonly used mathematical models, namely, the Gaussian model, Pearson VII model (P7), Voigt model, Pseudo-Voigt model (PsV), and the Lorentzian model, quantitatively using the well known χ^2 value (Korn and Korn, 2000) to find which model would best estimate the rocking curves.

The P7, Voigt, and the PsV models were tested as potential candidates to estimate the intrinsic rocking curve. These models were compared by estimating the average χ^2 for 935×780 pixels, which was estimated by fitting each model individually on a pixel-by-pixel basis. The average χ^2 values estimated for the P7 and the Voigt models found to be 77% and 76% higher than that of the χ^2 value for the PsV model, respectively. This significant difference gave confidence that the PsV model is the best candidate to estimate all the intrinsic rocking curves in this project. This initial testing was done without using any weights. Therefore, two type of sample weightings, namely $1/y$ and $log(y)$ were tested in an attempt to improve the PsV model fitting. However, χ^2 analysis indicated that the application of no weights was the best solution. Furthermore, the visual comparison of a randomly selected rocking curve displayed that when $1/y$ weighting was applied, the PsV model fit the tails of the intrinsic rocking curve significantly better. However, the estimated peak seem to shift significantly towards lower angles (see figure 4.3 (a) and (b)). Considering the PsV model is symmetrical function, this clearly shows that the intrinsic rocking curve is not truly symmetric. This agrees with the existing literature regarding ABI and this asymmetry can be attributed to the Bormann effect[7](Kitchen et al., 2010). Furthermore, the average α (see equation 4.1) value for all the intrinsic rocking curve estimations was calculated to be 7.64×10^{-1} with a standard deviation of 5.7×10^{-2} indicating that the intrinsic rocking curve is more closely related to the Lorentzian model than the Gaussian model. However, the literature (Arfelli et al., 2018) also uses the Gaussian model as an acceptable model to estimate the rocking curve.

Both the intrinsic centroid and the intrinsic FWHM image displayed identical artefacts at the same locations (see figure 4.4). The detector was ruled out as the origin of these artefacts by fitting the PsV model on a pixel-by-pixel basis to the transmitted rocking curves and extracting the centroid image of the transmitted beam (see appendix B.1.1). This was possible because the FOT detector having a large field of view allowed the capture of both the transmitted beam and the diffracted beam on two separate locations on the detector surface. Essentially, the transmitted beam centroid image displayed the same artefacts confirming that the origin of

[7]See e.g. Authier (2001)

these artefacts must be from the analyser crystal or any other optical element (monochromator crystals, windows, etc) upstream of the detector.

This chapter introduced a method to estimate the angular position of the analyser crystal for a given working point using the Lorentzian model. This was only possible because the Laue geometry allows the acquisition of both the transmitted and the diffracted components simultaneously. The angular position was found to fluctuate during tomographic acquisition for both samples at every working point (see figure 4.12). These rapid fluctuations are largely due to the positional variations of the analyser crystal. The analyser crystal is rotated using a stepping motor. Naturally, stepping motors exhibit small variations with each step because of the inertia of the moving rotor. This results in the motor either slightly overshooting the angular position or oscillating until it is settled at the correct angular position. Furthermore, if the frequency of these oscillations were to match the natural frequency of the motor, resonance will occur leading to vibrations or even losing steps. Furthermore, the anomalous behaviour of the analyser crystal angular position illustrated by the arrows in figure 4.12 could likely be due to the increase in intensity because of the topping up of the electron beam current in the storage rings in the synchrotron. For both the three-material sample and the clay loam sample, the largest variation of intensity due to analyser crystal fluctuations were recorded at the ±50% working points. This is expected because the steepest section of the rocking curve coincides with this working point.

Four different mathematical models, namely the Gaussian model, P7, PsV, and Lorentzian model were tested as potential candidate to estimate the sample rocking curve.

Following the same process as for the intrinsic rocking curve estimation process, average χ^2 values for five pixel-rows were estimated for each model by fitting them on a pixel-by-pixel basis to randomly selected sample image stack. Although the χ^2 estimations clearly indicated that PsV or P7 are the ideal candidates to estimate the sample rocking curves, both of these models on average took 20 minutes (with multiprocessing) to estimate a single image stack using the LMFIT library. These high processing times are due to the iterative nature of the algorithm (Levenberg-Marquardt algorithm) required to fit such complex models. Therefore, this chapter presented a non-iterative method to fit the Lorentzian model (QF method). Due to its non-iterative nature it processed a single image stack in 4.3 seconds (without multiprocessing). However, a potential downside of this method is that during coordinate transformation to convert the Lorentzian model into a simple polynomial, the noise in the original data will also undergo the same transformation. It is difficult to predict how the error will propagate to the final result from the original data. An analysis on error propagation for this method can be found on O'Haver (2021) pages 165-166. To better understand the propagation of error, QF method was tested by comparing it to the iterative Lorentzian method using the LMFIT library (LMFIT method). As expected, when the data is not noisy the QF method estimations found to be in good agreement with the LMFIT method estimations. However, when the photon count is extremely low, the two methods drift apart. Therefore, the largest deviations were found to be within the metal strip on the three-material phantom (see figure 4.13 (a)). Since, for the three-material phantom, the subject of the reconstruction are the Perspex ($C_5H_8O_2$) cylinder, Teflon (C_2F_4) pin, and the Aluminium pin, the metal strip in the three-phantom can be completely

neglected.

Furthermore, the χ^2 images generated using both the QF method and the LMFIT method clearly show that the distribution of error in rocking curve estimation for both methods are very similar (see figure 4.15). For both fitting methods the χ^2 values seem to increase where USAXS is expected (e.g. edges of the phantom). In addition, for both samples, for locations which produces a high USAXS signal (see figure 4.13 (c) and see figure 4.14 (d)), the centroid is registered outside the bounds of $\pm 80\%$ working points. The reason behind these inconsistencies can be attributed to the erratic behaviour of the $+50\%$ working point. Another possibility for these inconsistencies are that during image stacking $+25\%$ and $+50\%$ projections were interchanged or the images are not well aligned. However, the rocking curves outside the sample (air) show no signs of such inconstancies (e.g. see figure 4.14 (b)) and the image alignment testing discussed in section 3.6 show that the projections corresponding to a given rocking curve are well aligned.

It was found that the QF method is 278 times faster at fitting the Lorentzian function compared to the LMFIT method. Considering the limited time available for this project, the sample integral, sample centroid, and the sample FWHM images were extracted for both samples using the QF method by fitting the rocking curves on a pixel-by-pixel basis. These images display artefacts (see figures 4.16 and 4.17), which are of equivalent to the ones in the intrinsic integral, intrinsic centroid, and the intrinsic FWHM images 4.4. Therefore, it can be expected for these artefacts to either completely cancel out or significantly reduced when the attenuation, refraction, and USAXS signals are extracted. Chapters 5 and 6 discuss these extractions in detail.

4.5 Conclusion

This chapter compared five different mathematical models as potential candidates to estimate the rocking curves and it was found that PsV model is the best candidate to estimate both the intrinsic rocking curve and the sample curve. It also introduced a Lorentzian based analytical method to accurately estimate the angular position of the analyser crystal. Furthermore, due to large processing times required for fitting the PsV model, this chapter have shown that fitting the Lorentzian model using QF method is the most feasible option to estimate the sample rocking curves. By comparing the QF method to LMFIT method, it was found that the QF method is also an extremely robust method to estimate the sample rocking curves. In addition, this chapter have also provided conclusive evidence that the Gaussian model is the least accurate model to use when estimating the rocking curve.

Chapter 5

Reconstruction of the Index of Refraction

This chapter is dedicated to the reconstruction of the β and δ components of the index of refraction for the three-material phantom and the clay loam samples. Here, the δ component reconstruction will follow the two-dimensional phase retrieval process described in section 2.4.3. The first section will describe the process of reconstruction for the three-material phantom. It will also quantitatively compare two reconstruction methods where the β and δ components for Perspex ($C_5H_8O_2$), PTFE (C_2F_4), and Aluminium are reconstructed using 261 points (261-point reconstruction) and eight points (eight-point reconstruction) to estimate the rocking curve without the sample in the beam (intrinsic rocking curve). The results from both reconstruction methods will be compared with the theoretical β and δ components of Perspex, PTFE, and Aluminium (see table 3.1). The second section will discuss the reconstruction of the β and δ components of the clay loam sample. Then the last two sections will provide a discussion and a conclusion for this chapter.

5.1 Three-Material Phantom

This section presents the process of reconstruction and the analysis of the 3D images of β and δ components of the index of refraction for the three-material phantom. The reconstructions were carried out using two methods to test for the optimal reconstruction procedure. The first method used all 261 angular positions of the analyser crystal (261-point method) to estimate the intrinsic rocking curve parameters, while the second method employed eight angular positions of the analyser crystal (eight-point method) to estimate the intrinsic rocking curve. The reasoning behind the use of eight points was to maintain consistency between the number of working points between the sample rocking curve and the intrinsic rocking curve[1]. Furthermore, to increase the consistency between the sample rocking curve and the intrinsic rocking curve, it was made certain that the eight angular positions of the intrinsic rocking curve used for the eight-point method corresponded to the eight average angular positions estimated for the eight working points in table 4.4.

[1]Section 3.2 and chapter 4 gave an extensive overview on data acquisition and the rocking curve estimation process, respectively.

5.2 Attenuation Image Reconstruction

The attenuation projections were extracted by taking the ratio between the sample integral image (e.g. see figure 4.16 (a)) and the intrinsic integral image (e.g. see figure 4.4 (a)). Figure 5.1 (a) displays the attenuation projection corresponding to the tomographic angular position 14° extracted using the 261-point reconstruction method. Here, as expected, the so called *"chicken wire"* pattern and other artefacts observed in the intrinsic integral image (see figure 4.4 (a)) and the sample integral image (see figure 4.16 (b)) have cancelled out.

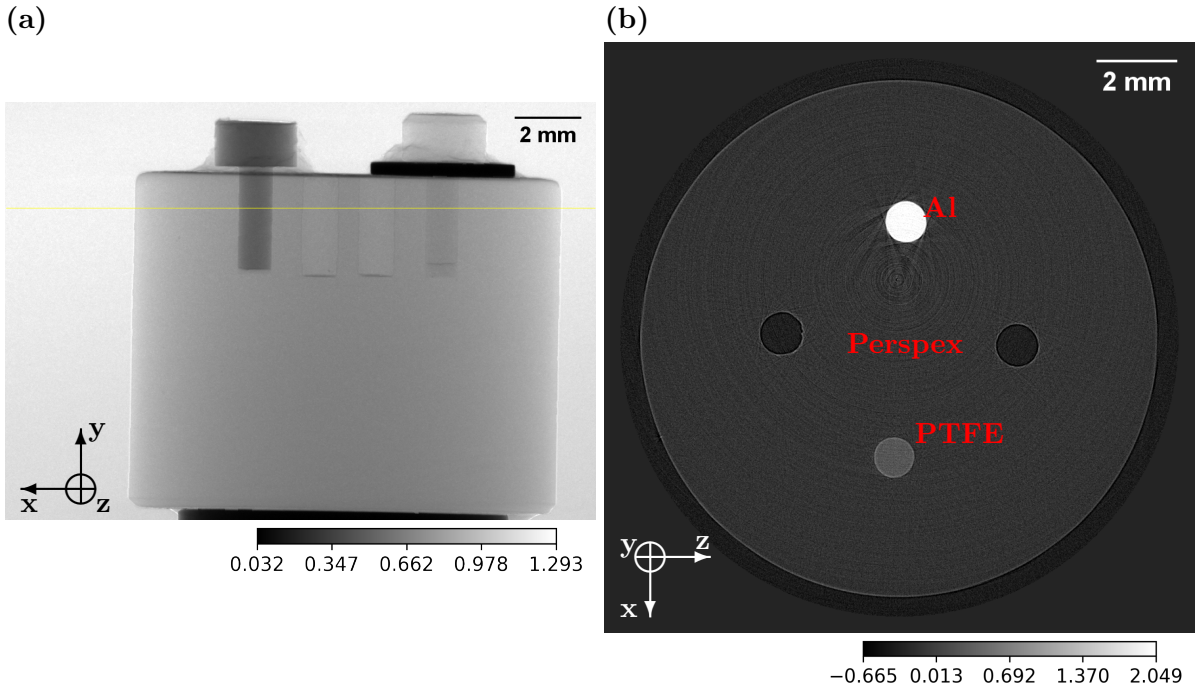

Figure 5.1: *(a) and (b) display the attenuation image generated by taking the ratio between the intrinsic integral (e.g. see figure 4.4 (a)) and the* 140^{th} *sample integral tomographic projection (e.g. see figure 4.16 (a)) and the reconstructed map of* β *values of the three-material phantom, respectively. Here,* x*,* y*, and* z *correspond to the horizontal, vertical, and the optical axes (see figure 3.2), respectively. The horizontal line on (a) illustrates the position of the reconstructed* β *map displayed in (b). The attenuation image contain* 1090×770 *pixels and the pixel dimensions of* β *map is* 900×900*. Here, the excess air regions of the* β *map were cropped. Here, In the attenuation image the left top knob and the accompanying pin corresponds to Aluminium and the right top knob and the accompanying pin corresponds to the PTFE pin. The two rectangles in the middle correspond to the empty holes containing air. In the* β *map* ($\times 10^{-9}$)*, the large centre circle corresponds to Perspex. The top and the bottom circles correspond to the Aluminium and the PTFE pins, respectively. The left and the right circles corresponds to the empty holes (air). The outer circle represents air outside the sample. Furthermore, in the* β *map, around the phantom edge and the edges of the pin holes, the propagation-based fringes are also clearly visible. The images displayed here were reconstructed using the 261-point method. Figure B.3 (a) in the appendix displays the* β *map corresponding to the* 195^{th} *pixel row reconstructed using the eight-point reconstruction method.*

The attenuation image in figure 5.1 (a) displays a clear delineation between the materials within the phantom and the top edge of the phantom appear to be considerably darker compared to the left and right edges of the phantom. This suggests a significant reduction in the area

under the sample rocking curves corresponding to the top edge of the phantom. This is likely due to the top edge of the three-material phantom producing higher USAXS signal. It was found that a larger USAXS signal leads to an increase in the FWHM and a decrease in the amplitude of the sample rocking curves (see figure 4.13 (c)). Chapter 6 will further discuss the increase in USAXS signal at the edges of this phantom in detail.

Following the extraction of attenuation projections, the CT reconstruction of the β map was carried out using the first 1800 attenuation projections covering the 0° to 180° tomographic angular region. The CT reconstruction was done using filtered back projection (FBP) with a Ram-Lak filter (see section 2.5). Figure 5.1 (b) displays the 195^{th} CT slice reconstructed using the 261-point reconstruction method. The position of this cross section in the three-material phantom is illustrated with the horizontal line across the attenuation projection in figure 5.1 (a). In figure 5.1 (b), the aluminium pin (top smaller circle) is considerably brighter than the PTFE pin (lower smaller circle) and some streaking artefacts can be observed around the aluminium pin. This is because the absorption coefficient β of Aluminium is factor of ten larger that of PTFE (see table 5.1).

Both the 261-point method and the 8-point method essentially produced the same β values for Persepx, PTFE, and Aluminium (see table 5.1). The deviation of the experimental β value from the theoretical β value for Perspex, PTFE, and Aluminium was estimated to be 7%, 5%, and 11%, respectively. Since, both the 261-point and the eight-point resonctruction methods, quantitatively gave the same outcome, 261-point reconstruction method was used to reconstruct the β maps of the clay loam sample. Section 5.4 discusses the clay loam sample reconstructions in detail.

Table 5.1: *A comparison between the theoretical β values and the experimental β values for Perspex, PTFE, and Aluminium. This table display experimental estimations of β values estimated using both the 261-point method and the eight-point method. The experimental values were measured by taking the mean value of a circular region for each material in the β map. Here, the displayed uncertainties correspond to the estimated standard deviation when measuring the mean over a circular region. The theoretical values were taken from https://henke.lbl.gov/optical_constants/. Accessed date: 10/02/2021.*

Material	$\beta(\times 10^{-10})$		
	Theoretical Value	261-Point Reconstruction	Eight-Point Reconstruction
Perspex ($C_5H_8O_2$)	1.4	1.3 ± 0.6	1.3 ± 0.6
PTFE (C_2F_4)	3.7	3.9 ± 0.6	3.9 ± 0.6
Aluminium	15.2	16.9 ± 0.7	16.9 ± 0.7

5.3 Two-Dimensional Phase Retrieval

Two-dimensional phase retrieval essentially follows the process described in section 2.4.3. First, the refraction angle maps $\boldsymbol{g}'_{0,y}$ and $\boldsymbol{g}'_{\pi,y}$, which correspond to the ψ and $\psi + \pi$ tomographic angular positions were estimated. This was accomplished by subtracting the intrinsic centroid image (e.g. see figure 4.4 (b)) from the corresponding sample centroid images (e.g. see figure

4.16 (b)). Figure 5.2 (a) and (b) display the extracted $\boldsymbol{g}'_{0,y}$ and $\boldsymbol{g}'_{\pi,y}$ projections corresponding to the tomographic angular positions 14° and 194°, respectively. In both images, the dark area illustrates the centroid of the sample rocking curve shifting to a higher angle giving a lower value compared to the intrinsic rocking curve centroid indicating an increase in the incident angle with respect to the crystallographic planes of the analyser crystal. The bright areas illustrate the effect of the centroid of the sample rocking curve shifting to a lower angle giving a higher value compared to the intrinsic rocking curve centroid. This indicates a decrease in the incident angle with respect to the crystallographic planes of the analyser crystal. Physically this illustrates the deviation of the wavefield as it traverses through the phantom.

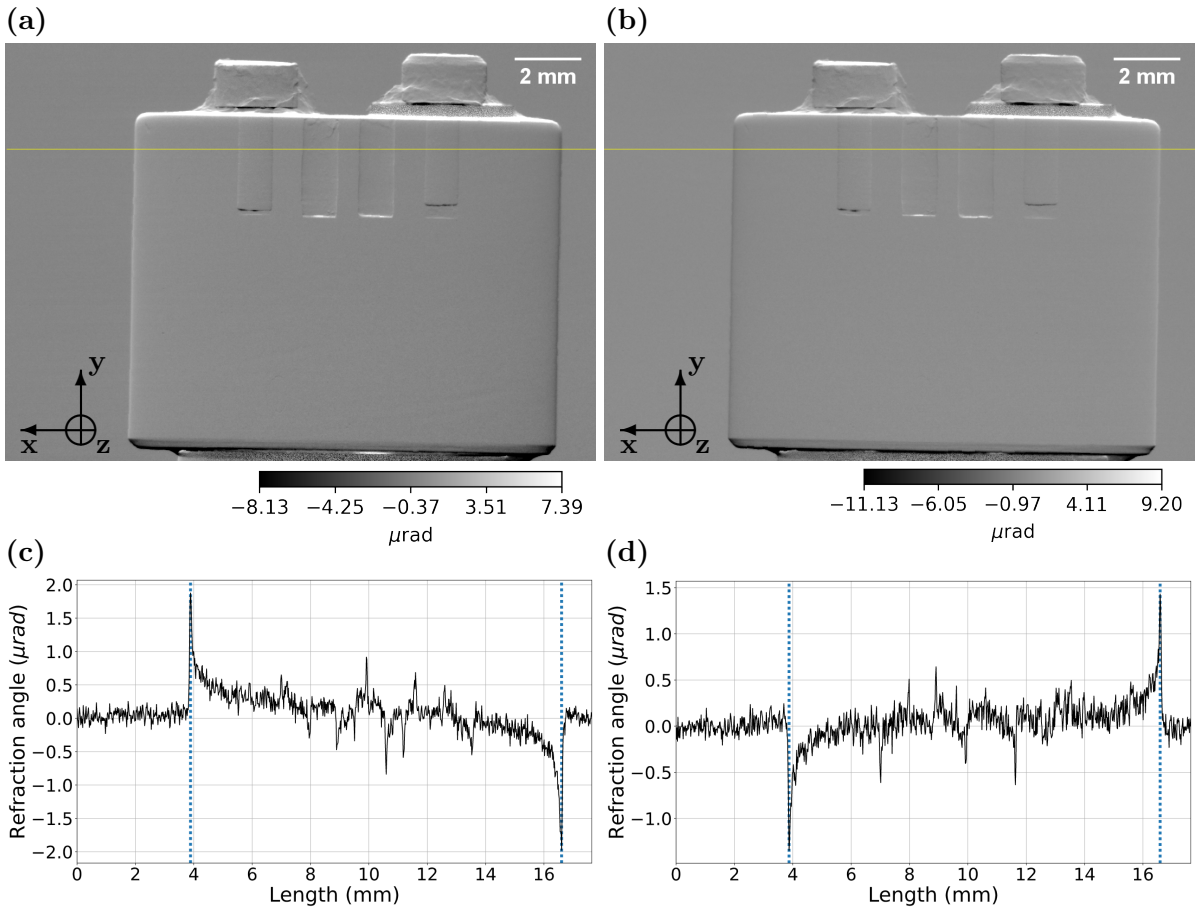

Figure 5.2: *(a) and (b) illustrate the refraction angle maps corresponding to the ψ ($\boldsymbol{g}'_{0,y}$) and the $\psi+\pi$ ($\boldsymbol{g}'_{\pi,y}$) tomographic projection angles, respectively. Here, the projection $\boldsymbol{g}'_{\pi,y}$ is horizontally flipped and translated so that the phantom edges are properly aligned with the projection $\boldsymbol{g}'_{0,y}$. The horizontal lines in (a) and (b) correspond to the ROI used to plot a line profiles (c) and (d) across the projections, respectively. In both (a) and (b) the horizontal lines correspond to the 195^{th} pixel row. From left to right, four rectangles in (a) and (b) correspond to the Aluminium pin, two empty holes containing air, and the PTFE pin. Here, in both (a) and (b) the phantom edges are well observed while the boundaries between the materials are fairly visible. This visibility is well defined in their corresponding line profiles (c) and (d). In these line profiles, the vertical dotted lines corresponds to the left and the right edges of the phantom, respectively. Furthermore, both (a) and (b) images contain 1090×770 pixels each. x, y, and z correspond to the horizontal, vertical, and the optical axis (see figure 3.2), respectively.*

The precise alignment of the phantom in the two projection images, namely the $\boldsymbol{g}'_{0,y}$ (see

figure 5.2 (a)) and the $\boldsymbol{g}'_{\pi,y}$ projections (see figure 5.2 (b)), is of great significance. This is because a misalignment could perturb the reconstructed phase for the materials in the phantom. The accuracy of the alignment between projections $\boldsymbol{g}'_{0,y}$ and $\boldsymbol{g}'_{\pi,y}$ were confirmed by comparing the lengths at which the left phantom edge and the right phantom edge peaks were registered in the corresponding line profiles (see figure 5.2 (c) and (d)). In the line profile 5.2 (c), the estimated lengths at which the maximum (left edge) and the minimum (right edge) peaks registered were 3.88 mm and 16.61 mm, respectively. For the line profile 5.2 (d) the minimum (left edge) and the maximum (right edge) peaks were registered at 3.87 mm and 16.59 mm, respectively. This suggests that the two projections are misaligned only by 0.03 mm (30 µm). This translates to about a 2 pixel misalignment.

In figure 5.2 (c), the left and the right edges of the phantom recorded the angular deviation of the x-ray wavefield to be 1.876 µrad and -1.977 µrad, respectively. In figure 5.2 (d), the respective edges of the phantom recorded the angular deviation of the x-ray wavefield to be -1.346 µrad and 1.432 µrad. This means that there is a clear asymmetry between the the angular deviation of the x-ray wavefield at the edges of the phantom in both figure 5.2 (a) and (b). This asymmetry can also be seen at the peaks and the troughs corresponding to the edges of the four holes in the phantom. This asymmetry is somewhat concerning because it could affect the final reconstructed δ values of the materials in the phantom.

Using the equations (2.51) and (2.52), the directional phase gradients were estimated. Figure 5.3 (a) and (b) display the horizontal ($\frac{\partial \Phi}{\partial x}$) and vertical ($\frac{\partial \Phi}{\partial y}$) components of the phase gradients generated using the $\boldsymbol{g}'_{0,y}$ and $\boldsymbol{g}'_{\pi,y}$ projections depicted in figure 5.2, respectively. Visual observations clearly indicate that the phantom is significantly more visible in the horizontal component of the phase gradient image compared to the vertical component of the phase gradient image. Most of the object features are vertical, hence most of the features are more strongly seen in the horizontal component of the phase gradient image (see figure 5.2 (a)). The distinct peaks and troughs observed in the line profile illustrated in figure 5.3 (c) attest to the increased visibility along the vertical edges in the horizontal phase gradient image (see 5.3 (a)). Furthermore, in figure 5.3 (c), the maximum and the minimum peaks corresponding to the left edge of the phantom recorded a refraction angle of 11.228 µrad and -11.751 µrad, respectively. The distinctive peaks and the troughs between the maximum and the minimum peaks correspond to edges of the four holes in the phantom.

Also note that the sensitive direction of the analyser crystal is roughly vertical. Therefore, vertical edges are barely visible in figure 5.3 (b), while horizontal edges are better pronounced. This is further observed in the line profile illustrated in figure 5.3 (d) corresponding to the figure 5.3 (b). Except for few discrepancies, most values across this line profile seem to lie close to zero. The discrepancies observed at the left and the right hand side edges are likely due to the two-pixel misalignment between the $\boldsymbol{g}'_{0,y}$ projection (see figure 5.2 (a)) and the $\boldsymbol{g}'_{\pi,y}$ (see figure 5.2 (b)) projection discussed earlier in this section.

Then the horizontal (e.g. see figure 5.2 (a)) and vertical components of the phase gradient (e.g. see figure 5.2 (b)) were combined using 2D Fourier integration (see equation (2.53)) to give the phase map. Appendix A.3.1 displays the Python program written to implement 2D Fourier integration. Figure 5.4 (a) and (c) display the phase projection corresponding to the tomographic

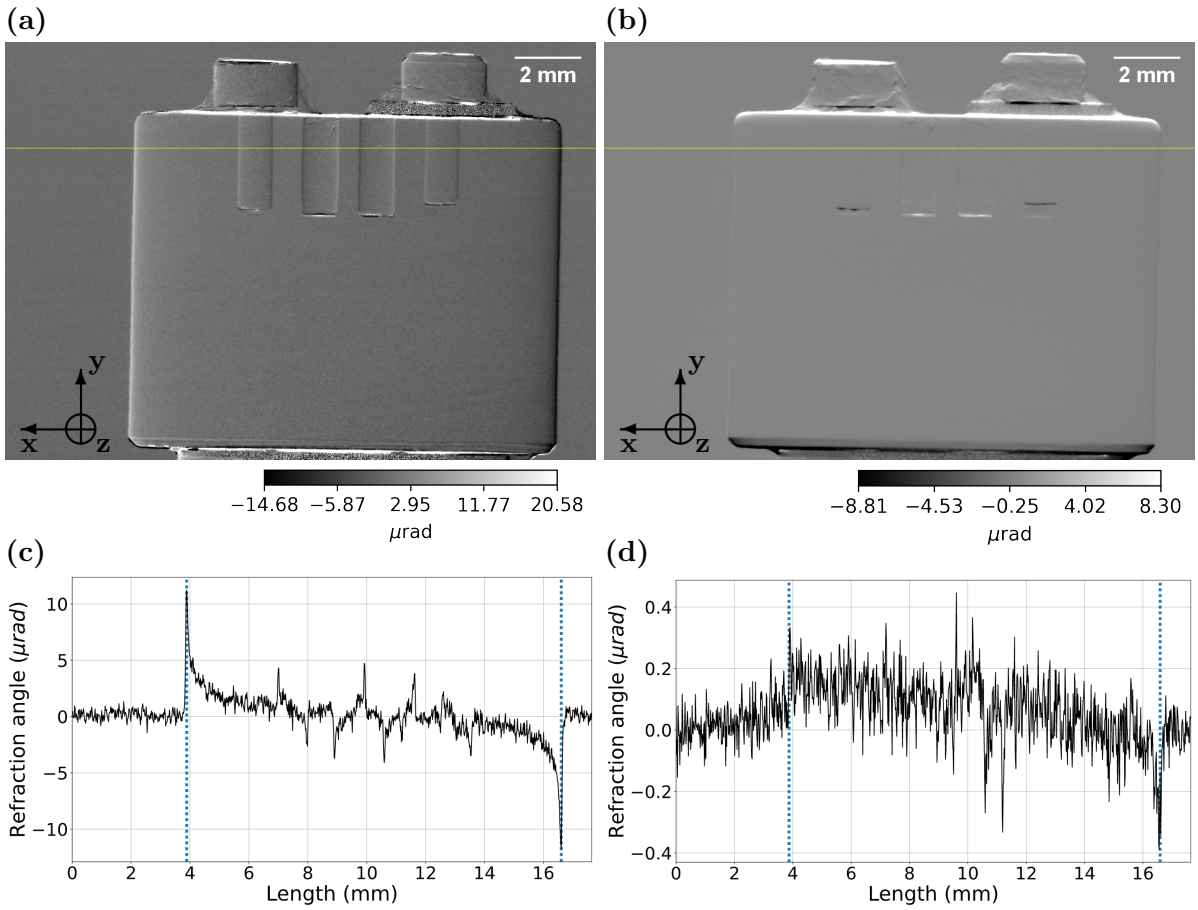

Figure 5.3: *(a) and (b) display the calculated component of gradient of phase in x (horizontal) and y (vertical) directions. These outputs were generated using the* $\boldsymbol{g}'_{0,y}$ *and* $\boldsymbol{g}'_{\pi,y}$ *projections displayed in figure 5.2 (a) and (b), respectively. The horizontal lines in (a) and (b) correspond to the ROI used to plot a line profiles (c) and (d) drawn across the projections, respectively. For both (a) and (b) the line profiles are drawn across the* 195^{th} *pixel row. Here, both (a) and (b) are of size* 1090×770 *pixels. In (a), the vertical edges of the phantom are clearly visible and it is well observed in the corresponding line profile (c). In (b), the vertical edges are barely visible while the horizontal interfaces are more pronounced. Although most of the values in the line profile (d) corresponding to the component of gradient of phase in vertical direction (b) are closely related to zero, some distinct peaks and troughs can be observed. In both line profiles, (c) and (d), the vertical dotted lines are drawn across the maximum and the minimum peak values taken from (c) for comparison. These dotted lines correspond to the left and the right edges of the phantom, respectively.*

angular position 14° and the line profile plotted across the 195^{th} pixel row, respectively. Visually, in figure 5.4 (a), the left hand side is brighter than the right hand side, indicating that the estimated phase shift in air on either side of the three-material phantom do not match, although they should. This is further confirmed by the lack of symmetry in the line profile depicted in 5.4 (c). This artefact was corrected by applying a row-by-row linearity and a background correction. This correction was based on the boundary condition that the phase shift in air must equal zero. Figure 5.4 (b) and (d) displays the linearity and background corrected phase projection and the line profile plotted across the 195^{th} pixel row, respectively. The linearity correction was accomplished by calculating the change in magnitude across a pixel row by fitting a line to the first 20 and the last 20 pixel values for any given row. Then the change in magnitude was

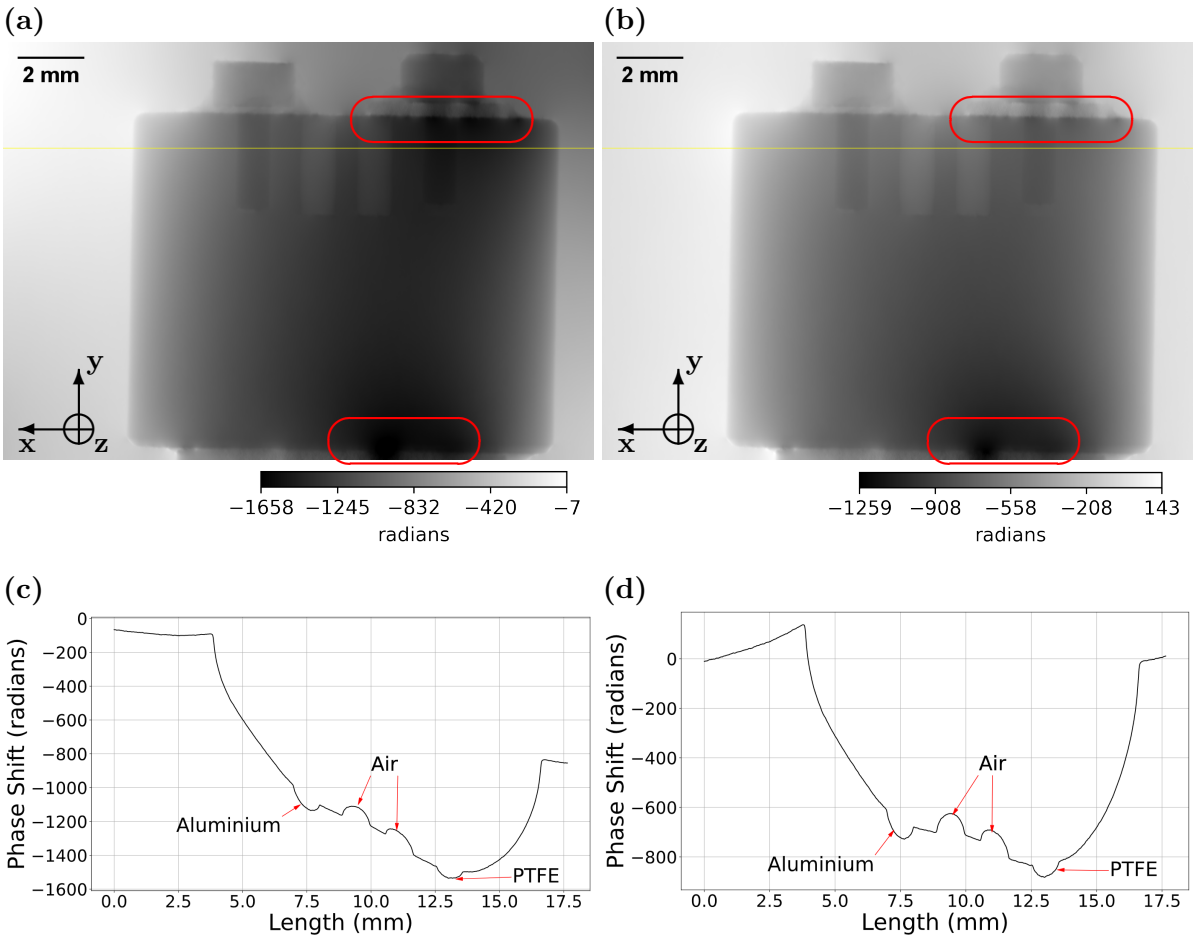

Figure 5.4: *The* 140^{th} *phase projection without (a) and with (b) the application of row-by-row linearity and background correction. Each projection have the pixel dimensions* 1090×770 *pixels. (c) and (d) display the line profile drawn across the horizontal lines illustrated in (a) and (b), respectively. Red ovals depict the noisy sections in the projections, which are responsible for some of the lack of uniformity observed across the Perspex in (a). Furthermore, in (a), the phase shift in the air on either side of the phantom is observed to be uneven. These uniformity issues are clearly visible in the line profile depicted in (c). Although the linearity and background corrections reduced the effects of amplified noise in (b), the lack of uniformity is still visible. This lack of uniformity is clearly evident in the line profile (d) as well. The four small protrusions in the middle of the line profiles corresponds to the four holes in the phantom containing. From left to right these small protrusions correspond to the Aluminium pin, two holes containing air, and PTFE, respectively.*

subtracted from every pixel in the row effectively, reducing the gradient of the linear fit to zero. This correction essentially shifted the pixel values on one end of the image to match the other end of the image. Since the phase shift in the air must equal to zero, an average of the first 20 and the last 20 pixel values of the linearly corrected pixel row was subtracted from the entire pixel row to bring the phase shift in air as close as possible to zero (background correction). Appendix A.3.2 displays the python function written to accomplish the linearity and background correction in phase images.

Although visually, figure 5.4 (b) displays a significant improvement in uniformity horizontally across the phantom, the corresponding line profile still display a lack of symmetry across the phantom (see figure 5.4 (d)). This is likely due to the amplification of low frequency noise during

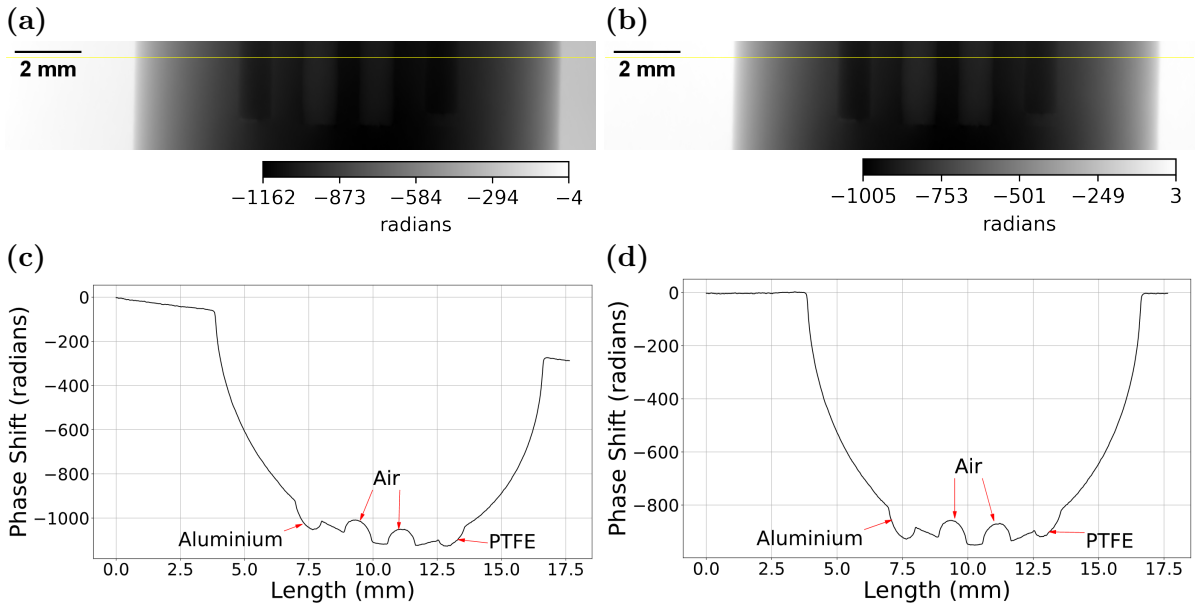

Figure 5.5: *The* 140^{th} *cropped phase projections and the corresponding line profiles. Here, the noisy sections depicted in 5.4 (a) and (b) were removed before the 2D Fourier integration process. (a) and (b) illustrate the linearity and background uncorrected and corrected phase images with pixel dimensions of* 1090×200 *pixels, respectively. The horizontal lines illustrated in (a) and (b) correspond to the positions of the line profiles depicted in (c) and (d), respectively. Here, the position of the line profile matches the position of the line profiles depicted in figure 5.4. Four small protrusions at the bottom of the line profiles in (c) and (d) correspond to the four holes containing the materials, which are the subject of the final reconstruction. Here, the left and right hand side small protrusions correspond to the Aluminium and PTFE pins, respectively. The two small protrusions at the centre correspond to the empty holes containing air.*

the 2D Fourier integration process. In principle, amplification of low-frequency noise in Fourier space leads to an increase in noise in real space. The two sections of the phantom identified by the ovals in figure 5.4 (a) and (b) combined with the 2-pixel misalignment identified earlier could be the likely culprits behind this lack of uniformity. The top oval corresponds to the metal strip where it was clearly illustrated in section 4.3 that due to high attenuating composition of this section, intensities detected around the rocking curve was too low to extract viable phase information. The bottom of the phantom also displayed similar effects when considering the χ^2 images in figure 4.15.

The features of interest in the three-material phantom are not found in the noisy sections illustrated by ovals in figure 5.4 (a) and (b). Therefore, by removing these sections from the horizontal and vertical components of the phase gradient (see figure 5.3) before applying 2D Fourier integration (see equation (2.53)) enabled a significantly better extraction of the 2D phase shifts. Figure 5.5 (a) and (c) display the cropped phase projections without applying the linearity and background correction and the line profile plotted across the horizontal line drawn across figure 5.5 (a), respectively. When comparing figure 5.5 (a) to figure 5.4 (a), the spread of low frequency noise across Perspex looks even, however, it still displays the lack of uniformity in air on either sides of the phantom. When looking at the line profile in figure 5.5 (c), it is evident that just by removing the noisy sections, the overall uniformity across the phantom has significantly improved. Then the application of row-by-row linearity and background correction

shifted both edges of the phantom close to zero, providing a significantly better 2D phase shift reconstruction (see figure 5.5 (a) and (b)).

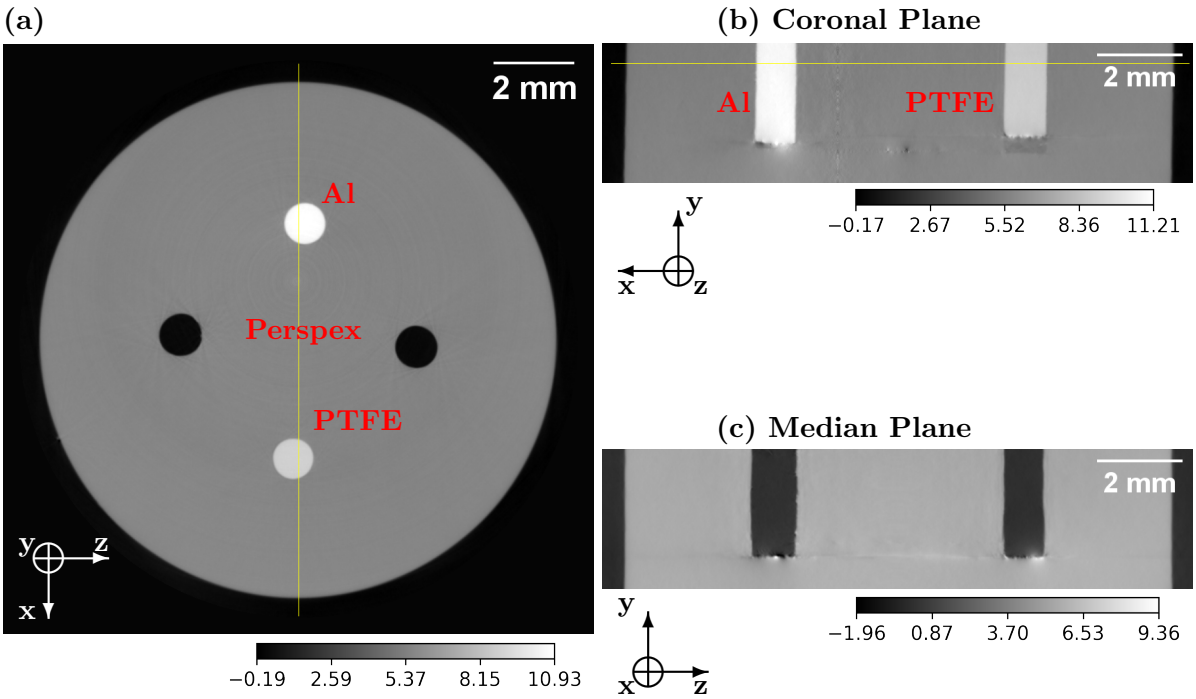

Figure 5.6: *(a), (b), and (c) represent reconstructed axial, coronal, and median CT slices of the δ ($\times 10^{-7}$) map of the three-material phantom, respectively. These reconstruction were carried out using the 261-point reconstruction method. Here, the position of the axial CT slice (a) is illustrated by the horizontal line drawn across the coronal CT slice (b). This horizontal line corresponds to the 195^{th} pixel row. The vertical line across the Aluminium and the PTFE pin illustrates the ROI used to draw the line profile depicted in figure 5.7. The coronal plane depicts the Aluminium pin and the PTFE pin while the median plane show a cross section of the empty hole inside the phantom. In both the coronal and the median planes, across the bottom edges of the pin holes, a distinct blurred line can be observed. The corresponding axial CT slice of the δ map reconstructed using the eight-point reconstruction method is displayed in the appendix (see figure B.3 (b)).*

Table 5.2: *A comparison between the theoretical δ values and the experimental δ values for Perspex, PTFE, and Aluminium estimated using the 261-point reconstruction method. It also displays the deviation of experimental estimations for δ from the theoretical estimation as a percentage for each material within the phantom. Possible reasons behind the dependency between the experimental and the theoretical values will be discussed further in section 5.5. The theoretical values were taken from https://henke.lbl.gov/optical_constants/. Accessed date: 10/02/2021.*

Material	$\delta(\times 10^{-7})$		
	Theoretical	261-Point Reconstruction	Deviation From Theoretical δ (%)
Perspex ($C_5H_8O_2$)	3.9	5.6 ± 0.1	43
PTFE (C_2F_4)	6.5	8.8 ± 0.1	35
Aluminium	8.0	10.9 ± 0.1	36

Using 2D Fourier integration, 1800 horizontal components of the phase gradients were com-

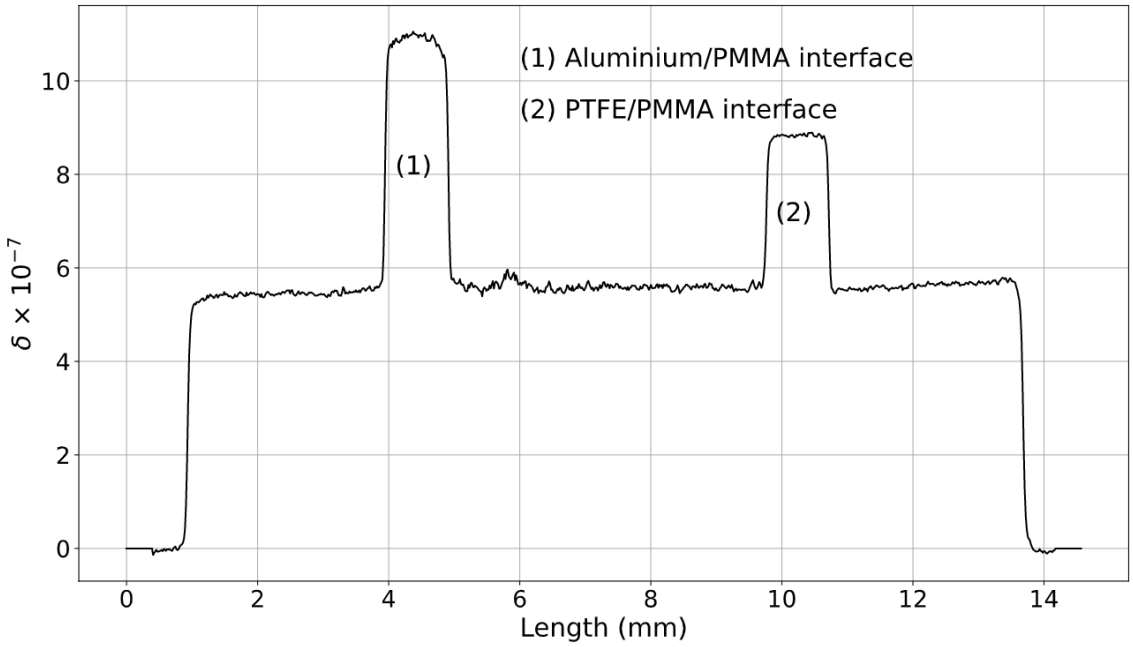

Figure 5.7: *The line profile drawn across the vertical line drawn across the axial CT slice (see figure 5.6). Here, clear boundaries between air and Perspex show that the δ value of air is nearly zero and the surface of Perspex across the whole thickness of the phantom is nearly flat. The small protrusion between (1) and (2) where length is approximately 5.8 mm corresponds to the centre of tomographic reconstruction rotation. The interfaces (1) and (2) further attest to the performance of the reconstruction process developed in this thesis displaying clear contrast between the objects within the three-material phantom.*

Table 5.3: *A comparison between the theoretical δ values and the experimental δ values for Perspex, PTFE, and Aluminium estimated using the eight-point reconstruction method. Here, the deviation of experimental estimations for δ for Perspex and Aluminium has slightly reduced compared to the 261-point reconstruction method (see table 5.2). These results will be discussed further in section 5.5. The theoretical values were taken from https://henke.lbl.gov/optical_constants/. Accessed date: 10/02/2021.*

Material	$\delta(\times 10^{-7})$		
	Theoretical	Eight-Point Reconstruction	Deviation From Theoretical δ (%)
Perspex ($C_5H_8O_2$)	3.9	5.5 ± 0.1	41
PTFE (C_2F_4)	6.5	8.8 ± 0.1	35
Aluminium	8.0	10.8 ± 0.1	35

bined with their respective vertical components producing a total of 1800 phase shift images covering 180° in 0.1°. Using all 1800 phase projections, the CT reconstruction of phase was done using filtered back projection with a Ram-Lak filter (see section 2.5). Then the reconstructed phase was divided by the wavevector to estimate the real part of the index of refraction δ (see equation (2.25)). Figure 5.6 (a) displays a reconstructed δ map of the materials in the three-material phantom, namely Perspex, PTFE, and Aluminium. Unlike in the β map (see figure 5.1 (b)), in the δ map, the outer ring corresponding to air is virtually non-existent. This

is likely due to the linearity and background correction forcing the air to be close to zero everywhere. Hence, it is essentially same as the masked out regions in the corners. Furthermore, compared to the β map, the streaking artefacts around the aluminium pin (top small circle) is less pronounced and the overall boundaries between the materials are better defined. The line profile drawn vertically across the δ map further illustrates the distinct boundaries between the materials in the three-material phantom (see figure 5.7). The coronal and the median plane images of the three-material phantom illustrated in figure 5.6 (b) and (c), respectively, display some edge smearing artefacts at the bottom edges of the holes. The noise amplification in Fourier space during the 2D Fourier integration procedure could be the likely the cause of these distortions. Furthermore, it could also be due to roughness from the drill bit or other foreign substance.

Using both the 261-point reconstruction method and the eight-point reconstruction method, the δ values for Perspex, PTFE, and Aluminium were estimated. Tables 5.2 and 5.3 display a comparison between the 261-point and the eight-point reconstruction method comparing experimental and theoretical δ values for the three materials. Since the quantitative comparison of the two reconstruction methods show that both methods perform similarly, only the 261-point reconstruction method was used to reconstruct the δ maps of the clay loam sample (see section 5.4)

5.4 Clay Loam Sample Reconstructions

This section presents the results for the clay loam sample attenuation and phase image reconstruction. Both the attenuation and the phase images of the clay loam sample were reconstructed using the 261-point reconstruction method.

Following the process described in section 5.2, the attenuation projections of the clay loam sample were extracted (see figure 5.8). Then, using the 1800 attenuation projection images covering the tomographic angular positions from 0° to 180°, the β map of the clay loam sample was reconstructed utilising FBP with a Ram-Lak filter (see section 2.5). Reconstructed axial, coronal and a median CT slices of the β map of the clay loam sample are displayed in figures 5.11 (a), 5.12 (a), and 5.12 (c), respectively. These images are placed next to the corresponding δ maps for direct qualitative comparison at the end of this section.

The phase images and the δ map of the clay loam sample were reconstructed following the process described in section 5.3. First, the $\boldsymbol{g}'_{0,y}$ and $\boldsymbol{g}'_{\pi,y}$ projections corresponding to the ψ and $\psi + \pi$ tomographic angular positions were extracted by subtracting the intrinsic centroid image from the sample centroid image (e.g. see figure B.4). Then the $\boldsymbol{g}'_{\pi,y}$ projection was horizontally flipped and translated to align the vertical edges of the syringe with the $\boldsymbol{g}'_{0,y}$ projection. Similar to the three-material phantom image processing (see section 5.3), the alignment of the these projections were tested using line profiles. It was found that the $\boldsymbol{g}'_{0,y}$ and $\boldsymbol{g}'_{\pi,y}$ projections were misaligned by approximately two pixels. Interestingly this misalignment agrees with the misalignment found between the three-material phantom $\boldsymbol{g}'_{0,y}$ and $\boldsymbol{g}'_{\pi,y}$ projections (see section 5.3). Possible point of origins of this misalignment and its consequences will be discussed further in section 5.5.

Thereafter, using the $\boldsymbol{g}'_{0,y}$ and $\boldsymbol{g}'_{\pi,y}$ projections, the horizontal (see figure 5.9 (a)) and the

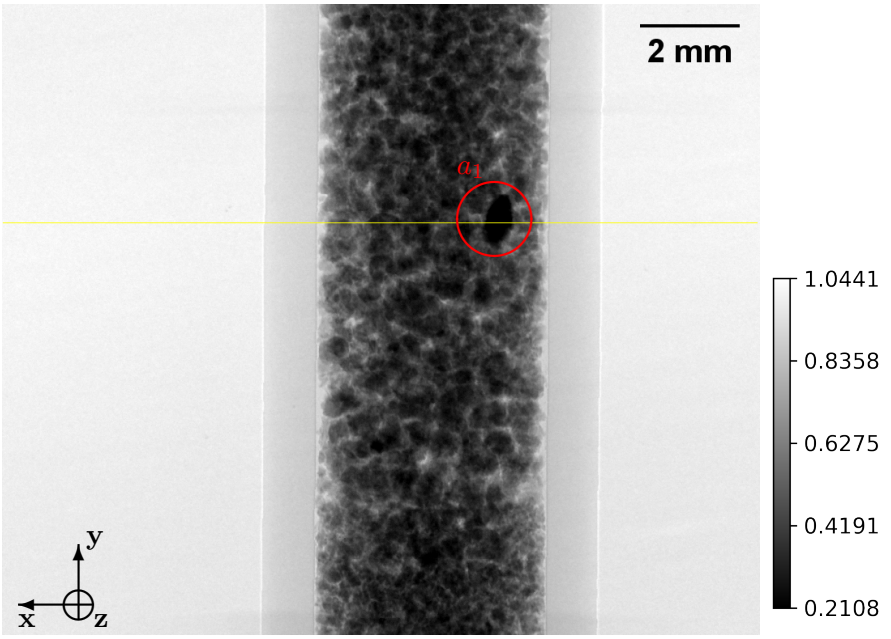

Figure 5.8: *140^{th} attenuation projection of the clay loam sample, which corresponds to the tomographic angular position of 14°. This was reconstructed by taking the ratio between the intrinsic integral image (e.g. see 4.4 (a)) and the 140^{th} sample integral image (e.g. see 4.17 (a)) of the clay loam sample. Here, the plastic syringe can be clearly observed. The bright spots between the clay loam particulates are either air gaps or low attenuating objects within the sample. The horizontal line depicts the row of pixels used to reconstruct the axial CT image displayed in figure 5.11 (a). The circle marked as a_1 display a highly attenuating object, which will be discussed further in the latter part of this section and in section 5.5.*

vertical (see figure 5.9 (b)) components of the phase gradient were extracted. As expected, in the horizontal component of the phase gradient (see figure 5.9 (a)) the vertical edges of the syringe are clearly visible. This is further illustrated in the corresponding line profile depicted in figure 5.9 (c). In the vertical phase gradient image, the vertical syringe edges are virtually non-existent (see figure 5.9 (b) and (d)). However, due to the high number of interfaces available in the clay loam particulates, one can observe a large number of rough protrusions.

Using the $\boldsymbol{g}'_{0,y}$ and $\boldsymbol{g}'_{\pi,y}$ projections of the clay loam sample and equation 2.53, the phase shift projections of the clay loam sample were generated (e.g. see figure 5.10 (a) and (c)). The linearity and background corrections were applied to these phase projections to bring the phase shift in air closer to zero (e.g. see figure 5.10 (b) and (d)). This process essentially produced 1800 phase shift images covering the tomographic angular region of 0° and 180°. These projections were then used to reconstruct the δ map using FBP with the Ram-Lak filter. The axial, coronal and a median plane of the δ map of the clay loam sample are displayed in figures 5.11 (b), 5.12 (b), and 5.12 (d), respectively.

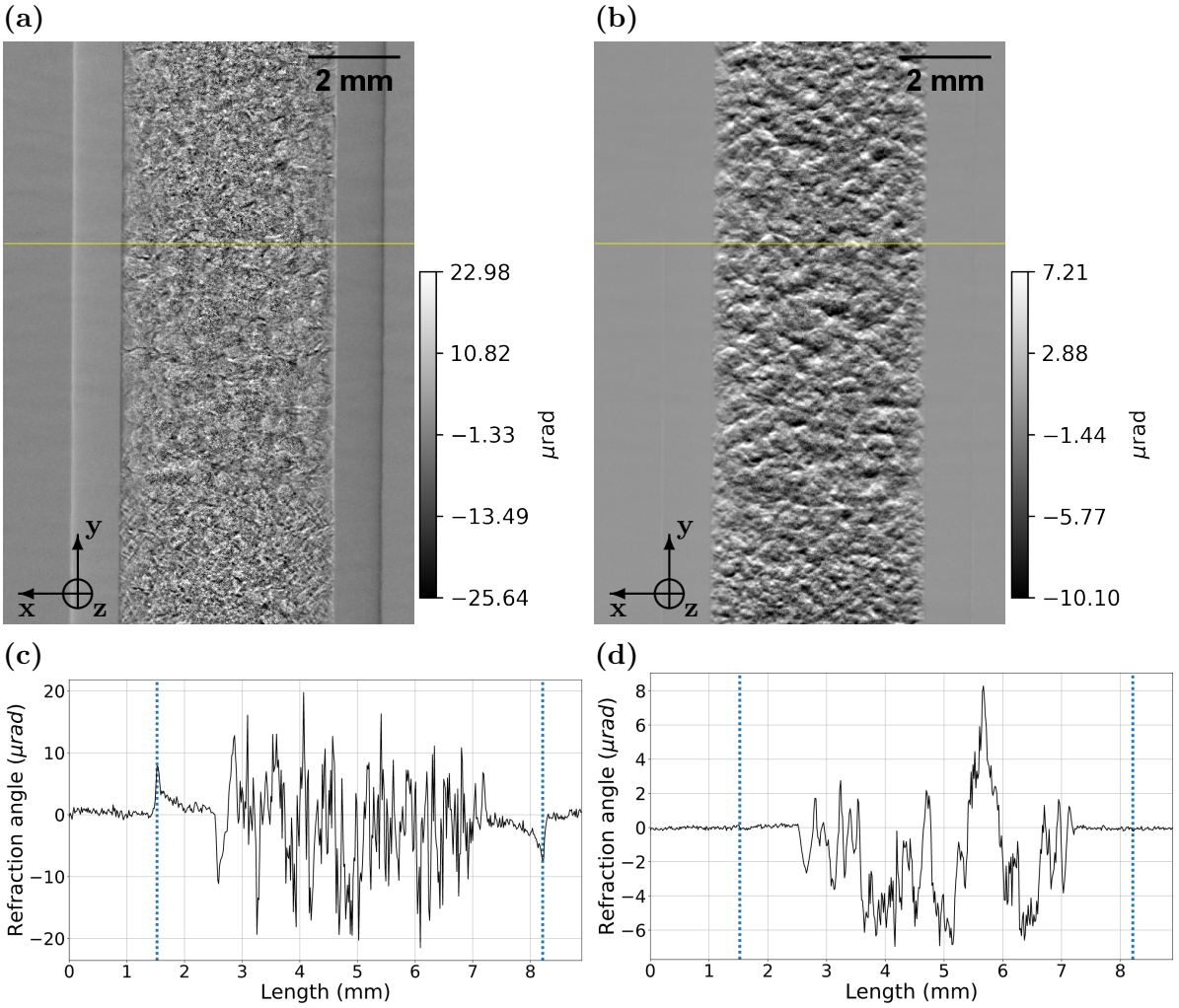

Figure 5.9: *Horizontal (a) and vertical (b) components of the phase gradient of the clay loam sample. (c) and (d) are line profiles drawn across the* 270^{th} *pixel-row corresponding to the horizontal and the vertical components of the phase gradient, respectively. The horizontal lines drawn across (a) and (b) illustrates the position of the* 270^{th} *pixel-row. In (c) and (d), the left and right hand side vertical dotted lines corresponds to the position of the left and right hand side edges of the syringe, which holds the clay loam particulates. x, y, and z correspond to the horizontal, vertical, and the optical axis (see figure 3.2), respectively.*

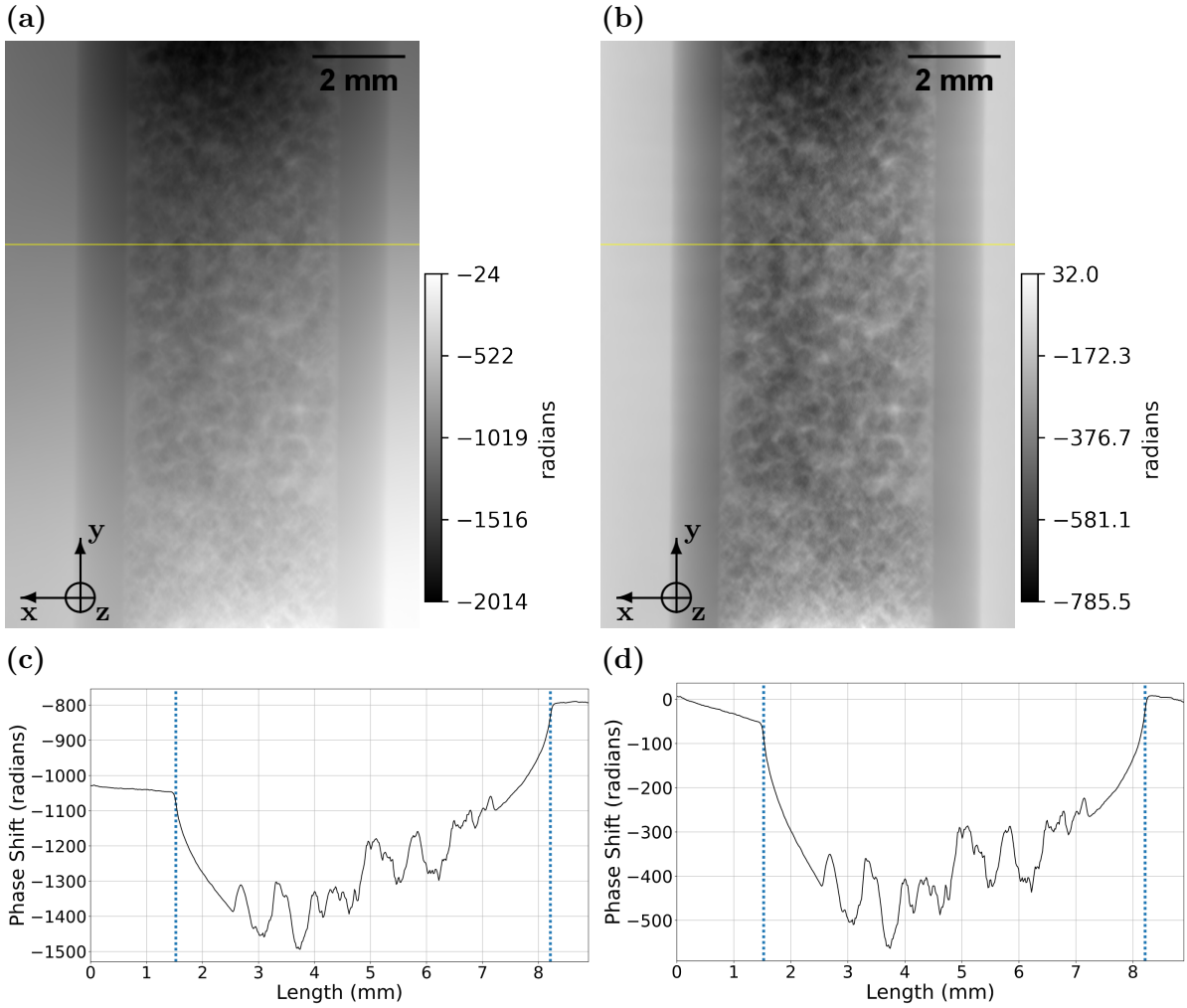

Figure 5.10: *(a) and (b) display the linear and background uncorrected and corrected phase images, respectively. (c) and (d) illustrate the line profiles drawn across the* 270^{th} *pixel-row of the linear and background uncorrected and corrected phase images, respectively. The position of the line profiles are shown by the horizontal lines on (a) and (b). In both (a) and (b), a large amount of low frequency noise can be observed. As seen from the line profile (c), the distribution of phase shift across the sample is heavily altered by the noise amplification and the phase shift in air on either side of the sample is far from zero. Although row-by-row background correction diminished some of the uniformity issues, the phase shift in the air immediately outside the left hand side of the sample is far from zero.*

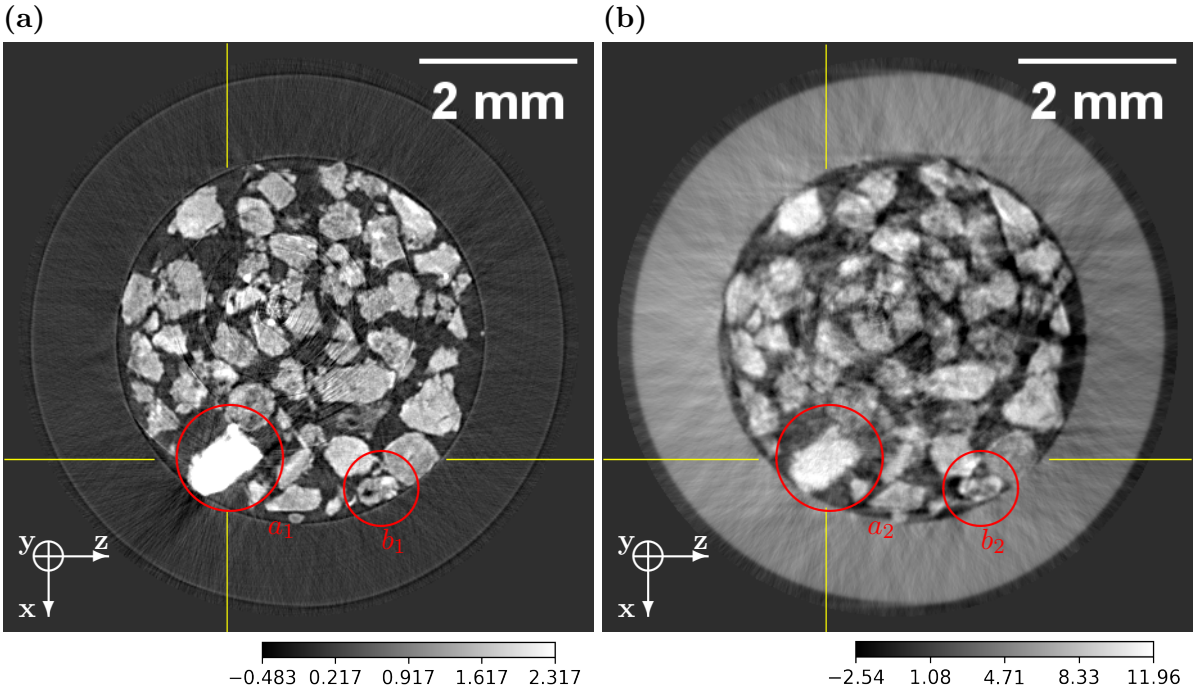

Figure 5.11: *A comparison between the* 270^{th} *reconstructed axial CT slices of (a) the* β *(*$\times 10^{-9}$*) map and (b) the* δ *(*$\times 10^{-7}$*) map of the clay loam sample. The horizontal and vertical lines on (a) and (b) corresponds to the locations of the coronal and the median planes depicted in figure 5.12. Some streak artefacts can be observed on the syringe in both the* β *map and the* δ *map. However, the syringe is more visible in the the* δ *map compared to the* β *map. In the* β *map, around the syringe edges, the propagation-based fringes are also clearly visible. The circles marked as* a_1 *and* a_2 *on (a) and (b), respectively, refer to a highly attenuating object. The mean of a circular ROI of the object depicted in* a_1 *gave a* β *value of* 8.4×10^{-9} *with a standard deviation of* 5.2×10^{-10}*, while for the same ROI inside the same object (*a_2*) on the* δ *map gave a* δ *value of* 1.1×10^{-6} *with a standard deviation of* 7.5×10^{-8}*. Furthermore, the circles marked as* b_1 *and* b_2 *on (a) and (b), respectively, display a particulate where, qualitatively, it is clear that the* β *map and the* δ *map reveal very different structural features of the object.*

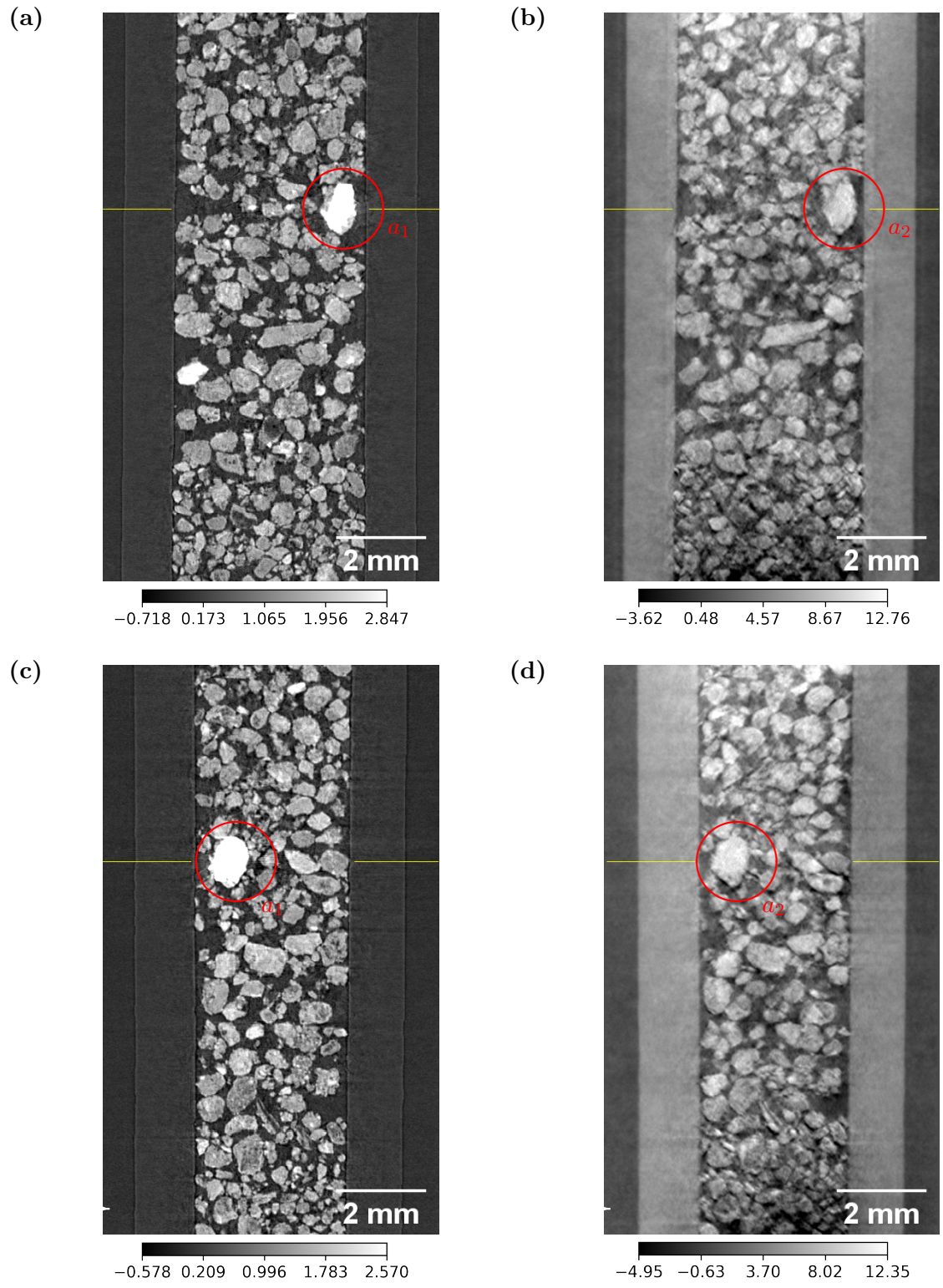

Figure 5.12: *(a) and (b) display the coronal planes of the β ($\times 10^{-9}$) and δ ($\times 10^{-7}$) maps of the clay loam sample, respectively. (c) and (d) show the median planes of the β and δ maps of the clay loam sample, respectively. The horizontal lines at the edges on all four images illustrate the position of the axial slices displayed in figure 5.11. The circled object defined as a_1 and a_2 in (a), (b), (c), and (d) refer to the same high attenuating object illustrated in figure 5.11 as a_1 and a_2. This was confirmed by measuring the mean β and δ values for an ROI inside this object from all four images.*

5.5 Discussion

For the three-material phantom, both the 261-point and the eight-point reconstruction methods, quantitatively and qualitatively produced similar results. In terms of β value estimations for Perspex, PTFE, and Aluminium, both reconstruction methods produced identical results (see table 5.1). It was estimated that the experimental β values for Perspex, PTFE, and Aluminium deviated from their theoretical β values by 7%, 5%, and 11%, respectively. Considering possible impurities in the sample and considering possibility that the theoretical estimation could vary between sources (Chalmers et al., 2021), these deviations are acceptable.

However, when comparing the estimated δ for Perspex, PTFE, and Aluminium, the eight-point reconstruction method produced slightly better results compared to the 261-point reconstruction method (see tables 5.2 and 5.3). Even though these two methods produced slightly different results, it was found that on average, experimental δ values from both methods for PTFE and Aluminium were 35.25% higher than their respective theoretical δ values and for Perspex it was 42% higher compared to its theoretical δ value on average. However, a reconstruction of Perspex, without other materials or horizontal edges present, reduced the overestimation of the experimental δ value from its theoretical value for Perspex to 36%. This suggested that the added deviation of Perspex was possibly a result of noise amplification during the 2D Fourier integration process.

In chapter 4 of this thesis, χ^2 analysis showed that the Pseudo-Voigt (PsV) model is the ideal candidate to estimate the sample rocking curve. Therefore, the 195^{th} pixel row was fitted with the PsV model on pixel-by-pixel basis and a single axial CT slice of a δ map was reconstructed to see if the 36% overestimation of δ values for Perspex, PTFE, and Aluminium can be reduced. The δ estimations from the PsV model fitting of the sample rocking curve gave similar results to the ones displayed in tables 5.2 and 5.3. This ruled out the possibility of using two different models, namely the PsV to estimate the intrinsic rocking curve and the Lorentzian model to estimate the sample rocking curve, is the point of origin of the discrepancy between the theoretical and experimental δ values. The use of the PsV model to estimate the sample rocking curves and reconstruct a single axial CT slice of the δ map took approximately two and half hours with the utilisation of python multiprocessing[2]. Therefore, considering the limited time allocated for this research, an extensive analysis of these results was not feasible. However, for reference, the reconstructed axial CT slice is displayed in the appendix (see figure B.5). Furthermore, Chalmers et al. (2021) reconstructed the δ values for Perspex, PTFE, and Aluminium using the same three-material phantom and the same experimental setup used in this thesis. However, in their reconstruction they only used two working points to reconstruct δ, while in this thesis used eight working points. In their study they reported an underestimation of the δ values for all three materials by approximately 45%. Therefore, in comparison, the 36% overestimation of all δ values in this study found to be marginally better.

Following the reconstruction of the three-material phantom, this chapter presented the reconstructions of the clay loam sample. Due to the lack of *"a priori'* knowledge regarding the clay loam sample, a quantitative analysis of reconstructed β and δ maps was not possible. However, qualitatively, the reconstruction process introduced in this thesis found to produce promising

[2]See section 3.7 for a description on python multiprocessing.

results despite the complex nature of the TLABI setup. The axial CT slices of the β and the δ maps displayed some streaking artefacts (e.g. see figure 5.11). These artefacts in the β map are likely due to the high attenuating properties of clay loam particulates. In the δ map these artefacts are most likely an outcome of the noise amplification during 2D Fourier integration process and the lack of uniformity across the phantom in the phase shift projections (see figure 5.10 (b) and (d)). Visual comparison between the β and δ maps in figures 5.11 and 5.12 show clear evidence that phase contrast imaging definitely provide complementary information regarding the sample. An example of this is the highly attenuating object (a_1 and a_2 in figures 5.11 and 5.12) with a δ value 131 times larger than its β value. In the β map this object shows up as a bright spot without displaying much of its internal structures, whilst in the δ map, its internal structures are clearly distinguishable.

All reconstructions discussed in this chapter utilised the GOA (see section 2.1.6). This approximation is a simple linear relationship, which only considers the scattering of the x-ray wavefield as it traverses through the object (see section 2.4.2). It does not consider factors such as the temporal coherence of the x-ray wavefield or the divergence of the x-ray wavefield (see figures 4.5 and 4.6). These factors, combined with the fact that TLABI is a highly sensitive experimental set-up, could explain the 36% overestimation of the experimental δ values from the theoretical δ values of the materials in the three-material phantom. Another point of origin for the overestimation of the experimental results could be the misalignment of the $\boldsymbol{g}'_{0,y}$ (e.g. see figure 5.2 (a)) and the $\boldsymbol{g}'_{\pi,y}$ projections (e.g. see figure 5.2 (b)) by approximately two pixels. This misalignment was recorded for both the three-material phantom images and the clay loam sample images. It is possible this pixel misalignments is originating from the asymmetrical distortion correction introduced in this thesis (see section 3.4). Although testing on synthetic images displayed an extremely high accuracy in correcting the FOT distortion, there is a considerable lack of understanding behind how well it behaves when used with an experimental dataset. Kitchen et al. (2010), using the Laue geometry without applying any tilt to the object successfully estimated with good agreement, the projected thickness of a cavity inside a Perspex block where one was empty and the other was filled with glass microspheres. In their reconstructions, they used IDL's `Warp_tri` function to correct the FOT asymmetrical distortion in their projection images. Therefore, one could rule out the asymmetrical distortion correction introduced in this thesis as a possible culprit for the overestimation of δ by redoing the reconstructions of the three-material phantom using the IDL's `Warp_tri` function to correct the asymmetrical distortion and comparing the results. The limited time available for this project restricted such further investigations into the asymmetrical distortion correction.

5.6 Conclusion

This chapter presented the reconstruction process of the δ and β maps for the three-material phantom and the clay loam sample. It investigated two reconstruction methods, namely the 261-point reconstruction and the eight-point reconstruction method using the three-material phantom. Both quantitative and qualitative analysis showed that both of these reconstruction methods performed nearly identically. Although the reconstructed δ maps overestimated the δ values of Perspex, PTFE, and aluminium by 36%, both reconstruction methods estimated the

β values of these three materials with a relatively high degree of accuracy. Furthermore, the clay loam sample reconstructions of the real (δ) and the imaginary (β) parts of the refractive index clearly illustrated that both of these parts provide complementary information regarding the sample. Overall, the reconstructions presented in this chapter clearly illustrate that the reconstruction methods and the algorithm, developed and introduced in this thesis, are both robust and efficient.

Chapter 6

Reconstruction of Ultra Small-Angle Scattering Information

As pointed out in section 2.4.2, for a quantitative reconstruction of the USAXS signal, the scatter curve must be deconvolved from the sample rocking curve (see equation (2.37)). Therefore, this chapter will investigate the process of deconvolving the scattering function from the sample rocking curve (see section 2.4.2) and the reconstruction of USAXS information. Specifically, this chapter will compare two deconvolution methods, namely, the Wiener deconvolution method and Richardson-Lucy (RL) iterative deconvolution method using simulations (section 6.1). Then using the clay loam sample rocking curves, a USAXS signal (scattering curve FWHM) image is produced utilising the RL deconvolution method. This deconvolved USAXS signal image will then be compared to the USAXS signal estimated by subtracting the intrinsic rocking curve width and the sample rocking curve width in quadrature (see section 6.2). This was done to understand the quantitative accuracy of the USAXS signal given by subtracting the intrinsic rocking curve width and the sample rocking curve width in quadrature. Furthermore, section 6.3 will present the reconstructed USAXS CT images for the three-material phantom and the clay loam sample. Finally, section 6.5 will discuss the results in detail and section 6.6 will provide a brief conclusion to this chapter.

6.1 Deconvolution Simulations

Since deconvolution is an ill-posed problem, it can be unstable, especially in the presence of noise. As illustrated by the rocking curves in figures 4.14 (c), (d) and 4.14 (d), the rocking curves corresponding to high scatter regions of a sample can be very unstable. Kitchen et al. (2010) reported that this instability can be mitigated by using Wiener deconvolution, given that one could estimate a stable regularization parameter λ. The Wiener deconvolution to estimate the scatter curve $S_{RC}(f_\theta)$ in Fourier space can be defined as (Gunturk and Li, 2012),

$$S_{RC}(f_\theta) = \frac{M_{RC}(f_\theta) I_{RC}(f_\theta)^*}{I_{RC}(f_\theta)^2 + \lambda}, \tag{6.1}$$

where $M_{RC}(f_\theta)$ and $I_{RC}(f_\theta)$ are the Fourier transforms of the sample rocking curve and the intrinsic rocking curve, respectively. The regularization parameter λ represents the noise-to-

signal power ratio.

The Wiener deconvolution was tested by simulating both the intrinsic rocking curve and the sample rocking curve as Gaussian functions. For simplicity, let us call this simulation Gaussian/Gaussian simulation. The simulation parameters used for this simulation are tabulated in table 6.1. Figure 6.1 displays the values of 38 sample rocking curve widths plotted against the FWHM of the deconvolved scatter function for seven regularization parameter values. The FWHM of each deconvolved scatter function was estimated by fitting a Gaussian function to the deconvolved scatter data. Here, the deconvolved FWHM using the Wiener deconvolution is compared to the theoretical scatter curve FWHM ω_{scatt} estimated through subtracting the intrinsic rocking curve width ω_I^2 and the sample rocking curve width ω_S^2 in quadrature, which is given by,

$$\omega_{scatt} = \sqrt{\omega_S^2 - \omega_I^2}, \tag{6.2}$$

For convenience let us call equation (6.2) the difference in quadrature (DQ) approximation. This theoretical estimation is strictly true for Gaussian distributions (Kitchen et al., 2020). From looking at figure 6.1, it is clear that as the width of the sample rocking curve increases, one must increase the regularization parameter to accommodate the increase in width for a stable deconvolution. Here, the optimal regularization value to deconvolve all 38 sample rocking curves with widths ranging from 10 µrad to 200 µrad in steps of five was found to be 1×10^2. Furthermore, for all simulations the ground truth was plotted for reference. The ground truth is simply a straight line with gradient 1 and y-intercept of 0, namely y=x. For Gaussian distributions, whose convolved widths add in quadrature, the quadrature subtraction (DQ approximation) should also have a y=x curve. This can be seen in figure 6.1, except for values closer to zero where the DQ approximation deviates from ground zero.

Since, in this thesis, the intrinsic rocking curves and the sample rocking curves will be estimated using Pseudo-Voigt (PsV) models and Lorentzian models, respectively, simulations were run using these two models. Let us refer to this simulation as the PsV/Lorentzian simulation. Figure 6.2 displays the PsV/Lorentzian simulation results and the simulation parameters used for this simulation are displayed in table 6.2. The FWHM of each deconvolved scatter function in this simulation was estimated by fitting a Lorentzian function to the deconvolved scatter data. Here, the intrinsic rocking curve parameters were kept the same for all deconvolution calculations.

From the simulation results displayed in figure 6.2, it is clear that even for well behaved simulated data, a large regularization value is required to stabilise deconvolution using Weiner deconvolution. From figure 6.2 (a), it is evident that at lower regularization parameters, the deconvolution can be highly unstable. However, similar to the Gaussian/Gaussian simulation illustrated in figure 6.1, as the regularization parameter increases, the deconvolution starts to stabilise. For regularization parameters greater than 1×10^3, deconvolution seems to be stable for sample rocking curves with widths up to 200 µrad (see figure 6.2). However, as the regularization parameter increases, the FWHM of the deconvolved scatter function seems to increase. Also, from figures 4.13 and 4.14, it is clear that the sample rocking curve parameters changes rapidly from pixel to pixel due to the lack of photon count, the USAXS or a combination

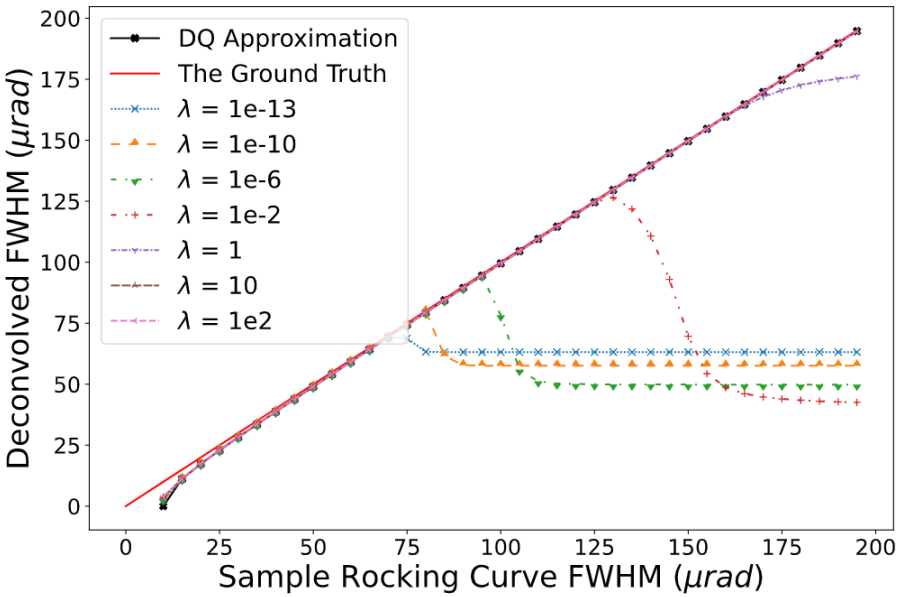

Figure 6.1: *Wiener deconvolution results of the Gaussian/Gaussian simulation. This plot displays a comparison between the deconvolved scatter curve FWHM and the theoretical scatter curve FWHM (DQ approximation) for 38 sample rocking curves with their widths ranging from 10 μrad to 200 μrad in steps of 5 μrad. It also compares the change in behaviour of Wiener deconvolution as the regularization parameter increases from* 1×10^{-13} *to* 1×10^{2}*. Here, both the intrinsic and sample rocking curve were simulated as Gaussian models using the parameters displayed in table 6.1. The ground truth, x=y, line is plotted for reference.*

of both. This suggests that the use of a single regularization parameter, which is assuming that all rocking curves behave in a relatively similar manner, to deconvolve all the scatter functions ($\sim 1 \times 10^6$ per image) could result in an undesirable outcome. Furthermore, interestingly the DQ approximation in figure 6.2 (a) and (b) only slightly underestimates the ground truth line.

The Richardson-Lucy (RL) iterative deconvolution is presented here as a better alternative for Wiener deconvolution. The RL deconvolution is a multiplicative algorithm, which is defined as (Gunturk and Li, 2012),

$$f^{(i+1)}(\theta) = f^{(i)}(\theta)\left[h^*(\theta) \otimes \frac{g(\theta)}{h(\theta) \otimes f^{(i)}(\theta)}\right], \tag{6.3}$$

where $f^{(i)}(\theta)$ is the initial guess of the sample rocking curve, $h(\theta)$ is the intrinsic rocking curve, $g(\theta)$ is the sample rocking curve, and $f^{(i+1)}(\theta)$ is the estimated scatter function after i iterations.

Since RL is an iterative process, noise amplification can be restricted by using a suitable stopping criterion. The stopping criteria could be implemented by restricting the number of iterations to a finite number, or it can be based on the difference between two estimations, $f^{(i)}$ and $f^{(i+1)}$. For example,

$$stop = \frac{\sum_\theta f^{(i+1)}(\theta) - f^{(i)}(\theta)}{\sum_\theta f^{(i)}(\theta)}. \tag{6.4}$$

Using the same parameters for the sample and intrinsic rocking curves as for the Wiener deconvolution (see tables 6.1 and 6.2), simulations were run to test the accuracy of the RL

Model Parameters	Sample Rocking Curve	Intrinsic Rocking Curve
Height	158	1750
Centre	0	0
Width	10 to 200 in steps of 5	10

Table 6.1: *Rocking curve parameters used for Gaussian/Gaussian deconvolution simulations. The parameters of the intrinsic rocking curve were kept constant for all deconvolution estimations.*

Model Parameters	Sample Rocking Curve	Intrinsic Rocking Curve
Height	158	1718
Centre	0	0
Width	21 to 200 in steps of 5	21
α	NA[a]	0.75

Table 6.2: *Rocking curve parameters used for PsV/Lorentzian deconvolution simulations. The parameters of the intrinsic rocking curve were kept constant for all deconvolution estimations. Here, α corresponds to the fraction in the PsV function (see equation 4.1). Since the sample rocking curve is simulated as a Lorentzian function, α do not apply.*

[a]Not Applicable

deconvolution method. Figures 6.3 (a) and (b) display the RL Gaussian/Gaussian simulation and its residuals, respectively. Figure 6.4 (a) displays the RL PsV/Lorentzian simulation. Here, for both simulations, the stopping criteria, defined in equation (6.4), was implemented with a tolerance of $\pm 5 \times 10^{-6}$. This tolerance defines the upper and the lower limit of the stopping criteria. From the residuals in figure 6.3 (b), it seems that as the deconvolved FHWM reaches ground truth as the sample rocking curve FHWM increases. When looking at figure 6.3 (a), the DQ approximation seem to behave identically to the RL deconvolution width. Here, for smaller values the DQ approximation tend to deviate from the ground truth.

Furthermore, figure 6.4 (a) displays the results of the RL PsV/Lorentzian simulations. From figure 6.4 (a), it is evident that the RL deconvolution method is much more stable and reliable than the Wiener deconvolution (see figure 6.2). This is especially true as the widths of the sample rocking curves increase. This reliability is an important factor because the sample rocking curve behaviour could change drastically from one pixel to another (see figures 4.13 and 4.14). However, it must be stressed that this stability and reliability is highly dependent upon choosing the correct tolerance levels for the stopping criteria (see equation (6.4)). For these simulations, the stopping criteria was estimated through trial and error. Furthermore, figure 6.4 (b) compares the results of the PsV/Lorentzian simulations run using the Wiener deconvolution method with a regularization parameter 1×10^3 and the RL deconvolution method with a stopping criteria tolerance of $\pm 5 \times 10^{-6}$. Interestingly, the DQ approximation results are closely related to the

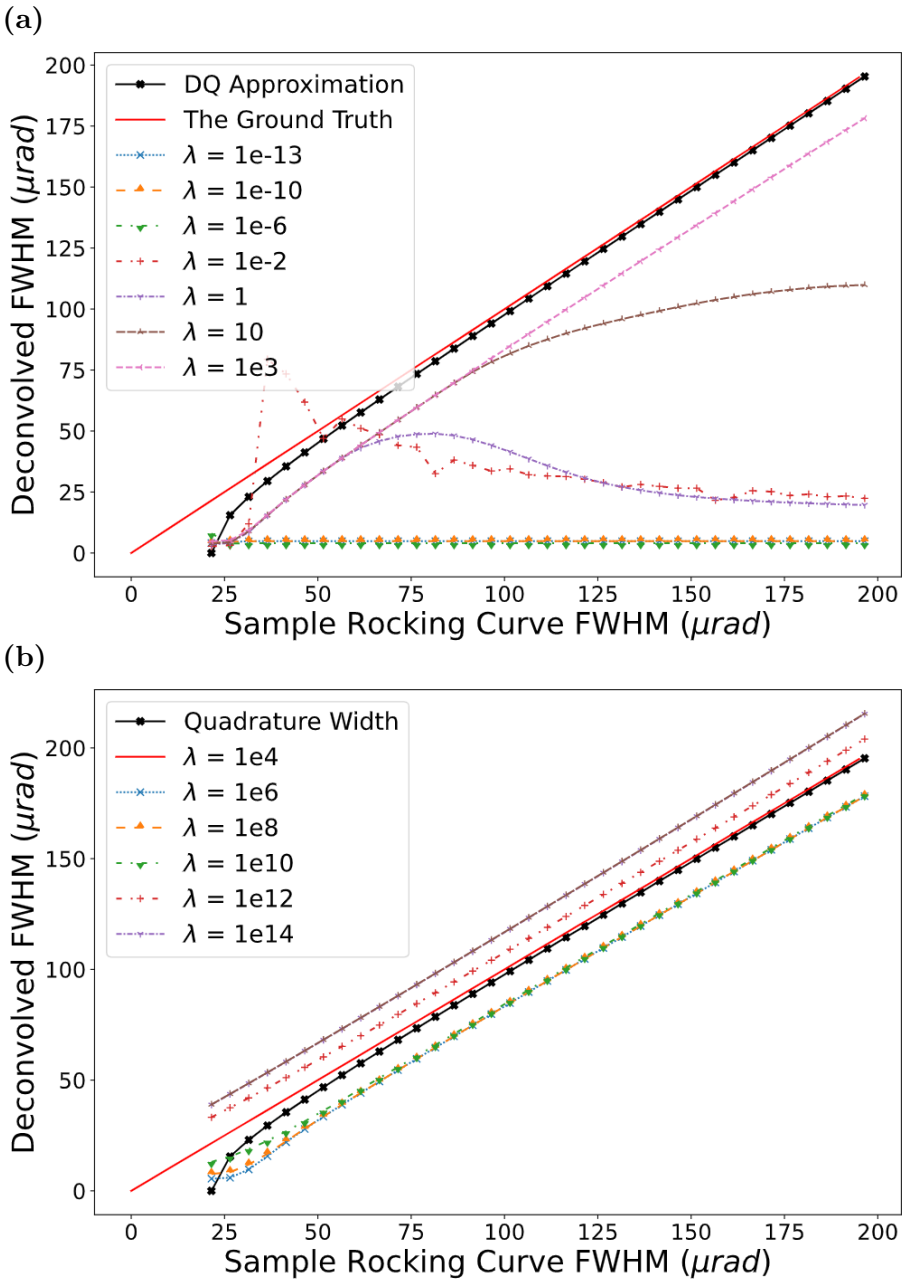

Figure 6.2: *Wiener deconvolution results of the PsV/Lorentzian simulation. (a) and (b) display the change in behaviour of Wiener deconvolution as the regularization parameter increase from* 1×10^{-13} *to* 1×10^{3} *and* 1×10^{4} *to* 1×10^{14}*, respectively. In both (a) and (b) the deconvolution was done for 36 sample rocking curves with their widths ranging from* $21\,\mu rad$ *to* $200\,\mu rad$ *in steps of* $5\,\mu rad$*. In both (a) and (b), the FWHMs estimated using the DQ approximation are plotting for comparison, and the ground truth, x=y, lines are also plotted as a reference. Here, the intrinsic and sample rocking curve were simulated using a PsV model and a Lorentzian model, respectively, and their parameters are displayed in table 6.2.*

ground truths than the RL deconvolution results (see figure 6.4 (a)). This suggests that in spite of these being PsV/Lorentzian simulations, the DQ approximation is actually more accurate at estimating the scatter function FWHM than RL deconvolution.

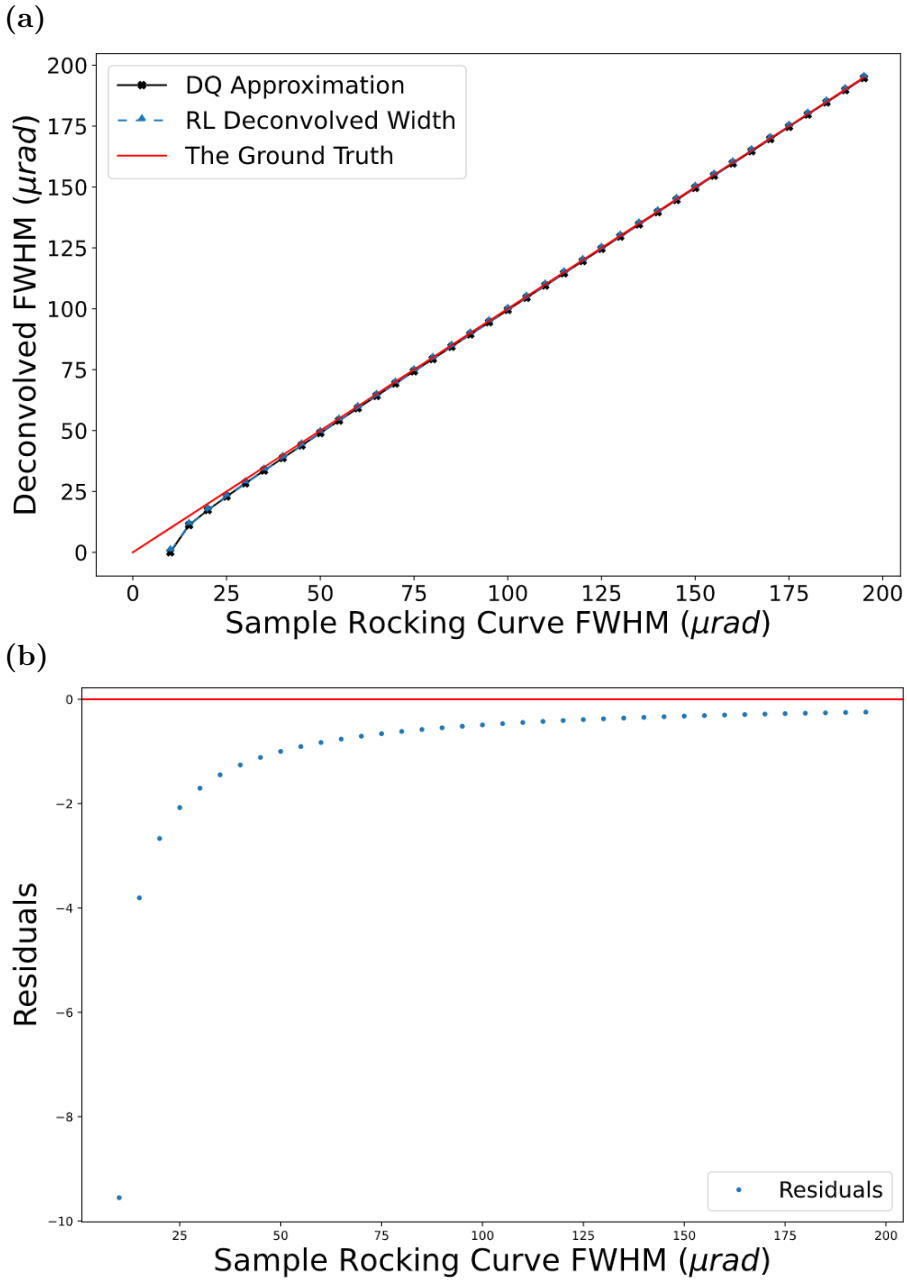

Figure 6.3: *Richardson-Lucy deconvolution results of the Gaussian/Gaussian simulation. (a) displays a comparison between the deconvolved scatter curve FWHM and the theoretical scatter curve FWHM (DQ approximation) for 38 sample rocking curves with their widths ranging from 10 μrad to 200 μrad in steps of 5 μrad. Here, the ground truth, x=y, line is also plotted as a reference. (b) displays the residuals between the ground truths and the deconvolved FWHM. Here both the intrinsic rocking curve and the sample rocking curve were simulated as Gaussian models using the parameters displayed in table 6.1.*

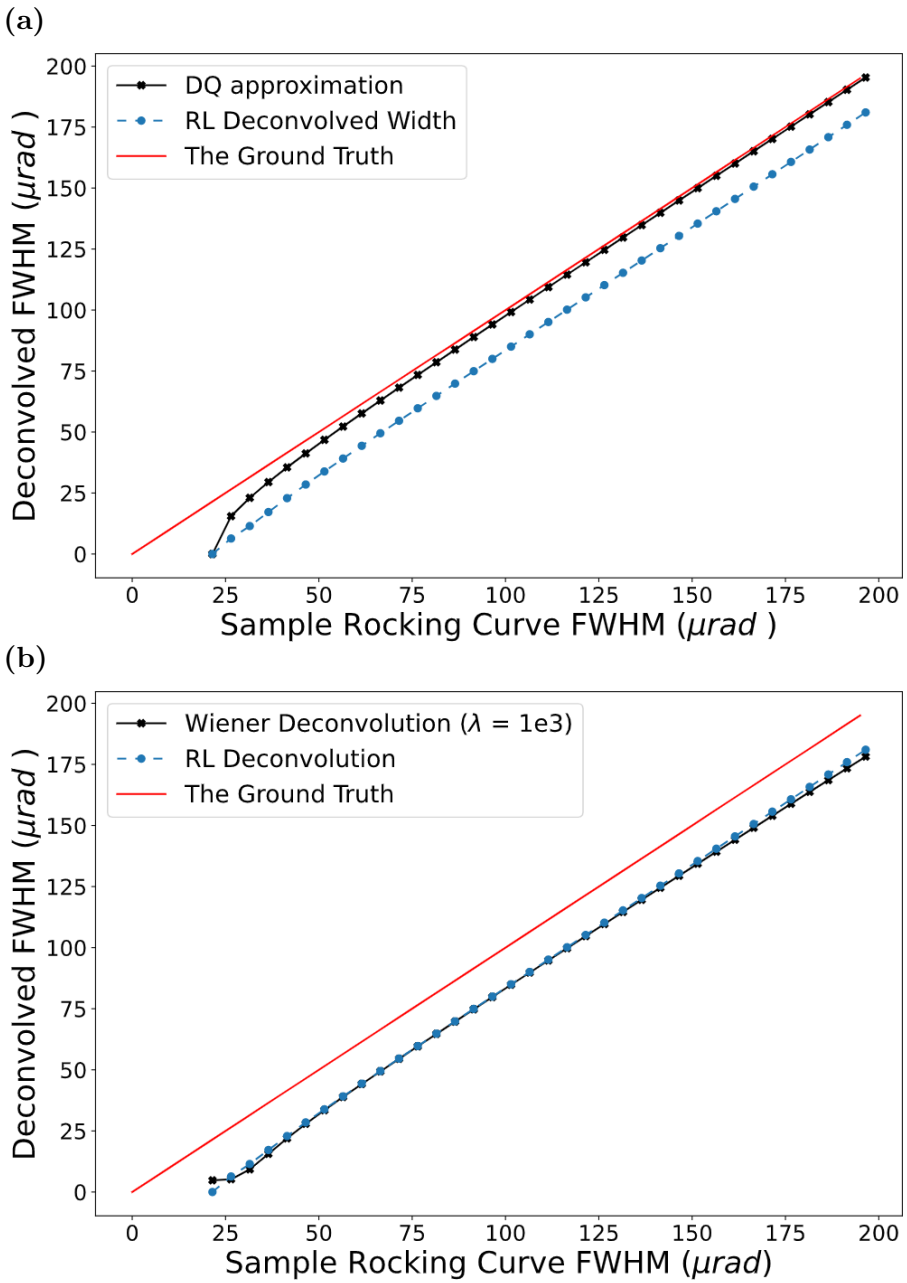

Figure 6.4: *Richardson-Lucy deconvolution results of the PsV/Lorentzian simulation. (a) displays a comparison between the deconvolved scatter curve FWHM and the theoretical scatter curve FWHM for 36 sample rocking curves with their widths ranging from 21 μrad to 200 μrad in steps of 5 μrad. In (a), the FWHMs of the scatter function estimated using DQ approximation are also plotted for comparison. (b) displays a comparison between the outputs of Wiener deconvolution method and the RL deconvolution method for the same sample rocking curves. Here, a regularization parameter used for Wiener deconvolution is* 1×10^3*. In both (a) and (b), the ground truth, x=y, line is also plotted as a reference.*

6.2 Comparing RL Deconvolution and DQ Approximation Using the Clay Loam Sample

Although deconvolution is the ideal method for extracting USAXS signal, the simulations in section 6.1 indicates that DQ approximation is more accurate at estimating the USAXS signal. Therefore, this was tested by comparing the DQ approximation and RL deconvolution using the clay loam sample. First, using the RL deconvolution method on a pixel-by-pixel basis, deconvolution was carried out for all the sample rocking curves in the 15^{th} clay loam sample tomographic projection. Then the FWHM of each scatter curve (USAXS signal) was estimated by fitting a Lorentzian function to the deconvolved scatter data. This process approximately took two and half hours to produce the USAXS signal image. Figure 6.5 (a) displays the extracted USAXS signal image for the 15^{th} clay loam sample tomographic projection. Here, to increase stability, the fitted sample rocking curve (using the Lorentzian model) and intrinsic rocking curve (using the PsV model) information for each pixel were used instead of the experimental sample rocking curves. Then, the DQ USAXS image was estimated by subtracting the intrinsic FWHM image (e.g. see figure 4.4 (c)) and the 15^{th} sample FWHM image corresponding to 0.15° tomographic angular position (e.g. see figure 4.17 (c)) in quadrature. The resulting DQ USAXS signal image is depicted in figure 6.5 (b).

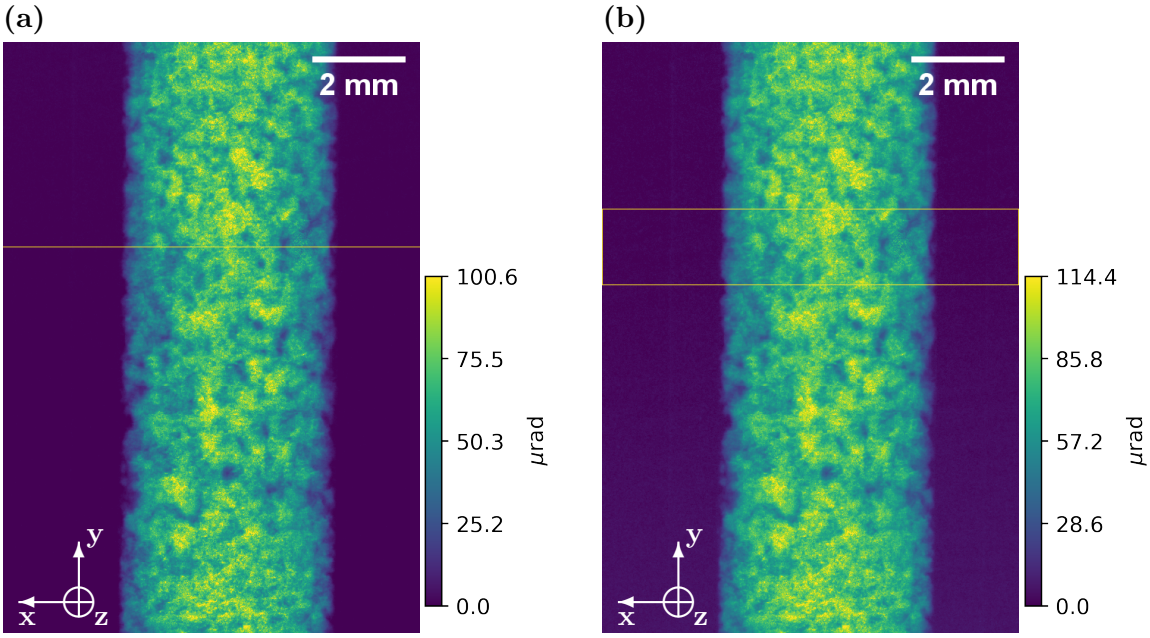

Figure 6.5: *Extracted USAXS images using the RL deconvolution method (a) and the DQ approximation method (b). Both (a) and (b) here are coloured for better visualisation of the USAXS signal intensities. Here, in (a), the horizontal line indicates the position of the line profiles illustrated in figure 6.6 (a). The pixel rows enclosed by the two horizontal lines in (b) indicate the pixel rows used to draw the averaged line profile depicted in figure 6.6 (b).*

When comparing the outputs by deconvolution (see figure 6.5 (a)) and the DQ approximation (see figure 6.5 (b)), it can be clearly seen that the DQ USAXS image is slightly brighter than the deconvolved USAXS image. This essentially means that the RL deconvolution slightly lower than the USAXS signal given by DQ approximation. This agrees with what is seen in

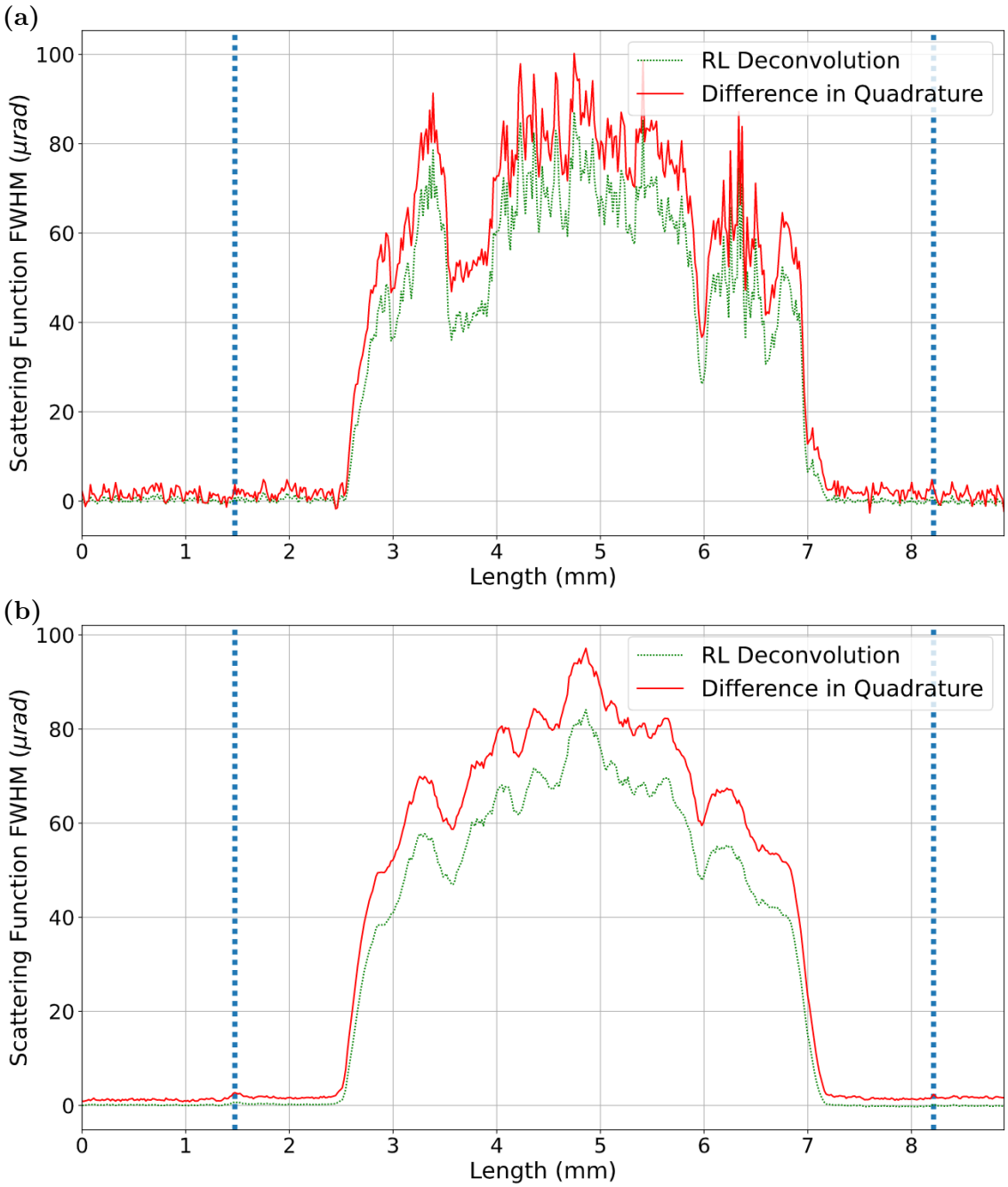

Figure 6.6: *(a) displays a comparison between the line profiles drawn across the same pixel row of the deconvolved USAXS image (see figure 6.5 (a)) and the DQ USAXS image (see figure 6.5 (b)) . The location of this line profile in the image is displayed by the horizontal line in figure 6.5 (a). (b) displays a comparison between averaged line profiles drawn using the same ROI on the deconvolved USAXS image and the DQ USAXS image. The position of the ROI is defined by the two horizontal lines depicted in figure 6.5 (b). In both (a) and (b), the vertical dashed lines indicate the position of the left and right hand side edges of the syringe. Furthermore, the USAXS signal in the air estimated by the RL deconvolution method is observed to be much closer to zero than the estimations by the DQ approximation method.*

the PsV/Lorentzian simulations depicted in figure 6.4 (a). The line profiles in figure 6.6 clearly illustrate this to be true. Although the overall USAXS signal is lower in the deconvolved USAXS

image, the peaks and troughs given by the deconvolved USAXS image line profiles seem to align well with the peaks and troughs given by the line profiles at the same position on the DQ USAXS image. Therefore, both the simulations and the experimental data estimations suggest that DQ approximation is the ideal method for USAXS information extraction (see section 6.3).

6.3 USAXS Image Reconstruction Results

This section presents the results of the USAXS image reconstruction for the three-material phantom and the clay loam sample. Here, all the reconstructions were done using the DQ approximation method.

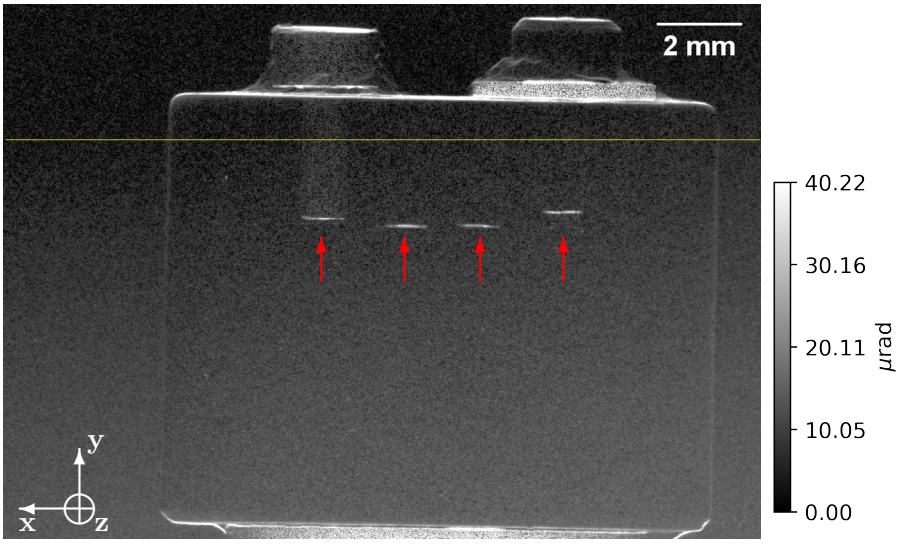

Figure 6.7: *140^{th} USAXS projection image of the three-material phantom. This projection corresponds to the tomographic angular position of* $14°$*. It was reconstructed by taking the difference in quadrature between the intrinsic FWHM image and the* 140^{th} *sample FWHM image of the three-material phantom. The horizontal line depicts the position of the axial CT images displayed in figure 6.8 (a) and (b). The four horizontal lines indicated by the arrows point to the bottom edges of the four holes, which contain the materials. The left and the right-hand-side holes contain the Aluminium pin and the PTFE pin, respectively. The two holes in the middle are the empty holes containing air. Here, only the Aluminium pin is visible and the horizontal edges of the phantom is more visible compared to the vertical edges.*

For each sample, namely the three-material phantom and the clay loam sample, 3600 USAXS projection images were extracted. These projections essentially covered a 360° tomographic angular range. When looking at the three-material phantom USAXS projections, the Aluminium pin found to be clearly visible indicating possible microstructures inside the Aluminium pin (see figure 6.7). This was further substantiated by the axial and coronal CT reconstructions depicted in figures 6.8 and 6.9.

In typical attenuation CT reconstructions, the sinogram repeats itself after 180°, essentially providing the same set of information, except the projections will be flipped. Therefore, typically in attenuation images, only the tomographic projections covering the first 180° is enough for a CT reconstruction. However, when comparing the reconstructions in figures 6.8 and 6.9, it is

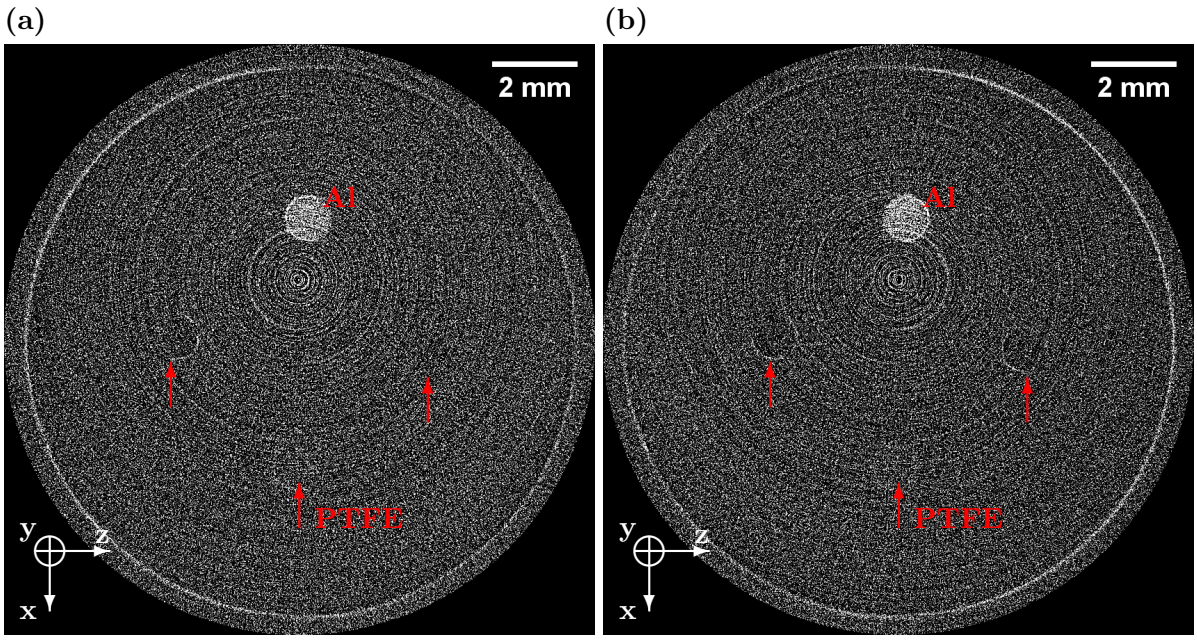

Figure 6.8: *Axial CT reconstructions of USAXS information produced by the three-material phantom. Axial CT slice (a) was reconstructed using the 1800 tomographic projections from* $0°$ *to* $180°$ *while (b) was reconstructed using the 1800 tomographic projections from* $180°$ *to* $360°$*. On both (a) and (b), only the Aluminium pin can be clearly observed. Red arrows on (a) and (b) point to the positions of the PTFE pin and the empty holes containing air. On (a), the edges of the left hand side empty hole is mildly observable, while on (b), the edges of both the left and the right hand side empty holes are mildly visible. Furthermore, on (a), the left edge of the phantom is brighter compared to the right edge while on (b), it is the opposite.*

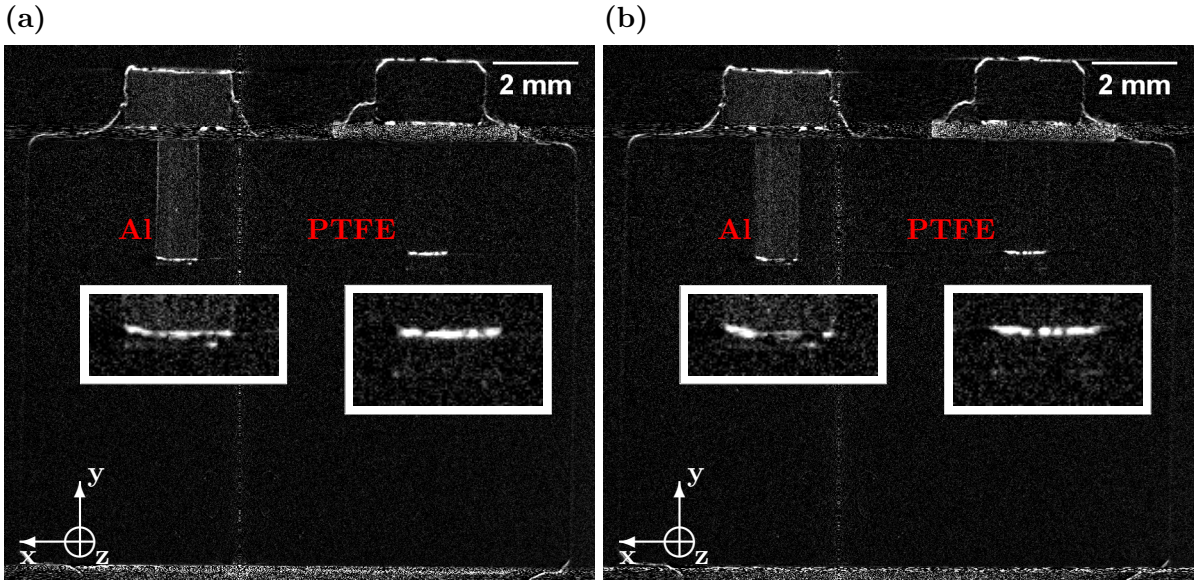

Figure 6.9: *(a) and (b) display the coronal CT slices of the three-material phantom, which were reconstructed using the 1800 tomographic projections from* $0°$ *to* $180°$ *and the 1800 tomographic projections from* $180°$ *to* $360°$*, respectively. When comparing the USAXS signals from the bottom edge of the Aluminium pin in (a) and (b), it is clear that the registered signal on the* $0°$ *to* $180°$ *CT reconstruction differ from the registered signal on the* $180°$ *to* $360°$ *CT reconstruction. This discrepancy can also be observed on the bottom edge of the PTFE pin. Furthermore, in both (a) and (b), the Aluminium pin is clearly visible while the PTFE pin is only faintly observable.*

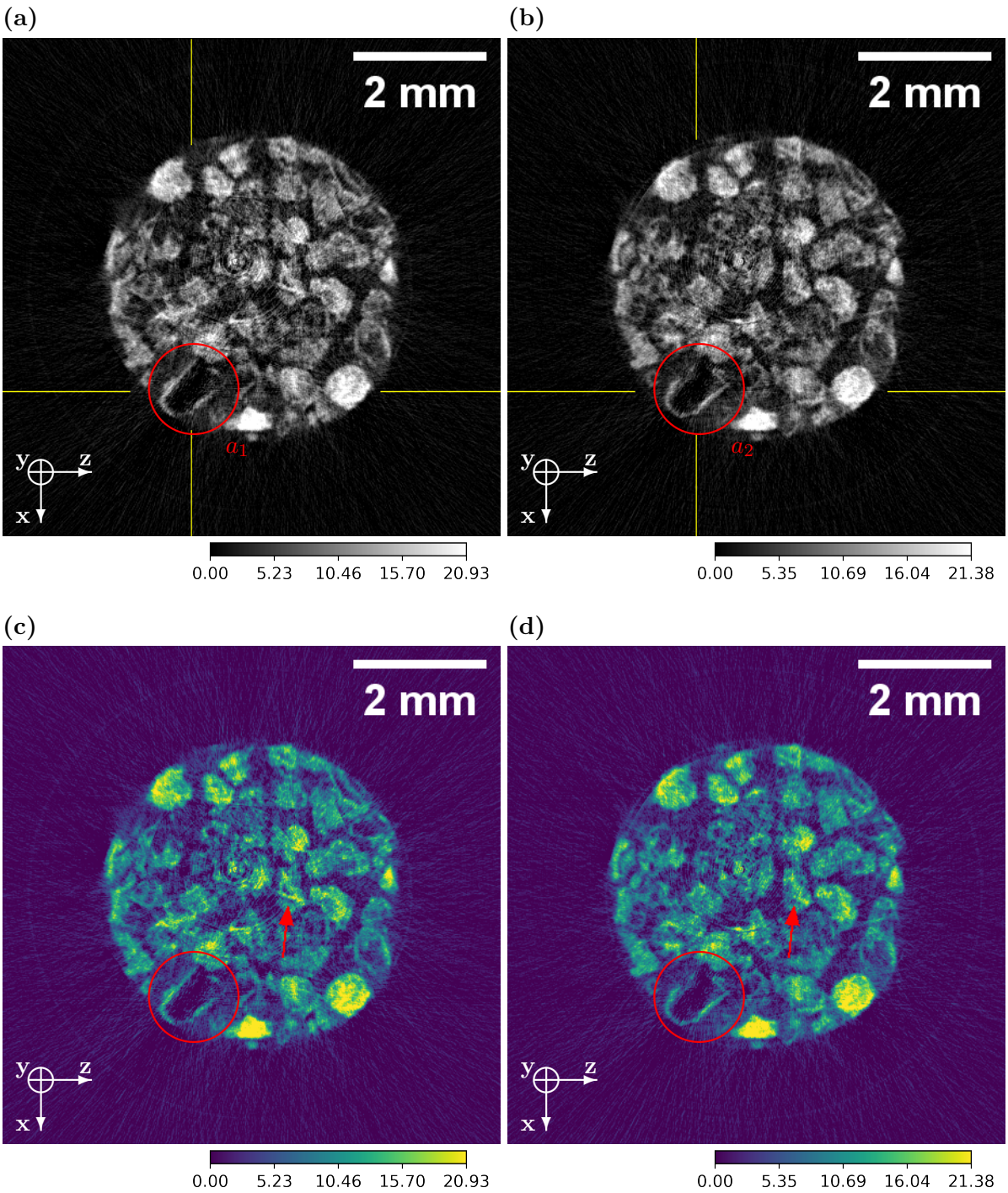

Figure 6.10: *A comparison between the* 270^{th} *reconstructed axial CT slices of (a) the* $0°$ *to* $180°$ *USAXS reconstruction* ($\times 10^{-8}$) *and (b) the* $180°$ *to* $360°$ *USAXS reconstruction* ($\times 10^{-8}$) *of the clay loam sample. The horizontal and vertical lines on (a) and (b) corresponds to the locations of the coronal and the median planes depicted in figures 6.11 and 6.13, respectively. (c) and (d) represents the coloured counterparts of (a) and (b), respectively. The edges of the object indicated by the red circle clearly show that (a) and (b) do not display the same information. Furthermore, the object pointed out by the arrows in (c) and (d) show small structural differences between the* $0°$ *to* $180°$ *and the* $180°$ *to* $360°$ *USAXS reconstructions.*

evident that USAXS information produced by the TLABI set up do not repeat after the 180° angular position, except it produces a slightly different set of information regarding the same objects.

Due to larger number of interfaces with air, unlike the three-material phantom, a large amount of USAXS signals can be observed in the clay loam sample USAXS projection images (see figure 6.5 (b)). It is worth noting that visually, the vertical syringe edges are not observable. However, the averaged line profile in figure 6.6 (b), display very small bumps indicating a very small amount of scattering by the vertical edges of the syringe edges. These vertical edges most likely produce a strong USAXS signal. However, this is a directional broadening in the horizontal direction. Because the analyser crystal used in this body of work is less sensitive to this horizontal direction, the USAXS signal produced by the vertical edges are not properly registered. In the CT reconstructions depicted in figures 6.10 and 6.11, similar to the three-material phantom CT reconstructions, slight differences between the 0° to 180° CT reconstruction and the 180° to 360° reconstruction can be observed. A hypothesis for the origins of these discrepancies will be discussed in section 6.5.

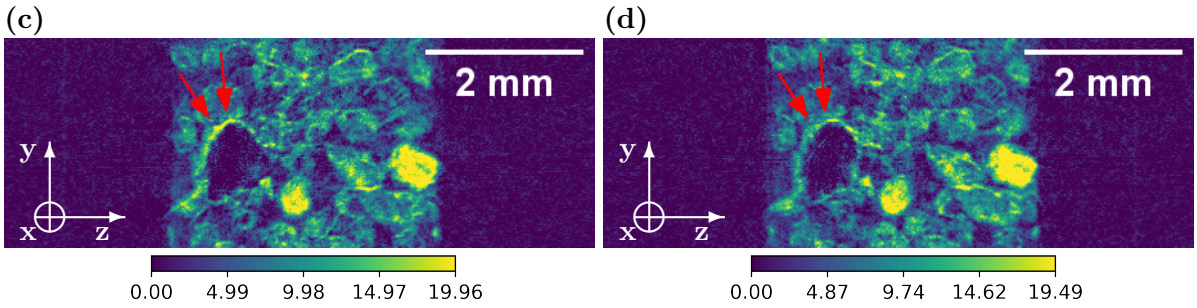

Figure 6.11: *(a) and (b) display the median CT slices of the* 0° *to* 180° *USAXS reconstruction* ($\times 10^{-8}$) *and the* 180° *to* 360° *USAXS reconstruction* ($\times 10^{-8}$) *of the clay loam sample, respectively. Colours were applied for better contrast between small structures. The arrows point to the same structure indicated by a circle in figure 6.10. The portrayal of the edges of this object is clearly different between (a) and (b).*

6.4 Comparing USAXS CT Reconstructions with Attenuation and Phase CT Reconstructions

When looking at the object identified by the arrows in figure 6.12, while the β map and the δ map provides very little information regarding the internal structures of the object, the USAXS reconstruction seems to highlight minute internal structures within the object. Furthermore, the object indicated in figure 6.13 (a), (b), and (c), the β map essentially display a very bright spot, while the δ map seems to provide some contrast between small structural changes within the object. Although the USAXS reconstruction display no information regarding the centre of this object due to its high attenuation properties, the boundaries are clearly illustrated. Moreover, when comparing the object pointed out in figure 6.13 (d), (e), and (f), the USAXS reconstruction display a considerable amount of internal structures, which cannot be seen or identified using the β or the δ maps.

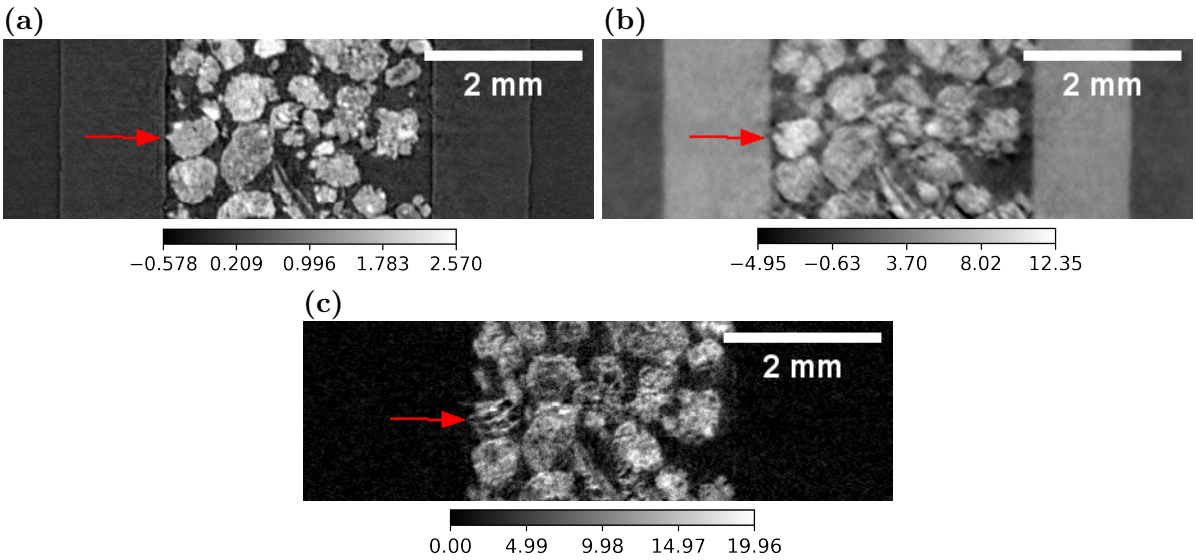

Figure 6.12: *(a), (b), and (c) display the median CT slices of the β map ($\times 10^{-10}$), δ map ($\times 10^{-7}$), and the USAXS reconstruction ($\times 10^{-8}$) of the clay loam sample. For an accurate comparison, it was made certain that the position of the median CT slices were identical for the β map, δ map, and the USAXS reconstruction. The position of these CT slices on the clay loam sample is illustrated by the horizontal lines in figure 6.10 (a). The arrows points to the same object for comparison.*

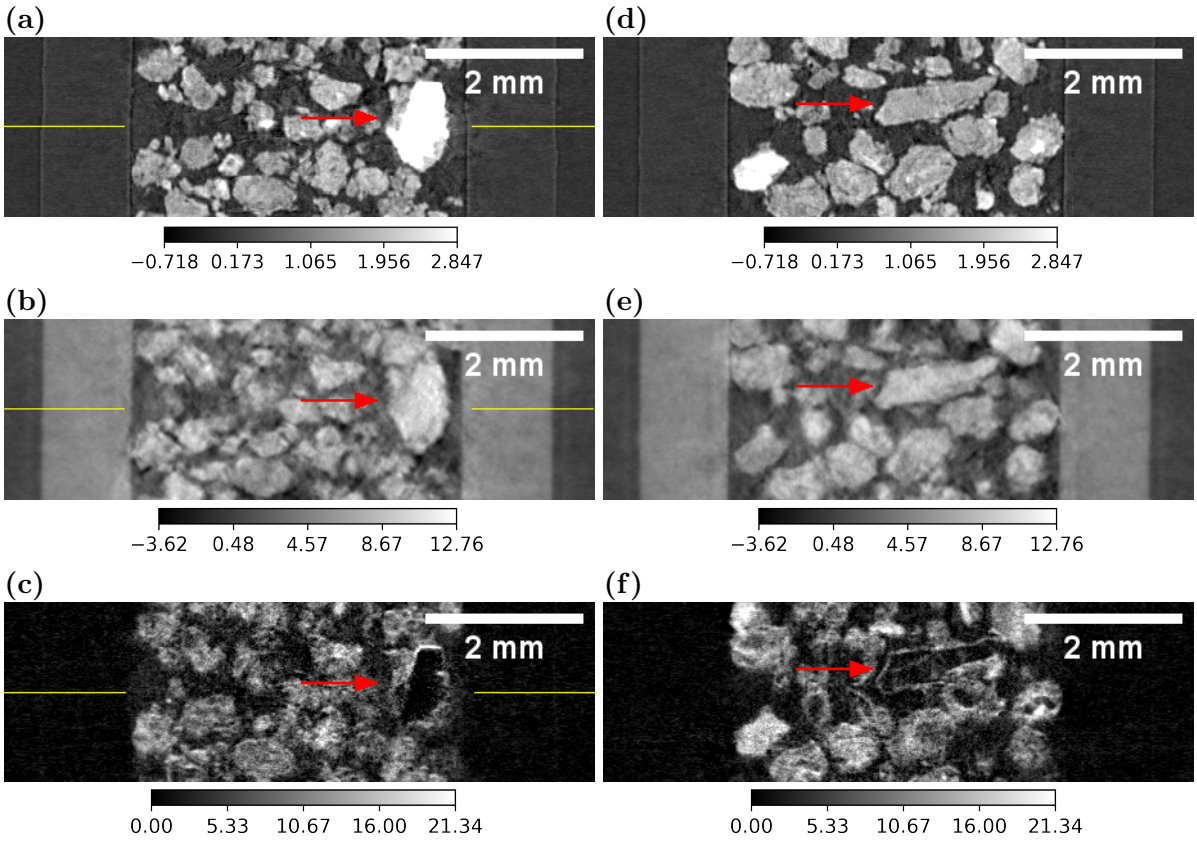

Figure 6.13: *A comparison between coronal CT slices of the β map ($\times 10^{-10}$), δ map ($\times 10^{-7}$), and the USAXS reconstruction ($\times 10^{-8}$) of the clay loam sample. Here, (a), (b), and (c) corresponds to the β map, δ map, and the USAXS reconstruction of the same highly attenuating object (red arrow), respectively. The horizontal lines correspond to the 270^{th} pixel row (see figures 5.11 and 6.10). Furthermore, (d), (e), and (f) compare the representation of another object (red arrows) by the β map, δ map, and the USAXS reconstruction, respectively.*

6.5 Discussion

Both the Weiner deconvolution and the RL deconvolution are capable of stabilising the deconvolution process. Although, in comparison, the RL deconvolution is considerably more stable than the Weiner deconvolution, since RL deconvolution is an iterative process it can be considerably slower. However, the Weiner deconvolution is a non-iterative process. Therefore, if one could find a process to accurately estimate a stable regularization parameter for all the rocking curves in a given image, it has the potential to deconvolve large number of rocking curves both stably and with considerably less computation time (see figure 6.4 (b)). Another option would be to decrease computation time for the RL deconvolution method by utilising a GPU in addition to a CPU. While CPUs are a general purpose processing unit, GPUs are purpose built processing units, which are capable of processing multiple sets of data simultaneously.

Regardless of the mathematical models employed to estimate the rocking curve, a large portion of the literature on the reconstruction of USAXS information for ABI found to employ the DQ approximation. (Suhonen et al., 2007; Kitchen et al., 2020). Therefore, the accuracy of using DQ approximation with functions other than a Gaussian distribution was tested through simulating the sample rocking curve with a Lorentzian model and the intrinsic rocking curve with a PsV model (see figure 6.4). When comparing the simulations in figure 6.4 (a), it was found that the DQ approximation results are actually much closer to the ground truths than the deconvolution results. This indicates that the DQ approximation is more accurate at estimating the USAXS signal. This provided significant confidence to use DQ approximation for all USAXS information reconstructions presented in this thesis.

When considering the reconstructions of the USAXS signal for the three-material phantom, since it can be considered as a quasi-homogeneous sample, the majority of the USAXS signals were observed at the edges of the sample. The horizontal edges found to produce a considerably larger signal compared to the vertical edges. The large USAXS signal registered at the horizontal edges of the sample is likely a directional broadening in the vertical direction. Since the analyser crystal used in this project is highly sensitive to the directional broadening of the USAXS fan in vertical direction, a larger USAXS signal is registered at the horizontal edges of the phantom (see figures 6.7 and 6.9). Furthermore, when considering the clay loam sample, reconstructions of similar edge effects were found especially around highly attenuating materials (e.g. see figure 6.11).

Typically, the USAXS fans produced by spatially-unresolved microstructures are modelled to be rotationally-symmetric (e.g. see Khelashvili et al. (2006)). The tilted experimental setup explored in this project allowed measurement of the FWHM of USAXS fans in different directions. Even though the tilt angle was very small (8°), when comparing the 0° to 180° CT reconstructions and the 180° to 360° reconstructions of the USAXS information in figures 6.8, 6.9, 6.10, and 6.11, it was clearly observed that the FWHM of the USAXS fans were actually different. This supports the hypothesis that the USAXS fan has an elliptical shape. The modelling of the USAXS fan as elliptical in shape is typically referred to as the directional dark-field imaging. Although no literature was found for directional dark-field imaging using ABI, directional dark-field imaging is a well-developed imaging modality in grating-based phase contrast imaging (e.g. see Jensen et al. (2010a) and Jensen et al. (2010b)).

As pointed out in section 2.5, the theoretical and the experimental basis for the use of CT reconstruction for the USAXS information was developed (Khelashvili et al., 2006), with the assumption that the scattering media is homogeneous in shape and, therefore, the USAXS fan is radially symmetric. Therefore, it is worth noting that the quantitative accuracy of using CT reconstruction of USAXS information given by an inhomogeneous sample (e.g. the clay loam sample) is questionable. However, when comparing the β map, the δ map, and the USAXS CT reconstructions of objects in the clay loam sample in figures 6.12 and 6.13, qualitatively, it is obvious that the USAXS CT reconstructions definitely provide complementary information regarding minute structures of a sample in micrometre length scale.

6.6 Conclusion

The aim of this chapter was to investigate the deconvolution process for the extraction of USAXS signals and the CT reconstruction of the USAXS information produced by the three-material phantom and the clay loam sample. Simulations of the Weiner deconvolution process and the RL deconvolution process found that RL deconvolution is more stable compared to Weiner deconvolution. However, due the iterative nature of RL deconvolution, the computational overhead was found to be extremely high. When comparing the DQ approximation and deconvolution to the ground truths during simulations, it was found that the DQ approximation is more accurate at estimating the USAXS signal. Therefore, the DQ approximation was used to reconstruct all USAXS information presented in this chapter. Furthermore, for both the three-material phantom and the clay loam sample, the CT reconstructions of USAXS information corresponding to the 0° to 180° tomographic angular range and the 180° to 360° tomographic angular range showed significant signs that the ABI can be extended to directional dark-field imaging using the new TLABI setup. Moreover, by comparing the β map, the δ map, and the USAXS CT reconstructions of clay loam particulates, this chapter clearly illustrated that the USAXS CT reconstruction is capable of providing complementary information regarding spatially-unresolved microstructures in inhomogeneous samples.

Chapter 7

Future Works and Conclusion

The first section of this chapter will present potential future developments identified during the course of this research. The second section will provide a detailed conclusion for this thesis.

7.1 Future Work

Chapter 3 of this thesis introduced a new Python-based asymmetrical distortion correction (OpenCV implementation). Although preliminary results show great accuracy in correcting the distortion, due to time restrictions, a detailed quantitative analysis was not conducted using x-ray images. An extensive analysis similar to the one conducted by Islam et al. (2010) in their work could potentially help identify whether the OpenCV implementation was the root cause behind the 36% overestimation of δ reported for the three-material phantom in chapter 5.

One of the highly likely causes of the poor estimate of the delta values is that the tilt angle was only 8°. As seen from equations (2.51) and (2.52) in section 2.4.3, it is clear that a 45° tilt angle would yield equal gradient of phase in both the x and y directions. Therefore, another avenue of future research would be to perform tilted-Laue analyser-based imaging (TLABI) experiment again with a 45° tilt angle to verify this.

It was identified during curve fitting that iterative curve fitting algorithms (e.g. Levenberg-Marquardt algorithm) are considerably better at fitting a mathematical model to the experimental data than a non-iterative polynomial fitting (see chapter 4). However, these iterative curve fitting algorithms come with tremendous computational overheads. It was identified that these computational overheads could potentially be reduced significantly by utilising a GPU instead of the CPU. A GPU-based curve fitting library, GPUfit, developed by Przybylski et al. (2017) have claimed that GPU-based iterative curve fitting can be approximately 42 times faster than a CPU based iterative curve fitting. Here, Przybylski et al. (2017) used the Levenberg-Marquardt algorithm. A downside of this library is that it only contains a handful of inbuilt mathematical models, which restricted the use of GPUfit library in this body of work. However, considering the GPUfit is an open-source library, there is a potential to add the necessary mathematical functions. In the future, it would be interesting to see if one could decrease the run-time of estimating pixel-by-pixel curve fitting using a GPU-based curve fitting program, such as GPUfit, without compromising the accuracy of the fit. Furthermore, considering pixel-by-pixel curve fitting is a requirement in other phase contrast image modalities such as grating-based phase-

contrast x-ray imaging, a GPU based curve fitting program will certainly benefit phase contrast research in general.

Although directional dark field imaging has been studied using grating-based phase-contrast X-ray imaging for a while (Jensen et al., 2010a,b), no literature was found on it being done using ABI. Considering the preliminary results presented in chapter 6, a possible future development of the TLABI experimental set-up would be to extend it to the directional dark-field regime. Furthermore, another potential development would be the utilisation of GPUs for deconvolution. It could potentially help decrease processing times considerably, and help with extracting quantitatively accurate USAXS information.

7.2 Thesis Conclusion

The aim of this body of work was to implement Multiple Image Radiography (MIR) (Wernick et al., 2002) using Tilted Laue Analyser Based Imaging (TLABI) (Chalmers et al., 2021) and to reconstruct the three-dimensional (3D) images of attenuation, phase, and USAXS information of two samples, namely the three-material phantom and the clay loam sample.

The process of reconstructing the 3D images of attenuation, phase, and USAXS information were divided into three stages. First was the preprocessing of raw images where this thesis introduced two Python-based asymmetrical distortion correction methods to correct the asymmetrical distortion inherent to Fibre Optic Taper (FOT) detectors. First was the Scikit image implementation and the second was the OpenCV implementation. The accuracy of these implementations were tested using synthetic images by comparing the outputs of these implementations to the output given by the well-established `Warp_tri` function in IDL. Although the scikit image implementation successfully corrected the distortion, in comparison to the `Warp_tri` function, it lacked the accuracy required for an accurate phase retrieval. However, it was found that the OpenCV implementation outperformed IDL's `Warp_tri` function. Furthermore, this thesis compared two crystal distortion correction methods named the OpenCV affine transform, which was a reduced variation of the OpenCV implementation, and the crystal distortion correction method developed by Kitchen et al. (2010) (Kitchen's method). The crystal distortion is the combination of accurately aligning the diffracted images with the transmitted images and correcting for the vertical stretch of the diffracted images by a factor of $1/cos(\theta_B)$. Here θ_B is the Bragg angle. The accuracy of this correction is important for accurate phase retrieval. A direct qualitative comparison between the output of OpenCV affine transform and the output from Kitchen's method showed that the OpenCV affine transform method was better at correcting the crystal distortion.

The second stage identified the best mathematical functions to estimate the intrinsic rocking curves and the sample rocking curves using χ^2 analysis. Using the Python curve fitting library LMFIT, the Pearson VII model, Voigt model, and the Pseudo-Voigt (PsV) model were tested as potential candidates to estimate the intrinsic rocking curves. Here, for each model, the average χ^2 values and their standard deviations were estimated by fitting 261 diffracted beam projections of size 935×780 pixels on a pixel-by-pixel basis. The Pearson VII model, Voigt model, and the PsV model gave average χ^2 values of 793.41, 790.63, and 449.33 with standard deviations of 216.71, 170.36, and 49.33, respectively. This provided statistical evidences that the PsV

model is the best model to estimate the intrinsic rocking curves. Following the same process, the Gaussian model, Pearson VII model, PsV model, and the Lorentzian model was tested as potential candidates for sample rocking curve fitting. Here, eight diffracted beam projections with the sample present in the beam were fitted using each model on a pixel-by-pixel basis. For the three-material phantom, the Gaussian model, Pearson VII model, PsV model, and the Lorentzian model gave average χ^2 values of 155, 15.4, 14.9, and 15.9 with standard deviations of 45.4, 8.30, 7.45, and 7.97, respectively. For the clay loam sample the Gaussian model, Pearson VII model, PsV model, and the Lorentzian model gave average χ^2 values of 141.0, 5.97, 5.10, and 7.18 with standard deviations of 84.4, 4.14, 3.33, and 3.33, respectively. Although these results suggested that the PsV model better estimates the sample rocking curves, the iterative curve fitting process required to fit the PsV model came with high computational overheads. Since, the Lorentzian model is an inverse of a second order polynomial, χ^2 regression allowed fitting a Lorentzian to the experimental data through coordinate transformation (the QF method). When comparing this QF method to the LMFIT Lorentzian fitting, it was found that QF method was 278 times faster than the LMFIT Lorentzian fitting. However, it was found that the χ^2 estimation of LMFIT Lorentzian fitting was 39% lower than the χ^2 estimation of QF method. Due to the limited time available for this project, the Lorentzian model was used to estimate the sample rocking curves for both the three-material phantom and the clay loam sample. Furthermore, this thesis successfully introduced an analytical method using a Lorentzian function to estimate the rocking curve angular position at each working point during sample rocking curve image acquisition.

The third stage was the reconstruction of 3D images of attenuation, phase, and USAXS information. In this thesis, two reconstruction methods were tested. Namely, they were the 261-point and the eight-point reconstruction method. Here, the 261-point method used 261 angular positions of the analyser crystal to estimate the intrinsic rocking curve, while the eight-point reconstruction method only used eight angular positions of the analyser crystal to estimate the intrinsic rocking curve parameters. First, the attenuation projections were calculated by taking the ratio between the area under the curve of the intrinsic rocking curve and the area under the curve of the sample rocking curve. Then the 3D images of the imaginary part, β, of the index of refraction were reconstructed using the Filtered Back Projection (FBP) with a Ram-Lak filter. The experimental β values for Perspex ($C_5H_8O_2$), PTFE (C_2F_4), and Aluminium in the three-material phantom using both reconstruction methods gave $1.3 \pm 0.6 \times 10^{-10}$, $3.9 \pm 0.6 \times 10^{-10}$, and $16.9 \pm 0.6 \times 10^{-10}$, respectively. It was found that the experimental β values deviated from the theoretical β values by 7% for Perspex, 5% for PTFE, and 11% for Aluminium.

By tilting the sample and the detector by 8°, the TLABI setup enabled the reconstruction of two orthogonal components of the phase gradient. The TLABI setup provided two opposing centroid shift images, one at the tomographic angular position ψ and the other at $\psi + 180°$. The centroid shift images were calculated by taking the difference between the centroid of the sample rocking curve and the intrinsic rocking curve on a pixel-by-pixel basis. Then, flipping and translating the centroid shift image at $\psi + 180°$ to overlap the centroid shift image at ψ enabled the separation of the horizontal and the vertical components of the phase gradient. Following that, the 2D phase maps of the sample were calculated using the 2D Fourier integration

process. Thereafter, the 3D images of real part, δ, of the index of refraction were reconstructed using FBP with a Ram-Lak filter. For the 261-point reconstruction method, the experimental δ values for Perspex, PTFE, and Aluminium in the three-material phantom were estimated to be $5.6 \pm 0.1 \times 10^{-7}$, $8.8 \pm 0.1 \times 10^{-7}$, and $10.9 \pm 0.1 \times 10^{-7}$, respectively. For the eight-point reconstruction method, the experimental δ values for Perspex, PTFE, and Aluminium were calculated to be $5.5 \pm 0.1 \times 10^{-7}$, $8.8 \pm 0.1 \times 10^{-7}$, and $10.8 \pm 0.1 \times 10^{-7}$, respectively. The theoretical δ values for Perspex, PTFE, and Aluminium were 3.9×10^{-7}, 6.5×10^{-7}, and 8.0×10^{-7}, respectively. It was found that, on average, both reconstruction methods overestimated the δ values for PTFE and Aluminium by 35%, while they overestimated the δ value for Perspex by 42%. Furthermore, a reconstruction of the δ value for Perspex without PTFE, the Aluminium pin or other horizontal edges, reduced the overestimation of its δ value to 36%. This suggested that the amplification of noise during the 2D Fourier integration process possibly affected the estimation of δ for Perspex.

Two deconvolution methods, namely the Wiener deconvolution and the Richardson-Lucy (RL) iterative deconvolution were tested as potential candidates to deconvolve the scatter function. It was found that while both methods were capable of stabilising the deconvolution process, RL iterative deconvolution outperformed the Wiener deconvolution. However, due to its iterative nature, it was found to have a large computational overhead. When comparing the PsV/Lorentzian deconvolution simulation results and the difference in quadrature (DQ) approximation to the ground truth, it was found that the DQ approximation is more accurate at estimating the USAXS signal. This provided confidence to use the DQ approximation for all USAXS inconstructions presented in this thesis.

Using the DQ approximation, for each sample, namely the three-material phantom and the clay loam sample, 3600 USAXS projections covering 360° tomographic range were estimated. During the analysis of the CT reconstructions of the USAXS information, this body of work found evidence that the USAXS fan is non-circular in shape. Essentially, the CT reconstructions done using the projections covering the tomographic range from 0° to 180° provided slightly different results to the CT reconstructions produced using the projections covering the tomographic range from 180° to 360°. This essentially illustrated that by tilting the sample and the detector, even by a small angle 8° allows the USAXS signal to be measured in different directions. Therefore, it was found that the TLABI has the potential to develop directional dark field imaging.

As pointed out earlier, both the 261-point reconstruction method and the eight-point reconstruction method basically gave nearly identical β and δ values for the three-material phantom. Therefore, the β and δ reconstructions of the clay loam sample were done using only the 261-point reconstruction method. Following the same processes as for the three-material phantom β and δ reconstructions, this thesis successfully reconstructed 3D images of the β and δ of an inhomogeneous clay loam sample. A close comparison between the β, the δ and the USAXS information CT reconstructions found that USAXS is capable of producing details regarding minute structures in the micrometre length scale that were not evident from the Beta or delta maps. Therefore, despite the complex nature of the TLABI setup, this study has shown that the proposed variation of MIR is capable of producing quantitatively and qualitatively significant

results for any given sample.

Bibliography

Als-Nielsen, J. and McMorrow, D. (2011). *Elements of Modern X-Ray Physics*. Wiley.

Ando, M. and Hosoya, S. (1972). An attempt at X-ray phase-contrast microscopy. In *Proceedings 6th International Conference of X-Ray Optics and Microanalysis*, pages 63–68. University of Tokyo Press.

Andrejewski, J., De Marco, F., Willer, K., Noichl, W., Gustschin, A., Koehler, T., Meyer, P., Kriner, F., Fischer, F., Braun, C., Fingerle, A. A., Herzen, J., Pfeiffer, F., and Pfeiffer, D. (2021). Whole-body x-ray dark-field radiography of a human cadaver. *European Radiology Experimental*, 5(1):6.

Arfelli, F., Astolfo, A., Rigon, L., and Menk, R. H. (2018). A Gaussian extension for Diffraction Enhanced Imaging. *Scientific Reports*, 8(1):362.

Authier, A. (2001). *Dynamical Theory of X-Ray Diffraction*. Oxford University Press.

Authier, A. and Malgrange, C. (1998). Diffraction Physics. *Acta Crystallographica Section A Foundations of Crystallography*, 54(6):806–819.

Berger, M., Hubbell, J., Seltzer, S., Chang, J., Coursey, J., Sukumar, R., Zucker, D., and Olsen, K. (2010). XCOM: Photon Cross Section Database (version 1.5). [Online] Available: http://physics.nist.gov/xcom. National Institute of Standards and Technology, Gaithersburg, MD.

Bonse, U. and Hart, M. (1965a). An X-ray interferometer. *Applied Physics Letters*, 6(8):155–156.

Bonse, U. and Hart, M. (1965b). An X-ray interferometer with long seperated interfering beam paths. *Applied Physics Letters*, 7(4):99–100.

Bradley, W. G. (2008). History of Medical Imaging. *Proceedings of the American Philosophical Society*, 152(3):349–361.

Bradski, G. (2000). The opencv library. *Dr Dobb's J. Software Tools*, 25:120–125.

Bravin, A., Coan, P., and Suortti, P. (2013). X-ray phase-contrast imaging: From pre-clinical applications towards clinics. *Physics in medicine & biology*, 58(1):R1–R35.

Bushberg, J. T., Seibert, J. A., Leidholdt, E. M., and Boone, J. M. (2011). *The Essential Physics of Medical Imaging*. Wolters Kluwer Health.

Bushuev, V., Ingal, V., and Belyaevskaya, E. (1996). Dynamical theory of images generated by noncrystalline objects for the method of phase-dispersive introscopy. *Crystallography Reports*, 41(5):766–774.

Caciuffo, R., Melone, S., Rustichelli, F., and Boeuf, A. (1987). Monochromators for x-ray synchrotron radiation. *Physics Reports*, 152(1):1–71.

Chalmers, M. C., Kitchen, M. J., Uesugi, K., Falzon, G., Quin, P., and Pavlov, K. M. (2021). Tomographic reconstruction using tilted Laue analyser-based X-ray phase-contrast imaging. *Journal of Synchrotron Radiation*, 28(1):283–291.

Chapman, D., Thomlinson, W., Johnston, R. E., Washburn, D., Pisano, E., Gmür, N., Zhong, Z., Menk, R., Arfelli, F., and Sayers, D. (1997). Diffraction enhanced x-ray imaging. *Physics in Medicine & Biology*, 42(11):2015.

Chen, D., Chen, Q., Wu, J., Yu, X., and Jia, T. (2019). Face Swapping: Realistic Image Synthesis Based on Facial Landmarks Alignment. *Mathematical Problems in Engineering*, 2019:8902701.

Chou, C.-Y., Anastasio, M. A., Brankov, J. G., Wernick, M. N., Brey, E. M., Connor, D. M., and Zhong, Z. (2007). An extended diffraction-enhanced imaging method for implementing multiple-image radiography. *Physics in Medicine and Biology*, 52(7):1923–1945.

Cierniak, R. and Cierniak, R. (2011). Some Words About the History of Computed Tomography. *X-ray computed tomography in biomedical engineering*, pages 7–19.

Cootes, T. and Taylor, C. (2004). Statistical Models of Appearance for computer vision.

David, C., David, C., Nöhammer, B., Solak, H. H., and Ziegler, E. (2002). Differential x-ray phase contrast imaging using a shearing interferometer. *Applied physics letters*, 81(17):3287–3289.

Davis, T. J., Gao, D., Gureyev, T. E., Stevenson, A. W., and Wilkins, S. W. (1995). Phase-contrast imaging of weakly absorbing materials using hard X-rays. *Nature*, 373(6515):595–598.

Davison, A., Merghani, W., Lansley, C., Ng, C.-C., and Yap, M. H. (2018). Objective micro-facial movement detection using facs-based regions and baseline evaluation. In *2018 13th IEEE International Conference on Automatic Face & Gesture Recognition (FG 2018)*, pages 642–649. IEEE.

Diemoz, P. C., Bravin, A., and Coan, P. (2012). Theoretical comparison of three X-ray phase-contrast imaging techniques: Propagation-based imaging, analyzer-based imaging and grating interferometry. *Optics Express*, 20(3):2789.

Diemoz, P. C., Hagen, C. K., Endrizzi, M., and Olivo, A. (2013). Sensitivity of laboratory based implementations of edge illumination X-ray phase-contrast imaging. *Applied Physics Letters*, 103(24):244104.

Endrizzi, M. (2018). X-ray phase-contrast imaging. *Radiation Imaging Techniques and Applications*, 878:88–98.

Endrizzi, M., Diemoz, P. C., Millard, T. P., Louise Jones, J., Speller, R. D., Robinson, I. K., and Olivo, A. (2014). Hard X-ray dark-field imaging with incoherent sample illumination. *Applied Physics Letters*, 104(2):024106.

Förster, E., Goetz, K., and Zaumseil, P. (1980). Double crystal diffractometry for the characterization of targets for laser fusion experiments. *Kristall und Technik*, 15(8):937–945.

Gasilov, S. V. and Coan, P. (2012). X-ray phase contrast imaging of objects with subpixel-size inhomogeneities: A geometrical optics model. *JOSA A*, 29(9):1870–1876.

Gunasekera, J. (2020). Asymmetrical Geometrical Distortion Correction Implemented in Python to Correct Camera Distortion in High-Resolution X- ray Images. In *ANSTO User Meeting 2020. Abstract 198. https://events01.synchrotron.org.au/event/122/overview.*

Gunturk, B. K. and Li, X. (2012). *Image Restoration: Fundamentals and Advances*, volume 7. CRC Press, Boca Raton, FL, first edition.

Gureyev, T. E., Mayo, S. C., Nesterets, Y. I., Mohammadi, S., Lockie, D., Menk, R. H., Arfelli, F., Pavlov, K. M., Kitchen, M. J., Zanconati, F., Dullin, C., and Tromba, G. (2014). Investigation of the imaging quality of synchrotron-based phase-contrast mammographic tomography. *Journal of Physics D: Applied Physics*, 47(36):365401.

Gureyev, T. E., Nesterets, Y. I., Stevenson, A. W., Miller, P. R., Pogany, A., and Wilkins, S. W. (2008). Some simple rules for contrast, signal-to-noise and resolution in in-line x-ray phase-contrast imaging. *Optics Express*, 16(5):3223–3241.

IAEA (2014). *Diagnostic Radiology Physics: A Handbook for Teachers and Students.* International Atomic Energy Agency.

ICRU (1989). Tissue substitutes in radiation dosimetry and measurement. Technical Report Report 44 of the International Commission on Radiation Units and Measurements (Bethesda, MD).

Ingal, V. N. and Beliaevskaya, E. A. (1995). X-ray plane-wave topography observation of the phase contrast from a non-crystalline object. *Journal of Physics D: Applied Physics*, 28(11):2314–2317.

Islam, M. S., Lewis, R. A., Uesugi, K., and Kitchen, M. J. (2010). A high precision recipe for correcting images distorted by a tapered fiber optic. *Journal of Instrumentation*, 5(09):P09008–P09008.

Jensen, T. H., Bech, M., Bunk, O., Donath, T., David, C., Feidenhans'l, R., and Pfeiffer, F. (2010a). Directional x-ray dark-field imaging. *Physics in Medicine and Biology*, 55(12):3317–3323.

Jensen, T. H., Bech, M., Zanette, I., Weitkamp, T., David, C., Deyhle, H., Rutishauser, S., Reznikova, E., Mohr, J., Feidenhans'l, R., and Pfeiffer, F. (2010b). Directional x-ray dark-field imaging of strongly ordered systems. *Physical Review B*, 82(21):214103.

Kak, A. C. and Slaney, M. (2001). *Principles of Computerized Tomographic Imaging*. Society for Industrial and Applied Mathematics.

Khelashvili, G., Brankov, J. G., Chapman, D., Anastasio, M. A., Yang, Y., Zhong, Z., and Wernick, M. N. (2006). A physical model of multiple-image radiography. *Physics in Medicine and Biology*, 51(2):221–236.

Kielkopf, J. F. (1973). New approximation to the Voigt function with applications to spectral-line profile analysis. *JOSA*, 63(8):987–995.

Kitchen, M. J., Buckley, G. A., Kerr, L. T., Lee, K. L., Uesugi, K., Yagi, N., and Hooper, S. B. (2020). Emphysema quantified: Mapping regional airway dimensions using 2D phase contrast X-ray imaging. *Biomedical Optics Express*, 11(8):4176–4190.

Kitchen, M. J., Lewis, R. A., Yagi, N., Uesugi, K., Paganin, D., Hooper, S. B., Adams, G., Jureczek, S., Singh, J., Christensen, C. R., Hufton, A. P., Hall, C. J., Cheung, K. C., and PAvlov, K. M. (2005). Phase contrast X-ray imaging of mice and rabbit lungs: A comparative study. *The British Journal of Radiology*, 78(935):1018–1027.

Kitchen, M. J., Paganin, D. M., Uesugi, K., Allison, B. J., Lewis, R. A., Hooper, S. B., and Pavlov, K. M. (2010). X-ray phase, absorption and scatter retrieval using two or more phase contrast images. *Optics Express*, 18(19):19994.

Kitchen, M. J., Paganin, D. M., Uesugi, K., Allison, B. J., Lewis, R. A., Hooper, S. B., and Pavlov, K. M. (2011). Phase contrast image segmentation using a Laue analyser crystal. *Physics in Medicine and Biology*, 56(3):515–534.

Kitchen, M. J., Pavlov, K. M., Siu, K. K. W., Menk, R. H., Tromba, G., and Lewis, R. A. (2007). Analyser-based phase contrast image reconstruction using geometrical optics. *Physics in Medicine and Biology*, 52(14):4171–4187.

Kohn, V. (1998). X-ray imaging of inhomogeneous objects by coherent wave (phase contrast). *Hamburg lectures*.

Korn, G. and Korn, T. (2000). *Mathematical Handbook for Scientists and Engineers: Definitions, Theorems, and Formulas for Reference and Review*. Dover Civil and Mechanical Engineering Series. Dover Publications.

Kottler, C., David, C., Pfeiffer, F., and Bunk, O. (2007). A two-directional approach for grating based differential phase contrast imaging using hard x-rays. *Optics express*, 15(3):1175.

Lam, S., Pitrou, A., and Seibert, S. (2015). *Numba: A LLVM-Based Python JIT Compiler*.

Levenberg, K. (1944). A method for the solution of certain non-linear problems in least squares. *Quarterly of applied mathematics*, 2(2):164–168.

Lyra, M. and Ploussi, A. (2011). Filtering in SPECT Image Reconstruction. *International Journal of Biomedical Imaging*, 2011:693795.

Mandel, L. and Wolf, E. (1995). *Optical Coherence and Quantum Optics*. Cambridge University Press, Cambridge.

Marquardt, D. W. (1963). An algorithm for least-squares estimation of nonlinear parameters. *Journal of the society for Industrial and Applied Mathematics*, 11(2):431–441.

Mocella, V. (2005). Negative refraction in Photonic Crystals: Thickness dependence and Pendellösung phenomenon. *Optics Express*, 13(5):1361–1367.

Momose, A. (1995). Demonstration of phase-contrast X-ray computed tomography using an X-ray interferometer. *Nuclear Instruments and Methods in Physics Research Section A: Accelerators, Spectrometers, Detectors and Associated Equipment*, 352(3):622–628.

Momose, A., Kawamoto, S., Koyama, I., and Hamaishi, Y. (2003). Demonstration of X-Ray Talbot Interferometry. *Japanese Journal of Applied Physics*, 42(part 2, no. 7b):L866–L868.

Morgan, K. S. and Paganin, D. M. (2019). Applying the Fokker–Planck equation to grating-based x-ray phase and dark-field imaging. *Scientific Reports*, 9(1):17465.

Nesterets, Y. I., Coan, P., Gureyev, T. E., Bravin, A., Cloetens, P., and Wilkins, S. W. (2006). On qualitative and quantitative analysis in analyser-based imaging. *Acta Crystallographica Section A Foundations of Crystallography*, 62(4):296–308.

Nesterets, Y. I., Gureyev, T. E., Mayo, S. C., Stevenson, A. W., Thompson, D., Brown, J. M. C., Kitchen, M. J., Pavlov, K. M., Lockie, D., Brun, F., and Tromba, G. (2015). A feasibility study of X-ray phase-contrast mammographic tomography at the Imaging and Medical beamline of the Australian Synchrotron. *Journal of Synchrotron Radiation*, 22(6):1509–1523.

Nesterets, Y. I., Nesterets, Y., Wilkins, S., Gureyev, T., and Pogany, A. (2005). On the optimization of experimental parameters for x-ray in-line phase-contrast imaging. *Review of scientific instruments*, 76(9).

Newville, M., Stensitzki, T., Allen, D. B., and Ingargiola, A. (2014). LMFIT: Non-Linear Least-Square Minimization and Curve-Fitting for Python. Zendo.

O'Haver, T. (2021). *A Pragmatic Introduction to Signal Processing: With Applications in Scientific Measurement (2021 Edition)*. CreateSpace Independent Publishing Platform.

Olivo, A., Arfelli, F., Cantatore, G., Longo, R., Menk, R., Pani, S., Prest, M., Poropat, P., Rigon, L., Tromba, G., Vallazza, E., and Castelli, E. (2001). An innovative digital imaging set-up allowing a low-dose approach to phase contrast applications in the medical field. *Medical physics*, 28(8):1610–1619.

Oltulu, O., Zhong, Z., Hasnah, M., Wernick, M. N., and Chapman, D. (2003). Extraction of extinction, refraction and absorption properties in diffraction enhanced imaging. *Journal of Physics D: Applied Physics*, 36(17):2152–2156.

Paganin, D. (2006). *Coherent X-Ray Optics*. Oxford Series on Synchrotron Radiation. Oxford University Press, Oxford.

Paganin, D. M., Labriet, H., Brun, E., and Berujon, S. (2018). Single-image geometric-flow x-ray speckle tracking. *Physical Review A*, 98(5):053813.

Pagot, E., Pagot, E., Cloetens, P., Fiedler, S., and Bravin, A. (2003). A method to extract quantitative information in analyzer-based x-ray phase contrast imaging. *Applied physics letters*, 82(20):3421–3423.

Pavlov, K. M., Gureyev, T. E., Paganin, D., Nesterets, Y. I., Morgan, M. J., and Lewis, R. A. (2004). Linear systems with slowly varying transfer functions and their application to x-ray phase-contrast imaging. *Journal of Physics D: Applied Physics*, 37(19):2746–2750.

Pavlov, K. M., Kewish, C. M., Davis, J. R., and Morgan, M. J. (2001). A variant on the geometrical optics approximation in diffraction enhanced tomography. *Journal of Physics D: Applied Physics*, 34(10A):A168–A172.

Pelliccia, D., Kitchen, M. J., and Morgan, K. S. (2018). *Theory of X-Ray Phase-Contrast Imaging*, pages 971–998. CRC Press, Boca Raton FL USA, first edition.

Pfeiffer, F., Herzen, J., Willner, M., Chabior, M., Auweter, S., Reiser, M., and Bamberg, F. (2013). Grating-based X-ray phase contrast for biomedical imaging applications. *Zeitschrift für Medizinische Physik*, 23(3):176–185.

Pfeiffer, F., Weitkamp, T., Bunk, O., and David, C. (2006). Phase retrieval and differential phase-contrast imaging with low-brilliance X-ray sources. *Nature Physics*, 2(4):258–261.

Podgoršak, E. B. (2010). *Radiation Physics for Medical Physicists*. Number Book, Whole. Springer, Heidelberg, 2nd, enl. edition.

Press, W. H., H, W., Teukolsky, S. A., Vetterling, W. T., A, S., and Flannery, B. P. (2007). *Numerical Recipes 3rd Edition: The Art of Scientific Computing*. Cambridge University Press.

Przybylski, A., Thiel, B., Keller-Findeisen, J., Stock, B., and Bates, M. (2017). Gpufit: An open-source toolkit for GPU-accelerated curve fitting. *Scientific Reports*, 7(1):15722.

Qinghe Li, Bong-Jae Lee, Zhuomin M. Zhang, and David W. Allen (2008). Light scattering of semitransparent sintered polytetrafluoroethylene films. *Journal of Biomedical Optics*, 13(5):1–12.

Ramlau, R. and Scherzer, O. (2018). The first 100 years of the Radon transform. *Inverse Problems*, 34(9):090201.

Rayleigh, L. (1881). XXV. On copying diffraction-gratings, and on some phenomena connected therewith. *The London, Edinburgh, and Dublin Philosophical Magazine and Journal of Science*, 11(67):196–205.

Rigon, L., Arfelli, F., and Menk, R.-H. (2007). Generalized diffraction enhanced imaging to retrieve absorption, refraction and scattering effects. *Journal of Physics D: Applied Physics*, 40(10):3077–3089.

Ruiz-Yaniz, M., Zanette, I., Rack, A., Weitkamp, T., Meyer, P., Mohr, J., and Pfeiffer, F. (2015). X-ray-refractive-index measurements at photon energies above 100 keV with a grating interferometer. *Physical Review A*, 91(3):033803.

Rutishauser, S., Donath, T., David, C., Pfeiffer, F., Marone, F., Modregger, P., and Stampanoni, M. (2011). A tilted grating interferometer for full vector field differential x-ray phase contrast tomography. *Optics Express*, 19(25):24890.

Snigirev, A., Snigirev, A., Snigireva, I., Kohn, V., and Kuznetsov, S. (1995). On the possibilities of x-ray phase contrast microimaging by coherent high-energy synchrotron radiation. *Review of scientific instruments*, 66(12):5486–5492.

Spiers, F. W. (1946). Effective atomic number and energy absorption in tissues. *The British journal of radiology*, 19(Journal Article):52.

Suhonen, H., Fernández, M., Bravin, A., Keyriläinen, J., and Suortti, P. (2007). Refraction and scattering of X-rays in analyzer-based imaging. *Journal of Synchrotron Radiation*, 14(6):512–521.

Suortti, P., Keyriläinen, J., and Thomlinson, W. (2013). Analyser-based x-ray imaging for biomedical research. *Journal of Physics D: Applied Physics*, 46(49):494002.

Suortti, P. and Thomlinson, W. (2003). Medical applications of synchrotron radiation. *Physics in Medicine and Biology*, 48(13):R1–R35.

Takeda, M., Ina, H., and Kobayashi, S. (1982). Fourier-transform method of fringe-pattern analysis for computer-based topography and interferometry. *Journal of the Optical Society of America*, 72(1):156–160.

Takeda, T., Momose, A., Ueno, E., and Itai, Y. (1998). Phase-contrast X-ray CT image of breast tumor. *Journal of synchrotron radiation*, 5(Pt 3):1133–1135.

Talbot, H. F. (1836). LXXVI. Facts relating to optical science. No. IV. *The London, Edinburgh, and Dublin Philosophical Magazine and Journal of Science*, 9(56):401–407.

Teague, M. R. (1983). Deterministic phase retrieval: A Green's function solution. *Journal of the Optical Society of America*, 73(11):1434.

Uesugi, K., Hoshino, M., and Yagi, N. (2011). Comparison of lens- and fiber-coupled CCD detectors for X-ray computed tomography. *Journal of synchrotron radiation*, 18:217–23.

van der Walt, S., Schönberger, J. L., Nunez-Iglesias, J., Boulogne, F., Warner, J. D., Yager, N., Gouillart, E., Yu, T., and scikit-image contributors, t. (2014). Scikit-image: Image processing in Python. *PeerJ*, 2:e453.

Vine, D. J., Paganin, D. M., Pavlov, K. M., Kräußlich, J., Wehrhan, O., Uschmann, I., and Förster, E. (2007). Analyzer-based phase contrast imaging and phase retrieval using a rotating anode x-ray source. *Applied Physics Letters*, 91(25):254110.

Vo, N. T., Atwood, R. C., and Drakopoulos, M. (2015). Radial lens distortion correction with sub-pixel accuracy for X-ray micro-tomography. *Optics Express*, 23(25):32859.

Wernick, M., Wirjadi, O., Chapman, D., Oltulu, O., Zhong Zhong, and Yongyi Yang (2002). Preliminary investigation of a multiple-image radiography method. In *Proceedings IEEE International Symposium on Biomedical Imaging*, pages 129–132, Washington, DC, USA. IEEE.

Wernick, M. N., Wirjadi, O., Chapman, D., Zhong, Z., Galatsanos, N. P., Yang, Y., Brankov, J. G., Oltulu, O., Anastasio, M. A., and Muehleman, C. (2003). Multiple-image radiography. *Physics in Medicine and Biology*, 48(23):3875–3895.

White, D. R. (1977). An analysis of the Z-dependence of photon and electron interactions. *Physics in Medicine and Biology*, 22(2):219–228.

White, D. R., Booz, J., Griffith, R. V., Spokas, J. J., and Wilson, I. J. (2016). Report 44. *Journal of the International Commission on Radiation Units and Measurements*, os23(1):NP–NP.

Wilkins, S. W., Gureyev, T. E., Gao, D., Pogany, A., and Stevenson, A. W. (1996). Phase-contrast imaging using polychromatic hard X-rays. *Nature*, 384(6607):335–338.

Willmott, P. (2011). *An Introduction to Synchrotron Radiation: Techniques and Applications*. Wiley.

Yashiro, W. and Momose, A. (2015). Effects of unresolvable edges in grating-based X-ray differential phase imaging. *Optics Express*, 23.

Zernike, F. (1942). Phase contrast, a new method for the microscopic observation of transparent objects. *Physica*, 9(7):686–698.

Zernike, F. (1955). How I Discovered Phase Contrast. *Science*, 121(3141):345.

Zhong, Z., Thomlinson, W., Chapman, D., and Sayers, D. (2000). Implementation of diffraction-enhanced imaging experiments: At the NSLS and APS. *Nuclear Instruments and Methods in Physics Research Section A: Accelerators, Spectrometers, Detectors and Associated Equipment*, 450(2):556–567.

Zhou, S.-A. and Brahme, A. (2008). Development of phase-contrast X-ray imaging techniques and potential medical applications. *Physica Medica*, 24(3):129–148.

Zysk, A. M., Brankov, J. G., Wernick, M. N., and Anastasio, M. A. (2012). Adaptation of a clustered lumpy background model for task-based image quality assessment in x-ray phase-contrast mammography. *Medical Physics*, 39(2):906–911.

Appendices

Appendix A

Python Programs

This appendix contain all the code written for the extracting of absorption, gradient of phase, and USAXS images presented in this thesis. Section A.1 presents the source code for FOT and crystal distortion corrections.

A.1 FOT and Crystal Distortion Correction Code

```
"""
Created on Wed Aug 19 11:31:41 2020

@author: - Jayan Gunasekera
FOT and Crystal Distortion
Saved as Distortion_Corrections.py
"""
import numpy as np
import numba as nb
from PIL import Image
from astropy.convolution import Gaussian2DKernel, interpolate_replace_nans
import cv2
import os

def input_file_list(input_dir):
    """This function generate a list of files names with the extension .img
    in a given folder
    Parameters:
        input_dir: path to the folder containg .img files or .tif files
    Return:
        A sorted list of names of the .img or tif files as strings"""
    input_filename = []
    # r=root, d=directories, f = files
    for r, d, f in os.walk(input_dir):
        for file in f:
            if file.endswith('.img') or file.endswith('.tif'): # in file:
                input_filename.append(file)
        input_filename.sort()
```

```
        return input_filename

def open_file(input_dir,input_filename):
    """This function open and read .img file.
    Parameters:
        input_dir: path to the input directory as a string
        input_filename: input file name as a string
    Return:
        2D numpy array"""
    with open(input_dir+input_filename, 'rb') as fid:
        Data_Array = np.fromfile(fid, np.uint16)
        fid.seek(64+Data_Array[1])
        Image_Array = np.asarray(np.fromfile(fid, np.uint16)).astype('float32')
        Image_Array = Image_Array.reshape((Data_Array[3],Data_Array[2]))
        return Image_Array

def Ave_Dark(input_dir):
    """Calculate the average of Dark field images
    Parametres:
        input_dir: directory of the input files as a string
    Return:
        Average of the input images as a 2D numpy array."""
    input_filename = input_file_list(input_dir)
    Dark_array = np.zeros((1448,2288))
    for i in range(len(input_filename)):
        Image_Array = open_file(input_dir,input_filename[i])
        Dark_array = np.add(Image_Array,Dark_array)
    DarkAvg = Dark_array/(len(input_filename))
    return DarkAvg

def dark_correction(Image_Array, dark_ave):
    """This function subtract the dark current signal. Dimensions of
    Image_Array must match the dimensions of dark_ave.
    Parameters:
        Image_Array: Projection image as a tif file/ If it is given as a
                    2D numpy array comment out the first line of this function.
        dark_ave: Average of dark field projections
    Return:
        2D numpy array"""
    DarkAve = np.array(Image.open(dark_ave))
    Image_Dark_corr = Image_Array - DarkAve
    return Image_Dark_corr

def recreate_image(Image_Array,Offset):
    """This function create an empty array of 4000x2672 and position the image
    using the OFFSET.
    Parameters:
```

```
        Image_Array: 32 bit(float) np.array of the image
        Offset = [Xlower, Xupper, Ylower, Yupper]
        Offsets used for this thesis taken from the experimental logbook are:
            Xlower = 735
            Xupper = 3023
            Ylower = 544
            Yupper = 1992
    Return:
        2D numpy array of size 4000x2672"""

    empty_image = np.zeros((2672,4000))
    empty_image[Offset[2]:Offset[3], Offset[0]:Offset[1]] = Image_Array
    image = empty_image
    return image
```

A.1.1 FOT Distortion Correction (Method 2)

How to use OpenCV for this process was learnt from the youtube tutorial series 'Face swapping Opencv with Python by Pysource (https://www.youtube.com/watch?v=hcINR237U6E)'. Code bellow contain parts from the code shown on this tutorial series. The presenter give permission to use the code during his last session.

Delaunay Triangulation

Following three functions were executed once and the output was saved as .dat file to be imported later. This was possible because the distortion in all projections were the same and it reduced the total runtime for FOT distortion correction significantly.

```
def extract_index(nparray):
    '''Extract an intiger our of an array. This is used in
    Triangulation_Data_Extraction function.
    Parameters:
        nparray: numpy array
    Return:
        Integer or None'''
    index = None
    for num in nparray[0]:
        index = num
        break
    return index


def Delaunay_triangulation(ROI, src_points):
    '''This function perform the Delaunay Triangulation.
    Parameters:
        ROI: Region Of Interest of the image to perform Delaunay
            Triangulation as a tuple - (x_start, y_start, x_end, y_end)
        src_points: Source tie points as a numpy array
```

```
    Return:
        An array of triangles. For more information:
        https://docs.opencv.org/3.4/df/dbf/classcv_1_1Subdiv2D.html
         '''
    src_points = src_points.tolist()
    subdiv = cv2.Subdiv2D(ROI)
    subdiv.insert(src_points)
    triangles = subdiv.getTriangleList()
    triangles = np.array(triangles, dtype=np.int32)
    return triangles

def Triangulation_Data_Extraction(ROI, src_points):
    '''This function sort the triangle indecies to be used in Triangulated_Dewarping
        function.
    Parameters:
        ROI: Region Of Interest of the image to perform Delaunay
            Triangulation as a tuple - (x_start, y_start, x_end, y_end)
        src_points: Source tie points as a numpy array.
    Return:
        Sorted list of triangle indecies'''

    triangles = Delaunay_triangulation(ROI, src_points)
    src_points = np.asarray(src_points, dtype=np.float32)
    triangle_indexes = np.empty((0,3), dtype=np.int32)
    for tri in triangles:
        # Rearranging the triangles according to indexes
        pt1 = tri[0], tri[1]
        index_pt1 = np.where((src_points == pt1).all(axis=1))
        index_pt1 = extract_index(index_pt1)

        pt2 = tri[2], tri[3]
        index_pt2 = np.where((src_points == pt2).all(axis=1))
        index_pt2 = extract_index(index_pt2)

        pt3 = tri[4], tri[5]
        index_pt3 = np.where((src_points == pt3).all(axis=1))
        index_pt3 = extract_index(index_pt3)

        if index_pt1 is not None and index_pt2 is not None and index_pt3 is not None:
            triangle1 = np.array([[index_pt1, index_pt2, index_pt3]], dtype=np.float32)
            triangle_indexes = np.append(triangle_indexes, triangle1, axis=0)
    return triangle_indexes
```

Piecewise Affine Transformation Application

```
def Triangulated_Dewarping(Input_Image, triangle_indexes, src_points, dst_points):
    """This function uses apply PWA to correct geometrical distortion in a given image.
    Parameters:
        Input_Image: Distorted imaged to be dewarped (2D numpy array).
        Output_Image: Blank 2D numpy array (same shape as the Input_Image).
        triangle_indexes: List of triangle indecies generated using tie points
            (src_points)
                        - See function Triangulation_Data_Extraction.
        src_points: list of x and y coordinates as numpy array (distorted coordinates).
        dst_points: list of x and y coordinates as numpy array (destination
            (undistorted)
                                                            coortdiantes).
        Return:
            Output_Image: Distortion corrected 2D numpy array."""
    triangle_indexes = np.int32(triangle_indexes).tolist()
    Output_Image = np.zeros((Input_Image.shape[0], Input_Image.shape[1]),
        dtype=np.float32)
    for triangle in triangle_indexes:
        # Src image Triangulated points
        src_pt1 = tuple(src_points[triangle[0]])
        src_pt2 = tuple(src_points[triangle[1]])
        src_pt3 = tuple(src_points[triangle[2]])
        src_triangle = np.array([src_pt1, src_pt2, src_pt3], np.int32)

        # Dst image Triangulated points
        dst_pt1 = tuple(dst_points[triangle[0]])
        dst_pt2 = tuple(dst_points[triangle[1]])
        dst_pt3 = tuple(dst_points[triangle[2]])
        dst_triangle = np.array([dst_pt1, dst_pt2, dst_pt3], np.int32)
        # src_pt1 corresponds to dst_pt1, src_pt2 corespond to dst_pt2 etc.
        # therefore, src_triangle corresponds to dst_triangle

        #Selecting the rectagle consisting the triangle of src image
        rect_src_triangle = cv2.boundingRect(src_triangle)
        x_src, y_src, w_src, h_src = rect_src_triangle

        #Creating a mask of the size of the rectangle comprise of the src_triangle
        cropped_mask1 = np.zeros((h_src, w_src), np.uint8)

        points_src_tri = np.array([[src_pt1[0] - x_src, src_pt1[1] - y_src],
                          [src_pt2[0] - x_src, src_pt2[1] - y_src],
                          [src_pt3[0] - x_src, src_pt3[1] - y_src]], np.int32)

        cv2.fillConvexPoly(cropped_mask1, points_src_tri, 255)
        cropped_src_tri = cv2.bitwise_and(cropped_src_tri, cropped_src_tri,
            mask=cropped_mask1)
```

```
    #
        #=============================================================================================
        # selecting the rectagle consisting the triangle of dst image
        rect_dst_triangle = cv2.boundingRect(dst_triangle)

        x_dst, y_dst, w_dst, h_dst = rect_dst_triangle
        points_dst_tri = np.array([[dst_pt1[0] - x_dst, dst_pt1[1] - y_dst],
                           [dst_pt2[0] - x_dst, dst_pt2[1] - y_dst],
                           [dst_pt3[0] - x_dst, dst_pt3[1] - y_dst]], np.int32)

        cropped_mask2 = np.zeros((h_dst, w_dst), np.float32)
        cv2.fillConvexPoly(cropped_mask2, np.int32(points_dst_tri), (1.0), 16, 0)

    #
        #=============================================================================================
        # Warp each triangles
        points_src_tri = np.float32(points_src_tri)
        points_dst_tri = np.float32(points_dst_tri)
        # Calculating the Affine transformation for each triangle and warping it
        M = cv2.getAffineTransform(points_dst_tri, points_src_tri)
        warped_triangle = cv2.warpAffine(cropped_src_tri, M, (w_dst, h_dst), None,
            flags=cv2.WARP_INVERSE_MAP , borderMode=cv2.BORDER_REFLECT_101)

        # Adding triangles to output image
        warped_triangle = warped_triangle*cropped_mask2
        # Adding individual triangles to create the output image
        Output_Image[y_dst:y_dst + h_dst, x_dst:x_dst + w_dst] =
            Output_Image[y_dst:y_dst + h_dst, x_dst:x_dst + w_dst] * ( (1.0) -
            cropped_mask2 )
        Output_Image[y_dst:y_dst + h_dst, x_dst:x_dst + w_dst] =
            Output_Image[y_dst:y_dst + h_dst, x_dst:x_dst + w_dst] + warped_triangle
    return Output_Image

def pixel_interpolation2(Input_Image, Offset):
    """This function does a NN Interpolation to mask the leftover empty
    pixels after image dewarping. Uses Gaussian Kernel.
    Parameters:
        Input_Image: Output Image (2D numpy array) from Triangulated Dewarp.
    Return:
        Input_Image: Corrected Input Image as a 2D numpy array."""

    kernel = Gaussian2DKernel(x_stddev=0.3)
    Output_image = np.zeros((Input_Image.shape[0], Input_Image.shape[1]))
    Input_Image = Input_Image[Offset[2]:Offset[3], Offset[0]:Offset[1]]
    Input_Image[Input_Image<=0] = np.nan
    Image_Array = interpolate_replace_nans(Input_Image, kernel)
    Image_Array[np.isnan(Image_Array)] = 0
```

```
    Output_image[Offset[2]:Offset[3], Offset[0]:Offset[1]] = Image_Array

    return Output_image
```

A.1.2 Separating Diffracted Image and Transmitted Image

```
def seperate(Image_Array):
    """ Seperate the Diffracted image from the Transmitted image
     Parameters:
        Image_Array : 2D numpy array of the image
    Return:
        image: return a new 2D numpy array"""

    Image_Array = np.rot90(Image_Array,3)
    length_image = np.shape((Image_Array))
    Ymid = int(length_image[0]/2)
    Yend = int(length_image[0])
    Xend = int(length_image[1])
    Trans_image1 = Image_Array[Ymid:Yend, 0:Xend]
    Trans_image = np.fliplr(Trans_image1)
    Diff_image = Image_Array[0: Ymid, 0:Xend]
    return Trans_image, Diff_image
```

A.1.3 Crystal Distortion Correction

```
def Crystal_Dist_Correction(Input_Image, src_triangle,dst_triangle):
    """Affine transform the diffracted image to correct the vertical stretch of the
    diffracted image by a factor of 1/cos(2theta_B).
    parameters:
        Input_Image: Diffracted image
        src_triangle: Diffracted image fiducial points as a numpy array
                    eg:- src_triangle = np.array([(DUpper), (DLower), (DCentre)])
        dst_triangle: Transmitted image fiducial points as a numpy array
                    eg:- dst_triangle = np.array([(TUpper), (TLower), (TCentre)])
    Return:
        corrected and flipped image as a 2D numpy array."""

    points_src_tri = np.float32(src_triangle)
    points_dst_tri = np.float32(dst_triangle)
    # Calculating the Affine transformation for each triangle and warping it
    M = cv2.getAffineTransform(points_dst_tri, points_src_tri)
    Image_Array = cv2.warpAffine(Input_Image, M, (2672, 2000), None, \
        flags=cv2.WARP_INVERSE_MAP , borderMode=cv2.BORDER_REFLECT_101)
    dewarped_image = np.fliplr(Image_Array)
    return dewarped_image
```

A.1.4 Distortion Correction Multiprocessing

This function put all of the code above and use Python's multiprocessing to correct distortion corrections.

```
"""
Created on Fri Aug 21 13:22:56 2020

@author: - Jayan Gunasekera
Multiprocessing Distortion Corrections and Ratio Calculations.
Saved as Multiprocessing(Distortion Corrections).py
"""
import numpy as np
from PIL import Image
import concurrent.futures
import Distortion_Corrections as dc

def distortion_correction_processing(input_img_dir,output_img_dir,input_filename,
                                     dark_ave, Offset, triangle_indexes, src_points,
                                     dst_points,Final_Crop_Offset, ROI_Offset,
                                     src_triangle, dst_triangle):
    '''Processing both FOT and crystal distortion corrections and calculating I_D/I_T
        ratios.
    Parameters:
        input_img_dir: Location of the .img projection files.
        output_img_dir: Output directory as a string.
        input_filename: File name as a string.
        dark_ave: Averaged dark field image (same size as the input projection image).
        Offset: To use in recreate_image function.
        triangle_indexes: List of triangle indecies generated using tie points
            (src_points).
        src_points: list of x and y coordinates as numpy array (distorted coordinates).
        dst_points: list of x and y coordinates as numpy array (destination
            (undistorted)
                                                              coortdiantes).
        Final_Crop_Offset: Coordinates to crop the sample area of the projections.
                            - np.array([y_start, y_end , x_start, x_end])
        ROI_Offset: ROI of air (outside the sample) to calculate I_D/I_T ratios.
                            - np.array([y_start, y_end , x_start, x_end])
        src_triangle: Diffracted beam figucial marker points as a numpy array of
            tuples.
                            - np.array([(DUpper), (DLower), (DCentre)], np.int32)
        dst_triangle: Transmitted beam figucial marker points as a numpy array of
            tuples.
                            - np.array([(DUpper), (DLower), (DCentre)], np.int32)
    Return:
        Save processed files and prints the processed filename with the calculated
            ratio. '''
```

```
    Image_Array1 = dc.open_file(input_img_dir,input_filename)
    Image_Dark_corr = dc.dark_correction(Image_Array1, dark_ave)
    Input_Image = dc.recreate_image(Image_Dark_corr,Offset)
    Dewarped_Image = dc.Triangulated_Dewarping(Input_Image, triangle_indexes,
        src_points, dst_points)
    Output_Image = dc.pixel_interpolation2(Dewarped_Image, Offset)
    Trans_image, Diff_image = dc.seperate(Output_Image)

    ## Crop Transmitted and save it to Transmitted Images folder.
    Trans_image_cropped = Trans_image[Final_Crop_Offset[2]:Final_Crop_Offset[3],
        Final_Crop_Offset[0]:Final_Crop_Offset[1]]
    Image.fromarray(Trans_image_cropped).save(output_img_dir + 'Transmitted Images/t'
        + input_filename[1:-3] + 'tif')

    # Crystal distortion correction for diffracted image.
    Diff_cryst_corr = dc.Crystal_Dist_Correction(Diff_image, src_triangle,dst_triangle)
    # Crop Diffracted (crystal distortion corrected) image and save it to Diffracted
        Images folder.
    Diff_image_cropped = Diff_cryst_corr[Final_Crop_Offset[2]:Final_Crop_Offset[3],
        Final_Crop_Offset[0]:Final_Crop_Offset[1]]
    Image.fromarray(Diff_image_cropped).save(output_img_dir + 'Diffracted Images/d' +
        input_filename[1:-3] + 'tif')

    # I_D/I_T Calculation and saving it to Ratios folder.
    I_T = Trans_image_cropped[ROI_Offset[2]:ROI_Offset[3], ROI_Offset[0]:ROI_Offset[1]]
    I_D = Diff_image_cropped[ROI_Offset[2]:ROI_Offset[3], ROI_Offset[0]:ROI_Offset[1]]
    Ratio = np.mean(I_D)/np.mean(I_T)
    output_name = output_img_dir + 'Ratios/r' + input_filename[1:-4]
    np.save(output_name, Ratio)
    return print(input_filename[0:-4] + ' ===== done', Ratio)


if __name__ == '__main__':
    # Access and generate a sorted list of .img file names.
    input_filename_list = dc.input_file_list(input_img_dir)
    with concurrent.futures.ProcessPoolExecutor() as executor:
        for input_filename in input_filename_list:
            result = executor.submit(distortion_correction_processing,
                input_img_dir,output_img_dir,input_filename,
                                dark_ave, Offset, triangle_indexes, src_points,
                                    dst_points, Final_Crop_Offset, src_triangle,
                                    dst_triangle)
```

A.1.5 FOT Distortion Correction (Method 1)

This method is an adaptation of the code published at https://github.com/TimSC/image-piecewise-affine. The original source code is available under the Simplified BSD License as specified in https://github.com/TimSC/image-piecewise-affine/blob/master/COPYING.

```
import numpy as np
from scipy.spatial import Delaunay
from PIL import Image
import matplotlib.pyplot as plt
import time
import numba as nb

def triangulate_points(dst_points):
   """Delaunay triangulation of 2D points.
   Parameters:
   dst_points = 2D array containing xy coordinates
   Return:
   Delaunay estimation"""
   tri = Delaunay(dst_points)
   return tri
```

Calculating Transformation

This section was only run once since the distortion is the same in all images.

```
def T_estimate(vertices, src_points, dst_points):
   """Calculate the transformation T = S.T^-1 where, T = transformation matrix, S =
       src coords, D = dest coords.
   Parameters:
      src_points = 2D array containing xy coordinates of src
      dst_points = 2D array containing xy coordinates of dst
   Return:
      Transformation matrix array for the whole image"""
      T = []
   for i in range(len(vertices)):
      Pos_Vert_Src = np.hstack((src_points[vertices[i]], np.ones((3,1)))).transpose()
      Pos_Vert_Dst = np.hstack((dst_points[vertices[i]], np.ones((3,1)))).transpose()

      # Here we do the matric calculation to find the Transfomation matrix for each
          triangle
      T_per_tri = np.dot(Pos_Vert_Src, np.linalg.inv(Pos_Vert_Dst))
      T.append(T_per_tri)
   return T
```

Generating the Pixel Map

The following function was only run once and the output was save as a TIFF file so it can be imported later. This was because the distortion is the same in all images.

```
@nb.jit
def pixel_map_per_tri(dst_img, dst_points, tri):
   '''Generate the map of which pixel correspond to which triangle in the destination
   image.
   Parameters:
      dst_img = Destination image (2D numpy array)
      dst_points = Destination tie points
      tri = Delaunay estimation
   Return:
      2D numpy array'''
   x_min, x_max = dst_points[:,0].min(), dst_points[:,0].max()
   y_min, y_max = dst_points[:,1].min(), dst_points[:,1].max()
   Triangle_tess = np.ones((dst_img.shape[1],dst_img.shape[0]), dtype= np.int) *-1
   for i in range(int(x_min), int(x_max+1.)):
      for j in range(int(y_min), int(y_max+1.)):
         if i < 0 or i >= Triangle_tess.shape[0]: continue
         if j < 0 or j >= Triangle_tess.shape[1]: continue
         norm_space_coord = (float(i),float(j))
         simplex = tri.find_simplex([norm_space_coord])
         Triangle_tess[i,j] = simplex
   return Triangle_tess

@nb.njit
def Bilinear_interp_pix(src_img, posX, posY):
   '''Does Bilinear interpolation.
   Parameters:
      src_img = Source image
      PosX and PosY: Destination pixel x and y position
   Return:
      Interpolated pixel value'''
   modXi = int(posX)
   modYi = int(posY)
   modXf = posX - modXi
   modYf = posY - modYi

   #Get pixels in four corners
   bl = src_img[modYi, modXi]
   br = src_img[modYi, modXi+1]
   tl = src_img[modYi+1, modXi]
   tr = src_img[modYi+1, modXi+1]

   #Calculate interpolation
   b = modXf * br + (1. - modXf) * bl
   t = modXf * tr + (1. - modXf) * tl
```

```
    pxf = modYf * t + (1. - modYf) * b
    out = int(pxf+0.5)
    return out

@nb.njit
def warp(src_img, dst_img, Triangle_tess, T, dst_points):
    '''Map pixel intensities from source image to destination image.
    Parameters:
        src_img: Source image
        dst_img: Destination image
        Triangle_tess: output of function pixel_map_per_tri()
        T: Transformation matrix array for the whole image
        dst_points = Destination tie points
    Return:
        Dewarped image'''

    homog_coord = np.ones((3,), dtype = np.float64)
    x_min, x_max = dst_points[:,0].min(), dst_points[:,0].max()
    y_min, y_max = dst_points[:,1].min(), dst_points[:,1].max()
    x_maxi = (x_max +1.)
    y_maxi = (y_max +1.)
    for i in range(int(x_min),int(x_maxi)):
        for j in range(int(y_min), int(y_maxi)):
            homog_coord[0] = i
            homog_coord[1] = j
            pixel = Triangle_tess[i,j]
            if pixel == -1:
                continue
            affine = T[pixel]
            dst_img_coords = np.dot(affine,homog_coord)

            out1 = Bilinear_interp_pix(src_img, dst_img_coords[0], dst_img_coords[1])
            dst_img[j,i] = out1
    return dst_img
```

A.2 Curve Fitting Code

A.2.1 Intrinsic Rocking Curve Fitting

```
"""
Created on 5/09/2020

@author: - Jayan Gunasekera
"""
from lmfit.models import PseudoVoigtModel
import multiprocessing
import numpy as np
import itertools
from PIL import Image
from scipy import integrate

'''This Program fit RC3 no sample image stack using multiprocessing'''

input_dir = 'D:/RESEARCH 2020/DATA/Intrinsic RC Stack/'
output_dir = 'D:/RESEARCH 2020/DATA/Estimated Outputs/'

# Analyser crystal angular position
theta = np.arange(261) *(0.01/3600.)* (np.pi/180)*15/10**-6
# Open intrinsic RC stack as a numoy array (this is a 3D array)
image_stack = np.load(input_dir+'Intrinsic_RC_Stack.npy')
rows = image_stack.shape[0]
cols = image_stack.shape[1]
weights = None

# Pseudo-Voigt Function defined for integration.
def pseudo_voigt(x,A,frac,mu,g,s):
   '''This function calculate the Pseudo-voigt
   Parameters:
      x = theta values (independent variable)
      A = Amplitude
      a = fraction
      mu = centre
      g = sigma_g
      s = sigma '''

   y = (((1-frac)*A)/(g*np.sqrt(2*np.pi)))*np.exp(-((x-mu)**2)/(2*g**2)) +
       ((frac*A)/np.pi)*(s/(((x-mu)**2 +  s**2)))
   return y

def curve_fit_per_pixel(param):
   '''This function fit the Pseudo-Voigt model on pixel-by-pixel basis
   to intrinsic RC Stack.
   Parameters:
```

```
      Param: A list of tuples.
   Return:
      Estimated parameters of pixel-by-pixel intrinsic RC fitting.'''
   row = param[0]
   col = param[1]
   weights = 1/image_stack[row,col,0:261]
   mod_Pseodo = PseudoVoigtModel()
   pars1 = mod_Pseodo.guess(image_stack[row,col,0:261], x=theta)
   result1 = mod_Pseodo.fit(image_stack[row,col,0:261], pars1, x=theta,
       weights=weights)
   expected = image_stack[row,col,0:261]
   amplitude = result1.params['amplitude'].value
   fwhm = result1.params['fwhm'].value
   fraction = result1.params['fraction'].value
   centre = result1.params['center'].value
   sigma = result1.params['sigma'].value
   g = sigma/np.sqrt(2*np.log(2))

   # Calculating Area under the curve
   end = 260 *(0.01/3600.)* (np.pi/180)*15/10**-6
   integral = integrate.quad(pseudo_voigt,0,end,
       args=(amplitude,fraction,centre,g,sigma))
   area_under_curve = integral[0]

   # Chi-Square Calculation
   observed = result1.best_fit
   chisqr = np.sum(((observed - expected)**2)/expected)

   return (amplitude, fwhm, fraction, centre, g, sigma, area_under_curve, chisqr)

if __name__ == '__main__':
   row = range(rows)
   col = range(cols)
   paramlist = list(itertools.product(row,col))
   # Using python multiprocessing to increase processing efficiency
   pool = multiprocessing.Pool(processes=8)
   result = pool.map(curve_fit_per_pixel,paramlist)
   amplitude1, fwhm1, fraction1, centre1 = [], [], [], []
   g1, sigma1, area_under_curve1, chisqr1 = [], [], [], []
   for curve in result:
      amplitude1.append(curve[0])
      fwhm1.append(curve[1])
      fraction1.append(curve[2])
      centre1.append(curve[3])
      g1.append(curve[4])
      sigma1.append(curve[5])
      area_under_curve1.append(curve[6])
      chisqr1.append(curve[7])
```

```
    # Reshaping the outputs into a 2D array of size equivelent to the
    # size of intrinsic projection image and saving them in TIF format.
    amplitude_array = np.reshape(amplitude1, (len(row),len(col)))
    Image.fromarray(amplitude_array).save(output_dir+'RC3_amplitude.tif')

    fwhm_array = np.reshape(fwhm1, (len(row),len(col)))
    Image.fromarray(fwhm_array).save(output_dir+'RC3_fwhm.tif')

    fraction_array = np.reshape(fraction1, (len(row),len(col)))
    Image.fromarray(fraction_array).save(output_dir+'RC3_fraction.tif')

    centre_array = np.reshape(centre1, (len(row),len(col)))
    Image.fromarray(centre_array).save(output_dir+'RC3_centre.tif')

    g_array = np.reshape(g1, (len(row),len(col)))
    Image.fromarray(g_array).save(output_dir+'RC3_g.tif')

    sigma_array = np.reshape(sigma1, (len(row),len(col)))
    Image.fromarray(sigma_array).save(output_dir+'RC3_sigma.tif')

    area_under_curve_array = np.reshape(area_under_curve1, (len(row),len(col)))
    Image.fromarray(area_under_curve_array).save(output_dir+'RC3_area.tif')

    chi2_array = np.reshape(chisqr1, (len(row),len(col)))
    Image.fromarray(chi2_array).save(output_dir+'RC3_chisqr.tif')
```

A.2.2 Measured Rocking Curve Fitting

```
import numpy as np
import numba as nb
import PIL.Image as Image

def theta_calc(I_Ratios, Height,Position, Width):
    ''''Analyser crystal angular position calculation
    Parameters:
      I_Ratios = Measured I_D/I_T for a measured stack.
      Height = Left and right Intrinsic ratio curve Heights as a 1 x 2 numpy array.
      Position = Left and right Intrinsic ratio curve Centres as a 1 x 2 numpy array.
        Width = Left and right Intrinsic ratio curve Widths as a 1 x 2 numpy array.
    Return:
      2D numpy array of theta values each corresponding to a working point.'''
    theta_left = np.abs(-(np.sqrt((Height[0]/I_Ratios[0:4])-1))*0.5*Width[0] +
        Position[0])
    theta_right = np.abs((np.sqrt((Height[1]/I_Ratios[4:8])-1))*0.5*Width[1] +
        Position[1])
    theta_array = np.concatenate((theta_left,theta_right))
```

```
    return theta_array
```

Quadratic Fitting Method (QF)

Following functions estimate the Lorentzian parameters by fitting a second order polynomial to the reciprocal of equation 4.2 using χ^2 regression for each rocking curve in a given image stack.

```
@nb.njit
def lorentz_fit(x,y,sigma):
    '''Chi^2 regression to fit a Lorentzian model.
    Parameters:
        x = Analyser crystal angular positions.
        y  = Intensities of pixels at each working point from -5% to +5%.
        sigma = Experimental uncertainties.
    Return:
        Matrix elements for 3 simultaneous equations.'''
    p = 3
    y_var = (1/y)
    sigma_var = (1/y) *sigma
    alpha = np.zeros((p,p))
    beta = np.zeros((p,1))
    for k in range(1,p+1):
        for j in range(1,p+1):
            alpha[k-1,j-1] = np.sum(((x**(p-j))*(x**(p-k)))/(sigma_var**2))
        beta[k-1] = np.nansum(y_var*x**(p-k)/sigma_var**2)
    return alpha,beta

@nb.njit
def Stack_curvefit(theta, image_stack, sigma):
    '''Pixel-by-pixel Lorentzian curve fitting.
    Parameters:
        theta = Analyser crystal angular position.
        y  = Independent variable
        sigma = Experimental uncertainties (Here this was set to an array of ones).
    Return:
        Curvefit parameters for each image stack as 2D arrays.'''
    rows = image_stack.shape[0]
    cols = image_stack.shape[1]
    chi2_array = np.ones((rows,cols))
    Center = np.ones((rows,cols))
    FWHM = np.ones((rows,cols))
    Height = np.ones((rows,cols))
    Integral_sum = np.ones((rows,cols))
    for i in range(cols):
        for j in range(rows):
            alpha,beta = lorentz_fit(theta,image_stack[j,i],sigma)
            c = np.linalg.inv(alpha)
            coef = np.dot(c,beta)
```

```
            Height1 = 4*coef[0] / ((4*coef[0]*coef[2])-coef[1]**2)
            Position1 = -coef[1]/(2*coef[0])
            Width1 = np.sqrt(((4*coef[0]*coef[2])-coef[1]**2)/coef[0])/np.sqrt(coef[0])

            # Calculating area under the curve.
            x0 = 0
            x1 = 261 *(0.01/3600.)* (np.pi/180)*15/10**-6
            Lower_lim = -0.5*Height1*Width1*np.arctan((2*(Position1-x0))/Width1)
            Upper_lim = -0.5*Height1*Width1*np.arctan((2*(Position1-x1))/Width1)
            Area_Under_Curve = Upper_lim-Lower_lim
            y_lorentz = Height1/(1+((theta-Position1)/(0.5*Width1))**2)

            # Calculating Chi^2.
            chi2 = np.sum(((image_stack[j,i]-(y_lorentz))**2)/image_stack[j,i])
            FWHM[j,i] = Width1[0]
            Center[j,i] = Position1[0]
            Integral_sum[j,i] = Area_Under_Curve[0]
            Height[j,i] = Height1[0]
            chi2_array[j,i] = chi2

    return FWHM, Center, Integral_sum, Height, chi2_array
```

A.3 2D Fourier Integration and Linearity correction

A.3.1 2D Fourier Integration

This program implements 2D Fourier integration (see equation (2.53)) to combine the horizontal and the vertical components of the phase gradient to generate the 2D phase shift.

```
#%%
@author: - Jayan Gunasekera

import numpy as np
import matplotlib.pyplot as plt
import os
import PIL.Image as Image
import scipy.ndimage as ndimage
import itertools
import math
import time
import concurrent.futures

def input_file_list(input_dir):
    """This function generate a list of files names with the extension .img
    in a given folder
    Parameters:
        input_dir = path to the folder containg .img files"""
```

```
    input_filename = []
    # r=root, d=directories, f = files
    for r, d, f in os.walk(input_dir):
        for file in f:
            if file.endswith('.img') or file.endswith('.tif'): # in file:
                input_filename.append(file)
        input_filename.sort()
        return input_filename

def denominator_calculation_alternative(rows,cols):
    '''This function estimates the denominator of the
    2D integration equation (see equation 2.55)
    Parameters:
        rows = number of rows of the recreated image for continuity
        cols = number of rows of the recreated image for continuity'''
    denominator_array = np.zeros((rows,cols), dtype=complex)
    pixel_size = 16.2*10**-6
    dt = pixel_size
    k = (np.fft.fftfreq(cols, dt)) #cols
    l = (np.fft.fftfreq(rows, dt)) #rows
    l = l*1j
    for i in range(len(l)): #cols
        for j in range(len(k)): #rows
            denominator = 2*np.pi*1j*(l[i]+k[j])
            denominator_array[i,j] = denominator
    return denominator_array

def denominator_calculation(rows,cols):
    '''This function estimates the denominator of the
    2D integration equation (see equation 2.55)
    Parameters:
        rows = number of rows of the recreated image for continuity
        cols = number of rows of the recreated image for continuity'''
    pixel_size = 16.2*10**-6
    Nx, Ny = rows,cols
    kx = (np.arange(Ny) - Ny/2 + 1)/(Ny*pixel_size)
    kx = np.roll(kx, -int(math.floor(Ny/2))+1)
    unitx = np.zeros(Nx) + 1
    kx = 2*np.pi*np.outer(kx,unitx).T

    ky = (np.arange(Nx) - Nx/2 + 1)/(Nx*pixel_size)
    ky = np.roll(ky, -int(math.floor(Nx/2))+1)
    unity = np.zeros(Ny) + 1
    ky = 2*np.pi*np.outer(ky,unity)
    denominator = 1j*kx - ky
    return denominator

def Fourier_2D_Integration(image, input_filename_0,input_filename_180):
```

```
'''This function reconstructs the phase shift using equation 2.55.
Parameters:
    image = index of the image name in the input filename list
    input_filename_0 = names of the 0th position projections as a list
    input_filename_180 = names of the 180th position projections as a list
Output:
    Reconstructed phase shift image in radians'''
# Reconstructing Phase in radians
wavelength = 4.7686*10**-11
wave_vector = 2*np.pi / wavelength

image_0 = np.array(Image.open(input_dir_0+input_filename_0[image]))* 1*10**-6 # in
    Radians
image_180 = np.array(Image.open(input_dir_180+input_filename_180[image]))*
    1*10**-6 # in Radians
image_180 = np.fliplr(image_180)

# Translation for Clay Loam (uncomment when processing the Clay Loam sample)
# image_180 = ndimage.shift(image_180,(0, 75))
x_Direction = (image_0 - image_180)/(2*np.sin(8*np.pi/180))
y_Direction = (image_0 + image_180)/(2*np.cos(8*np.pi/180))

# Saving horizontal (x) and vertical (y) phase derivatives
# Image.fromarray(x_Direction).save(output_dir + 'x_direction_images/' +
    input_filename_0[image])
# Image.fromarray(y_Direction).save(output_dir + 'y_direction_images/' +
    input_filename_0[image])

# ROI selection for 3M with Aluminium and Teflon
x_Direction = x_Direction[165:365,0:1090] #-ROI_0  # Cropping the noisy sections 3M
y_Direction = y_Direction[165:365,0:1090] #-ROI_180 # Cropping the noisy sections
    3M


# ROI selection for Clay Loam
# x_Direction = x_Direction[:,230:780] #-ROI_0 # Cropping the excess air sections
# y_Direction = y_Direction[:,230:780] #-ROI_180 # Cropping the excess air sections


rows_image_180 = y_Direction.shape[0]
cols_image_180 = y_Direction.shape[1]

# Rearranging images for continuity
S_x_rearr = np.concatenate((x_Direction,-np.fliplr(x_Direction)), axis=1)
x_Direction = np.concatenate((S_x_rearr,np.flipud(S_x_rearr)), axis=0)

S_y_rearr = np.concatenate((y_Direction, -np.flipud(y_Direction)), axis=0)
y_Direction = np.concatenate((S_y_rearr, np.fliplr(S_y_rearr)), axis=1)
```

```
    rows = x_Direction.shape[0]
    cols = x_Direction.shape[1]

    # Determining the x,y coordinates in the fourier domain
    Denominator = denominator_calculation(rows,cols)
    Nx, Ny = x_Direction.shape
    Mx, My = y_Direction.shape


    n = Nx*Ny
    m = Mx*My
    numerator = np.fft.fft2(x_Direction)/n + 1j*np.fft.fft2(y_Direction)/m
    F_S = numerator/Denominator
    F_S[0,0] = 1e-30
    n_F_S = F_S.shape[0]*F_S.shape[1]
    phase = np.fft.ifft2(F_S)*n_F_S
    phase = phase - np.amin(phase)
    phaseimage = phase.real

    # Isolating a single phase image
    phaseimage = phaseimage[0:rows_image_180, 0:cols_image_180]
    phaseimage = phaseimage *(-wave_vector)

    # Running the row by row linearity and background correction
    phaseimage = linearity_and_background_correction(phaseimage)

    Image.fromarray(phaseimage).save(output_dir + input_filename_0[image])
    return print(input_filename_0[image] +'==== Done')


input_filename_0 = input_file_list(input_dir_0)
input_filename_180 = input_file_list(input_dir_180)

if __name__ == '__main__':
    # Using python multiprocessing to increase runtime
    start = time.time()
    with concurrent.futures.ProcessPoolExecutor() as executor:
        for image in range(1800):
            result = executor.submit(Fourier_2D_Integration, image,
                input_filename_0,input_filename_180)

    end = time.time()
    print('Run Time: ',end-start)
```

A.3.2 Linearity Correction

This function applies a row-by-row linearity and background correction to the 2D phase images.

```
def linearity_and_background_correction(image):
    '''This function do a row-by-row linearity and background correction.
    Parameters:
        image = image that needs coorection as 2D numpy array.
    Output:
        Linearity and background corrected image'''
    rows = image.shape[0]
    cols = image.shape[1]
    Horz_corr_image = np.zeros((rows,cols))
    x_L = np.linspace(0,19,20)
    x_end = cols - 1
    x_R = np.linspace(x_end-20,x_end,20)
    x_array = np.append(x_L,x_R)
    for row in range(rows):
        y_L = image[row,0:20]
        y_R = image[row,cols-20:cols]
        y_Fit = np.append(y_L,y_R)

        p = np.poly1d(np.polyfit(x_array,y_Fit,1))
        columns = np.linspace(0,cols-1,cols)
        y_Fit = p(columns)
        delta_y = y_Fit - min(y_Fit)
        # Correcting Horrizontal linear error in projections
        y_new = image[row,:] -(delta_y)
        # background correction
        background = (np.mean(y_new[0:20]) +
            np.mean(y_new[len(y_new)-20:len(y_new)]))/2
        y_new = y_new - background
        Horz_corr_image[row,:] = y_new
    return Horz_corr_image
```

Appendix B

Additional Plots and Figures

B.1 Chapter 4: Additional Results

B.1.1 Transmitted Beam Centroid image

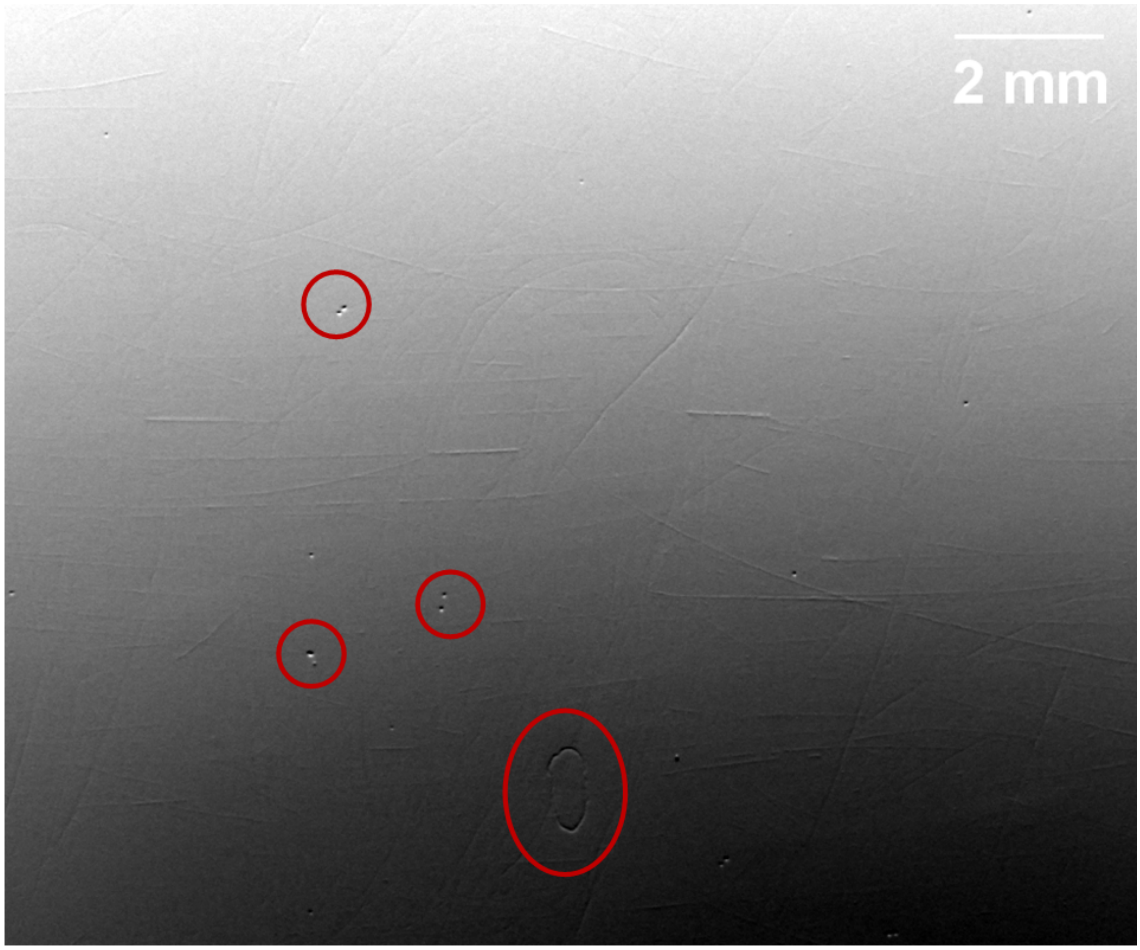

Figure B.1: *The transmitted beam centroid image by fitting* 935×780 *pixels on pixel-by-pixel basis, respectively. These were extracted using the 261 transmitted intrinsic rocking curve projections taken for the clay loam sample. The circles indicate the same artefacts that are also seen in the diffracted beam intrinsic centroid image.*

B.1.2 Three-Material Intrinsic RC Extractions

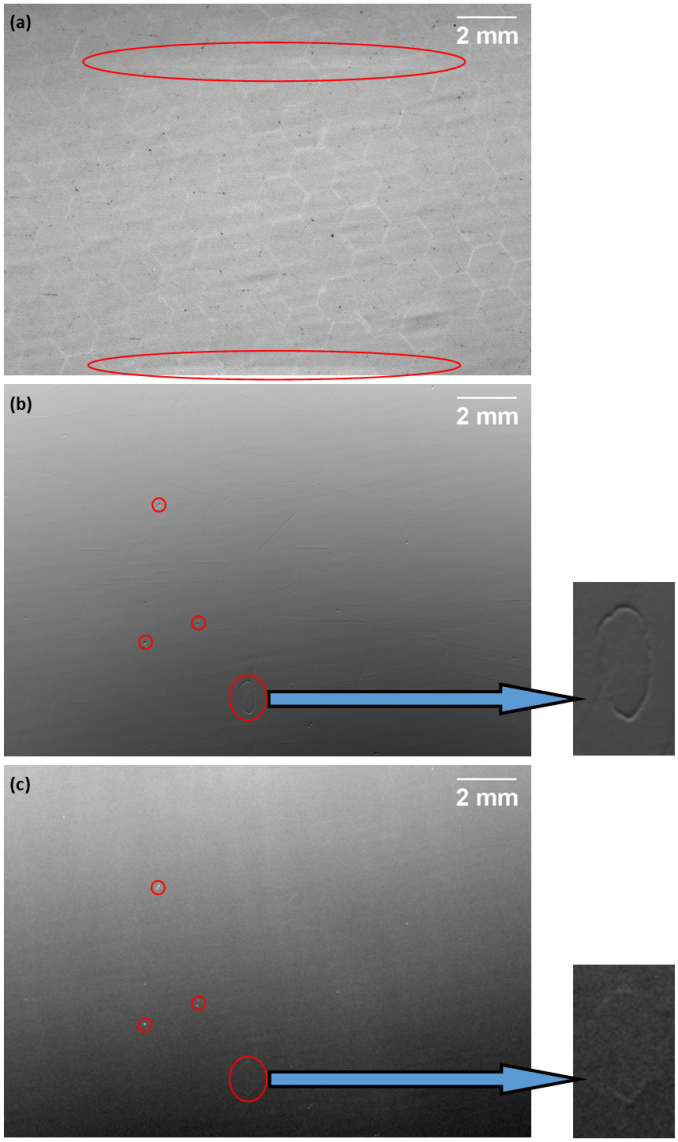

Figure B.2: *(a), (b), and (c) display the extracted area under the curve, centroid, and full with at half maximum by fitting* 1090×770 *pixels on pixel-by-pixel basis, respectively. These were extracted using the 261 intrinsic rocking curve projections taken for the 3-material phantom. The horizontal markings indicated by the two ellipses in (a) seem to correspond to the upper and lower edges of a phantom. Same anomalies can be seen in both (b) and (c), which are highlighted by the red circles.*

B.1.3 Chapter 5: Additional Results

(a)

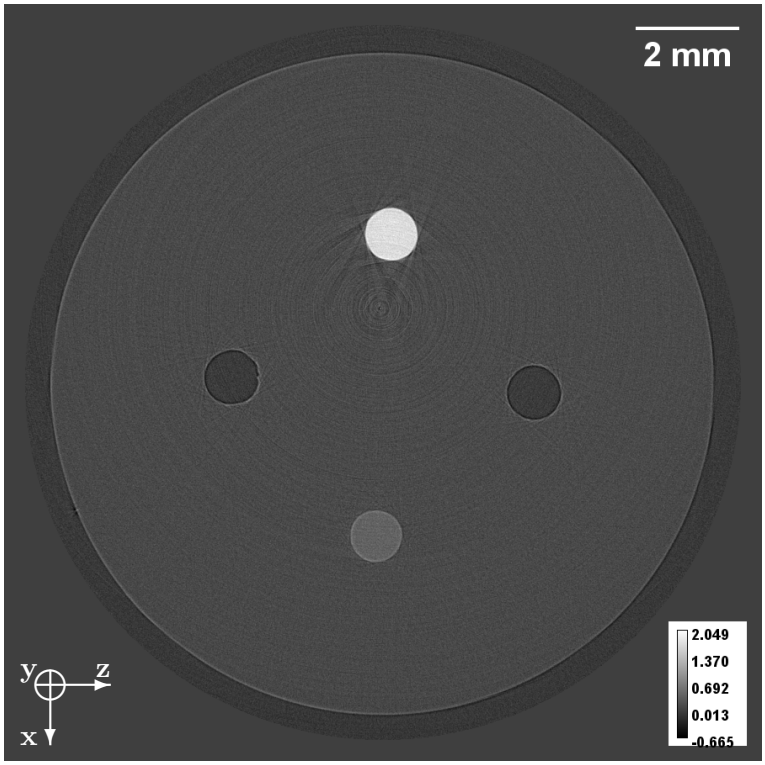

(b)

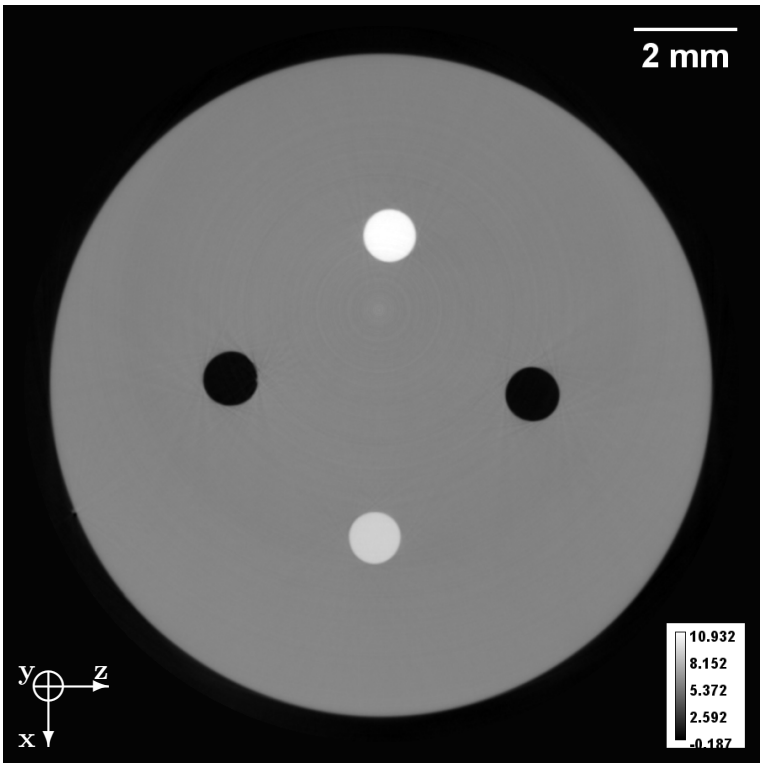

Figure B.3: *(a) and (b) represents the* 195^{th} *axial CT slice of the* β *and the* δ *map reconstructed using the eight-point reconstruction method.*

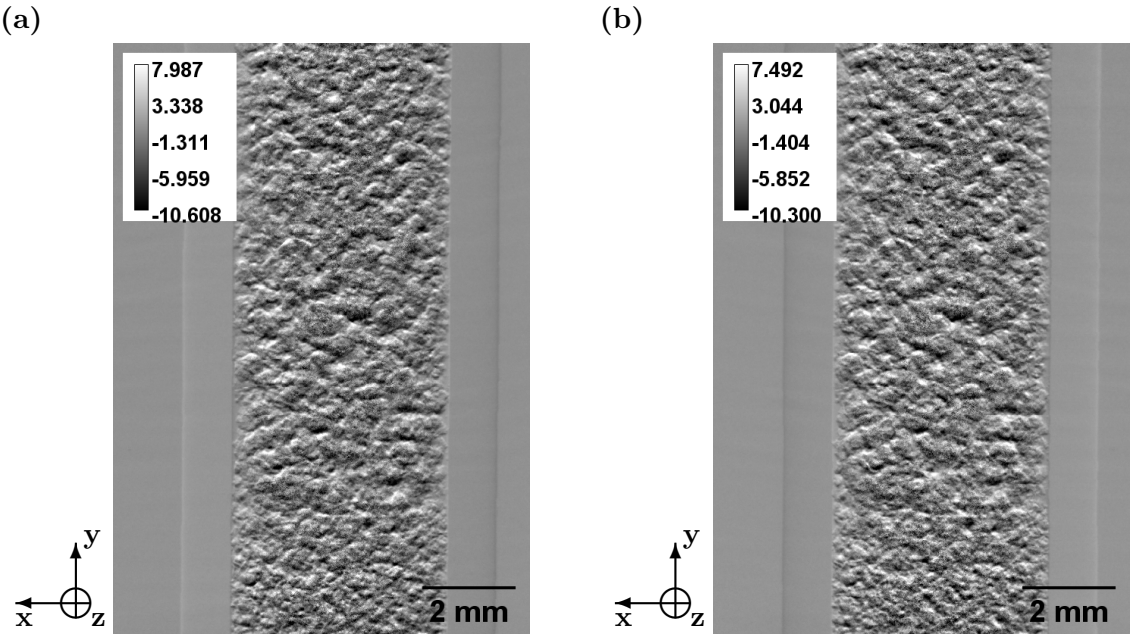

Figure B.4: *(a) and (b) display the $\mathbf{g}'_{0,y}$ and $\mathbf{g}'_{\pi,y}$ projections of the clay loam sample corresponding to the ψ and $\psi+\pi$ tomographic angular positions, respectively. These were extracted by subtracting the intrinsic centroid image from the sample centroid image. x, y, and z correspond to the horizontal, vertical, and the optical axis (see figure 3.2), respectively.*

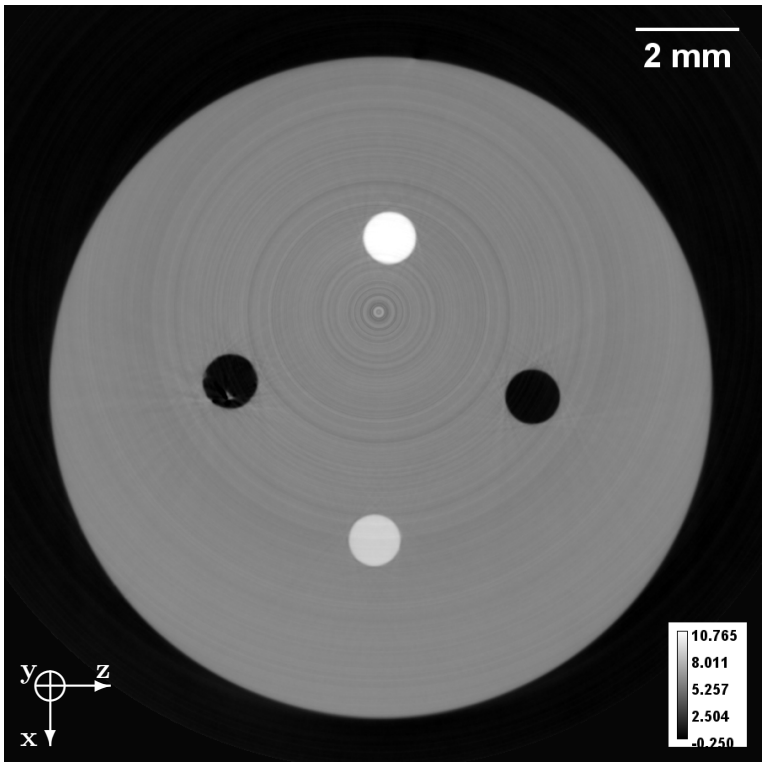

Figure B.5: *195^{th} axial CT slice reconstruction of the δ of the three-material phantom using the PsV model to estimate the sample rocking curves instead of the Lorentzian model.*

Table B.1: *A comparison between the theoretical δ values and the experimental δ values for Perspex, PTFE, and Aluminium estimated using figure B.5 . The theoretical values were taken from https://henke.lbl.gov/optical_constants/. Accessed date: 10/02/2021.*

Material	$\delta(\times 10^{-7})$		
	Theoretical	Eight-Point Reconstruction	Deviation From Theoretical δ (%)
Perspex ($C_5H_8O_2$)	3.9	5.5 ± 0.1	41
PTFE (C_2F_4)	6.5	8.7 ± 0.1	35
Aluminium	8.0	10.9 ± 0.1	35